

# Northumbria Research Link

Citation: Mokhtarimehr, Mehrnoush (2018) Sustainable photovoltaics – Cu<sub>2</sub>ZnSnS<sub>4</sub> thin films produced by the conversion of mechano-chemical synthesised precursors. Doctoral thesis, Northumbria University.

This version was downloaded from Northumbria Research Link:  
<https://nrl.northumbria.ac.uk/id/eprint/39988/>

Northumbria University has developed Northumbria Research Link (NRL) to enable users to access the University's research output. Copyright © and moral rights for items on NRL are retained by the individual author(s) and/or other copyright owners. Single copies of full items can be reproduced, displayed or performed, and given to third parties in any format or medium for personal research or study, educational, or not-for-profit purposes without prior permission or charge, provided the authors, title and full bibliographic details are given, as well as a hyperlink and/or URL to the original metadata page. The content must not be changed in any way. Full items must not be sold commercially in any format or medium without formal permission of the copyright holder. The full policy is available online: <http://nrl.northumbria.ac.uk/policies.html>



**Northumbria**  
**University**  
NEWCASTLE



**UniversityLibrary**

# Northumbria Research Link

Citation: Mokhtarimehr, Mehrnoush (2018) Sustainable photovoltaics – Cu<sub>2</sub>ZnSnS<sub>4</sub> thin films produced by the conversion of mechano-chemical synthesised precursors. Doctoral thesis, Northumbria University.

This version was downloaded from Northumbria Research Link:  
<http://nrl.northumbria.ac.uk/id/eprint/39988/>

Northumbria University has developed Northumbria Research Link (NRL) to enable users to access the University's research output. Copyright © and moral rights for items on NRL are retained by the individual author(s) and/or other copyright owners. Single copies of full items can be reproduced, displayed or performed, and given to third parties in any format or medium for personal research or study, educational, or not-for-profit purposes without prior permission or charge, provided the authors, title and full bibliographic details are given, as well as a hyperlink and/or URL to the original metadata page. The content must not be changed in any way. Full items must not be sold commercially in any format or medium without formal permission of the copyright holder. The full policy is available online: <http://nrl.northumbria.ac.uk/policies.html>



**Northumbria**  
**University**  
NEWCASTLE



**UniversityLibrary**



**Sustainable photovoltaics –  $\text{Cu}_2\text{ZnSnS}_4$   
thin films produced by the conversion of  
mechano-chemical synthesised  
precursors**

Mehrnoush Mokhtarimehr

PhD

2018





**Sustainable photovoltaics –  $\text{Cu}_2\text{ZnSnS}_4$   
thin films produced by the conversion of  
mechano-chemical synthesised  
precursors**

Mehrnoush Mokhtarimehr

A thesis submitted in partial fulfilment of the  
requirements of the University of Northumbria at  
Newcastle for the degree of Doctor of Philosophy  
Research undertaken in the Faculty of Engineering  
and environment

September 2018



## Abstract

To develop sustainable photovoltaic materials in a competitive power-generation market, several parameters such as cost, resource availability, environmental constraints in both material selection, and processing should be taken into account. In this context,  $\text{Cu}_2\text{ZnSnS}_4$  (CZTS) compound can be a promising candidate for Photovoltaic (PV) applications since apart from its material properties, which make it a suitable choice for PV applications; all its constituent elements are abundant in the crust. This leaves us to focus on synthesising such a compound in order to improve the quality and consequently enhance the performance of devices fabricated from CZTS thin films.

The purpose of the work proposed for this PhD project is to develop a low cost and energy efficient non-vacuum deposition processing and to gain an in-depth understanding of the key parameters required to synthesise the CZTS thin film absorber layers for PV solar cells. The research includes the processing technique to (i) prepare a precursor solution with the use of metal oxide/sulphide compounds, (ii) establish a scalable deposition technique, and (iii) study the sulphurisation process by varying the conversion condition. To achieve this, a preliminary study has been done on the established technology of fabricating the  $\text{Cu}_2\text{ZnSnSe}_4$  (CZTSe) thin films via vacuum deposition technique in order to provide a key insight into critical process parameters in developing Kesterite formation and the CZTS thin films. Finally, the life cycle assessment of fabricating CZTS thin films using vacuum and non-vacuum deposition methods has been studied. The four main damage categories of climate change, human health, eco-toxicity, and resources have been estimated using SimaPro Software with regard to the consideration of  $\text{CuIn}_x\text{Ga}_{(1-x)}\text{Se}_2$  (CIGS) (as a reference) processed via vacuum deposition technique.

The present study suggests an optimising route to prepare CZTS compound from metal oxide/sulphide compounds using a non-vacuum deposition technique. The study offers promising results using two techniques of spraying and slot-die for producing the deposition at lab-scale, which has a potential for large-scale processing. The results illustrated the impacts of conversion conditions on the micro and crystal structures of the CZTS thin films. In terms of environmental impacts, both vacuum and non-vacuum deposition techniques exhibited a significant potential benefit over CIGS thin films. However, the environmental impacts were found to depend critically on the compounds selected for the precursor and the processing.



*“The day I become aware of my ignorance is  
the day I can see myself as knowledgeable”*

*Avicenna*

## Table of Contents

Abstract .....	i
Declaration .....	vii
Acknowledgements .....	viii
List of Abbreviations.....	xi
List of Symbols .....	i
1 Introduction.....	1
1.1 Solar energy and the use of Photovoltaic devices .....	1
1.2 Towards sustainable materials: solar cells thin film technology .....	1
1.3 The aims of the current research project .....	3
1.4 The structure of the thesis .....	4
2 Principles of Solar Cells .....	6
2.1 Solar Spectrum .....	6
2.2 Semiconductor materials .....	7
2.3 The Introduction of p-n Junction and Diode .....	8
2.4 Light Absorption .....	10
2.5 Solar cell operation.....	11
2.5.1 Ideal solar cell: Diode in Dark .....	11
2.5.2 Ideal solar cell: Diode under illumination.....	11
2.5.3 Solar Cell Parameters .....	13
2.5.4 Non-ideal Solar Cells: losses and efficiency limits.....	14
2.6 Possible Materials for use in heterojunction solar cells .....	17
3 Literature Review .....	18
3.1 Cu-Chalcogenide based absorber layers.....	18
3.1.1 CIGS device configurations .....	19
3.1.2 Fabrication techniques and challenges of CIGS thin films.....	21
3.2 CZTS(e) based absorber layer .....	22
3.3 Challenges in fabrication of CZTS(e) thin films.....	24
3.3.1 Formation of secondary and ternary compounds .....	24
3.3.2 Defects in CZTS(e) .....	26
3.3.3 Interfaces of CZTS(e) thin film .....	27
3.4 Parameters affecting the quality of CZTS(e) thin films .....	29
3.4.1 Phase evolution of CZTS(e) thin films .....	29
3.4.2 Ambient gas composition and total pressure during conversion .....	31
3.4.3 Conversion Time, Temperature, and Heating profile .....	32
3.4.4 Chalcogen Source (S and/or Se) .....	33

3.4.5	Surface etching .....	34
3.4.6	Post-conversion heat treatment with extra chalcogen source (sulphur and/or selenium) .....	35
3.5	Possible fabrication techniques to prepare CZTS(e) absorber layers.....	35
3.5.1	Vacuum Deposition Technique.....	35
3.5.2	Non-Vacuum Deposition techniques .....	36
3.6	Part of previous work at Northumbria University .....	41
3.7	Sustainability assessment of photovoltaics .....	41
4	Methodology, Experimental Procedure, and Characterisation Techniques.....	45
4.1	Methodology .....	45
4.2	Experimental Procedure .....	47
4.2.1	Preparing the substrates and the Mo back contact .....	48
4.2.2	Absorber layer processing techniques.....	48
4.2.3	Preparing buffer layer by Chemical Bath Deposition (CBD) .....	58
4.2.4	Front Contact.....	59
4.3	Characterisation Techniques .....	59
4.3.1	DektakXT Profilometer: Film Thickness.....	59
4.3.2	Mastersize Particle Analyser.....	60
4.3.3	Contact Angle Analyser .....	61
4.3.4	Scanning electron microscope and elemental composition analysis (SEM/EDX) .....	61
4.3.5	X-ray Diffraction (XRD).....	64
4.3.6	Raman spectroscopy.....	70
4.3.7	Intensity modulated photocurrent spectroscopy (IMPS).....	71
4.3.8	External quantum efficiency (EQE).....	73
5	Preliminary investigations .....	76
5.1	CZTSe absorber layer fabricated by vacuum deposition technique.....	76
5.1.1	Preheating and method of supplying the selenium .....	76
5.1.2	Pre-treatment by varying conversion pressure and temperature .....	84
5.1.3	Summary of Results and Discussion.....	86
5.2	The fabrication of precursor solution via ball milling, non-vacuum deposition technique .....	89
5.2.1	Milling time.....	89
5.2.2	Ball size.....	90
5.2.3	Suspension solution.....	92
5.2.4	Thin film fabrication via various non-vacuum deposition techniques.....	93
5.2.5	Summary of Results and Discussion.....	93



5.3	Conclusion.....	94
6	CZTS thin films' fabrication via non-vacuum deposition technique .....	97
6.1	Conversion parameters .....	97
6.1.1	Ambient gas composition and total pressure .....	97
6.1.2	Precursor's composition.....	99
6.1.3	Sulphurisation time (conversion time).....	100
6.1.4	Heating profile during the sulphurisation process .....	103
6.1.5	Ambient gas composition and conversion/sulphurisation dwell time ....	105
6.1.6	Phase evolution by varying the conversion temperature .....	110
6.1.7	Supplying the Sulphur during the conversion/sulphurisation .....	111
6.1.8	Conversion/ Sulphurisation temperature.....	112
6.1.9	Total ambient pressure and Temperatures .....	115
6.1.10	Conversion/Sulphurisation time with the new conversion conditions ....	118
6.1.11	Post-conversion heat treatment with excess mass of Chalcogen .....	120
6.1.12	Surface etching.....	122
6.1.13	Summary of Results and Discussion.....	124
6.2	Follow-up trials .....	127
6.2.1	CZTS thin film fabrication using Slot-Die as a method of deposition ...	128
6.2.2	Supplying sulphur in precursor solution .....	131
6.2.3	CZTSSe thin film fabrication via non-vacuum deposition technique.....	133
6.2.4	Summary of Results and Discussion.....	138
6.3	Conclusion.....	139
7	Sustainability assessment of CZTS thin films as an absorber layer of PV solar device .....	142
7.1	Introduction .....	142
7.2	Experimental design and System description.....	143
7.2.1	Goal and Scope of the study.....	143
7.2.2	Life Cycle Inventory analysis (LCI) .....	147
7.2.3	Life Cycle Impact Assessment (LCIA).....	150
7.2.4	Life Cycle Interpretation .....	155
7.3	Results and Discussion .....	155
7.3.1	Part (i). The environmental impacts of fabricating CZTS thin films considering only material input .....	155
7.3.2	Part (ii): The environmental impacts of fabricating CZTS thin films, considering material input and energy consumption .....	161
7.4	Conclusion.....	168
8	Conclusion and outlook .....	171

8.1	Development in Kesterite absorber layer .....	171
8.1.1	CZTSe absorber layers through preliminary investigations.....	171
8.1.2	Development of the precursor solution and deposition technique for the fabrication of CZTS thin films through preliminary investigations .....	172
8.1.3	Development of the conversion conditions for the fabrication of CZTS thin films .....	173
8.2	Environmental impacts of the fabrication of CZTS absorber layers via vacuum and non-vacuum processing techniques .....	175
8.3	Suggestions for future research .....	176
8.4	Original Contribution .....	177
	Appendices .....	180
	Appendix A: Liquid redox electrolyte and p-semiconductor junction.....	180
	Appendix B: The use of surfactant in precursor solution preparation .....	182
	Appendix C: Comparison of converted samples prepared via vacuum or non-vacuum deposition technique.....	185
	Appendix D: Process Assumptions .....	188
	References .....	190



## **Declaration**

I declare that the work contained in this thesis has not been submitted for any other award and that it is all my own work. I also confirm that this work fully acknowledges opinions, ideas and contributions from the work of others. All the external contributions made to this research and to this thesis, are highly acknowledged.

Any ethical clearance for the research presented in this thesis has been approved. Approval has been sought and granted by it was granted by the University Ethics Committee on 13/Feb/2015.

The word count for this thesis is 44992 words.

Name: Mehrnoush Mokhtarimehr

Signature:

Date: 27/09/2018

## **External Collaboration**

Part of this research was carried out in collaboration with Swansea University with the help of Dr. Trystan Watson, Dr, Wei Zhengfei, Dr Peter Greenwood for the Slot-Die Coating Technique and Raman Analyses and Bath University with kind consideration of Professor Laurie Peter and Dr. Sara Dale for the Raman analyses and EQE measurements.

## Acknowledgements

Throughout my PhD journey, I discovered myself and rediscovered who I am. I felt that I matured both personally and professionally, beyond what I expected of myself. Living and studying in the UK was a unique chapter of my life, one in which I met so many along the way who became the cornerstone of my new path. It is impossible to remember all who through their beautiful smile and heart made this project possible.

This PhD opportunity was granted to me by University of Northumbria. I value their support and thank them and appreciate it.

First and foremost, I want to express my sincere gratitude to my supervisors who through their dedication and leadership, this project led to the conclusion. My appreciation goes to Dr. Ian Forbes for his support, patience, warm advice, and honest counsel. He always accompanied me in difficult circumstances, offering his firm guidance. I cannot forget the devotion and commitment of Professor Nicola Pearsall. She offered me strength and the will to persevere throughout my project. I am grateful for her support and being there for me with her wise and valuable advice through my PhD journey. Her serene and determined character was one which inspired me to improve day by day.

Throughout this project, there were collaborations with Swansea University and University of Bath. I am indebted to Dr. Peter Greenwood, Dr. Trystan Watson, Dr. Wei Zhengfei, Dr. Sara Dale, and Prof. Laurie Peter who offered to cooperate on experiments for this thesis.

My respectful colleague, Dr. Jose Marquez Prieto, contributed to the scientific advancement of the project in a very warm and friendly manner.

This project required many experiments to be conducted in the Northumbria University laboratory. I thank Dr. Pietro Maiello and Rebecca Payne for their support and assistance. I also offer my appreciation to Dr. Svetlana Tatarkova for being my best friend and mentor.

I thank my family for their support and being there for me with their unconditional love. My parents always believed in me and my brother and sister offered advice. I love them till eternity. My special thanks go to my dear father, Enayat, my loving mother, Shekooh, my special sister, Maryam, and my respecting brother, Alireza.

I have to remember friends who through their smiles and loyalty, made this journey enjoyable. These friends were more than mere acquaintances, but acted in the role the family. I wish to thank of my very kind and unique friends Linh, Malcolm, Francesco, also I would like to thank Fahimeh, Cecil, Alma, Hamid, and Laure.

*I dedicate this work to my Parents,  
Shekooh Faazeli and Enayat Mokhtarimehr,  
for all their unconditional sacrifices to nurture my growth.*



## List of Abbreviations

AM	Air Mass
CBD	Chemical Bath Deposition
CIGS	$\text{CuIn}_x\text{Ga}_{(1-x)}\text{Se}_2$
CZTS	$\text{Cu}_2\text{ZnSnS}_4$
CZTSSe	$\text{Cu}_2\text{ZnSn}(\text{S}_x\text{Se}_{1-x})_4$
DALY	Disability-Adjusted Life Years
EDX	Energy Dispersive X-ray Spectroscopy
EQE	External Quantum Efficiency
GWP	Global Warming Potential
IMPACT 2002+	Impact Assessment Methodology
IMPS	Intensity Modulated Photocurrent Spectroscopy
IPA	Isopropyl Alcohol
ISO	International Organization for Standardization
ITO	Indium Tin Oxide
LCA	Life Cycle Assessment
LCI	Life Cycle Inventory analysis
LCIA	Life Cycle Impact Assessment
LED	Light-Emitting Diode
PDF	Potentially Disappeared Fraction of species
PM	Particle Matter
PV	Photovoltaic
RTP	Rapid Thermal Processing
SEM	Secondary Electron Microscopy
SLG	Soda-Lime Glass
TCO	Transparent Conductive Oxide
XRD	X-ray Diffraction



## List of Symbols

$\phi_{ph}$	Spectral photon flux of the incident light
$\mu$	Mobility of generated charge carriers ( $\mu_n$ for electrons/ $\mu_p$ for holes)
$2\theta$	The angle between incident and reflected beam in X-ray diffraction technique
$d$	Lattice spacing
$E_b$	Energy of incident electron beam
$E_g$	Energy of band gap
FF	Fill factor
$G_{est}$	Photo-generation current density
$h$	Planck Constant
$I$	Current (in equations related to solar cell parameters) / Light intensity (in Beer-Lambert equation) / $I/I_0$ Peak intensity (in X-ray database tables)
$I_0$	Initial light intensity (in Beer Lambert equation)
$J$	Current density
$J_D$	Current density of diode
$J_L$	Current density due to illumination
$J_o$	Saturation current density
$J_{sc}$	Short circuit current density
$k$	Boltzmann constant
$L$	Diffusion lengths of minority carriers ( $L_n$ at n-type/ $L_p$ at p-type) / Thickness (in Beer-Lambert equation) / Penetration depth from the surface (in Grün range formula)
$\eta$	Efficiency
$R_s$	Series resistance
$R_{SH}$	Shunt Resistance
$T$	Temperature
$V$	Voltage at the p-n junction
$V_{oc}$	Open circuit voltage
$w$	Depletion layer width
$\alpha$	Absorption coefficient
$\lambda$	Wavelength
$\nu$	Frequency
$\tau$	Life time of carriers ( $\tau_p$ for holes, $\tau_n$ for electrons)



# **Chapter 1**

## **Introduction**

# 1 Introduction

## 1.1 Solar energy and the use of photovoltaic devices

With increasing world population and over consumption, there is a growing concern on how to meet the energy demand. Moreover, the use of fossil fuels threatens the global climate due to the creation of greenhouse gases. One of best possible solutions is to reduce the world's dependence on non-renewable resources as well as introduce new and clean energies. In this context, the use of solar energy can be an elegant technology. This involves the conversion of sunlight into electricity using an electronic device named a solar cell. The process of converting solar energy to electricity occurs due to the photovoltaic effect, and the specific materials (semiconductors) which facilitate such a phenomenon are called photovoltaic (PV) materials.

It is estimated that the coverage of 0.16% of the earth's surface with 10% efficient solar cells, would provide more energy than the estimated current global demand [1]. If the PV market would intend to promote a significant contribution to the global energy demand, the development of high performance solar devices is required. This should be provided alongside the fabrication and development of solar devices with the use of low cost and environmental friendly material and processing [2]. In this context, new materials and techniques are developed daily in laboratories with the aim of being reasonable for large-scale production.

## 1.2 Towards sustainable materials: solar cells thin film technology

Silicon-based devices are highly known in today's industry, showing a high efficiency of 20-25%. However, due to their low absorption coefficient and having an indirect band gap, a relatively large thickness of material is required to fabricate a silicon based solar device [3, 4]. This encouraged the idea of substituting thin film solar cells instead of the thicker solar devices (silicon based solar devices), in order to reduce the material usage and manufacturing capital costs. Thin-film PV cells includes a semiconductor layer with a direct band gap and few micrometres ( $\mu\text{m}$ ) of thickness, which is about 100 times thinner than the current silicon solar cells. As examples of two successful thin film solar devices,  $\text{CuIn}_x\text{Ga}_{(1-x)}\text{Se}_2$  (CIGS) and CdTe have shown the efficiency of 22.6% and 21%, respectively at laboratory scale [5, 6]. The Miasolé

Company has recently reported the efficiency of 16% for commercialised CIGS thin films with an area of approximately  $2\text{m}^2$  [7]. However, in spite of the high efficiency of CIGS and CdTe, due to the toxicity of cadmium and resource restrictions of indium, gallium, and tellurium, the production of solar devices based on CdTe or CIGS absorber layers at high level of gigawatt deployment of PVs, could be constrained. This limitation can affect the cost and production of solar devices in large-scale production.

According to the reports stated by Fraunhofer-Institute for Solar Energy Systems, the total global PV production in 2016 was estimated at 75 GW with 4.9 GW (~7% of total PV production) attributed to the thin film technologies of CdTe, CIGS, CIS, and a-Si [8]. With a relatively conservative estimation assumed by IEA 2014 on the cumulative PV installed capacity (4670 GW by 2050), and with regards to the ~7% contribution of thin films in PV market, as it was in 2016, it is expected that at least 327 GW of the PV market will be provided by thin film technology by 2050 [9]. Among the thin film PV cells, the  $\text{Cu}_2\text{ZnSnS}_4$  compound (CZTS) could be regarded as a promising substitution since it consists of elements, which are present at relatively high concentrations in the crust and can be produced at a quantity of hundreds of thousands to millions of tonnes, annually. Moreover, CZTS has similar properties to that of the CIGS compound. CZTS was first synthesised in 1966 and the first CZTS solar cell with the efficiency of 0.66% was fabricated in 1988. Afterwards, the efficiency reached 2.3% in 1997 [10]. Consequently, the idea of using this compound as an absorber layer has been regarded as an attractive and promising research area [11-13]. The studies on fabricating CZTS compound have been developed alongside the  $\text{Cu}_2\text{ZnSnSe}_4$  (CZTSe) and the  $\text{Cu}_2\text{ZnSn}(\text{S},\text{Se})_4$  (CZTSSe) compounds. Although the selenium containing compounds have shown a higher efficiency compared to the pure sulphide (CZTS), the study on developing the CZTS thin film absorber layer is of great significance due to the absence of the toxic element of selenium [14]. Compared to sulphur, selenium has less abundance in the earth's crust. Nevertheless, selenium's relative abundance in copper extraction, as being a by-product, and its potential to be extracted from coal, especially from high sulphur coal, might make Se-containing compounds reasonably attractive for large-scale thin film deployment [15]. The p-type chalcogenide semiconductor CZTS(e) has a high absorption coefficient (over  $\sim 10^4\text{cm}^{-1}$ ), and a direct band gap with the values of  $\sim 1.0\text{ eV}$  for pure selenide (CZTSe) and  $\sim 1.5\text{ eV}$  for the pure sulphide (CZTS). Strategies to improve the performance of devices have resulted in increasing the efficiency from 3.2%

in 2009 for CZTSe [16], to 12.6% in 2015 for a CZTSSe based solar device [17]. Although the production of  $\text{Cu}_2\text{ZnSn}(\text{S},\text{Se})_4$  (CZTS(e)) thin films has not been commercialised yet, it is predicted that this material has a potential to meet a significant proportion of electricity generation without adverse impact on mining and refining capacity [9, 18, 19]. These factors have motivated researchers to develop CZTS(e) using processes compatible with large-scale production [20, 21].

In the current research, the metal oxide powders has been used in order to fabricate the CZTS thin films, the reason being the more stable material during the processing and more environmentally friendly compared to the metal sulphide powders. Moreover, it is assumed that the non-vacuum deposition technique compared to the vacuum deposition techniques has the advantage of higher throughput less expensive and consequently it could be more appropriate for large-scale fabrication.

### 1.3 The aims of the current research project

The main objectives of this study can be summarised as follows:

- Synthesising the CZTS precursor solution with a non-vacuum processing technique of ball milling. The precursor solution is made of the metal oxide/sulphide compounds using a carrier solution of isopropyl alcohol (IPA). To the best of our knowledge, this is the first time that such materials have been used to fabricate the CZTS compound.
- Fabricating the CZTS thin films via non-vacuum deposition technique of spraying, and evaluating the influence of ‘precursor composition and conversion parameters’ on ‘material and optical characteristics’ of CZTS thin films.
- Evaluating the environmental impacts of manufacturing CZTS thin films via vacuum and non-vacuum deposition techniques on four main damage categories of climate change, human health, eco-toxicity, and resources. This part of the research has been carried out with the use of SimaPro software.

The above studies have been conducted with preliminary investigations on:

- Synthesising the CZTSe thin films via a vacuum deposition technique (magnetron sputtering), and subsequently evaluating the synthesising processes on the composition and microstructure of fabricated CZTSe thin films.
- Establishing a homogenous precursor solution with optimisation of the relevant parameters of Ball Milling and synthesising process.

#### 1.4 The structure of the thesis

The current thesis contains 7 chapters. As stated in the present chapter, chapter 1 contains an introduction of the thesis. Chapters 2 contains an overview on the theory of solar cell operation together with relevant previous studies, respectively. Chapter 3 presents the methodology used for the thesis, the experimental procedures, and an introduction of the characterisation techniques used for evaluating the acquired data. Chapters 4 and 5 include the studies and the experimental results, which have been achieved through the PhD thesis. Chapter 6 presents an evaluation of sustainability for fabricating the CZTS absorber layer via two different methods of vacuum and non-vacuum deposition techniques by simulation using SimaPro Software. Chapter 7 provides a summary of the study presented in this PhD thesis. This chapter also offers several suggestions for further investigations.

## **Chapter 2**

# **Theory and the Literature Review**



## **2 Theory and the literature review**

The first part of this chapter presents the principles of solar cells including several concepts such as the introduction of solar spectrum and solar irradiance as an input of a solar device, the importance of light absorption, the fundamental concepts of physics of p-n junctions and solar cells, and the performance of solar cells. Moreover, important parameters such as short circuit current, open circuit voltage, fill factor, and solar energy conversion efficiency will be explained as well as imperative concerns that contribute to losses in solar devices.

This second part this chapter presents an overview of Cu-chalcogenide thin film solar cells and the development in the technology from Chalcopyrite to Kesterite structures. Special emphasis is put on the challenges and the development of synthesising CZTS(e) (Kesterite crystal structure), as one of the aims of this study is to develop the CZTS thin films. Moreover, a summary of the achievements so far and progress in synthesising CZTS(e) thin film solar cells using different fabrication techniques will be presented. Finally, the achievements that been reported in previous literature on LCA and PV sustainability evaluation will be presented.

### **2.1 The principle of solar cells**

#### **2.1.1 Solar Spectrum**

Sunlight is a portion of electromagnetic radiation. The Sun radiates sunlight over a range of wavelengths known as the solar spectrum (250-2500nm). According to the electromagnetic spectrum, the solar spectrum is divided into three bands of 1. Ultra-violet light (UV) (290 nm-380 nm), 2. Visible light (380 nm-780 nm), and 3. Infrared light (IR) (780-2500 nm). The visible and the IR light account for a considerably higher portion of solar spectrum than the UV light (see Figure 2-1) [22].

The spectral irradiance from the sun is very similar to black body radiation at ~6000K. However, when sunlight reaches the earth, the spectral distribution of solar radiation is attenuated. A significant portion of the visible irradiance is scattered and even reflected back to space by clouds and aerosols. Solar irradiance could also be affected by factors such as the sun's location in the sky, the daytime, time of year, and the geographical

location. For more information on this topic the reader is referred to the related text books [3, 4].

In this context, a Standard Test Condition (STC) for both industry and test laboratories is recommended to be used, which is an irradiance of  $1000\text{W/m}^2$ , with the Air mass (AM) of 1.5, and a cell temperature of  $25^\circ\text{C}$ . The AMx is defined as a factor indicating the global spectrum on the earth's surface with  $x=1/\cos\theta$ , where  $\theta$  is a deviation from normal incidence (see Figure 2-2) [3, 23].

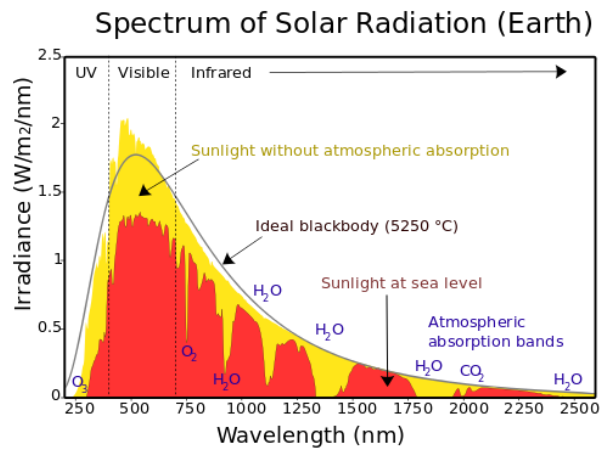


Figure 2-1. The spectrum of solar radiation with respect to wavelength [22].

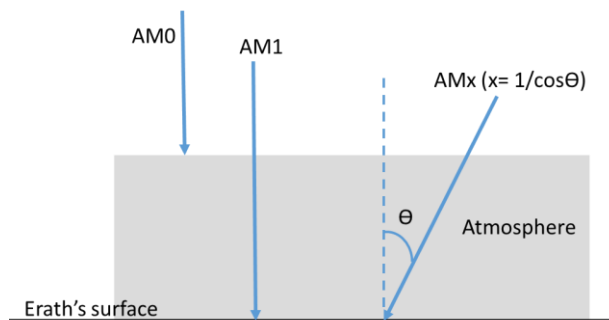


Figure 2-2. A schematic illustrating the Air Mass definition. The angle  $\Theta$  is a function of the time of day, longitude, and latitude

### 2.1.2 Semiconductor materials

The study of semiconductors has been conducted for over 135 years when it was claimed that some materials may have a behaviour between metals and insulators, depending on

the occupation of electrons at energy levels. For semiconductor materials, all the electrons are present at the energy states in the valence band and at absolute zero temperature there is no electron at the energy states in the conduction band. The difference between the energy at the maximum valence band ( $E_v$ ) and the minimum conduction band ( $E_c$ ) is called the band gap energy ( $E_g$ ) which is an important characteristic of all semiconductors. In this case, at higher temperature and depending on how narrow the band gap is, electrons present in the valence band can move to the conduction band. While, there is no band gap for metals and electrons can freely move at conduction level and at any temperature. However, the band gap energy of insulators is too large for electrons to shift from valence band to conduction band energy levels.

Semiconductors are divided into two main categories of intrinsic and extrinsic semiconductors. The former include those semiconductors in which free electrons in the conduction band and holes in the valence band can be excited and freely move across the band gap with only thermal energy. A doping process can form the extrinsic semiconductors. Depending on the characteristic of the dopant, the n-type and p-type semiconductors will be created. N-type semiconductors are those accepting so-called donor impurities, giving them free electrons in the lattice which do not belong to any covalent bonds and can easily move to the conduction band. P-type semiconductors form when the guest atoms (impurities) have not enough electrons to satisfy the host structure. The space left behind by the electron allows a covalent bond to move from one electron to another, thus appearing to be a positive charge moving through the crystal lattice. This empty space is called a "hole" which has a positive charge and such impurities are named acceptors [3, 4].

### **2.1.3 The Introduction of p-n Junction and Diode**

If the p-type and n-type semiconductors are interconnected to form a p-n junction, then a diffusion of electrons occurs from the region of high electron concentration into the region of low electron concentration. This will eventually lead to the recombination of electrons and holes across the p-n junction, creating a so-called depletion region or Space Charge Region (SCR) (see Figure 2-3). The presence of donor and acceptor atoms with positive and negative charges within the SCR lead to the formation of an electric field known as built-in electric field. This electric field forces the charge carriers to move in the opposite direction of the concentration gradient. The diffusion of carriers due to the

concentration gradient continues to flow until the internal electric field created across the SCR gets large enough to prevent further flow. Such an electrical component is called a diode [3, 4].

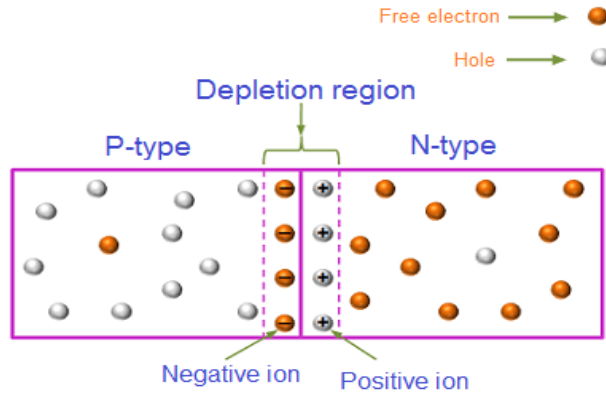


Figure 2-3. A schematic diagram of a p-n junction and the depletion region or SCR. The figure is adapted from [24]

Under equilibrium conditions when no external voltage, magnetic field, illumination, or other perturbing force is applied, the Fermi level is constant across the junction. Fermi level is the chemical potential of semiconductors which describes the average energy necessary to add or remove a small quantity of electrons to the system. This level as shown in Figure 2-4a, is located close to the conduction band and valence band for n-type and p-type semiconductors, respectively. When the n-type and p-type semiconductors are connected to each other, the band edges bend to equalise the Fermi level (see Figure 2-4b) [3, 4]

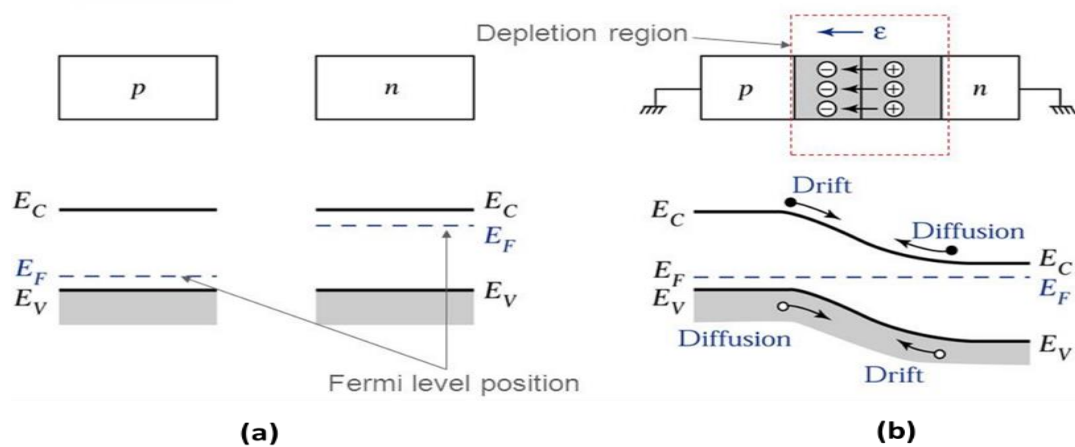


Figure 2-4. The location of Fermi level (a) before and (b) after p-n junction under equilibrium condition [25]

However, if a voltage is applied to a diode, there is no equilibrium anymore and this can affect the width of the SCR. The external electric field can be in forward or reverse bias modes. In forward bias mode, the internal electric field and the width of SCR is decreased. Thus, current can flow through the external electrodes. While in reverse bias mode, the width of the SCR is increased and that prevents the flow of current through the electrode, as shown in Figure 2-5.

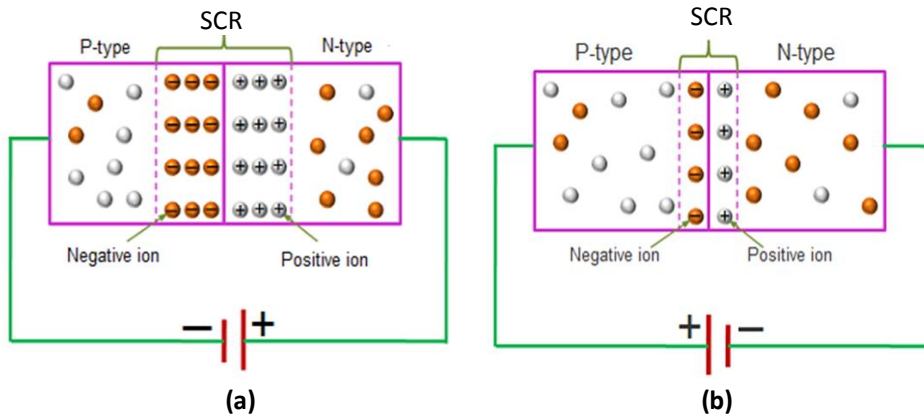


Figure 2-5. A schematic of diode a) Reverse bias, b) Forward bias [24]

#### 2.1.4 Light Absorption

For photovoltaic devices, reflection and transmission are typically considered as loss mechanisms, since photons that are not absorbed do not generate power. Photons falling onto a semiconductor material can be divided into three groups based on their energy quantity compared to that of the semiconductor band gap [3],  $E$  and  $E_g$  denote to energy of photons and band gap energy, respectively :

- If  $E < E_g$ , photons interact weakly with the semiconductor and pass through it.
- If  $E = E_g$ , photons will be absorbed and the generation of electron-hole pairs will occur.
- If  $E > E_g$ , photons will be strongly absorbed. However, for photovoltaic applications, the photon energy larger than the energy value of the band gap will be wasted as thermalisation losses.

The light intensity that passes through the material can be calculated using the Beer–Lambert law (equation (2-1)).  $I$  is the light intensity,  $I_0$  is the initial light intensity,  $\alpha$  is an

intrinsic material parameter known as the absorption coefficient, and  $L$  is the total thickness (it should be noted that the effect of reflection is ignored in the equation (2-1)).

$$I = I_0 e^{-\alpha L} \quad (2-1)$$

The absorption coefficient ( $\alpha$ ) is an indicative of the length that incident light with a certain wavelength penetrates into a material before being absorbed. As the name indicates, the absorption coefficient could determine the minimum thickness which is required to design a material in order to absorb the light effectively [3].

### 2.1.5 Solar cell operation

A solar cell, in principle, includes a p-n junction or semiconductor diode which can collect and absorb the electromagnetic energy coming from the sun and use that to generate electric power. This section presents a summary of the characteristics of ideal and non-ideal solar cells.

#### 2.1.6 Ideal solar cell: Diode in dark

In a dark situation, the diode equation for an ideal p-n junction is calculated by the equation (2-2) known as Shockley equation. The term  $J_0$  is the saturation current density of the p-n junction ( $A/cm^2$ ) which is also called dark current density,  $V$  refers to the voltage at the junction,  $K$  is the Boltzmann constant,  $q$  is the electron charge, and  $T$  is the absolute temperature. It should be noted that the term  $I$  is the current which depends on the area of diode or solar cell. However, the current density ( $J$ ) is independent of the solar cell area and is usually used to describe the current of solar cells [3]. For an ideal diode in dark, the J-V curve illustrates that  $J = J_D$  (see Figure 2-6(a)).

$$J_D = J_0 \left( e^{\frac{qV}{kT}} - 1 \right) \quad (2-2)$$

#### 2.1.7 Ideal solar cell: Diode under illumination

Under illumination, an incoming light will produce electron-hole pairs and create a forward bias condition for a diode. Thus, as shown in Figure 2-6(b), the total current density follows the equation (2-3). Thus, under illumination, the current density-voltage curve of a solar cell shifts downwards, (see Figure 2-7).

$$J = J_D - J_L \quad (2-3)$$

The total current density for a diode under illumination obeys the equation 2-4, where  $J_L$  is the photo-generation current density. This term indicates the current created from those electron-hole pairs generated per unit of area due to the light excitation, and collected

before being recombined. In fact, in order to create the current, the free minority electron carriers in the p-type region and free minority hole carriers in the n-type region need to diffuse towards the junction, pass through the junction, diffuse to the other side, and finally pass through the external circuit. During the above stages, the minority charge carriers need to be safe and not be removed or recombined. Equation 2-5 shows that  $J_L$  depends on  $G_{est}$  which is defined as the photo generation rate of the carriers. The terms of  $L_n$  and  $L_p$  (equation 2-6) representing the diffusion lengths of minority carriers;  $w$  denotes the depletion layer width,  $\mu$  specifies the mobility of generated charge carriers, and  $\tau$  indicates the mean life time. More details in this area are presented in several text books [3, 4].

$$J = J_0 \left( e^{\frac{qV}{kT}} - 1 \right) - J_L \quad (2-4)$$

$$J_L = qG_{est} (L_n + L_p + w) \quad (2-5)$$

$$L_n = \sqrt{\mu_n \tau_n \frac{kT}{q}} \quad (2-6)$$

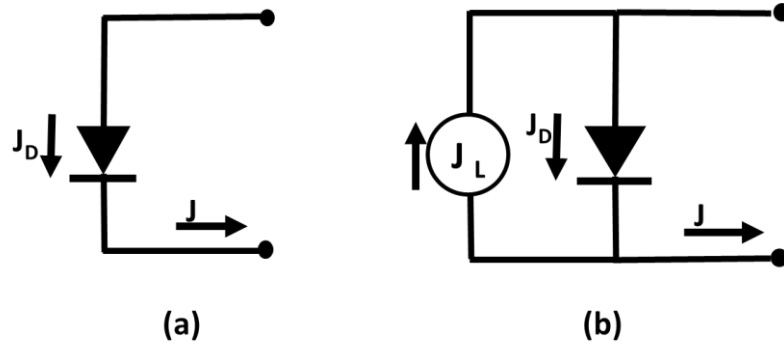


Figure 2-6. The equivalent circuit of (a) a diode in dark (b) a diode under illumination

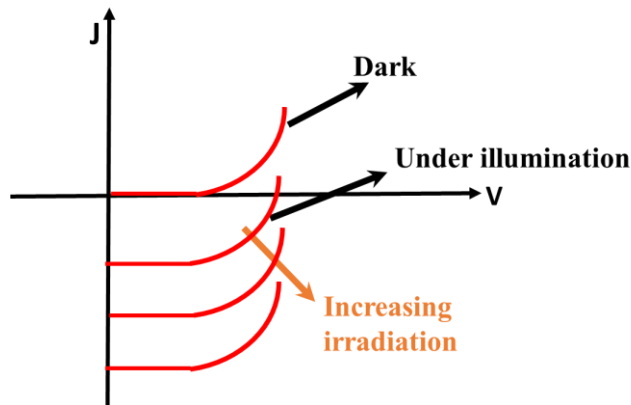


Figure 2-7. The J-V curve characteristics of a p-n junction in the dark and under illumination

### 2.1.8 Solar Cell Parameters

There are five main parameters that are usually used to characterise the performance of solar cells including maximum power, short circuit current density, open circuit voltage, fill factor, and conversion efficiency. This section presents the definition of the mentioned parameters.

✚ The short-circuit current density:  $J_{sc}$

The short circuit current density refers to the current per unit area that can be achieved under illumination when the device is short-circuited and no bias voltage is applied.

$$J_{sc} = -J_L \quad (2-7)$$

✚ The open circuit voltage

The open circuit voltage is the voltage when the circuit is open and thus the total current density is zero.

$$V_{oc} = \frac{kT}{q} \ln\left(\frac{J_L}{J_0} + 1\right) \quad (2-8)$$

✚ Maximum power point and Fill Factor

A circuit needs both current and voltage. Thus, a point known as maximum power point ( $P_{max}$ ) on the curve (see Figure 2-8) is studied which shows the highest power that a solar cell can generate. The associated voltage and current density are  $V_m$  and  $J_m$ , respectively. The ratio between the theoretical power ( $J_{sc} \times V_{oc}$ ) and the maximum possible power ( $V_m \times J_m$ ) is defined as Fill Factor (FF) [3]. Graphically, the fill factor is the area of a rectangle within the J-V curve, which is determined by  $P_{max}$  (see Figure 2-8).

$$FF = \frac{J_m \times V_m}{J_{sc} \times V_{oc}} \quad (2-9)$$



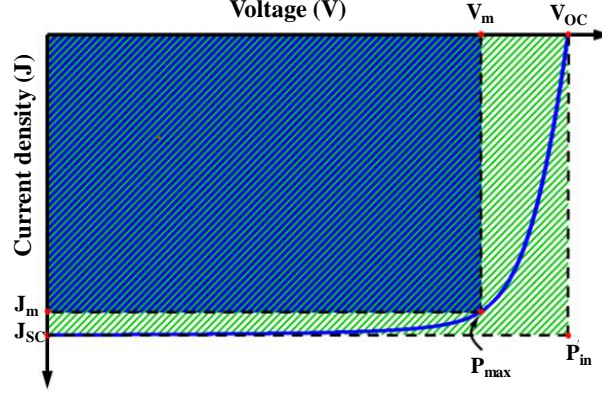


Figure 2-8. A schematic of J-V curve under illumination is shown. The figure is adapted from [26]. In case of an ideal solar cell, the J-V curve is a rectangular (green area) with the fill factor equal to one.

### Conversion Efficiency

The efficiency of a solar cell ( $\eta$ ) is determined as the ratio between the maximum power generated ( $P_{\max}$ ) and the incident power of radiation ( $P_{\text{in}}$ ).

$$\eta = \frac{P_{\max}}{P_{\text{in}}} = \frac{\text{FF} \times J_{\text{sc}} \times V_{\text{oc}}}{P_{\text{in}}} \quad (2-10)$$

#### 2.1.9 Non-ideal Solar Cells: losses and efficiency limits

A real solar cell experiences several losses, which limit its performance. Considering all the possible losses that might occur for a real solar cell, the conversion efficiency is defined through the Equation 2-11. The influence of each term is briefly presented in the following equation, for more details the reader is referred to the text books [3, 4].

$$\eta = \underbrace{\frac{E_G \int_0^{\lambda_G} \phi_{I,\lambda} d\lambda}{\int_0^{\infty} \frac{hc}{\lambda} \phi_{I,\lambda} d\lambda}}_1 \underbrace{(1-R^*)}_2 \underbrace{\text{IQE}_{op}^*}_3 \underbrace{\eta_G^* \text{IQE}_{el}^*}_4 \underbrace{\frac{A_f}{A_{total}}}_5 \underbrace{\frac{eV_{oc}}{E_G}}_6 \text{FF} \quad (2-11)$$

1. **Spectral mismatch:** The first term of Equation 2-11 is indicative of the efficiency loss due to the non-absorption of long wavelength radiation. This can simply describe as spectral mismatch of the energy distribution of photons in the solar spectrum and the band gap of a semiconductor material (absorber layer).  $\phi_{ph}$  denotes to the spectral photon flux of the incident light,  $E_G$  is the energy of band gap, and  $\lambda_G$  denotes the wavelengths of photons corresponding to the band gap energy of the absorber layer of a solar device.

2. Reflection losses: Since the solar cell is not completely black, always a part of the incident energy that can be converted into a usable energy by the solar cell is lost due to the reflection.  $R^*$  refers to the reflectivity in the wavelength range of interest (see part 2 of equation 2-11).
3. Incomplete absorption due to finite thickness: When light penetrates into a material, it will be partially absorbed by the absorber layer, depending on the material thickness and its absorption coefficient. Besides, the absorption in other layers of a solar device may also take place which is regarded as parasitic absorption. Moreover, due to the limited thickness, not all the incoming light is absorbed across the absorber layer. The incomplete absorption loss is described by the internal optical quantum efficiency  $IQE_{op}$  that is defined as the probability of a photon being absorbed in the absorber material (see part 3 of equation 2-11).
4. Recombination due to electronic and optical properties of materials: it should be noted that not all the carriers generated in a solar cell are collected at the front or rear contacts. The carriers can recombine in the bulk, at the interfaces, and at the surfaces of the junctions. Impurity atoms, lattice defects, and spurious phases can act as recombination traps. Reduction in the concentration of such impurities and defects can enhance the diffusion length of minority carriers and this can decrease the recombination losses in a solar cell [1, 27]. Thus, the chemical properties and the micro and crystal structure of absorber layers can affect the efficiency of solar cells. This is mainly dependent on the material utilised and the synthesising procedure employed.

The term External Quantum Efficiency (EQE) is regarded as one of the common characteristics often used to evaluate the performance of a solar device. This indicates the ratio of those charge carriers successfully collected and the number of photons incident on the solar device creating electron hole pairs in the absorber. The External Quantum Efficiency (EQE) is presented versus wavelength (nm) (see Figure 2-9) [3]. The EQE can be approximated by part 2, 3, and 4 of equation 2-11 [3].

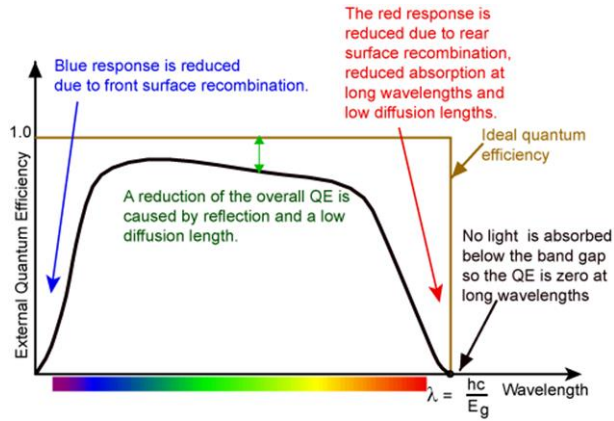


Figure 2-9. The EQE spectrum of a high quality crystalline silicon based solar cell [28]

5. Shading losses: the design of the front electrodes is of great importance to minimise the loss which occurs due to shading phenomenon. Thus, the optimal design of front contacts is a trade-off between a coverage factor and the shading areas. This influences the efficiency (see part 5 of equation 2-11).
6. Voltage drop due to series and shunt resistance; Electrical losses: In a real device, the reduction in efficiency is also defined by dissipation of power through parasitic resistance. Two common resistances are the Shunt ( $R_{SH}$ ) and Series resistance ( $R_S$ ). The voltage drop due to the ( $R_S$ ) of a solar cell could result from the bulk resistance of the junction, the contact resistance between the junction and electrodes, and the resistance of the electrodes themselves.

The voltage drop due to the ' $R_{SH}$ ' can result due to the leakage current through the local defects in the junction (see Figure 2-10).

$$J = J_0 \left( e^{\frac{q(V - AJR_S)}{KT}} - 1 \right) + \left( \frac{V - AJR_S}{R_{SH}} \right) - J_L \quad (2-12)$$

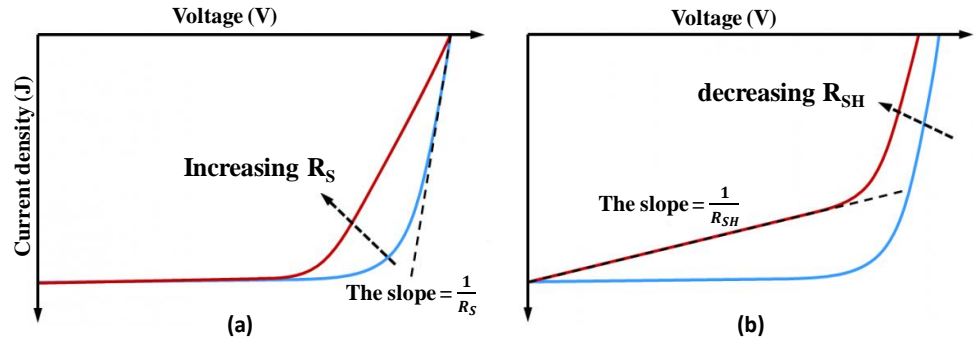


Figure 2-10. Schematic diagrams showing the influence of (a)  $R_s$  (b)  $R_{sh}$  on the J-V curve for an ideal solar cell; the figure is adapted from [26].

In analysing the solar cells' performance, the equation 2-11 can simply be expressed by equation 2-10, since all above parameters (1 to 6) affect the  $I_{sc}$  and  $V_{oc}$  of a solar device.

#### 2.1.10 Possible materials for use in heterojunction solar cells

In order to choose an appropriate material as an absorber layer, it is of great significance to consider the two initial characteristics: 1) having a large absorption coefficient ( $\alpha$ ) in that the incident light is absorbed in a few micrometres of thickness. Therefore, a thin layer of absorber layer can be sufficient for the purpose. 2) having an appropriate band gap in the range of 1-1.6 eV in order to achieve the highest possible efficiency, according to Shockley-Queisser limit. With only the consideration of these two factors, quite a lot of materials and compounds can be selected. However, some parameters such as availability, cost, and environmental safety, limit the choice of materials. Moreover, the synthesising processes is also a crucial factor in terms of cost and its influence on the properties of the finished material. In the next chapter, the Cu-chalcogenide compounds and the common synthesising methods that are often used for solar cell fabrication will be presented.

## 2.2 Literature Review

This chapter presents an overview of Cu-chalcogenide thin film solar cells and the development in the technology from Chalcopyrite to Kesterite structures. Special emphasis is put on the challenges and the development of synthesising CZTS(e) (Kesterite crystal structure), as one of the aims of this study is to develop the CZTS thin films. Moreover, a summary of the achievements so far and progress in synthesising CZTS(e) thin film solar cells using different fabrication techniques will be presented. Finally, the achievements that have been reported in previous literature on LCA and PV sustainability evaluation will be presented.

### 2.2.1 Cu-Chalcogenide based absorber layers

Cu<sub>2</sub>S was the first of Cu-chalcogenide materials used as an absorber layer. This was due to having a direct band gap of 1.2 eV and a high absorption coefficient. In 1981, Hall et al reported an efficiency of 10% using Cu<sub>2</sub>S based devices with Cd<sub>1-x</sub>Zn<sub>x</sub>S as an n-junction [29]. However, one of the problems of using Cu<sub>x</sub>S/CdS (x=1.8-2) solar cells is the aging and the degradation of this material when it is exposed to illumination. This was attributed to the diffusion of copper into the CdS, forming the Cu<sub>2-x</sub>S. The loss of copper contributes to a reduction in minority carrier diffusion length and absorption coefficient, and also it leads to an increase in band gap value [30].

Further studies in order to find an alternative materials instead of Cu<sub>x</sub>S led to the creation of ternary semiconductor compounds such as CuInSe<sub>2</sub> (CIS). In 1976, Kazmerski et al reported the record efficiency of 5% fabricating CIS via co evaporation technique [31]. Some researchers have used sulphur instead of selenium to prepare CuInS<sub>2</sub> which usually has the same abbreviation of CIS. These compounds were identified as promising candidates due to their high absorption coefficient of 10<sup>5</sup>cm<sup>-1</sup> and the band gap value of 1.0eV for pure selenide and 1.5eV for pure sulphide. However, the former is not regarded as an environmentally friendly material compared to the latter because of the replacement of sulphur instead of toxic element of selenium [32]. Studies have shown that the partial substitution of Ga instead of In in CuInSe<sub>2</sub> causes an increase in band gap to larger values. The band gap values of CuInSe<sub>2</sub> can be changed to a range of 1.1-1.24 eV for Cu(InGa)Se<sub>2</sub> with a Ga/(Ga+In) ratio of 0.25 and 0.35, respectively [33]. It was also reported that a higher performance can be achieved in case of tuning the band gap value across the absorber layer via grading the gallium content [34].

### 2.2.2 CIGS device configurations

Thin film based solar cells can be fabricated with two configurations of substrate and superstrate (see Figure 2-11). In the substrate configuration, the substrate (usually glass) is an inert component which needs to be mechanically and thermally stable. In superstrate configurations, the glass substrate acts as a window which transmits light into the solar device. Although both configurations have been successful models, it is reported that the superstrate configuration is less favourable due to the diffusion of CdS into the absorber layer at high temperature of CIGS synthesising [35, 36]. Moreover, in case of the substrate configuration, the diffusion of sodium from the glass substrate into CIGS has resulted in a higher performance of CIGS based devices. Although the incorporation of sodium could improve the cell performance, in order to avoid the non-uniform Na diffusion from Soda Lime Glass (SLG) and the irreproducibility, several groups have conducted studies on the use of barrier layers such as  $\text{Na}_2\text{Se}$ ,  $\text{NaF}$ ,  $\text{Na}_2\text{S}$  on top of the Mo layer [37-39]. In the following, the common materials and techniques used for the fabrication of other layers of CIGS based solar cells will be presented.

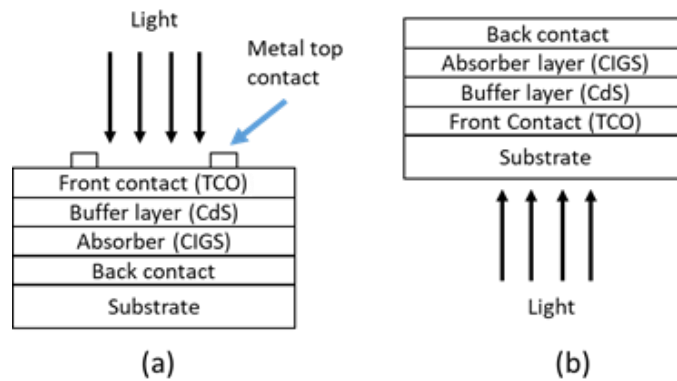


Figure 2-11. The schematic cross section of (a) substrate and (b) superstrate configuration of CIGS solar cell. The picture is adapted from [40].

#### Back contact

A Mo layer is often used as a back contact material for CIGS and CIS since it shows low resistivity, and a good adhesion between CIGS and SLG. It also has a very high melting temperature ( $\sim 2600^\circ\text{C}$ ) which contributes to a better stability at high temperature processing. Moreover, it acts as a reflector so it can reflect the unused light back into the absorber layer. However, a non-ohmic back contact may be created due to the formation of a thick layer of  $\text{MoS}(\text{e})_2$  at the interface of CIGS/Mo. The thick layer of  $\text{Mo}(\text{Se})_2$  will limit the device performance due to a high resistivity and weak adhesion [41], while, a

thin layer of  $\text{MoS}(\text{e})_2$  could be beneficial in that the transportation of holes can occur via tunnelling across the junction [42].

#### Absorber layer

The p-type conductivity of CIGS arises because of the copper, indium, and gallium vacancies ( $V_{\text{Cu}}$ ,  $V_{\text{Ga}}$ ,  $V_{\text{In}}$ ), and the antisite of  $\text{Cu}_{\text{In/Ga}}$  acting as shallow acceptors. The Fermi level rises close to conduction band in case of In-rich or Se-poor conditions, since these defects act as shallow donors [43, 44]. Moreover, in Cu-rich conditions, a conductive compound of  $\text{Cu}_2\text{Se}$  may form at the surface or may be created at the grain boundaries, which causes lower shunt resistance. In either cases, it leads to a reduction in solar cell performance [36].

The highest record efficiency has been obtained in Cu-poor condition and with the Ga/(Ga+In) and Cu/(Ga+In) ratio of 0.26 and 0.88-0.92, respectively [36]. The Zentrum für Sonnenenergie-Wasserstoff-Forschung Baden-Württemberg (ZSW) and the Solibro GmbH reported the best efficiency of 22.6% and 17.5% in lab scale with an area of  $0.5\text{cm}^2$  and commercial scale with an area of  $0.9\text{ m}^2$ , respectively [45-47].

#### Buffer layer

The advantage of using CdS as an n-type buffer layer ( $E_g \sim 2.4\text{eV}$ ) has shown a considerable progress in improving the performance of CIGS solar cells [48]. The Chemical Bath Deposition (CBD) is often used for the fabrication of CdS buffer layer. The CBD is usually prepared using three components of cadmium salt, such as  $\text{CdSO}_4$  as a cadmium source, ammonia ( $\text{NH}_3$ ) as a complexing agent, and thiourea ( $\text{CH}_4\text{N}_2\text{S}$ ) as a sulphur source. The presence of  $\text{NH}_3$  in CBD enables cleaning of the CIGS surface from the oxide compounds or any contamination before CdS nucleation. The CBD technique can provide thin layers of coating with a good coverage. The reduction of CdS thickness to 40-80 nm makes the n-junction act as a buffer layer rather than an emitter layer [36]. Moreover, the difference in lattice parameters of CdS and CIGS ( $a_{\text{CIGS}}=5.76\text{\AA}$ ,  $a_{\text{CdS}}=5.83\text{\AA}$ ) is not significant and that makes a good junction between these two compounds. This in turn, contributes to less structural defects at the interface [49]. Under illumination, the CdS layer transmits light up to 2.4eV to the absorber layer where electron-hole pairs are generated. The built-in electric field across the p-n junction (interface of CIGS/CdS) can sweep away and collect the generated electrons within the diffusion length region from p-type absorber to the n-type buffer layer. Oppositely, the holes are swept away

from n-type and collected by p-type layer. Moreover, the use of a CdS buffer layer can also protect the CIGS surface from ion damage during sputtering of the ITO layer, as a subsequent layer [36, 49]. Although the CdS buffer layer has shown good compatibility with CIGS absorber layer, due to the toxicity of cadmium and the material used in CBD, an alternative material has to be substituted in order to fabricate an environmentally friendly buffer layer. In this context, several studies have been done and for more details, the reader is referred to the related articles [50, 51]. As an example, the achievement by Solar Frontier can be referred, which was the fabrication of CIGS thin films using of 19.8% efficiency using the Cd-free buffer layer of (Zn,Mg)O/Zn(O,S,OH) and CBD method of deposition [5].

#### Transparent Conducting Oxide (TCO)

A Transparent conducting oxide should have good electrical conductivity to collect and transport the charge carriers to the contacts. The TCO should also have a high transparency to transmit light to the absorber layer. Thus, it needs to have a high band gap value. In addition to optoelectronic properties, this layer needs to have thermal, chemical, and mechanical stability. Two common TCOs are ZnO:In (IZO) and In<sub>2</sub>O<sub>3</sub>:Sn (ITO) with a resistivity of  $8 \times 10^{-4}$  and  $2 \times 10^{-4}$   $\Omega\text{cm}$  and a transparency of >80 and 85% of visible light, respectively. Both mentioned TCOs have a band gap with values between 3-4 eV, and can be fabricated via different techniques. One of the common techniques of deposition is sputtering [52, 53].

### **2.2.3 Fabrication techniques and challenges of CIGS thin films**

The fabrication of CIGS thin films consists of the deposition of thin layers with a subsequent thermal processing at high temperatures in a chalcogenide atmosphere (S and/or Se). The heat treatment step has a key role in improving the crystallinity and the quality of the absorber layer. However, providing a uniform temperature for a large area is one of the difficulties in scale-up processing techniques.

Various techniques have been used to synthesis the CIGS absorber layers. The most common approaches are sputtering, co-evaporation, and non-vacuum deposition. In the sputtering technique, the Cu/In/Ga are sputtered onto the substrate. Afterwards, the deposited layers are converted in an atmosphere saturated with chalcogen by the use of an elemental source (S and/or Se) or flowing H<sub>2</sub>S(e) gas during the heat treatment procedure. The co-evaporation technique has shown successful results in the fabrication



of CIGS thin films, especially when the development from two stage to three stage processing was reported. In such a technique, a precise control of the chemical composition and diffusion of elements across the absorber layer can be achieved. This provides the grading of gallium content by tuning the band gap which was led to a high efficiency. However, using a vacuum technique is time consuming and expensive in scale-up production [33, 54]. Thus, one of the challenges of the CIGS fabrication technique in industry is the high capital cost of processing.

Furthermore, commercialisation of CIGS in large-scale fabrication is one of the main concerns due to the toxicity of indium, gallium, and selenium elements. More importantly, indium is mainly a by-product of zinc extraction which shows that its availability is restricted by zinc production. The annual production for zinc and indium is 11900000 ton and 655 ton, respectively. Furthermore, gallium is regarded as a scare element. Only 5% of its global production is provided by zinc processing and 95% of that is processed as a by-product of bauxite ore or during aluminium processing. The scarcity of these elements increases the price of CIGS modules in scale-up production [36].

In addition, selenium is a relatively unreactive element. Thus, in order to avoid the creation of shallow donor level due to selenium vacancies ( $V_{Se}$ ), it is necessary to provide an excess mass of selenium during the sintering process. This, at times, causes the condensation of selenium on the sides of reactor walls and this will need to be recycled. Since selenium is a toxic element, this process might be challenging for the environment and induces limitation for the CIGS processing in large-scale fabrication [36, 55].

#### **2.2.4 CZTS(e) based absorber layer**

Kesterite semiconductor compounds have been introduced with the idea of substituting rare elements of Indium(In) in CIS with Tin(Sn) and Zinc(Zn) and preparing the  $Cu_2ZnSnS_4$  (CZTS) or  $Cu_2ZnSnSe_4$  (CZTSe) compound. Such a compound has several advantages over CIGS. Except selenium, all constitute elements in CZTSSe are non-toxic. It is reported that the abundance of Zn and Sn in earth's crust is 500 times and 14 times greater than In, respectively. This makes it an appropriate candidate for the thin film photovoltaic solar cell [56]. The similarity of Kesterite and Chalcopyrite in structure and electronic properties, turns the CZTS(e) Kesterite structure into a promising substitute instead of Chalcopyrite CIGS thin films. Due to the certain similarities between these two compounds, similar fabrication processing has been suggested for the synthesising of

CZTS(e), as well [57]. Thus, the achievements in improving the CIGS PV cells have not only introduced a high efficiency of over 22%, but have also led to a rapid progression in the fabrication of new promising material of CZTS(e) for thin film solar cells. Nevertheless, there is still a considerable gap between the highest efficiency achieved by CZTS(e) (with an efficacy of 12.6%[58]) and CIGS thin films (with an efficiency of 22.6%[6]) which is mainly attributed to the existing differences between the two structures as will be explained later in this chapter.

CZTS(e) is a quaternary semiconducting material based on the Kesterite mineral structure ( $A^I_2B^{II}C^{IV}X^{VI}_4$ ), in which  $A = \text{Cu}$ ;  $B = \text{Zn}$ ;  $C = \text{Sn}$ ;  $X = \text{S}$  or  $\text{Se}$ . This compound can be also correlated with the Stannite crystal structure. The difference between these two structures is the distributions of the cations  $A^+$ ,  $B^{2+}$ , and  $C^{4+}$  (see Figure 2-12) [21, 59]. Theoretical calculations have shown that the Kesterite CZTS(e) has a lower energy than the Stannite structure and should be more stable. However, this difference is not very significant. Thus, both structures may coexist in the synthesised thin film but cannot be distinguished by X-ray diffraction. In literature, the Stannite structure is mostly reported as a partially disordered Kesterite structure. The disordered distribution of atoms may cause defects such as vacancies and antisites, which in turn may affect the electronic properties of materials. For more details, the reader is referred to related documents [21, 60].

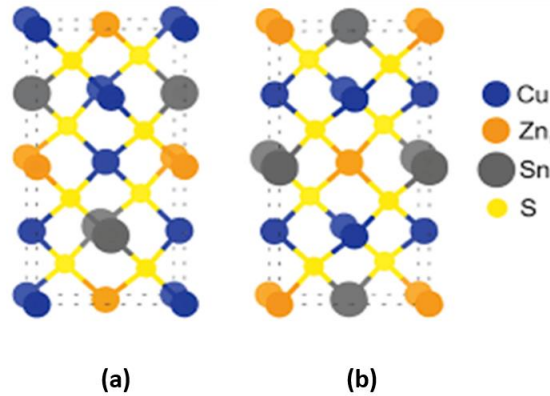


Figure 2-12 A schematic of a unit cell representing the different arrangements of Cu and Zn atoms of the two crystal structures of (a) Kesterite (b) Stannite [61]

According to the Shockley-Queisser limit, for a single junction solar cell, the absorber material with an energy band gap between 1eV and 2eV could have the maximum theoretical efficiency between 20% to approximately 32% [1]. CZTS and CZTSe thin

film absorber layers have the band gap of 1.5 eV and 1.0 eV, respectively. In case of the formation of pentenary structure of CZTSSe, the energy band gap can be tuned between 1 to 1.5 eV by controlling the S/(S+Se) ratio [62]. Therefore, a single junction solar cells made of these two compounds have the potential to yield the maximum conversion efficiency of 30%. Furthermore, due to having an ideal absorption coefficient of more than  $10^4\text{cm}^{-1}$ , a thin layer of  $1\mu\text{m}$  can absorb a most of the incident light, contributing to the creation of charge carriers across the thin film absorber layer, as well as reducing the material cost and weight.

### **2.2.5 Challenges in fabrication of CZTS(e) thin films**

Although CZTS(e) Kesterite thin film could be a promising candidate to be regarded as a p-type semiconductor for solar devices, there is still a considerable gap between the performance efficiency of CIGS and CZTS, as noted before. CZTS(e) is quite a new material with considerable uncertainty with regards to the crystal structure, as well as the kinetics and thermodynamics of intermediate reactions during processing. Thus, in order to improve the performance efficiency and make this compound a better substitution of CIGS thin films, a better understanding of the crystal structure of materials, and their processing, is required. Several studies have been carried out to identify the challenges in the fabrication of CZTS(e) thin films with this section presenting the most important challenges reported so far.

#### **2.2.5.1 Formation of secondary and ternary compounds**

The multitude of elements in CZTS(e) or CZTSSe compounds lead to a narrow compositional region (see Figure 2-13). This implies a very specific route of processing to synthesise the pure CZTS(e) absorber layer [63]. Thereby, the formation of secondary compounds that can be detrimental is highly likely to occur. Studies have shown that the high performance Kesterite based solar cells have been improved with the elemental composition of Cu-poor and Zn-rich [64]. Taking this into account, the presence of ZnS(e) in the process of Kesterite formation is highly probable. ZnSe and ZnS have wide band gaps of  $\sim 2.8$  eV and  $\sim 3.5$  eV, respectively. These value, especially for ZnS, is wide enough to be considered as an insulator. Such compounds could prevent the transportation of charge carriers, if formed at the surface of absorber layer. This is due to the large spike in the conduction band offset (CBO), (approximately 1.32eV) between ZnS(e) and CZTS(e), which leads to a reduction in  $J_{sc}$  and is also responsible for creating a high series

resistance through the device [65-69]. Other possible secondary compounds that can be formed are those in the Cu-S(e) system that appear under Cu-rich or Sn-poor conditions. These compounds are detrimental to the solar cells due to their high conductivity and small band gap of ~1.1-1.2 eV. They can reduce the open circuit voltage, especially when they are formed as large grains [20, 70]. In such a case, they may make a connection between the front and the back electrode and can shunt the device. As Saucedo et al and Temgoua et al showed in their studies, the presence of SnSe could be also detrimental for the solar cell performance due to its low band gap ( $E_g$  equal to 1eV) [71, 72]. The presence of such compound can act as a trap for minority charge carriers producing shunt paths, consequently, increasing the rate of recombination. Although the formation of ternary compounds such as  $\text{Cu}_2\text{SnSe}_3$  (CTSe) and  $\text{Cu}_2\text{SnS}_3$  (CTS) have been considered as thin film absorber layers [73], their presence together with CZTS(e) is detrimental. This is due to the smaller band gap of  $\text{Cu}_2\text{SnS(e)}_3$  compared to that of CZTS(e). Depending on the crystal structure formed during the fabrication process, the energy band gap value of CTS and CTSe varies between 0.93 - 1.35 eV and 0.74 - 0.9 eV, respectively. These ternary compounds can act as a recombination centre or may create shunting effects within the cell, eventually decreasing the performance of solar device [70, 74]. Accordingly, the formation of secondary and ternary compounds is highly dependent on the composition of precursors and the synthesising procedure.

Moreover, they can be formed at the front surface, in the bulk, or at the back contact of the absorber layer. If they form at the surface, etching with an appropriate etchant can be used to remove them; otherwise, the synthesising process should be manipulated to reduce the formation of such phases. The  $\text{KMnO}_4$ , KCN,  $(\text{NH}_4)_2\text{S}$ ,  $(\text{Br}_2\text{-MeOH})$  are the proper etchant for removing the  $\text{ZnS(e)}$ ,  $\text{Cu}_x\text{S}$ , SnS and  $\text{Cu}_2\text{SnS(e)}_3$ , respectively [11].

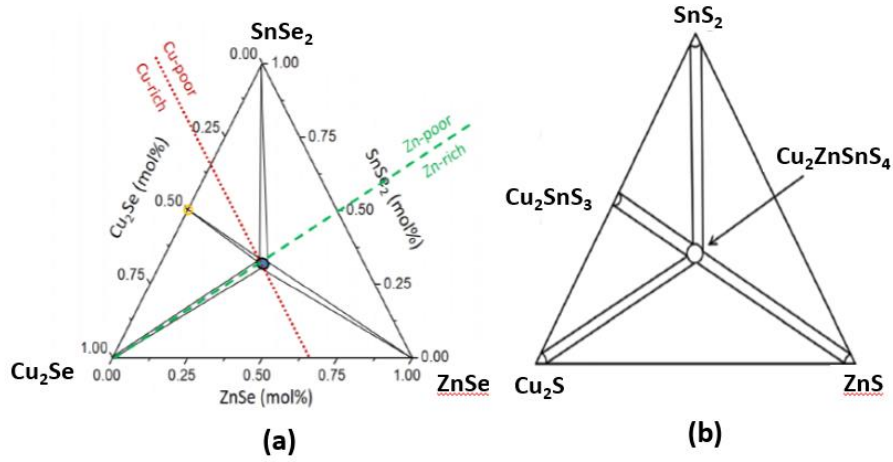


Figure 2-13. Pseudo-ternary phase diagram (a) Cu<sub>2</sub>Se-ZnSe-SnSe<sub>2</sub> (b) Cu<sub>2</sub>S-ZnS-SnS<sub>2</sub> at 670K [75, 76].

### 2.2.5.2 Defects in CZTS(e)

The probable defects for Kesterite can be divided into three groups including (i) vacancies such as  $V_{Cu}$ ,  $V_{Se}$ , (ii) interstitials such as  $Cu_i$ ,  $Zn_i$ ,  $Se_i$ , ..., and antisites like  $Cu_{Zn}$ ,  $Sn_{Cu}$ ,  $Cu_{Sn}$ ,  $Zn_{Cu}$ , and (iii) defect clusters due to the atomic substitutions such as  $[V_{Cu}+Zn_{Cu}]$ ,  $[Zn_{Sn}+2Zn_{Cu}]$ , ... [77, 78]. These defects could be detrimental or beneficial depending on their concentration and also considering the position of their energy level within the bandgap of CZTS(e).

Here, a summary of the impact of such defects on device performance is presented which is studied by Chen et al [27].

- (1) The formation of Se or S vacancies ( $V_{Se}$  or  $V_S$ ) induce an energy level in the middle of CZTS(e) band gap, thus they act as active recombination sites. This is one of the reasons that the sufficient sulphurisation/selenisation has been recommended in the synthesising process in order to improve CZTS(e) solar cell performance.
- (2) The formation of  $[Cu_{Zn}+Zn_{Cu}]$  cluster has a very low formation energy and they might have high concentration in the sample. Although such a cluster decreases the band gap by  $\sim 0.1$  eV, it does not have a significant influence on the electronic structure and optical properties. Thus, these clusters are known as benign defects.
- (3)  $[Cu_{Sn} + Sn_{Cu}]$  and  $[Zn_{Sn} + Sn_{Zn}]$  can decrease the band gap. For instance,  $[Zn_{Sn} + Sn_{Zn}]$  decreases the band gap by 0.3 eV in CZTS and 0.1 eV in CZTSe. However, they have very high formation energy and the resulting population can be negligible.

- (4) Copper vacancy ( $V_{Cu}$ ) and  $Cu_{Zn}$  antisite both act as acceptors. Such acceptors enhance the hole concentration in CZTS(e) that is responsible for the intrinsic p-type conductivity of the material. The formation energy of  $V_{Cu}$  in Kesterites is higher than  $Cu_{Zn}$  in the stoichiometric condition. In the Cu-poor and Zn-rich conditions,  $V_{Cu}$  becomes dominant. This reflects the situation of the  $Cu/(Zn + Sn) = 0.8$  ratio which has been reported as the optimum composition to provide a high performance solar device.
- (5) The  $[2Cu_{Zn} + Sn_{Zn}]$  clusters induce electron-trapping states in the absorber materials, and are detrimental to the solar cell performance. The electron-trapping states formed due to the formation of  $[2Cu_{Zn} + Sn_{Zn}]$  in CZTSe are weaker than in CZTS. Moreover, the population of isolated deep donor defects such as  $Sn_{Zn}$  and  $V_{Se}$  in CZTSe is lower than CZTS. For these two reasons, the low  $S/(S+Se)$  ratio is often suggested in order to achieve a better performance.

Bosson et al and Lafond et al have defined 8 models of CZTS types considering the non-stoichiometric conditions. From all models, four types of A to D are presented in Table 2-1 [63, 79]. According to previous studies and considering the influence of intrinsic defects on the electronic and optical properties of solar devices, the Cu-poor and Zn-rich region (A-type) is the most favourable stoichiometric type, since it contributes to the best device performance so far [64].

Table 2-1. Types of CZTS as defined by Lafond et al [79].

<b>CZTS type</b>	<b>Defect complex</b>	<b>stoichiometry</b>
<b>S-type</b>	$[Cu_{Zn}^{-} + Zn_{Cu}^{+}]$	stoichiometry
<b>A-type</b>	$[V_{Cu}^{-} + Zn_{Cu}^{+}]$	Cu-poor, Zn-rich
<b>B-type</b>	$[Zn_{Sn}^{2-} + 2Zn_{Cu}^{+}]$	Cu-poor, Zn-rich
<b>C-type</b>	$[2Cu_{Zn}^{-} + Sn_{Zn}^{2+}]$	Cu-rich, Zn-poor
<b>D-type</b>	$[Cu_{Zn}^{-} + Cu_i^{+}]$	Cu-rich, Zn-poor

### 2.2.5.3 Interfaces of CZTS(e) thin film

Although a significant progress has been achieved in the fabrication of Kesterite solar cells, the record efficiency of such devices is still much lower than that of CIGS. The

major reason for lower performance of Kesterite PV cells is claimed to be the large open circuit ( $V_{oc}$ ) deficit which is partly due to the interface recombination [80]. The interface recombination occurs due to several situations: (i) A non-optimal band alignment at CdS/CZTS(e) (ii) Secondary compounds at the interface (iii) A non-ohmic back contact (the over thick  $\text{MoS(e)}_2$ ) [70]. This section describes the effect of these three situations.

#### ✚ Band alignment at CdS/CZTS interface

Band alignment is introduced with two kinds of conduction band offset (CBO): cliff-type and spike-type. It is reported that at the interface of CdS with CZTS or CZTSe, the cliff-type and the spike type band alignment will appear, respectively. The cliff-type configuration will contribute to an increase in recombination of the majority carriers via buffer/absorber interface. Whereas, the spike at CdS/CZTSe interface may block the transportation of photo generated electrons which leads to a current loss. Nevertheless, previous studies showed that when the CBO is less than 0.5eV, the photo-generated electrons can cross the spike barrier. It could be possible to improve the performance of a solar device by manipulating the CBO via variation in composition of absorber layer. In this context, substituting selenium instead of sulphur in CZTS PV cells could be beneficial [70, 81].

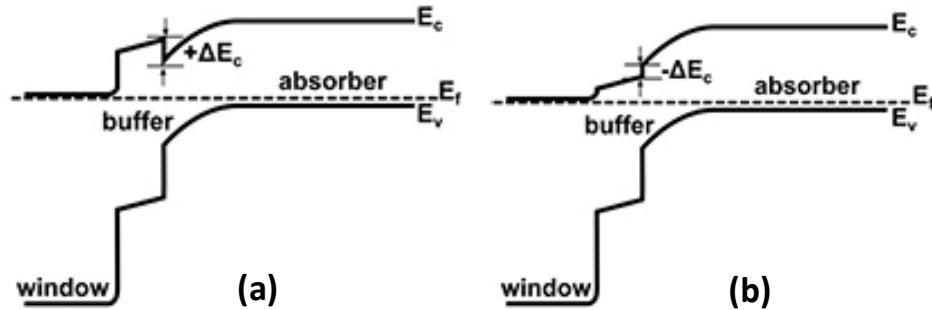


Figure 2-14. Schematics of the band diagrams of window/buffer/absorber layers for (a) spike-type (b) cliff-type conduction band alignments [82].

#### ✚ Secondary compounds at the interface

As discussed in section 3.3.1, secondary compounds could easily form due to a narrow stable region of CZTS. Such compounds can reduce the performance of solar device.

#### ✚ Mo/CZTS interface - Non-ohmic back contacts

A Non-ohmic back contact may be created due to the formation of a thick layer of  $\text{MoS(e)}_2$  at the interface of CIGS or CZTS(e) with the Mo back contact [41].

Accordingly, to improve the performance of a solar device, the thickness of  $\text{MoS(e)}_2$  should be well-controlled. Decreasing the sulphurisation/selenisation temperature, time, and using low partial pressure of chalcogen would decrease the thickness of the  $\text{MoS(e)}_2$  layer. However, these variations in conversion procedure might affect the quality of the Kesterite grain size. Thus, an optimisation during the fabrication process is required [70].

### **2.2.6 Parameters affecting the quality of CZTS(e) thin films**

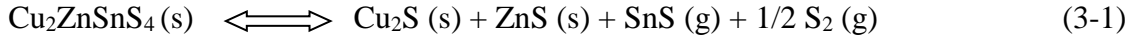
Since most of the current research has been concentrated on investigating the influence of fabrication techniques and processes to improve the crystal structure and morphology of CZTS(e) thin films, this subsection presents a review of other studies on (i) the chemical reactions and the thermodynamic models that have been reported during the synthesising of CZTS(e) thin films (ii) the effects of conversion conditions on the quality of CZTS(e) thin films.

#### **2.2.6.1 Phase evolution of CZTS(e) thin films**

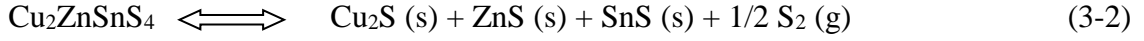
The chemical reactions highly depend on the precursor materials and the synthesising processes. That is why different models have been suggested based on the use of different material composition and synthesising procedure. Schorr et al have proposed that the CZTS kesterite structure starts to form just below  $300^\circ\text{C}$  with a mixture of CuS, ZnS and SnS. It is also reported that the Kesterite can be created by the reaction between the ternary compound of  $\text{Cu}_2\text{SnS(e)}_3$  with ZnS [83]. In contrast to CIGS, the formation of CZTS needs more control over the synthesising conditions. This is due to the fact that the elements and compounds involved in the fabrication of CZTS are easily evaporated and this promotes the CZTS decomposition [84]. Redinger et al have demonstrated that the formation of CZTS Kesterite can be restricted at high temperatures (above  $400^\circ\text{C}$ ) and through this process tin is lost due to the volatility of SnS[85]. It is mentioned elsewhere that decreasing the conversion time could limit the time available for the decomposition reactions and therefore reduce the tin loss [86].

Scragg et al have proposed two models to explain the decomposition phenomenon of CZTS compound [86]. According to the first model, demonstrated in reaction 3-1, the SnS compound is formed directly in the vapour state. Thus, both SnS and sulphur are prone to move away from the reaction site and that exacerbates the decomposition rate of CZTS.



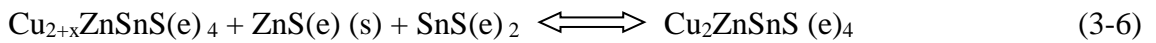
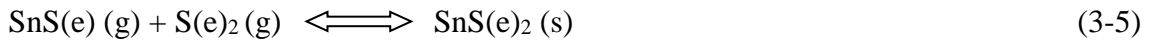
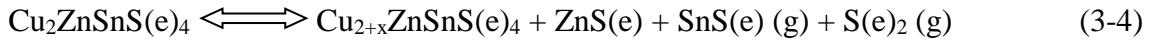


The second model is represented in reaction 3-2 and 3-3. In such a condition, if the sample is converted under vacuum, the  $\text{S}_2$ , which is the only product in gas state in reaction 3-2, will be removed from the system and the CZTS will decompose.



Through reaction 3-3 of the second model, SnS molecules could be absorbed to the surface and might reconvert to CZTS with the other decomposed binary compounds. However, the SnS compound may evaporate into gas state. Thus, if the evaporated SnS molecules are not substituted, the decomposition rate of CZTS will increase [86]. In such a condition, the rate of decomposition is only affected by the partial pressure of sulphur, which is suggested to be sufficient to proceed the reaction towards the formation of the CZTS structure [86]. However, the high partial pressure of chalcogen (S/Se) could affect the formation of a thick layer of  $\text{MoS}(\text{e})_2$  which can decrease the performance of a solar device [42].

Zhong et al have introduced another model which is shown in reaction 3-4 to reaction 3-6. They have stated that for the precursors with Cu-poor and Zn-rich composition, the following reactions will occur [87].



Scragg et al reported similar trend for CZTSe synthesising procedure in that Sn (IV) is prone to evolve to Sn (II) in a chalcogen environment at low pressures (1mbar) at the temperature of  $\sim 550^\circ\text{C}$ . This is claimed due to a much smaller free energy required for the formation of SnSe from  $\text{SnSe}_2$  at low pressures (reaction 3-7), comparing to that of the formation of other binaries in CZTSe processing. In addition, the SnSe has the highest vapour pressure in the temperature range of interest for Kesterite formation, as shown in Table 2-2. Because of  $\text{Se}_2$  lost from the system, it is expected that the  $\text{SnSe}_2$  phase decomposes more severely [84].

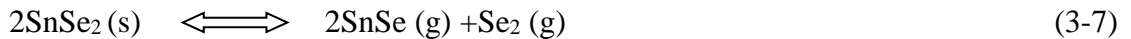


Table 2-2. Equilibrium vapour pressure of the by-products of Se loss from CZTSe [84].

Vaporisation Reaction	Vapour pressure at 550°C (mbar)
$\text{Cu}_2\text{Se (s)} \rightleftharpoons \text{Cu(s)} + \text{CuSe (g)}$	$1.2 \times 10^{-13}$
$\text{ZnSe (s)} \rightleftharpoons \text{ZnSe (g)}$	$6.4 \times 10^{-15}$
$\text{ZnSe (s)} \rightleftharpoons \text{Zn(g)} + \frac{1}{2} \text{Se}_2 \text{ (g)}$	$5 \times 10^{-6}$
$\text{SnSe (s)} \rightleftharpoons \text{SnSe (g)}$	$3.6 \times 10^{-3}$

It is also proved that with the same conversion conditions, CZTSe compound is more at risk of being decomposed than ClSe. This is due to significantly lower  $\Delta G_R$  for the reduction of Sn(IV) to Sn(II) and In(III) to In (I) with  $45\text{KJmol}^{-1}$  and  $270\text{KJmol}^{-1}$  at  $550^\circ\text{C}$ , respectively. Additionally, in the same study during the synthesising process of CZTSe, the number of moles of vapour evolved from CZTSe including the selenium and tin selenide is  $10^6$  times higher than that of the vapour products in the ClSe [84].

#### 2.2.6.2 Ambient gas composition and total pressure during conversion

As explained in section 2.2.6.1, the quantity of ambient pressure can have a significant effect on the quality of the absorber layer. He et al demonstrated that when sulphur powder is used as a chalcogen supply together with precursors in a graphite box(GB), the pressure inside the GB would change through three stages in order to reach its equilibrium state including (i) evaporation of elemental S powders (ii) then the over-pressure S vapour released into the tube furnace since the GB is not absolutely sealed. This will continue till the internal pressure inside the GB is equal to the external pressure inside the tube furnace (iii) the equilibrium situation is achieved with a stable internal partial pressure of sulphur that can diffuse and react with the precursor [88]. According to the former study, the increase in the ambient pressure contributes to the increase in the average grain size, plus the smoother, and more uniform layer [88]. Increasing the ambient gas pressure can, to some extent, suppress the evaporated chalcogen source or any compounds that may form in vapour state inside the GB rather than allowing them to be emitted into the tube furnace [68]. The influence of escaping  $\text{SnS(g)}$  and  $\text{S/Se(g)}$  have been explained in section 2.2.6.1.

Besides the quantity of the ambient pressure, the gas composition is also important, especially when the precursor contains metal oxide compounds. As Hironori Katagiri et

al have reported, the metal oxides should be removed from CZTS thin films since they do not absorb the light and may decrease the conversion efficiency of the solar device [89]. The previous studies done at Northumbria University have shown that  $\text{Cu}_2\text{O}$  is easily converted to  $\text{Cu}_2\text{S}$  or  $\text{CuS}$  when it is heated under vacuum or inert gas atmosphere such as  $\text{N}_2$  or  $\text{Ar}$ , as long as the atmosphere is saturated with sulphur. However, the  $\text{SnO}$  does not easily convert to tin or tin sulphide. According to previous literature, removing oxygen from  $\text{SnO}_2$  requires the use of specific pressure of forming gas ( $\text{H}_2/\text{N}_2$ ) and heating at high temperatures of  $550^\circ\text{C}$  [90].

### ***2.2.6.3 Conversion Time, Temperature, and Heating profile***

It has been demonstrated that varying the conversion time and temperature can significantly improve the grain size and crystallinity of CZTS thin films [91]. The grain growth would decrease the density of grain boundaries which are usually known as defects of a material due to the creation lattice mismatch between the grains. Thus, it is expected that they contribute to a reduction in electrical properties of a semiconductor. However, the studies have shown that grain boundaries could be beneficial or detrimental for a device performance depending on the composition and properties with respect to the grains. For instance, in Cu-poor condition, the grain boundaries can behave as hole barriers enhancing carrier collection by preventing recombination. On the contrary, in Cu-rich condition, grain boundaries act as active recombination sites. Moreover, the formation of any conductive compounds such as  $\text{Cu}_2\text{S(e)}$  during synthesising process at the grain boundary may decrease the shunt resistance and eventually lead to a reduction in device performance [92, 93]. Nevertheless, one of the advantages of grain growth is to ensure a dense microstructure and decrease the pinholes across the absorber layer. The presence of pinholes cause a reduction in shunt resistance and reduce the device performance. Two effective strategies in order to avoid decreasing the shunt resistance are (i) passivating the grain boundaries with oxides or non-conductive compounds (ii) increasing the conversion temperature or time to improve the grain growth. However, it should be noted that an optimum conversion time and temperature is required for the synthesising process, since these two parameters could contribute to a loss of tin and subsequently the decomposition of the CZTS compound [86, 94]. Besides, it is demonstrated that at very high synthesising temperature, the effective film thickness might be reduced due to an increase in surface roughness contributing to a poor p-n

junction [95, 96]. Furthermore, the optimum conversion time and temperature is important due to preventing the use of high quantity of energy for manufacturing in large-scale production [97-101].

The reviewed literature has shown that the fast cooling contributes to the formation of disordered crystal structure in which a number of Cu and Zn atoms relocate to each other's position. However, a slow cooling rate gives more ordered CZTS crystal structure [102]. It is revealed that when the cooling rate decreases to a rate of 1K/h, an approximate 70% of Cu and Zn atoms are located on the correct crystallographic sites. Nevertheless, even this amount of ordering contributes to a variation of 0.1eV in band gap value [103]. It is also stated that CZTS is fully grown with disordered crystal structure at the range of approximately 450-560°C, and the ordered crystal structure forms only during the cooling when the temperature drops below 260°C [103].

#### **2.2.6.4 Chalcogen Source (*S and/or Se*)**

The chalcogen source can be introduced in different methods such as (i) as a cap layer for a CZT substrate (evaporation) (ii) as pellets or powders (iii) H<sub>2</sub>S(e) during conversion (iv) as elemental or compound source during the sputtering (v) elemental or compound source during solution synthesising.

When the chalcogen is in intimate contact with the precursor (using a cap layer), it requires a very precise control over the kinetics of reaction which makes the synthesising process very complex. It is believed that during the heat treatment, when a mixture of solid, vapour, and liquid states are present simultaneously, different routes may take place. These include (i) the melting or vaporization of a solid (ii) the solidification of a liquid or deposition of a vapour. According to previous literature, for several elements including sulphur, selenium, and tellurium, a liquid-liquid-solid triple point has been experimentally observed [104]. The investigation of viscosity drop for selenium showed a drastic structural reconstruction of Se, when it melts, indicating the liquid-liquid transition which occurs in the vicinity of selenium melting point [104]. On the other hand, the formation of metastable phase of selenium with the creation of two distinct liquid states could lead to even more complex phase changes and the nucleation processes. To trigger the change in the phase, some transition in chemical potential must be applied which in turn requires a very precise control on temperature, pressure, mass, and volume of each component in the system [105, 106].

The use of chalcogen as pellets or powders is safer than the use of  $\text{H}_2\text{S}$  (e) gas during the conversion procedure. The latter method of introducing the chalcogen has been avoided to use due to its toxicity despite the very good results achieved in similar processing [107]. As explained in section 2.2.6.1, in order to avoid the decomposition, it is important to provide sufficient pressure of chalcogen during the synthesising process. This can be performed by introducing enough mass of chalcogen (powders/pellets) in the graphite box. The partial pressure can be calculated according to ideal gas law  $PV=nRT$ , assuming that the conversion procedure has been carried out at near vacuum condition and there is no leakage of sulphur in its vapour state from the graphite box [108].

A study on fabricating CZTS thin films was also conducted by Bjorkman et al. The former study has shown a comparison of the two sulphurised films of (i) when the sulphur quantity was directly applied as a component in precursor (ii) the sulphurisation of CZT thin films. It should be noted that their study was based on synthesising thin film precursors via sputtering. Results showed that sulphurisation of sulphide films had fewer voids and were denser compared to the sulphurisation of CZT films, but with smaller grain size of Kesterite. They have claimed that the large number of nuclei due to the presence of elemental sulphur in the precursor prevent the grain growth [109].

#### **2.2.6.5 Surface etching**

Since one of the challenges in the current study was to remove SnS binary compounds from the surface, the explanation here is just concentrated on the method of etching this compound.

The SnS compounds could appear either at the interfaces (surface and back contact) or in the bulk. If SnS compound forms in the CZTS/CdS interface, sub-energy levels may be created and the  $V_{oc}$  of the device decreases. In such a case, the yellow  $(\text{NH}_4)_2\text{S}$  etchant can remove SnS compounds, as well as passivating the surface by removing the surface oxides. If the SnS compound is present in the bulk or at the CZTS/Mo interface, it cannot be removed easily by the use of etchant and the only solution is to use an ideal synthesising process. Nevertheless, it is reported that the SnS compound formed at the CZTS/Mo interface has the potential to improve the solar cell performance. This has been discussed due to the creation of spike like CBO at the interface of CZTS and back contact. Consequently, the electron cannot pass through the back contact. It is also stated that when the SnS is present at the CZTS/Mo interface, the back surface reflection of the near

infrared light could be increased, leading to a higher magnitude of light absorption. Such a claim shows that the presence of SnS binaries could be useful in facilitating the light management of the solar cell if it form at CZTS/Mo interface [72, 110]. For more information on the mechanism of dissolving SnS in  $(\text{NH}_4)_2\text{S}$  solution, the reader is referred to the related publication in this area [72].

#### ***2.2.6.6 Post-conversion heat treatment with extra chalcogen source (sulphur and/or selenium)***

A few studies have been published on post-conversion heat treatment of the CZTS thin film. According to one of these studies, the post treatment contributed to the ‘in diffusion’ and ‘out diffusion’ of elements from the CZTS structure and eventually, the creation of secondary compounds, defects, and inhomogeneity [67]. The post-conversion with selenium has demonstrated the grain growth and improvement in the crystal structure [111, 112]. It is believed that selenium is a better vapour transport agent than sulphur, which contributes grain growth forming densely packed grains. The fabrication of CZTSSe thin films would be beneficial for the solar cell performance since (i) it is expected that large grains may lead to less recombination of photo-generated carriers at the grain boundaries (ii) it is assumed that the passivation of grain boundaries with selenium results in a lower band gap surface layer, which removes the potential barriers for grain to grain carrier transport (iii) the selenium quantity increases the crystallinity of Kesterite structure [111, 112].

#### **2.2.7 Possible fabrication techniques to prepare CZTS(e) absorber layers**

Various techniques have been studied for fabricating CZTS(e) thin film absorber layers. These techniques can be classified into two main categories of Vacuum and Non-vacuum based deposition approaches.

##### ***2.2.7.1 Vacuum deposition technique***

One typical method of coating is the vacuum processing in which the composition and thickness can be well-controlled across the thin film. Thus, a very good coverage and uniform thin film can be achieved. However, the complexity in vacuum processing may affect the final cost for mass production which could limit its application as a scale-up production route. The two major vacuum deposition routes that are used to process CZTS absorber layer are co-evaporation and sputtering [113].

Co-evaporation technique has been one of the earliest methods to fabricate CZTS thin films, conducted in the experiment by Katagiri et al in 2001. This was done by using sequential deposition of precursors of ZnS, Sn, and Cu. This technique has led to the CZTS solar cell with an efficiency of 2.62% [114]. During this process, the bulk of deposition material transforms from solid to vapour state by the use of thermal heating or electron bombardment. Then, the evaporated materials are carried to the substrate where the thin film is growing. The 9.15% and 11.6% efficiency of CZTSe, using the co-evaporation technique, has been conducted by Repins et al and IBM, respectively [17, 115]. The latter research group still holds the highest efficiency record among the fabricated CZTSe solar cells to date, using the vacuum deposition technique.

Sputtering as a deposition technique is performed by the use of elemental target sources with a specific pressure and temperature in a high vacuum chamber. In 1988, Ito et al utilized the sputtering method to fabricate CZTS thin films for the first time [116]. They sputtered the CZTS film from target material by employing the method of atomic beam sputtering and obtained CZTS films with an optical band gap of 1.45eV. In 2009, a 3.2% efficient CZTSe solar cell was reported at Northumbria University using sputtering procedure [16]. In 2008, Katagiri et al, elaborated CZTS thin films via sputtering Cu, SnS, and ZnS targets, obtaining the efficiency of 6.7% [89]. In 2011, Ito et al studied the method of sputtering a Cu–Sn–Zn metal precursor and obtained the CZTS cells with an efficiency of 3.7% [117]. The world record efficiency of CZTS fabrication with the use of sputtering technique is held by Tajima et al in 2017 with a 9.4% efficient CZTS solar cell using Cu, Sn, and ZnS targets [118]. The use of this technique has still been one of the frequently investigated approaches in producing thin film absorber layers. Although the vacuum deposition technique can provide reproducible and high quality thin films, due to the necessity of vacuum chambers, load-lock, pumps, and heavy power units for sputtering or evaporation, this technique consumes a very high amount of energy. Consequently, it is regarded as an expensive method which limits its application in large-scale production.

#### ***2.2.7.2 Non-vacuum deposition techniques***

Electrodeposition and direct liquid coating approaches can be named as the most commonly used non-vacuum deposition routes. For electrodeposition, the reader is referred to the related literature [119]. The highest efficiency achieved with this technique

stands at 8% and 8.2% for CZTS and CZTSe thin films, respectively [120, 121]. The direct liquid coating approach refers to those techniques in which the precursor containing liquid or solution is deposited on the substrate by different methods such as spin coating, spraying, doctor blade, slot-die, etc. The deposition processing is followed by drying and heat treatment with the specific synthesising process depending on the material used in the precursor solution.

Compared to vacuum processing techniques, the manufacturing facilities used for the non-vacuum deposition technique are significantly less expensive. Moreover, some non-vacuum deposition routes have the potential to prepare high throughput, especially in roll-to-roll configurations. However, the use of reagents (i.e. metal sulphide, metal oxides, etc.), the solvent or suspension solution (i.e. respecting the parameters of stability, viscosity, boiling point, etc.), the additives (which is optional and might be used in case of increasing the stability of solvent), and the deposition processing parameters, can all affect the quality of the fabricated thin films. For instance, carbon and oxygen usually present in the solvents. These elements, if they remain in the final thin films, can decrease the grain growth [122]. Incomplete removal of such components during the conversion procedure may cause the deterioration of the device [89]. Therefore, a precise selection of additives and solvents is required. In order to fabricate the precursor solution, various studies have been carried out using metal oxides, metal chalcogenides, and metal acetates [123, 124]. As for the choice of appropriate solution, several parameters need to be considered including reactivity, volatility, toxicity, and cost. The precursor film usually needs to be dried in air or inert atmospheric condition so that the solvent residues evaporate from the surface.

Moreover, the precursor films should be deposited uniformly and a high degree of adhesion. Thus, the choice of deposition route is of great significance. In this context, doctor blade, spraying, and slot-die, have the advantage of being scalable techniques with less waste of material compared to the spin coating method. More details of these techniques will be explained in Chapter 3.

The first fabricated CZTS solar cells with non-vacuum deposition technique dates back to 2009 reported by Kunihiko et al with an efficiency of 1% via sol-gel deposition technique and the use of metal acetates [125]. In 2010, Todorov et al fabricated a 9.6% CZTSSe solar cell using hydrazine based solution processing with spin coating as a method of deposition [126]. In 2012, a 5.14% efficient CZTS was reported by Woo et al



using non-toxic precursor solution including  $\text{Cu}_2\text{S}$ , Zn, Sn, and S dispersed in ethanol [127]. The use of nanoparticle solutions has been investigated and demonstrated promising results within the past few years with the highest efficiency standing at 9.0% CZTSSe solar cells [128]. The highest performances of solution based Kesterite solar cells so far have been reported in 2015 by IBM with a 12.6% efficient CZTSSe solar cells [129].

In recent years, a few studies have been done using metal oxide compounds in order to fabricate the CZTS absorber layer with a record efficiency of 1.4% [130]. The idea of using metal oxide compounds is obtained from promising results reported where metal oxide particles have been successfully used to synthesise a 13.6% efficient CIGS absorber layer [131, 132]. The former study reported a relatively higher stability of tin oxides, compared to copper oxides and zinc oxides. Chen et al has claimed that the use of  $\text{SnO}_2$  has an advantage compared to the use of  $\text{SnS}_2$ . They believe that the probability of SnS loss could be less when the oxides are used as initial materials due to the high stability of  $\text{SnO}_2$  compared to  $\text{SnS}_2$  at temperatures of about  $550^\circ\text{C}$  [130]. On the other hand, the main issue for the conversion of the vacuum deposited precursors is the loss of tin due to the volatility of SnS during the conversion procedure. As mentioned before, this accelerates the decomposition rate of CZTS compounds [84, 86]. In another study by Chen et al, they have reported the fabrication of CIS and CZTSe thin film absorber layers using nano-particles of metal oxides, using doctor blade following by sintering the thin film at selenium vapour atmosphere. The research has led to the formation of 3.4% efficient PV cells made of CISE absorber layer [133].

#### Ball Milling

Since the method of ball milling has been one of the most frequently used techniques for the current research to fabricate the precursor solution, the most important parameters together with the previous studies related to this method of solution production will be summarised in this subsection.

Ball Milling technique can be considered at industrial-scale dimensions, and is a simple material processing technique which can be used to reduce particle size, mix materials, and synthesise the precursor solution. One of the distinct advantages of ball milling is that no expensive vacuum facilities are required [134-136]. Studies have shown that an increase of milling time and an increase in the 'ball to powder ratio' could lead to a reduction in particle size [137]. As reported by Kotake et al, the product size in wet

grinding is less than that of dry grinding [138]. A carrier or suspension solution needs to be used to suspend and disperse the metal compounds in the solution uniformly. The selected suspension solution should be compatible with the precursor powders and not create a complex reaction with the other components. It should also have a low boiling point to evaporate organic residuals. Moreover, it is preferred to be non-toxic, safe, and inexpensive [139]. Deionized water (DI) could be a safe and inexpensive solvent. Furthermore, the lack of carbon in DI water could make this option as a preferable suspension solution. Isopropyl alcohol with the chemical formula of  $C_3H_8O$ , Methanol ( $CH_4O$ ), and Ethanol ( $C_2H_6O$ ) are the conventional solutions that have been used for the process of milling [140, 141]. Although the boiling point of IPA ( $82.6^{\circ}C$ ) is a bit higher than the two latter options, it could be a better alternative since IPA is less toxic than Methanol and is considerably cheaper than industrial Ethanol. Finally, it is important to note that both mentioned solvents of water and IPA are easy to handle under ambient environment condition [139].

In 2000, a study was published on the fabrication of CIS with the low cost technique of ball milling. The study employed the milling of Cu-In powder using water as a suspension solution, spraying the precursor solution on SLG/Mo layer, and selenisation in  $H_2Se$  atmosphere at  $440^{\circ}C$ . The efficiency of the fabricated device has been reported in the range of 7-8% [142]. In 2009, a Japanese group has fabricated a CIGSe device with an efficiency of 3.1% using ball milling of metal powders in an organic solvent [143]. Other researchers used non-vacuum processing techniques in order to synthesise the precursor solution from metal oxide powders [144-146]. In this context, Zhou et al in 2010, used ball milling to mix and grind the metal powders of Zn, Sn, and Cu with Ethanol as a suspension solution. The powders were milled, pressed, double milled and printed using screen-printing on the substrates, and finally converted. This technique contributed to a 0.4% efficiency of fabricated solar devices [147]. In 2012, Woo et al fabricated CZTS solar cells with an efficiency of 5.14% using the ball milling of  $Cu_2S$ , Zn, Sn, S powder together with Ethanol as a suspension solution [127]. In 2015, the process of milling of  $Cu_2S$ , ZnS,  $SnS_2$  with Ethanol has shown the efficiency of 4.2% [148]. Pareek et al synthesised CZTS and CZTSe absorber layers using ball milling of the metal powders of Sn, Zn, and Cu with S/Se in 1-Butanol solution [149, 150]. However, the use of metallic powder needs caution since the fine particles may explode in the air and can easily be oxidised. The use of metal-sulphide cannot be a favourable choice due to the generation

of many toxic waste solutions. In the following table (Table 2-3), the most important achievements and the record efficiency of CZTS(e) PV cells fabricated using vacuum and non-vacuum deposition techniques are presented and summarised. The research by Kapur et al was one of the successful studies of CIGS thin film fabrication using a nanoparticle precursor solution achieving an efficiency of 13.6% [131]. However, the use of ball milling and metal oxide powders to fabricate the CZTS precursor solution have not been studied before.

Table 2-3. The highest record efficiencies of CZTS(e) PV device prepared using vacuum and non-vacuum deposition techniques.

	<b>Material</b>	<b>Method</b>	<b><math>\eta</math> (%)</b>	<b>Institute</b>	<b>Year</b>	<b>Ref</b>
<b>Vacuum</b>	CZTS	Sputtering	10.8	Solar Frontier	2013	[151]
	CZTS	Sputtering	9.4	Toyota R&D Labs, Japan	2016	[152]
	CZTSe	Sputtering	10.4	National University, Korea	2016	[153]
	CZTSSe	Sputtering	10.8%	Erlangen University	2013	[154]
	CZTS	Co-evaporation	8.6%	Solar Frontier	2013	[155]
	CZTSe	Co-evaporation	11.6	IBM	2016	[16]
	CZTSSe	Co evaporation	7.5%	IBM	2011	[156]
<b>Non-Vacuum</b>	CZTS(e)	Solution Hydrazine/	12.6	IBM	2014	[129]
	CZTS	Sol-gel/Spin coating	9.2	NTU	2015	[157]
	CZTS(e)	DMSO-processed /Spin Coating	11.2	IMPA	2015	[158]

### **2.2.8 Part of previous work at Northumbria University**

Among the research carried out at Northumbria University in the area of photovoltaics, it is worth referring to several important studies. Eric Don was a pioneer in synthesising the CISE thin films via co-evaporation of the copper, indium and selenium elements in 1986 [159]. Studies on characterisation of CISE materials have been reported later on, in 2008 and the CZTSe thin films have been fabricated and studied from 2009 to 2016 by several researchers [15, 16].

The most recent research which demonstrated promising results at the stage of initial trial was a study carried out by Guo Ming as a Master's project in 2014, at Northumbria University. The metal oxide compounds of SnO and Cu<sub>2</sub>O together with a metal sulphide of ZnS for the first time was used to synthesise the CZTS thin films. The idea of using ZnS rather than ZnO was due to the sublimation of Zn at ~430°C. It is suggested that in case of heat treatment at the presence of H<sub>2</sub>, the Zn loss can be prevented by the use of ZnS [21]. The study has revealed the formation of a CZTS thin film with the thickness of ~10 µm using doctor blade. According to this investigation, Cu<sub>2</sub>O (1 hour) and SnO (4 hours) have been reduced at temperatures of 400°C and 550°C, under 500mbar H<sub>2</sub>/N<sub>2</sub>, respectively. Moreover, a better reduction has been shown in the case of using extra sulphur quantity during the heat treatment procedure. Nevertheless, in the case of developing this technology for PV application, the film thickness should be taken into account. This requires establishing a uniform precursor solution, introducing a scalable and appropriate method of deposition, and finally developing the quality of CZTS thin films. The study in this area is the aim of the current research.

### **2.2.9 Sustainability assessment of photovoltaics**

Since part of the study in this PhD thesis is devoted to the evaluation of sustainability of CZTS thin films, a brief background of previous literature will be presented in the current section.

According to the definition proposed by Fthenakis (Brookhaven National Laboratory), the study on the sustainability of a system requires evaluating at least three main measurable aspects of cost, resource availability, and environmental impacts [160]. In case of considering the solar energy via the fabrication of solar devices as a system, the question of cost concerns the affordability of the solar energy (including the fabrication of solar device/modules, maintenance, and installation) compared to that for other energy

sources. The resource availability includes the restrictions of material resources for current and future generation. Finally, the environmental impacts include local, regional, and global effects that must be considered over a long term horizon [2, 160].

In this context, Life Cycle Assessment (LCA) is a useful tool for a systematic evaluation of the environmental aspects of a product or service for the entire life cycle of that product (the so-called “cradle to grave approach”). This involves a consideration of the input of materials and energy together with the output of pollutants and wastes during the life cycle stage of a system. The estimation of LCA, however, is a very extensive study including five stages of (i) the extraction of raw materials from the earth (ii) the processing and refining of these materials (iii) the fabrication of the modules and assembling the system components (iv) the transport, installation and use of the system (v) the decommissioning, disposal, and recycling procedure [161, 162]. Due to the very broad concept of LCA, the study on this area is often conducted by defining a system boundary as it is also recommended in the relevant standard (ISO 14040 (2006a)) [163]. So far most of the studies in this area have been focused on the commercial solar devices mainly silicon based solar cells and partly thin film technology [164-166]. However, a few publications have considered thin film photovoltaics that have not yet been commercialised. That is due to the uncertainty of the processing challenges that arise during large-scale production, installation and the recycling process.

In 2009, Fthenakis reported a study comparing three thin film options of CdTe, CIGS, and a-SiGe. The former study stated the concerns of cost and resource availability of some materials needed for the fabrication of thin film. They have reported that the PV growth rate and the final cost of PV modules would increase with (i) enhancing the extraction of primary ore, (ii) the development of techniques used for recovering and refining the by-products, (iii) producing thinner layers, (iv) improving the efficiencies of solar devices, and (v) recycling the spent modules [167].

Elsewhere, Fthenakis has reported an evaluation on the effect of environmental impacts of using solar devices. The former author has said that although operating the photovoltaic systems, in comparison with the use of non-renewable energies, do not generate any toxic or greenhouse gases, pollutions could be emitted in the manufacturing process. For instance, it is estimated that the in manufacturing CdTe thin film photovoltaics, under average US conditions, about 20g CO<sub>2</sub>/kWh is emitted to the environment. In case of using fossil fuel plants, 500-1000g CO<sub>2</sub>/kWh will be emitted to the environment. They

have also estimated that the photovoltaics can reduce the CO<sub>2</sub> emissions in 2050 by 62% than in 2005 [167, 168].

The report published by Celik et al [169], has focused on the effect of extracting/mining the elements on the environmental impacts. The study has shown that the environmental toxicity of elements such as indium, gallium, and cadmium are 1000 times higher than that of silicon, while this index for elements such as copper, tin, and selenium is 100 times more than that of silicon. In addition, the study has illustrated that a high degree of toxicity of tin and copper is mainly coming from their extraction/mining procedure. In another study published by Collier et al [170], the evaluation of several aspects of LCA by comparing CZTS (processed via vacuum processing), Zn<sub>3</sub>P<sub>2</sub>, CIGS, and CdTe thin films have been estimated. The results have shown that if CIGS replaced by CZTS thin films, it contributes to a less adverse effect for the ecosystem quality. However, the global warming index and the primary energy required for fabricating the CIGS is much higher than CZTS manufacturing.

### **2.3 Summary**

Despite the progress in the fabrication of thin film PV technology, the more development in this field requires more investigations on the fabrication of PV thin films in large-scale production. In this context, it is of great importance to focus on the use of sustainable materials and earth abundant elements together with a technique, which is reasonable to apply for large-scale production.

According to the previous literature, the Cu<sub>2</sub>ZnSnS<sub>4</sub> (CZTS) thin films is a promising compound to be used as an absorber layer. Among the so far studies in this context, the study on fabricating the CZTS thin films with the use of metal oxide compounds have been missed. On the other hand, it is supposed that the metal oxide compounds could be regarded as appropriate alternatives, the reason being the more stable materials during the processing compared to metal powders and the less toxic compared to the metal sulphides. The idea of using metal oxide compounds together with the use of a mechanochemical technique and a low cost and scalable technique of spraying is studies as the main aim of the current thesis.

# **Chapter 3**

## **Methodology, Experimental Procedure, and Characterisation Techniques**

### **3 Methodology, Experimental Procedure, and Characterisation Techniques**

This chapter presents the methods which have been used to fabricate the CZTS(e) solar devices based on the established technology and facilities at the University of Northumbria. Since the main focus of this thesis has been devoted to the fabrication of thin film absorber layers, this process has been elaborated. The chapter also includes introducing all the characterisation techniques used for the analyses. To do so, the chapter presents (i); a summary of the theory underpinning the characterisation techniques (ii); the specifications of the particular equipment used in this research and (iii); the specific set up for the particular case of experiment and characterisation technique employed for the current research.

#### **3.1 Methodology**

The initial study on fabricating CZTS thin films via a non-vacuum approach using metal oxide/sulphide powders has been carried out as a Master Project by Ming et al at Northumbria University in 2014. Although the quality and the composition of the fabricated thin films in the aforementioned study were not sufficiently applicable to photovoltaic purposes, their study showed a potential for further investigations. The current study is aimed at developing that process further, to improve the formation of CZTS thin films using a scalable method of deposition. To do so, several stages are required to be investigated. These stages include (i); preparing and developing a homogenous precursor solution with a correct composition by adjusting the ball milling parameters together with using an appropriate choice of suspension solution (ii); establishing a deposition technique to provide a good coverage of thin film on the substrate (iii); adjusting the conversion (sulphurisation) procedure to improve the quality of composition and morphology of CZTS absorber layers.

All the experiments in the current research were aimed at scrutinising the influence of various parameters on improving the quality of precursor solutions, the thin film uniformity, and the converted CZTS absorber layers. Based on previous literature, as mentioned in Chapter 2, one of the key points in fabricating the absorber layer is the conversion conditions. Therefore, in this thesis, most of the effort was devoted to examine the quality of microstructure and the composition of CZTS absorber layers by varying the conversion conditions.



The current study was initiated with evaluating the synthesising process in developing CZTSe thin films via vacuum deposition technique. This has been carried out in order to gain experience and knowledge on the influence of conversion factors for the fabrication of Kesterite absorber layer. The development of CZTSe thin films, together with fabricating a homogenous precursor solution, and establishing a scalable non-vacuum deposition route, were considered as preliminary investigations. Afterwards, the focus was put on synthesising the CZTS thin films by mainly adjusting the conversion parameters such as dwell time (sulphurisation time), temperature, heating profile, ambient gas pressure and its composition, and post heat treatment procedure. Moreover, the influence of chalcogen quantity (S) and precursor composition, together with, the impact of surface etching on the morphology and the composition of fabricated CZTS thin films, have been studied.

In addition to the aforementioned studies, several investigations have been carried out in order to improve the quality of absorber layers. These investigations have been performed based on the challenges that emerged during the synthesising of CZTS thin films, which are listed below and are entitled as follow-up trials in this thesis. Although some of them have shown promising results, further investigations require additional time and collaboration, which was beyond the scope of this PhD thesis.

- (i) The use of the slot-die technique as a scalable method of deposition, and comparing its results with the samples prepared via spraying technique. The slot-die samples have been fabricated by Dr. Greenwood at Swansea University in collaboration.
- (ii) The use of elemental mass of sulphur in the precursor solution and sulphurisation procedure, rather than its use in only the sulphurisation process.
- (iii) The pre and post selenisation of CZTS samples prepared via non-vacuum deposition routes. This has been carried out based on the premise that selenium substitution in sulphur positions may contribute to grain growth, consequently forming a compact and dense thin film structure.

Once the absorber layer was fabricated via either vacuum or non-vacuum deposition techniques, for a limited part of the study, the CdS to form a p-n junction, and subsequently, ITO as a TCO window layer have been developed. This has been carried out in order to prepare a complete solar device and to evaluate the optical characterisation of the p-n junction using EQE analysis. The following section in this chapter,

Experimental Procedure, a brief explanation of the methods, which have been used to fabricate each component of a device. The main characterisation techniques used to analyse the fabricated materials at each stage of processing are described and presented below (section 3.3).

Finally, the study in this thesis will follow by evaluating the LCA of CZTS thin film production using vacuum and non-vacuum deposition techniques. In this study, CIGS prepared via vacuum processing was selected as a reference. This was due to the similarity of CIGS and CZTS in device structure, configuration, and to the significance of CIGS as a commercially produced thin film PV. This evaluation presents the impacts of material usage and energy consumption used for the processing of CZTS and CIGS absorber layers on the four main environmental issues of human health, ecosystem quality, climate change, and resources. This will be explained in further details in chapter 6.

### 3.2 Experimental Procedure

The CZTS(e) device structure with a substrate configuration has been used in this thesis (see Figure 3-1b). Therefore, the absorber layer (p-junction) is grown on top of the back contact/substrate. Subsequently, the buffer layer (n-junction) is deposited on top of the absorber layer. In this thesis, soda-lime glass (SLG) has been used as a substrate. On top of the SLG, a Mo metallic layer is deposited by vacuum deposition technique. The CZTS(e) absorber layer is grown as a coating on the surface of the back contact (Mo layer). This process has been carried out, either via vacuum or non-vacuum deposition technique. The process is followed by deposition of CdS layer as a buffer layer through Chemical Bath Deposition (CBD). The device is completed via deposition of a transparent layer of ITO (indium tin oxide) using pulsed DC magnetron sputtering.

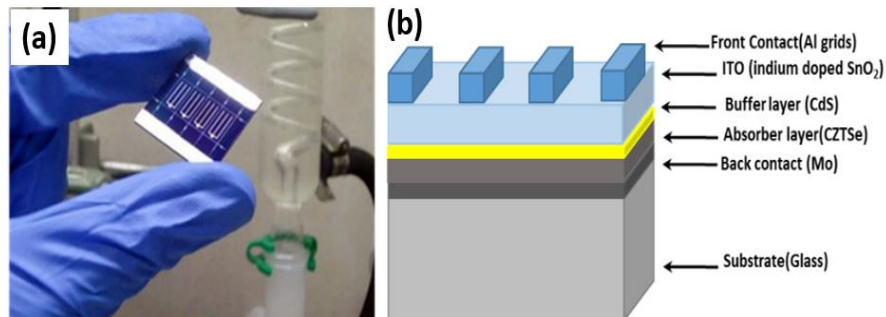


Figure 3-1. (a) IBM's CZTS solar cell device [171] (b) a schematic of a thin film solar cell with Mo back contact, chalcogenide absorber (CZTS), CdS buffer, ITO window layer, and aluminium front contact [67].

### **3.2.1 Preparing the substrates and the Mo back contact**

Soda-lime glass (SLG) has been used as a substrate for all processed samples. The cleaning and preparation processing of substrates have been done by brushing the surface of the samples with a nylon toothbrush using a 5% solution of Decon 90. This could remove any grease and dust particles from the surface. The cleaning process was followed by rinsing the glass substrates with deionized and ultra-pure water (18M $\Omega$ m), in the order mentioned. Afterwards, the glass substrates were dried with flowing nitrogen gas. The molybdenum coated soda-lime glasses (Mo/SLG) were mainly supplied through PVTEAM project by M-Solv Ltd. They have been fabricated using the magnetron sputtering method of deposition. The molybdenum thickness of all samples was approximately 1  $\mu$ m. The dimensions of the SLG were either 76 mm x 26 mm x 1 mm or 50 mm x 50 mm x 1 mm.

### **3.2.2 Absorber layer processing techniques**

The fabrication of the absorber layer consists of two and three-stage processes for vacuum and non-vacuum (solution processed) technique, respectively. For the former, the processing stages include (i) the deposition of precursors (ii) the heat treatment (sulphurisation and/or selenisation). For the latter, the processing stages include (i) preparing the precursor solution (ii) the deposition of precursors on substrate (iii) the processing of heat treatment (sulphurisation and/or selenisation).

The third stage for both mentioned techniques has been carried out in a tube furnace under vacuum or semi vacuum condition. In addition, Rapid Thermal Processor (RTP) has been used for a limited part of the research.

#### **3.2.2.1 Vacuum deposition**

The vacuum deposition technique involves deposition of the constituent elements on a substrate with the use of a high vacuum chamber.

##### Magnetron sputtering deposition

This technique involves the use of a DC or RF voltage which is established between the target (cathode) and the substrate (anode). The chamber is filled with an inert gas with low reactivity such as argon. Since the target is kept at negative voltage, the argon atoms are ionized and the ions ( $\text{Ar}^+$ ) are accelerated towards the targets which is made of the precursor elements. If the energy of ions are higher than the binding energy of the target atoms, the target atoms are extracted from the target surface moving through the vacuum

atmosphere, and eventually deposited onto a substrate to form a thin film [172]. The presence of magnets located in the area of the target can enhance the density of the sputtering ions, contributing to an increase in the sputtering efficiency. The coating deposition rate depends on several parameters including the magnetic field, the electric accelerating field, and the gas pressure.

The samples prepared for this thesis were fabricated using a DC magnetron sputtering deposition technique. The Cu-Zn-Sn metallic precursor layers were produced with a Nordiko 2000 magnetron sputtering system. The three targets were used with a diameter of 6" (15cm), and located in a sputter-down configuration (see Figure 3-2). The substrate table rotates with the speed of 2 rpm (revolutions per minute). A high purity of Cu, Zn, and Sn elemental targets (5N) were utilized. The chamber was evacuated to a base pressure of  $10^{-7}$  Torr prior to deposition. During the deposition, the chamber was filled with argon with a typical working pressure of  $10^{-3}$  Torr. The deposition time has been adjusted at 40 minutes, resulting in films with a thickness of  $\sim 0.8$   $\mu\text{m}$ . The composition of sputtered thin films was Cu-poor and Zn-rich, with the atomic ratio of  $\text{Cu}/(\text{Zn}+\text{Sn}) = 0.5-0.6$  and  $\text{Zn}/\text{Sn} = 1.1-1.3$  for the precursor used in fabricating CZTSe thin films.



Figure 3-2. A schematic of the side view of the Nordiko 2000 sputtering system displayed. The three targets (Cu, Zn, and Sn) are in a fixed position. The substrates are placed on four platens and rotate as shown by the arrow.

#### Thermal evaporator- Selenium cap layer

For a limited part of the study, during preliminary investigations, a thermal evaporator has been used to fabricate selenium cap layer on top of the CZT precursors.

Thermal evaporation is a PVD technique involving the fabrication of coating in a vacuum chamber when the solid material is located in a crucible and heated up to a temperature which allows for the formation of certain vapour pressures. Consequently, the evaporated material can fill the chamber and reach the substrate to create a coating [173].

In the current study, the crucible of the evaporated system was filled with ~20g of selenium pellets and worked under a pressure of  $10^{-7}$  Torr. Selenium melts in the crucible located at the bottom of the chamber, and then it evaporates. When the evaporation rate of selenium vapour reaches a constant rate, the shutter covering the crucible will be opened and the deposition commences. A selenium cap layer is formed on the surface of the precursor located at the top of the chamber.

### 3.2.2.2 *Non-vacuum deposition*

In order to use a non-vacuum deposition technique via using solution processing, the first step is to prepare the precursor solution. The technique implemented, involved the use of a mixture of binary metal oxide/sulphide powders suspended in a solvent that was subsequently deposited by wet processing (spray/printing) in order to form a precursor film. The solution suspension was prepared via ball milling to reduce and homogenise the particle size of the initial metal powders. The following sections detail the preparation of the precursor solution and the deposition techniques.

#### Ball Milling

Ball milling, as a mechano-chemical approach, is a simple material processing technique that can be used to reduce particle size and mix materials. The ball milling apparatus consists of a hollow cylindrical shell which rotates on its own axis with a certain speed, being fed with the desired material using grinding balls [134-136]. In order to grind the materials, grinding balls made of zirconia, stainless steel, or alumina are often used. Zirconia is slightly cheaper than stainless steel. Moreover, stainless steel may react with the solvent (alcohol). Zirconia also has low wear loss. Moreover, due to its higher density compared to alumina, it has higher grinding efficiency [174].

In the current study, the Fritsch P6 Planetary Ball Mill has been used. It contained two bowls (80 ml each) made of Zirconia. The grinding bowl was filled with  $\text{Cu}_2\text{O}$ ,  $\text{ZnS}$ ,  $\text{SnO}$ , grinding balls (with the composition of zirconia ( $\text{ZrO}_2$ )), and isopropyl alcohol (IPA) (as a suspension solution). The zirconia ( $\text{ZrO}_2$ ) balls with three different sizes,  $D = 5\text{mm}$ ,  $2\text{mm}$  and  $0.5\text{mm}$  were used. According to the guide from the manufacturer, it is stated that the typical achieved particle size is  $1/1000^{\text{th}}$  of the ball size diameter after the milling process. This means using a ball size of  $2\text{mm}$  can reduce the particle size down to  $2\mu\text{m}$ . The precursor materials were mixed and grounded with a speed of  $500\text{rpm}$ . To allow heat dissipation from the grinding bowls, after each step of milling, the sufficient pause time should be taken into consideration. This was fixed at 5 minutes of grinding and 7 min of

pause with total grinding time of 4 hours. Grinding can be carried out in either a wet or dry environment. In this study, three different compositions of carrier solvent were examined, including (i) 100 wt% ultra-deionized water ( $\text{H}_2\text{O}$ ) (ii) 90 wt% ultra-deionized water + 10 wt% Isopropyl alcohol (IPA,  $\text{C}_3\text{H}_8\text{O}$ ), and (iii) 100 wt% IPA. A picture of ball milling apparatus has been shown in Figure 3-3a. The precursor solution was separated from zirconia balls by passing the prepared solution from the specific sieves with an appropriate mesh number. The picture of prepared precursor solutions is shown in Figure 3-3c.

It should be noted that after each time of milling the powder, the grinding balls ( $\text{ZrO}_2$  balls) were cleaned. This process has been carried out with running the ball milling apparatus for at least 12 hours with the speed of 400rpm when a mixture of dirty  $\text{ZrO}_2$  balls and 2-3g of play sand were placed in bowls. Afterwards, the grinding balls were separated from sands. The balls and bowls were then cleaned with IPA and DI water using ultrasonic cleaner for couple of hours and finally they have dried in a glassware-drying oven.

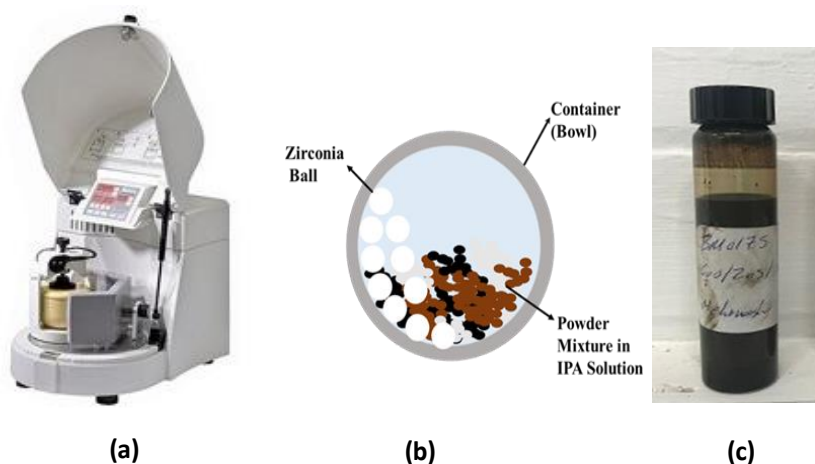


Figure 3-3 (a) a picture of ball milling apparatus (b) a schematic of grinding process (c) a typical picture of precursor solution

### Deposition Techniques

To establish a deposition technique to cover the substrate with precursor solution, different deposition approaches have been performed using doctor blade, and spraying. As a follow-up trial, the slot-die technique has also been used.

## I. Doctor Blade

Doctor blade is one of the common methods of deposition for coating wet films with thicknesses ranging from 20 to several hundred micrometres [175, 176]. In contrast to spin coating, the use of the doctor blade technique has led to less solution waste during the coating process. The technique involves the use of a sharp blade which is placed at a fixed distance from the substrate surface. The precursor solution is discharged at the front of the blade. When the substrate moves, the fixed blade pushes the solution forming a coating [177, 178].

In the current study, as preliminary trials, the doctor blade technique was simulated using an edge of cleaned SLG slide which was drawn across a fixed Mo-coated SLG substrate. For each step of coating, between 4-6 droplets of precursor solutions have been poured on the substrates. The thickness of the deposited precursors was typically between 5-7 micrometres.

## II. Spray Coating

An airbrush is a small and air-operated tool that is often used for painting (see Figure 3-4). The technique involves forcing the precursor solution through a nozzle where the fine aerosols are formed and dispatched to the substrate using a carrier gas [177]. The thickness of the wet thin film could be varied by several parameters such as the distance between the nozzle and the substrate, the viscosity of the solution, the formulation of the precursor solution, and the speed that the airbrush is moved during spraying. The fineness of the line is determined by multiple factors including nozzle size, particle size in the precursor solution, and the operating pressure. The gas and solution mix together inside the head assembly before spreading on the surface. This technique, if well-optimised, can be a promising method for fabricating thin films at both laboratory and scale-up production. In case of using this technique via a handheld strategy, practice is required to become proficient in developing the uniform and thin layer of coating on substrates.

For the current study, the BADGER SOTAR airbrush model 20/20 has been used. Figure 3-4 shows different segments of the airbrush. The nozzle at the front is the point where the precursor solution is spread onto the surface. The top-mounted cup with the capacity of 2.3 ml is where the precursor solution should be fed. The gas pressure and the amount of fluid spread on the surface increases by pressing down and pulling back the button located on top of the airbrush. The screw on the bottom needs to be connected to the gas source. The screws at the end of the airbrush can control the position of the needle which

comes out from the nozzle (see Figure 3-4, indicator 5). This screw, together with the one shown as indicator 6, can control the width of the sprayed line [179].

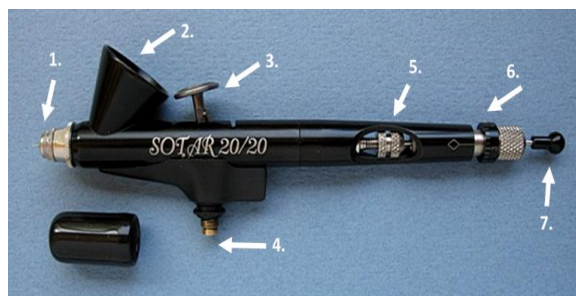


Figure 3-4. A picture of airbrush illustrating different parts: 1. Nozzle 2. Cup 3. Button to control the gas pressure and fluid quantity 4. Nozzle to connect the gas source 5. Screw to control the needle 6. Needle end knob [179].

In order to use spraying technique, the substrates were fixed and placed on a hot plate. When the temperature reached 50°C, the airbrush was moved manually in two X and Y-axes directions for 4-6 times (see Figure 3-5). After each step of spraying, the thickness of samples was measured using DekTak profilometer. The target thickness of the precursor layers was between 2 and 4  $\mu\text{m}$ . The deposited samples were left on a hot plate for 10 min at a temperature between 70°C-80°C. The as-deposited samples are shown in Figure 3-6. The working distance was set at  $\sim 8\text{-}10\text{cm}$  from the surface, and nitrogen has been used as a carrier gas.

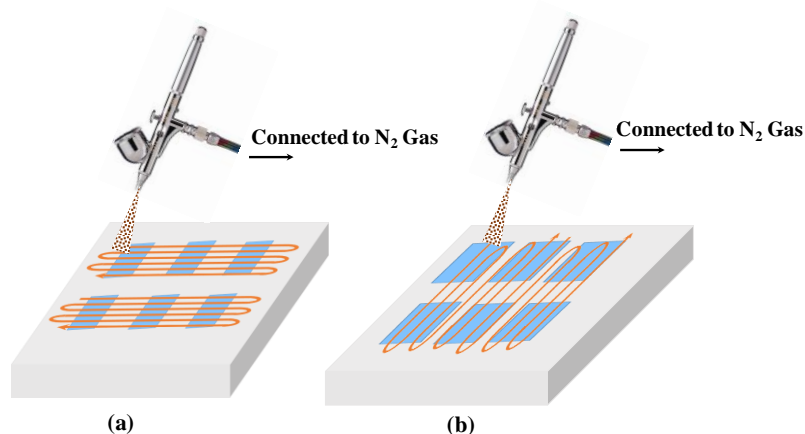


Figure 3-5. A schematic of spraying technique using airbrush with two configurations of (a) horizontal (b) vertical is illustrated. The blue rectangular areas demonstrate the positions of substrates located on the hot plate.





Figure 3-6. A picture of as-deposited precursors with spraying technique is presented. The kapton tape is placed at the edges of all samples to measure the thickness of deposited coating on the substrates.

### III. Slot-Die coatings

Slot-Die coating is a scalable method of deposition that is widely used to produce thin and uniform films [180]. In the slot-die coating technique, the precursor ink (precursor solution) is pumped through a coating head placed very close to the substrate, but without touching it. The constant quantity of precursor ink forms between the moving substrate and the slot-die head. The thickness of the coating is dependent on the width of the meniscus (the distance between the slot-die head and the substrate), and the web speed [178]. A schematic of roll-to-roll and single processes of the slot-die coating method is shown in Figure 3-7.

The trial samples that were prepared with the slot-die technique for this research have been fabricated using a Smart coater with a web width of 100 mm and a speed of 1m/min. This part of the research has been carried out by Dr. Greenwood at Swansea University.

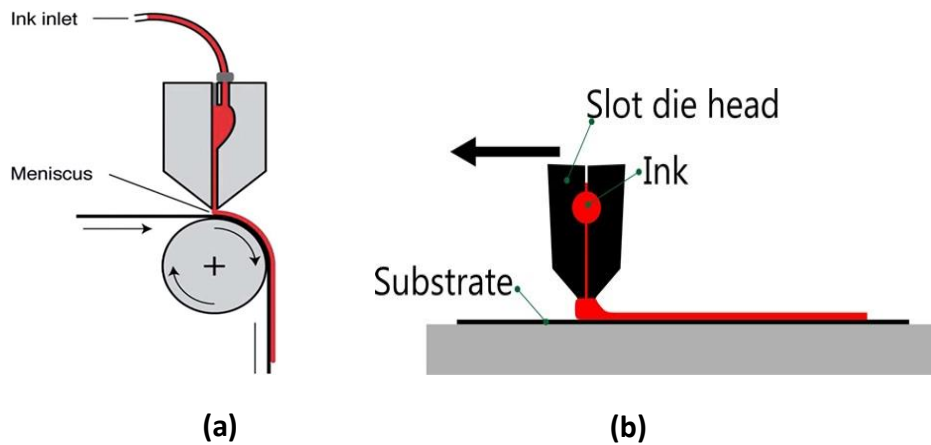


Figure 3-7. The schematic of slot-die coating system (a) a roll-to-roll process (b) a single process [178]

### 3.2.2.3 *Heat treatment*

The final step of fabricating absorber layer is the process of heat treatment or thermal conversion with a specific mass of chalcogen. This is a critical procedure for precursors processed via both vacuum and non-vacuum deposition techniques. The process is often performed in vacuum or semi vacuum conditions. The tube furnace and the Rapid Thermal Processing (RTP), as the most common techniques for this purpose, will be explained in this section.

#### Tube furnace approach

Tube furnace is often used for heat treatment of small samples. The temperature, the heating/cooling rate, and the dwelling time at particular temperature can be controlled by the power. Moreover, these equipment can be ideal choices when heat treatment is desired to be performed in an inert, vacuum, or hydrogen atmosphere.

In the current thesis, a 3-zone horizontal Carbolite tube furnace has been used for the purpose of sulphurisation and selenisation. The system can operate at temperatures of up to 1100°C.

The heat treatment process for both vacuum and non-vacuum deposited precursors has been carried out in five stages (i) the precursor together with a specific mass of chalcogen (S or Se) were placed in a graphite box according to the particular experiment. (ii) the quartz tube was pumped and purged three times with an inert gas of nitrogen in order to remove any oxygen from the system. Finally, the system was evacuated to a pressure of  $\sim 3 \times 10^{-3}$  and  $\sim 2 \times 10^{-2}$  for selenisation and sulphurisation, respectively (It should be noted that to avoid contamination and gaining accurate data, the sulphurisation and selenisation procedures have been carried out in two different tube furnaces). (iii) the specific ramp rate, temperature, and dwell time have been defined for the system (the first parameter was mainly fixed at a rate of 30°C/min. The other two parameters have been determined based on particular conditions used for each specific experiment throughout the thesis). (iv) the tube was backfilled with a certain pressure of argon and/or forming gas ( $H_2/N_2$  which contains 10%  $H_2$  + 90%  $N_2$ ) as an ambient gas according to each specific experiment prior to running the tube furnace. (v) After running and when the dwell period completed, the system was cooled down to room temperature for several hours. Afterwards, the tube was pumped and purged again, before taking out the sample. To provide rapid thermal processing without breaking the vacuum of the system within the tube furnace, a simple strategy has been used. This was achieved using a push-rod

part moving the sample along the length of the quartz tube. The push rod part was located in another smaller quartz tube connected to the main tube of the furnace at its aperture (see Figure 3-8). The push rod is also connected to a magnet with an external handle to move the sample along the graphite tray. With such a configuration, the sample can stay at cold zone until the temperature reaches and fixes at a desired value. A picture of the tube furnaces used for sulphurisation and selenisation is shown in Figure 3-9.

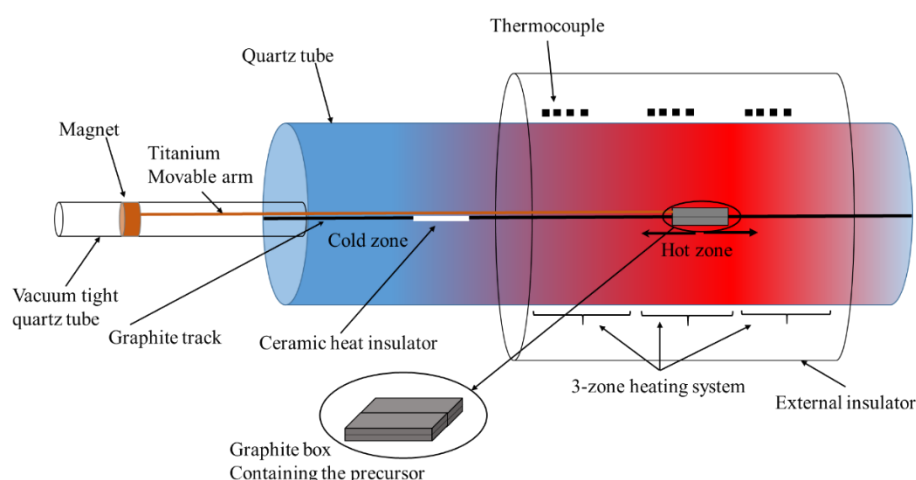


Figure 3-8. A schematic representation of quartz tube furnace used for sulphurisation is displayed. The vacuum tight quartz tube, equipped with a magnet, is used in case of providing a fast heat treatment. Otherwise, this part can be separated and the sample can be heated with a given heating ramp rate.

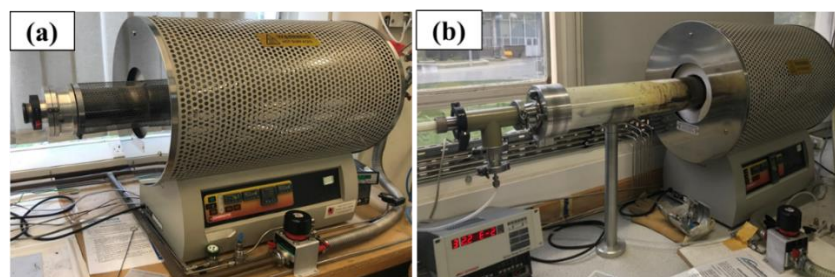


Figure 3-9. Picture of the tube furnace used for heat treatment processing of (a) Selenisation (b) Sulphurisation

Graphite boxes with two different configurations have been used to enclose the precursors inside the tube furnace. Figure 3-10 shows typical graphite boxes used for synthesising the CZTS(e) thin films. The specific graphite box used for heat treatment on the CZTSe thin film with selenium cap layer, had two different orientations; face up and face down. A schematic of a cross section view of this graphite box has been shown in Figure 3-10a. As can be seen, 4 samples can be placed in each graphite box. The second type of graphite box had a place for just one sample and the selenium pellets/sulphur powder were placed

at the sides (see Figure 3-10b and Figure 3-10c). The graphite box named a and b had an approximate internal volume of  $12\text{cm}^3$  and  $7\text{cm}^3$ , with the sample dimensions of  $7.6 \times 2.6 \times 0.1\text{ cm}^3$  and  $5 \times 2.5 \times 0.1\text{ cm}^3$ , respectively. The volume and the sample dimension of graphite boxes of b and c are equal.

The choice of the graphite boxes with the configuration shown in Figure 3-10 for the conversion procedure was based on the established facilities and the previous work done at Northumbria University. As it is reported elsewhere [15, 181], the better uniformity of absorber layer has been achieved using these configurations of graphite boxes.

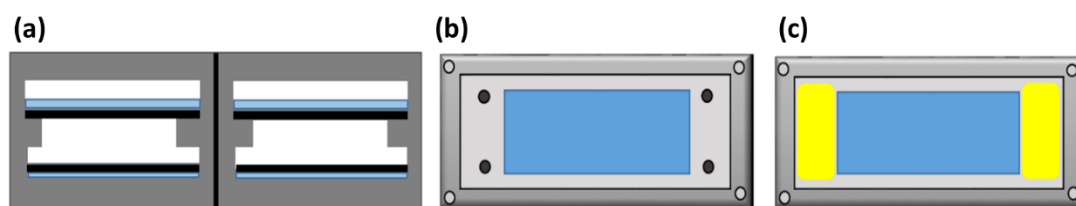


Figure 3-10. Schematic representations of (a) cross section of the graphite box utilised for the CZTSe thin film fabrication using selenium cap layer (the black layers show the selenium layers) (b) the top view of graphite box used to fabricate the CZTSe thin film with selenium pellets (the 4 black points illustrate the position of selenium pellets) (c) the top view of graphite box utilised for the CZTS thin film fabrication when the sulphur powder is used (yellow areas show the position of sulphur powder). The blue areas in all pictures indicate the position of precursor.

#### Rapid Thermal Processing (RTP)

Rapid thermal processing is regarded as an advanced processing technology to provide heating procedure over a short period of time. The term RTP refers to that equipment having the ability to ramp temperature up and down with a high speed.

For a limited part of the study in this thesis, the ‘Annelasys As-one RTP’ has been used to selenise the precursors or the sulphurised samples. According to each specific experiment, different quantities of selenium pellets were situated around the sample (see Figure 3-11b). Afterwards, the graphite box was placed inside the reactor and the samples were converted at  $550^\circ\text{C}$  for 15 min in atmospheric ambient pressure with the ramp rate of  $270^\circ\text{C}/\text{min}$ , for both heating and cooling steps. The heat treatment procedure has been used based on the optimum conversion conditions examined and reported in previous research performed by Dr. Jose Marquez at Northumbria University [15].

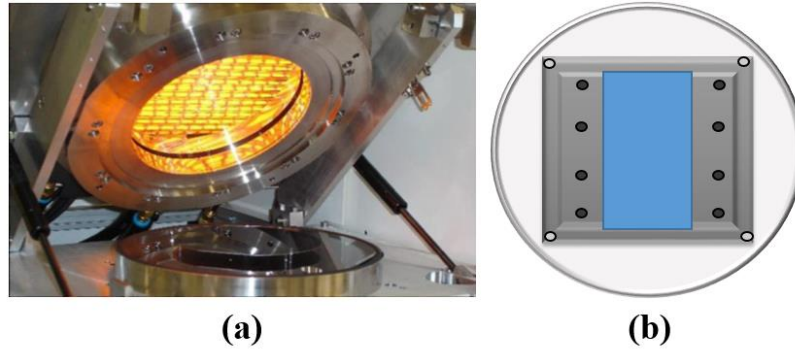


Figure 3-11. (a) an image of the Annelasys As-one rapid thermal processor (taken from [www.annealsys.com](http://www.annealsys.com)) (b) a top view schematic of an open graphite reactor (black points indicate the selenium pellets and the blue area displays the location of precursor)

### 3.2.3 Preparing buffer layer by Chemical Bath Deposition (CBD)

The choice of CdS and its fabrication via CBD has shown promising results in CIGS solar cell fabrication. This is due to the similarity in material and processing of CZTS and CIGS solar cells, as discussed in chapter 2. To prepare the buffer layer, a chemical bath deposition (CBD) method was prepared to deposit an approximately 50nm thick CdS layer.

All the CZTS(e) absorber layers were etched in a 10 wt% KCN aqueous solution and/or 20 wt%  $(\text{NH}_4)_2\text{S}$  for 0.5 and 3 minutes, respectively. The CBD was processed in a jacketed beaker, heated to a temperature of  $67^\circ\text{C}$  (see Figure 3-12). The 0.08g of cadmium sulphide ( $\text{CdSO}_4$ ) and 0.76g of thiourea  $(\text{NH}_2)_2\text{CS}$  were used as Cd and S sources, respectively. The 18.25 g ammonium hydroxide ( $\text{NH}_4\text{OH}$ ) solution has been used to control the PH of the solution. The corresponding chemical formulas are presented through Reaction 3-1 to 3-4 (shown below) [182]. The samples were immersed in the solution for approximately 8 minutes before being rinsed with deionized water. The end of the process can be determined by the appearance of the solution with a yellowish colour (see Figure 3-12).

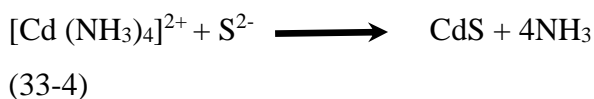
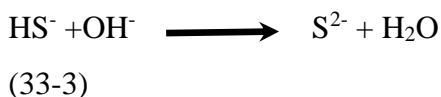
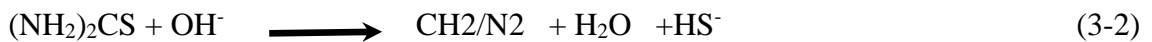




Figure 3-12. The figure shows the jacketed beaker containing the solution which is used to develop CdS thin film via CBD technique.

### 3.2.4 Front Contact

After the chemical bath deposition, a transparent layer of doped indium tin oxide ITO was deposited by a DC pulsed magnetron sputtering. All CZTS(e) solar cells were mechanically scribed to produce individual cells with an area of  $0.09 \text{ cm}^2$ .

## 3.3 Characterisation Techniques

This section presents the main characterisation techniques used to evaluate the material properties of precursor solutions, thin film precursors, and converted absorber layers. The section includes a description and specification of all used equipment and the experimental set up which has been used to carry out the analyses.

### 3.3.1 DektakXT profilometer: film thickness

A profilometer is a useful technique to measure the surface profile. It is mainly used to quantify the roughness and the thickness of thin films ranging from a few  $\mu\text{m}$  to  $20 \text{ nm}$  [183].

In the current study, a Bruker DektakXT Profilometer has been used to measure the thicknesses of the prepared thin films. That ensured by using a thin strip of Kapton tape at the edge of substrates before film deposition. Consequently, with pulling off the tape after deposition processing, the film thickness can be identified with the formation of a sharp step between the fabricated film and the substrate. To do so, one point on the coating and one on the substrate need to be defined manually, which facilitate the tip contacts scanning the surface. When the scan measurement completes, a two-dimensional profile appears (see Figure 3-13b). The difference between the two levels (regions in red and green shown in graph), is depicting the thin film thickness.

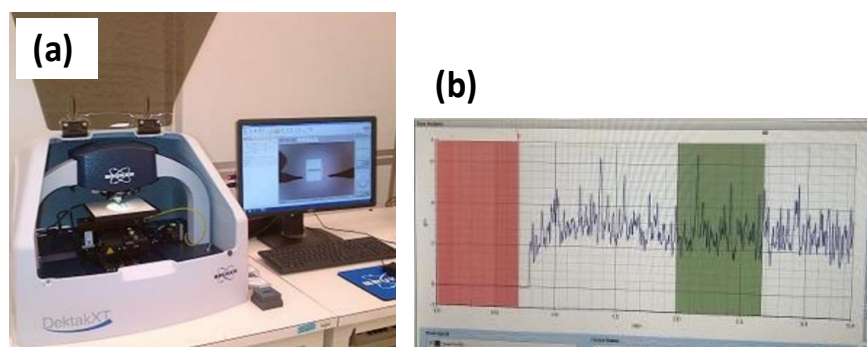


Figure 3-13. (a) a picture of DektakXT profilometer (b) a typical graph of a thickness measurement.

### 3.3.2 Mastersize Particle Analyser

Mastersizer is often used to measure the particle size of materials, when they are dispersed in a carrier solvent (a dispersed medium) using the technology of laser diffraction. When the laser passes through the dispersed medium, it will be diffracted according to the specific particle size of the sample. This process is based on Fraunhofer or Mie theory. For more details, the reader is referred to the related paper [184]. As mentioned earlier, the sample needs to be dispersed in an appropriate liquid medium in which the particles are insoluble. The sample preparation is one of the important stages since an inappropriate carrier liquid could affect the agglomeration or a non-uniform dispersion of particles through the liquid medium. This, if it occurs, will lead to the wrong data being obtained. The Tween 20 solution is one of the common solutions which has been used for most of the analyses, and is also recommended to be used by Malvern Mastersize analyser Ltd [185].

In the current research, Malvern Mastersizer 2000 system has been used to determine the particle size of milled powders. The system can measure particle size ranging from 0.02 to 2000 micrometres. The effect of using different ball sizes (grinders) on the final particle size of milled compounds has been evaluated by analysing the  $\text{Cu}_2\text{O}$  powder when it is milled with three ball sizes of  $D = 5, 2, \text{ and } 0.5 \text{ mm}$ . The particle size of the  $\text{Cu}_2\text{O}$  compound was measured before and after four hours of milling process. The ground compounds were dispersed, first in deionized water, but due to the weak dispersion of powders in the solution, they were then dispersed in a specific detergent called Tween 20 with the chemical formula of  $\text{C}_{58}\text{H}_{114}\text{O}_{26}$ . The sample was prepared by mixing 12 droplets of this solution in 1g of  $\text{Cu}_2\text{O}$  powder. The mixture of  $\text{Cu}_2\text{O}$  particles in the carrier liquid was placed in the ultrasonic cleaner for 10 min to be dispersed completely prior to



introducing the solution into the Mastersize analyser system. The system was filled with deionized water to a certain height level prior to the experiment. The sample solution was then added to the system by a rate of recurrence of one droplet per 3 seconds (between 7-10 droplets for each experiment to achieve the laser obscuration of 10-20%). The measurements have also been repeated several times to find stable and reproducible results (see Figure 3-14).



Figure 3-14. A picture of the Malvern Mastersizer 2000 is shown. The equipment and the typical graph achieved by the system (the Department of Geography in University of Northumbria)

### **3.3.3 Contact Angle Analyser**

Contact angle analysis is a useful technique to determine the quantitative measurements of the wetting capability of a solid surface by a liquid. Thus, a droplet of liquid is placed on the surface and the angle between these two states is measured at a specific time range. For a limited part of the current study, the wettability of using IPA and/or water (as a suspension solution) on substrates (SLG, SLG/Mo), has been measured at Swansea University by Dr. Peter Greenwood. This experiment has been carried out as a preliminary trial to evaluate the proper solvent in order to make a precursor solution with a better wettability when it covers the substrate.

### **3.3.4 Scanning electron microscope and elemental composition analysis (SEM/EDX)**

Scanning Electron Microscope (SEM) can be typically used for imaging the microstructure and characterisation of materials. The local elemental composition of



materials can be also measured if the SEM is equipped with energy-dispersive X-ray (EDX) detectors.

In SEM, the electron beam is produced from the electron gun and is affected when it passes through the condenser and objective lenses. The roles of these lenses are to narrow and adjust the electron beam down to the specimen level. Once the electron beam is incident on the specimen, the electrons may be absorbed into, reflected from, or be transmitted through the specimen. The reflected electrons can be collected by certain detectors to identify a specific characteristic of the sample (see Figure 3-15) [186-188].

When the incident electrons interact with loosely bound electrons in the conduction band of the specimen, then they will emit secondary electrons. This emission rate is extremely sensitive to the height difference in the surface and has a great role in identifying the topography of the surface specimen or imaging. These electrons (secondary electrons) have a very small energy, approximately less than 50eV. Less reflected secondary electrons indicate the deeper regions of the surface and are shown by dark areas in the SEM image. More reflected secondary electrons show the higher regions of the surface and can be observed as brighter features in the image. Thus, with the difference in quantity of reflected secondary electrons, the SEM image will be created [186, 187].

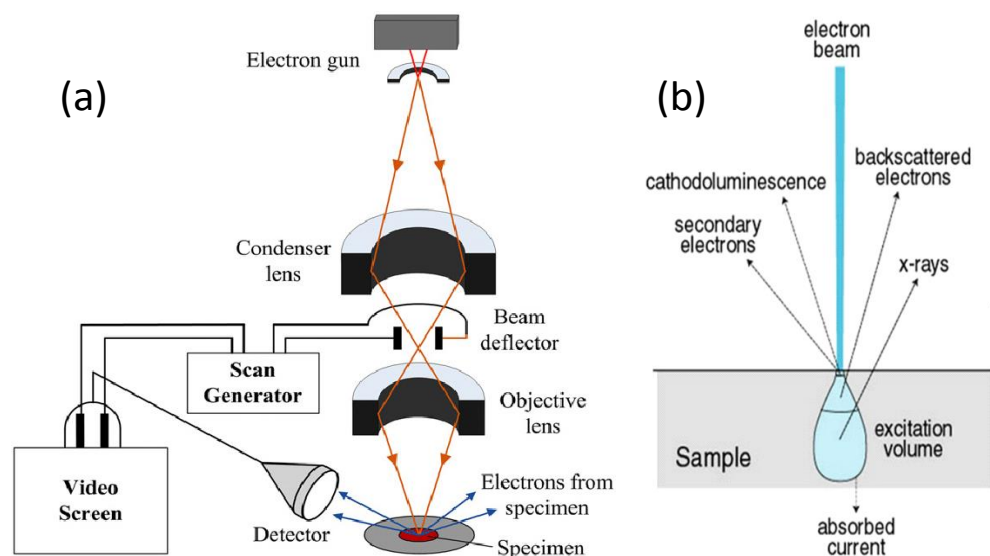


Figure 3-15. A schematic view of (a) Secondary Electron Microscope (SEM) and (b) signals emitted from different depths of the interacted sample is displayed. The figures are adapted from [189, 190]

As shown in Figure 3-15, when the electron beam hits the specimen, various electrons and electromagnetic waves can be emitted from the substance. The principle of the EDX function is based on detecting the X-rays (see Figure 3-15b), named ‘characteristic X-rays’, because they could be indicative of individual elements. Accordingly, the compositional elements of substances can be revealed. When an electron in the inner shell of atoms of a specimen is emitted from the inner shell by the incident electron beam, the vacant state is then re-occupied by an electron from the outer shells which has a different energy state. The difference between these two states of energy (the outer shells and the inner shells) corresponds to characteristic X-rays and can be detected via EDX analysis [188].

One of the important factors in analysing the surface through both SEM and EDX measurements is the acceleration voltage. This parameter should not be less than twice of the highest excitation energy of any element present in the specimen. This is to obtain sufficient intensity from all the presented elements. In the case of analysing CZTS compounds, the excitation energy should not be less than 7 KeV [191] . Moreover, an appropriate acceleration voltage is required to obtain sufficient X-rays from the specimen. According to the Grün range formula, each acceleration voltage corresponds to a specific range of penetration depth ‘R’ from the surface, when ‘ $\rho$ ’ is the density of material and ‘ $E_b$ ’ is the energy of incident electron beam (see equation 4-1) [192].

$$R (\mu\text{m}) = [0.0398/\rho] (E_b)^{1.75}$$

(3-1)

Another significant factor in EDX measurements is the working distance which refers to the distance from the final pole piece of the lens to the focused point on the specimen. It is important for the working distance to be adjusted, since the detector should be in line with the position at which the X-rays are generated. The working distance can be adjusted by the level of the stage and it depends on the type of microscope which is used. The X-ray spectrum can also be used for qualitative analyses (EDX mapping) to obtain a spectrum from a specific area. In addition, it can be used for line scanning which displays a one-dimensional distribution of elements on a specific line. Mapping, as another qualitative analysis, is observed when the electron probe is scanned over a specific area. Therefore, an image can display the presence of different elements across that scanned area [188].

SEM and EDX were widely used as characterisation techniques for the current study. The samples have been measured with two different system due to the substitution of new equipment at the laboratory of Northumbria University in April 2016. For further clarifications, it should be noted that all the data presented in chapter 4 (preliminary investigations) have been achieved using a FEI Quanta 200. The EDX measurements were achieved using a lithium-drifted silicon detector attached to the SEM. However, the data presented in chapter 5 have been analysed using TESCAN MIRA 3 scanning electron microscope which was equipped with an X-ray detector X-Max 150 mm<sup>2</sup> for EDX, using Aztec Energy software. The picture of both pieces of apparatus are shown in Figure 3-16. All the EDX compositional measurements have been accomplished at 20kV for the fabricated CZTSe thin films, and 15 kV for CZTS and CZTSSe thin films, corresponding to a penetration depth of approximately 1.6  $\mu\text{m}$  (for CZTSe thin films) and 1.0  $\mu\text{m}$  (for CZTS and CZTSSe thin films). The working distance was set at 10 mm for all the EDX analyses. It should be noted that when the analyses are done by EDX, due to the overlap of the sulphur  $K_{\alpha}$  peak and the Molybdenum  $L_{\alpha}$  peak [193], both substrates of SLG and Mo/SLG have been used to detect the exact quantity of sulphur across the thin film.

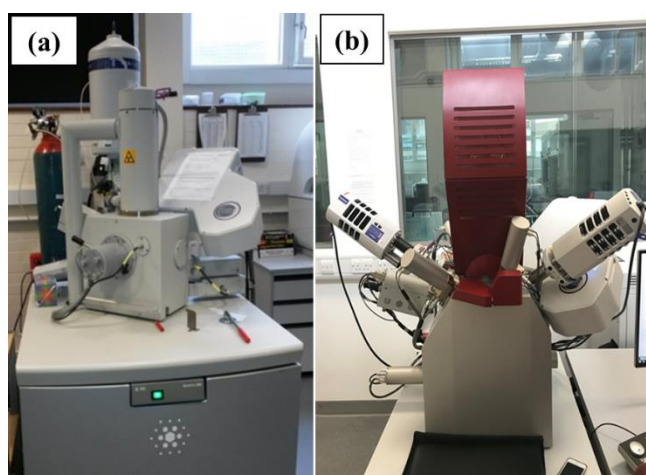


Figure 3-16. A picture of SEM and EDX equipment used during the current study (a) FEI Quanta 200 (b) Tescan Mira 3

### 3.3.5 X-ray Diffraction (XRD)

X-ray diffraction is one of the common non-destructive tests that is frequently used for the study of the crystal structure of materials. The X-ray diffraction is a consequence of reflected beams from the specific planes based on atoms' position in crystal structure. When the incident X-ray, with an angle of  $\Theta$ , hits an atomic plane in a crystalline material,

the energy transferred to atoms will be reflected with the same wavelength and energy, but with a different amplitude or intensity. The intensity is determined by the concentration of atoms in the specific planes of the crystal lattice. A signal which appears on the diffraction pattern is detected only if the atoms are located in a periodic manner through the atomic structure, meaning a crystalline material. The incoming X-ray radiation can be transmitted at different planes of atoms, which, in turn shows the arrangements of atoms within the structure. Thus, the material can be identified by its structural properties (i.e. the lattice) [194]. In 1913, William Lawrence Bragg represented an equation which shows the relationship between the X-ray diffraction and the lattice parameters. This equation is known as Bragg Law and is presented in equation (3-2). According to Bragg's Law, constructive interference occurs when the path difference of the beam is reflected from an array of lattice planes with Miller Indices (h,k,l). The specific set of planes spaced via lattice spacing is indicated by d. The wavelength is represented by  $\lambda$ .

As shown in Figure 3-17, the beams reflected from lower planes travel more than those reflected from upper layers by a magnitude of  $2d\sin\theta$ . When the conditions of Bragg's Law ( $n\lambda=2d\sin\theta$ ) are satisfied, the scattered waves interfere constructively, resulting in the appearance of a peak at that specific angle. It should be noted that in case of using a configuration of Bragg-Brentano, since the position of the detector is always given by  $2\theta$ , only the parallel planes with respect to the surface of the films can be detected. Thus, as the  $\theta$  varies, different families of planes with different lattice spacing (d) can be detected. The crystal structure of a specimen can be evaluated by analysing the intensity and orientations of the diffracted patterns. Bragg-Brentano Geometry (BBXRD) is a popular configuration of X-ray diffraction. In this technique, both the X-ray, as source of incident radiation, and the detector move at the same angle velocity (see Figure 3-17) [194, 195].

$$\lambda = 2 d_{(hkl)} \sin \theta \quad (33-2)$$

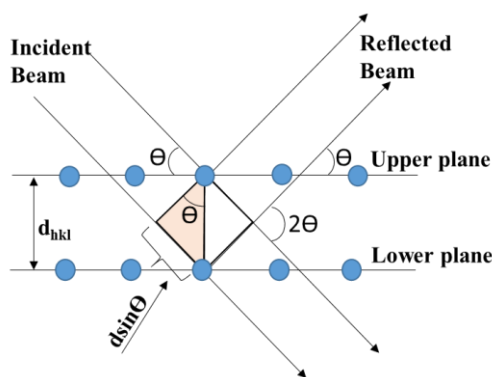


Figure 3-17. A two-dimensional illustration of an X-ray beam reflection from two parallel crystalline planes separated by distance  $d$ .

The system used for the current study was a Bruker D5000 diffractometer equipped with a Bragg-Brentano configuration. The X-ray source was Cu-K $\alpha$  at 1.54056 Å, with a standard range of 2-theta degrees ( $2\theta$ ) from 10 to 90 and a spot size of  $\sim 500\ \mu\text{m}$ . The measurements have been carried out with a voltage of 40 kV and current of 40 mA. The calculations and analyses were studied using EVA, from Bruker, and Power Cell software. The databases, as a reference, were extracted from ICSD online databases (Inorganic Crystal Structure Data). In Table 3-1 and Table 3-2, the powder diffraction file (PDF) of CZTS and CZTSe are presented, respectively. The term  $I/I_0$  is the relative peak intensity,  $d$  corresponds to the lattice space between the two neighbouring parallel planes,  $(hkl)$  denotes miller indices, and  $2\theta$  represents twice the diffraction angle.

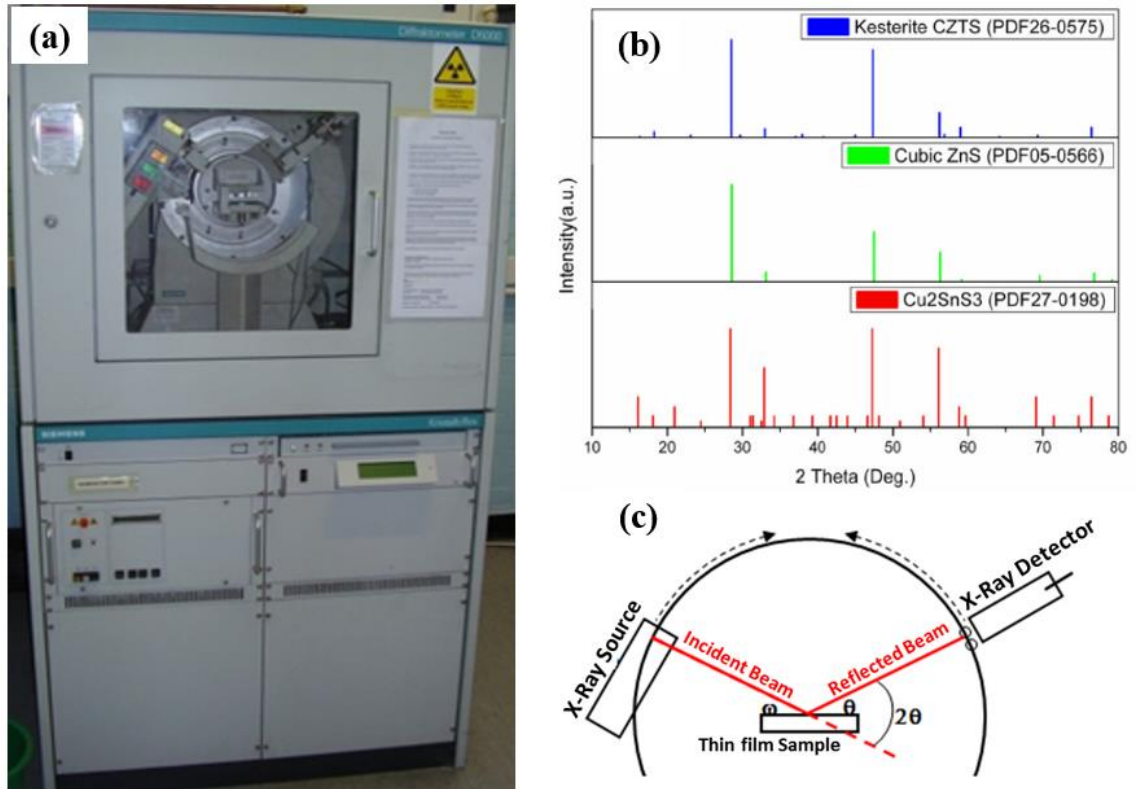


Figure 3-18. (a) A picture of the XRD apparatus (b) A typical XRD pattern of Kesterite CZTS crystal structure (c) A schematic of X-ray diffractometer with Bragg-Brentano geometry. The schematic diagram of part (c) is courtesy of Dr. Pietro Maiello from Northumbria University.

Table 3-1. Lattice data of a single crystal Kesterite CZTS (ICSD database)

<b>millor indices (hkl)</b>	<b>2<math>\Theta</math> (degree)</b>	<b>d (<math>\text{\AA}^\circ</math>)</b>	<b>I/I<sub>0</sub> (%)</b>
002	16.34	5.42	1
101	18.21	4.86	6
110	23.10	3.84	2
112	28.53	3.12	100
103	29.68	3.00	2
200	32.99	2.71	9
202	37.03	2.42	1
211	37.97	2.36	3
114	40.76	2.21	1
105	45.00	2.01	2
204	47.33	1.91	90
132	56.18	1.63	25
215	56.86	1.61	3
224	58.97	1.56	10
134	64.18	1.45	1
400	69.23	1.35	2
316	76.44	1.24	10

Table 3-2. Lattice data of a single crystal Kesterite CZTSe (ICSD database)

<b>millier indices (hkl)</b>	<b>2<math>\Theta</math> (degree)</b>	<b>d (<math>\text{\AA}</math>)</b>	<b>I/I<sub>0</sub> (%)</b>
002	15.61	5.67	1
101	17.39	5.09	2
110	22.03	4.03	2
112	27.12	3.28	100
103	28.30	3.15	2
202	35.21	2.54	1
211	36.08	2.48	1
204	45.07	2.00	45
312	53.28	1.71	13
116	53.50	1.71	12
400	65.44	1.41	6



### 3.3.6 Raman spectroscopy

Raman spectroscopy is an optical non-destructive technique. Raman scattering spectroscopy is based on the measurement of the scattered light from a material. When the molecules of a material are exposed to a monochromatic light beam, the molecules are excited to a virtual state with higher energy. However, this virtual state is a transient state, meaning, the molecules fall back down to the ground state. According to the energy of the final state, a photon is scattered and can be detected as a Raman characteristic [196]. The use of excitation wavelength is important since it affects the efficiency of Raman characteristic in that if it is too high, the efficiency is very low by a factor of  $1/\lambda^4$ . While, if the excitation wavelength is very low, fluorescence emission will occur leading to the Raman peaks becoming sharp peak. The line shape and position of the Raman bands are determined by the crystalline structure and chemical composition of the measured samples. However, to identify different compounds, the excitation wavelength should be in a specified range [197, 198].

The Raman spectra presented in chapters 5 were recorded by Dr. Sara Dale at Bath University and Dr. Wei Zhengfei at Swansea University. The analyses have been carried with a 'T64000 Horiba-Jobin Yvon spectrometer' using excitation wavelengths of 325nm and 532nm at Bath University. In addition, the analyses were also done by 'Renishaw in Via Raman spectrometer' using the excitation wavelengths of 532nm at Swansea University. This technique is quite a useful method, especially in characterising the Kesterite compounds, since with only the X-ray diffraction analysis, the indicative peaks of ZnS(e), CZTS(e), and CTS compounds overlap and cannot be distinguished.

Consistent with previous studies, the Raman fingerprints at 325nm excitation wavelength for Cu<sub>2</sub>O should appear at 109 cm<sup>-1</sup>, 154 cm<sup>-1</sup>, 218 cm<sup>-1</sup>, 308 cm<sup>-1</sup>, 436 cm<sup>-1</sup>, 515 cm<sup>-1</sup>, 635 cm<sup>-1</sup>, 665 cm<sup>-1</sup>, and 820 cm<sup>-1</sup>, while ZnS fingerprints at this excitation wavelength should be at 348 cm<sup>-1</sup>, 697 cm<sup>-1</sup>, and 1045 cm<sup>-1</sup>. The Raman fingerprints at excitation wavelength of 532nm for Cu<sub>2</sub>O observe the peaks at 150 cm<sup>-1</sup>, 220 cm<sup>-1</sup>, 218 cm<sup>-1</sup>, 308 cm<sup>-1</sup>, 416 cm<sup>-1</sup>, 515 cm<sup>-1</sup>, 630 cm<sup>-1</sup>, and 645 cm<sup>-1</sup>, whereas SnO is characterised by peaks at 112 cm<sup>-1</sup> and 210 cm<sup>-1</sup> [199-203]. Typical Raman spectra of CZTS thin films at different excitation wavelengths are shown in Figure 3-19.

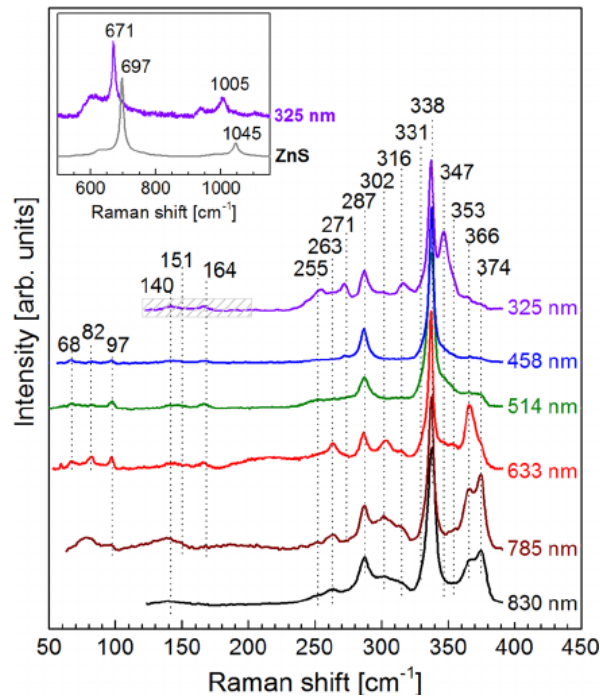


Figure 3-19. A typical Raman spectra of a CZTS thin films at different excitation wavelengths [203]

### 3.3.7 Intensity modulated photocurrent spectroscopy (IMPS)

The IMPS system is used to evaluate the optoelectronic characteristics of the absorber layer prior to depositing the subsequent device layers. This technique could be beneficial in both academic research and also in industry as a process of monitoring technique.

The technique can be performed with the use by providing a p-semiconductor/electrolyte junction. The use of transparent redox electrolyte solution is required to permit the light to be transmitted to the surface of a solid (absorber layer) under illumination. Photo electrochemical analyses on CIGSe have shown that under illumination, the presence of  $\text{Eu}^{2+}$  ions in the electrolyte can act as collectors for the electrons (minority carriers) generated on the surface of the absorber layer. This will occur when the energy of illuminated photons is higher than the band gap of the p-type semiconductor [204].

Two processes will occur under illumination: (i) photoexcitation (ii) electron transfer. When the light is incident, an overshoot effect can be seen due to the photoexcitation and generation of electrons and holes at the interface of p-n junction (see Figure 3-20).

Afterwards, the electrons are transferred to the electrolyte side by  $\text{Eu}^{+2}$  ions and consequently leave the hole at the interface. The further behaviour of photocurrent transients can be explained by the separation or recombination of electrons and holes.

Surface defects could act as a recombination site and therefore can reduce the electron flow. Thus, the generation of majority carrier leads to an overshoot of photocurrent, while recombination causes the photocurrent to decay quickly [205]. The current can be generated if the external potential overcomes the internal bias and consequently, the electron-hole separates at the interface before being recombined [206]. Therefore, applying sufficient reverse bias voltage can contribute to collection of approximately all the photo generated charge carriers [3]. More details on the formation of the solid/liquid junction is presented in Appendix A.

To study the photocurrent response of CZTS absorber layers, an optical measurement setup was used. The schematic view of the set-up is illustrated in Figure 3-21. The sample acts as a working electrode (WE) and was placed in a transparent glass box filled with a 0.2M aqueous electrolyte solution of  $\text{Eu}(\text{NO}_3)_3 \cdot 6\text{H}_2\text{O}$ , with the redox potential for the couple  $\text{Eu}^{3+}/\text{Eu}^{2+}$  of 0.557V vs Ag/AgCl. The reference electrode (RE) is Ag/AgCl, and Pt/FTO is the counter electrode which is a platinum electrode in fluorine doped tin oxide used to allow the current to flow through the external circuit. The three electrodes are connected to potentiostat. The sample also needs preparation before immersing into the electrolyte. To do so, a small part of the analysed sample, which was produced on a molybdenum/glass substrate, was polished with an abrasive paste (1 $\mu\text{m}$  Alumina paste) to expose the molybdenum surface. The square wave is formed by a waveform generator by applying the frequency of 0.1 to 5kHz. This can be visualised through the oscilloscope. The sample is then illuminated by a beam emitted with a pulsed LED light (a Thorlabs C17 LED) with different wavelengths of 940 nm (IR), 565 nm (VIS), and a broad white source (425-650 nm) with a central wavelength of 430 nm. The typical power of the LED was 800 mW (940 nm (IR)), 880 mW (565 nm (VIS)), and 800 mW (425-650 nm (broad white source)). The spectra of these three collimated LEDs are shown in Appendix A. The signals demonstrated on the oscilloscope can be observed and analysed through light on-off cycle. In this manner, high photocurrent response is associated with a higher current density. Consequently, depending on its configuration, different interpretation can be explained (see Figure 3-20).

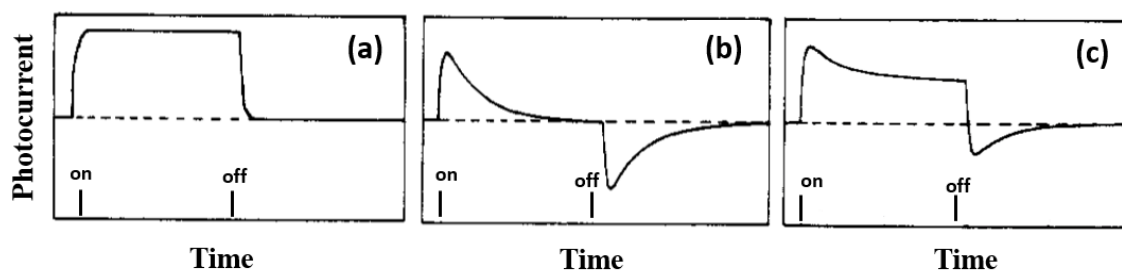


Figure 3-20. Three configurations of transient photocurrent responses to pulsed illumination with (a) no recombination (b) almost complete recombination (c) partial recombination [205].

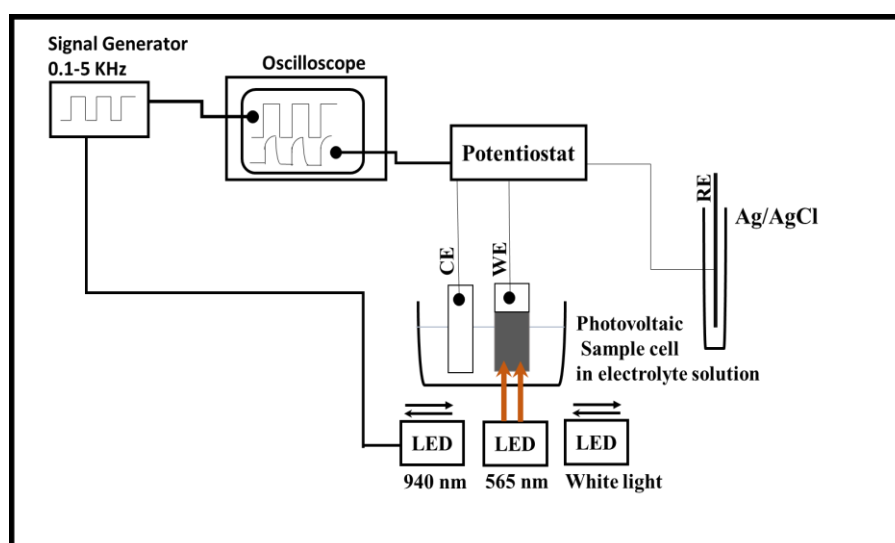


Figure 3-21. A schematic of IMPS measurements set up

### 3.3.8 External quantum efficiency (EQE)

The EQE measurement, as explained in Chapter 2, measure the ratio of collected electrons per time per incident photons with a certain energy. As mentioned before, this factor is influenced by the rate of recombination or optical losses. The EQE spectrum can depict the optical losses. For short wavelengths, only a small fraction of light is absorbed by the absorber layer and most of the light is absorbed at the layers prior to the absorber layer. For long wavelengths, the absorber layer acts as a transparent component. In the case of surface recombination, the EQE plot has lower intensity at lower wavelengths, and if the minority carrier diffusion length is shorter than the wafer thickness, the plot shows lower intensity at higher wavelengths reflecting the bulk recombination.

The band gap of the absorber layer can be calculated using the EQE measurements. For an ideal p-n junction, the EQE can be followed by the equation 3-3, where  $\alpha$  is the

absorption coefficient,  $w$  is the width of the SCR, and  $L_n$  is the minority carrier diffusion length.

$$EQE = 1 - \frac{\exp(-\alpha w)}{1 + \alpha L_n}$$

(33-3)

Assuming  $\alpha L_n < 1$ , meaning a very short  $L_n$ , equation 4-3 changes to equation 4-4.

$$EQE = 1 - \exp(-\alpha w) \quad (3-4)$$

For direct band gap semiconductors the equation 4-4 is approximated by equation 4-5.

$$\alpha h \propto (h \nu - E_g)^{1/2} \quad (3-5)$$

Consequently, the band gap of absorber layer is approximated by extrapolating the plots of  $[\ln(1-EQE)]^2$  vs.  $h\nu$  [16, 207].

The EQE measurements that have been reported in this thesis, presented in chapter 5, has been performed using a lock-in amplifier and a chopped white light source (900 W, halogen lamp, 360 Hz). It was combined with a grating monochromatic (calibrated with Si and Ge diodes) using 5 mM RuHex and 0.1 M sodium sulphate as an electrolyte solution. The illuminated area was approximately 2 mm<sup>2</sup>. The EQE measurement for this study has been carried out by Dr. Sara Dale at the University of Bath.

# **Chapter 4**

## **Preliminary Investigations**

## 4 Preliminary investigations

This Chapter includes three parts consisting of (i) the establishment of a process that enables investigation of the conversion/synthesis of absorber layers by the established technology at Northumbria University (ii) the establishment of a uniform and homogenous precursor solution by a mechano-chemical procedure of ball milling (iii) the establishment of a scalable non-vacuum deposition method.

### 4.1 CZTSe absorber layer fabricated by vacuum deposition technique

This experiment provides an overview of the important parameters affecting the quality of the CZTSe absorber layer based on the vacuum deposition of precursors, which was an established technology at Northumbria University. The study of this experiment is also considered, as a preliminary investigation, to develop an appropriate synthesising approach in order to fabricate the CZTS Kesterite based thin films which will be presented in the next chapter.

The fabrication parameters investigated for the synthesising of CZTSe Kesterite absorber layers included the following: (i) the influence of preheating and different methods of supplying selenium on macro/microscopic uniformity of absorber layer (ii) the influence of pre-treatment by varying conversion temperature and pressure on the micro and crystal structure of the absorber layers.

### 4.2 Preheating and method of supplying the selenium

This specific experiment has been developed from results of a Master's Project by Guo Ming at University of Northumbria aimed at understanding the origin of ball like features that formed on CZTSe films converted using a Se-cap layer. The study has showed that the formation of ball like structures on the surface that were composed of zinc selenide compounds with some tin selenide. This resulted in non-uniformity of CZTSe thin films. One of the proposed mechanisms for this non-uniformity was that it may result from when the selenium melts. The molten selenium would be likely to exhibit poor wetting of the surface resulting in balling (formation of balls of molten Selenium on the surface) that could also attract low melting point elements from the precursor film to form the binary compounds. To assess whether this was a result of heating above the melting point ( $T_m$ )

of Se and Sn and whether the solid-state diffusion of Se into the films at  $T < T_m$  would reduce or prevent this, the behaviour below the melting point of Se ( $T_{m\text{ Se}}$ ) was investigated in the current study.

To do so, the effect of preheating on the micro and crystal structure of CZTSe thin films using an evaporated cap layer of selenium has been examined. Afterwards, the process is compared with the CZTSe samples synthesised using Se pellets instead of Se-Cap layer. For all the executed experiments, the Cu-Zn-Sn metal precursors were deposited as described in section 3.2.2.1. Thin films were prepared with the composition of  $\text{Cu}/(\text{Zn}+\text{Sn}) = 0.5$  and  $\text{Zn}/\text{Sn} = 1.3$ , and the thickness of  $0.8\text{ }\mu\text{m}$ .

To determine the required Se-Cap thickness that is sufficient for the fabrication of CZTSe Kesterite absorber films, layers of Se-cap with different thickness were deposited on top of the CZT precursors by thermal evaporation technique. The Se-Cap thickness was controlled by adjusting the deposition time. Three different values of cap thickness were used with the values of 0.5, 1, and 1.5 times the thickness of CZT thin film (with the thickness of  $0.4$ ,  $0.8$ , and  $1.2\text{ }\mu\text{m}$ , respectively). The sample names for these are 1a, 1b, and 1c, respectively, and these are shown as highlighted in grey in Table 4-1.

From X-ray patterns (see Figure 4-1), the mass of selenium required to produce Kesterite CZTSe thin films was equivalent to a Se-layer with the thickness of  $1.2\text{ }\mu\text{m}$  (approximately 1.5 times the thickness of the precursor layer, sample 1c). The XRD pattern shows the presence of CZTSe Kesterite structure together with other binary compounds such as SnSe, when the cap layer of  $1.2\text{ }\mu\text{m}$  was used (see Figure 4-1c). It should be noted that the presence of ZnSe cannot be determined by XRD pattern due to the overlap of its peaks with those from CZTSe. Nevertheless, as it will be explained later in this section, it is highly likely that ZnSe compound has also been formed across the thin film. However, when the thickness is less than  $1.2\text{ }\mu\text{m}$ , Cu-Sn alloy and  $\text{Cu}_{1.8}\text{Se}$  compounds are formed rather than the formation of CZTSe Kesterite (see Figure 4-1a, and Figure 4-1b).



Table 4-1. The table shows the pre-treatment and conversion (selenisation) conditions for samples 1a, 1b, 1c with different selenium thickness and 1d to 1h with different heating profiles.

Sample	Method of supplying Selenium	Selenium thickness ( $\mu\text{m}$ ) [the ratio with regard to the precursor thickness]	Pre-treatment			Conversion (Selenisation)		
			Temp. ( $^{\circ}\text{C}$ )	Pressure (mbar)	Dwell Time (hours)	Temp. ( $^{\circ}\text{C}$ )	Pressure (mbar)	Dwell Time (hours)
<b>1a</b>	Cap layer	0.4 [0.5]	160 $\pm$ 5	300	3	550 $\pm$ 5	300	0.25
<b>1b</b>	Cap layer	0.8 [1]	160 $\pm$ 5	300	3	550 $\pm$ 5	300	0.25
<b>1c</b>	Cap Layer	1.2 [1.5]	160 $\pm$ 5	300	3	550 $\pm$ 5	300	0.25
<b>1d</b>	Cap Layer	1.2	160 $\pm$ 5	300	3	-	-	-
<b>1e</b>	Cap layer	1.2	220 $\pm$ 5	300	0.5	-	-	-
<b>1f</b>	Cap layer	1.2	160 $\pm$ 5	300	3	300 $\pm$ 5	300	0.5
<b>1g</b>	Cap layer	1.2	160 $\pm$ 5	300	3	550 $\pm$ 5	300	0.5
<b>1h</b>	Pellets	1.2	-	-	-	500 $\pm$ 5	300	0.25

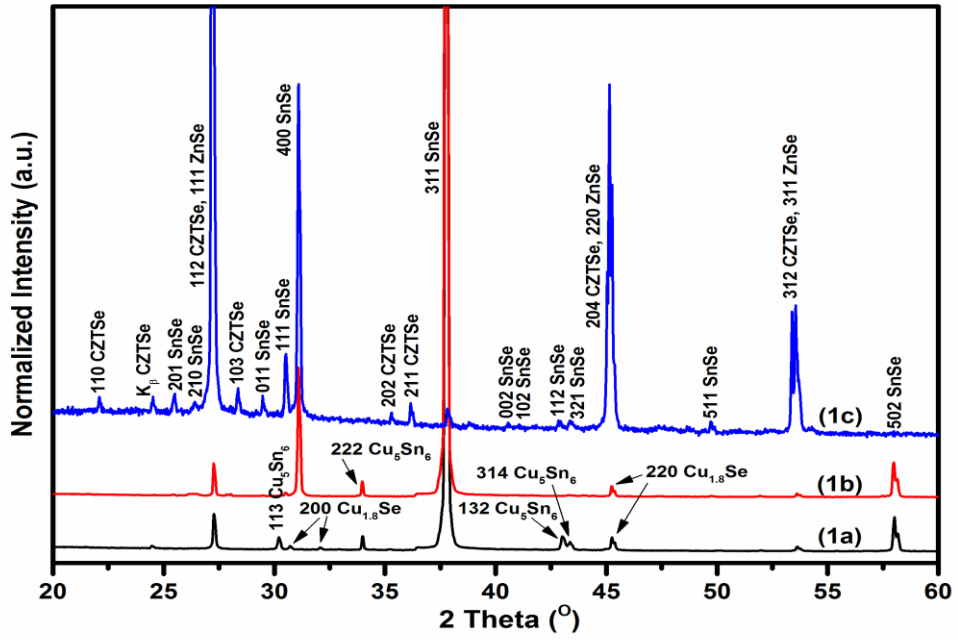


Figure 4-1. The XRD patterns of CZT thin films selenised with different Se-cap layers, heated at 550°C (1a) 0.4μm ( $t_{\text{Se}} = 0.5 t_{\text{CZT}}$ ) (1b) 0.8μm ( $t_{\text{Se}} = t_{\text{CZT}}$ ) (1c) 1.2μm ( $t_{\text{Se}} = 1.5t_{\text{CZTS}}$ ).

After determining the optimum Se layer thickness, subsequent investigations used as the reference. CZT precursors with Se-Cap layer having the thickness of 1.2μm ( $\sim 1.5t_{\text{CZT}}$ ) have been pre-heated at temperatures of  $160 \pm 5^\circ\text{C}$  ( $T < T_{\text{mSe}}$  and  $T_{\text{mSn}}$ ),  $220 \pm 5^\circ\text{C}$  ( $T_{\text{mSe}} < T < T_{\text{mSn}}$ ),  $300 \pm 5^\circ\text{C}$  ( $T > T_{\text{m(Se,Sn)}}$ ), and  $550 \pm 5^\circ\text{C}$  (for the direct formation of CZTSe Kesterite structure based on previous studies at Northumbria University). The samples were named 1d to 1g, respectively with details presented in Table 4-1.

This experiment shows the formation of different binary compounds and interesting morphology on the converted thin films, as it will be discussed in the following.

For Samples (1d) and (1e), heated to temperatures less than the melting point of selenium the formation of selenium island/star structures was observed (see Figure 4-2). The yellow and blue regions in Figure 4-2c indicate the precursor Cu-Zn-Sn and the selenium, respectively. This structure was also observed at  $220 \pm 5^\circ\text{C}$  where  $T_{\text{mSe}} < T < T_{\text{mSn}}$ . The star-like island features are consistent with a recrystallization of the selenium layer when the sample is heated to just below  $T_{\text{m(Se,Sn)}}$ .

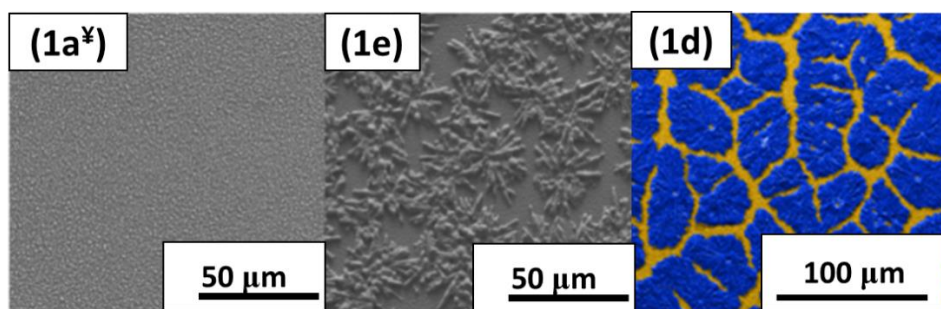


Figure 4-2. The plan-view SEM images of Se-capped CZT (1a\*) before conversion (1e) after being heated to  $220\pm5^{\circ}\text{C}$  for 0.5 hour (1d) EDX compositional map created with INCA software of the sample heated at  $160\pm5^{\circ}\text{C}$  for 3 hours are displayed. The yellow and blue regions in image 1d indicate the precursor Cu-Zn-Sn and the selenium, respectively.

The SEM images of samples 1d, 1f, and 1g are shown in Figure 4-3. The subsequent balling corresponds with the temperature exceeding the melting point of selenium and tin ( $\sim 220.8^{\circ}\text{C}$  and  $\sim 231.9^{\circ}\text{C}$ , respectively) by  $\sim 80^{\circ}\text{C}$ . When the temperature was increased to  $300^{\circ}\text{C}$ , ( $T > T_{\text{m}}(\text{Sn,Se})$ ), the ball-like features were seen to start growing on the surface of the thin films (see Figure 4-3b). The XRD pattern for this sample is consistent with the presence of Cu-Sn alloy, Sn, and ZnSe compounds, but no peaks that would correspond to SnSe were observed (see Figure 4-4, 1f). The SnSe binary compound appeared at a higher temperature ( $550^{\circ}\text{C}$ ), when the Cu-Sn alloy is melted (see Figure 4-4, 1f).

The XRD pattern of sample (1g), when the temperature increases to  $550^{\circ}\text{C}$ , confirms that the Kesterite compound emerges together with the binaries such as SnSe and probably ZnSe (see Figure 4-4, 1g). Due to the limited availability of Raman technique to investigate the presence of ZnSe binary compound across the converted thin films, studies by Colombara et al and Vora et al are referenced here, in which the ZnSe binary compounds were shown as bright regions in SEM images [208-210]. Since similar features to those observed in the Colombara et al and Vora et al studies were detected by SEM analysis in the current research as well, the features pointed with red arrows in Figure 4-5(1g\*) are attributed to the presence of the ZnSe compound. Together with the formation of binary compounds, the image shown in Figure 4-5(1g\*) reveals the typical Kesterite morphology, which is also consistent with the Kesterite structure obtained in Colombara et al study [208].

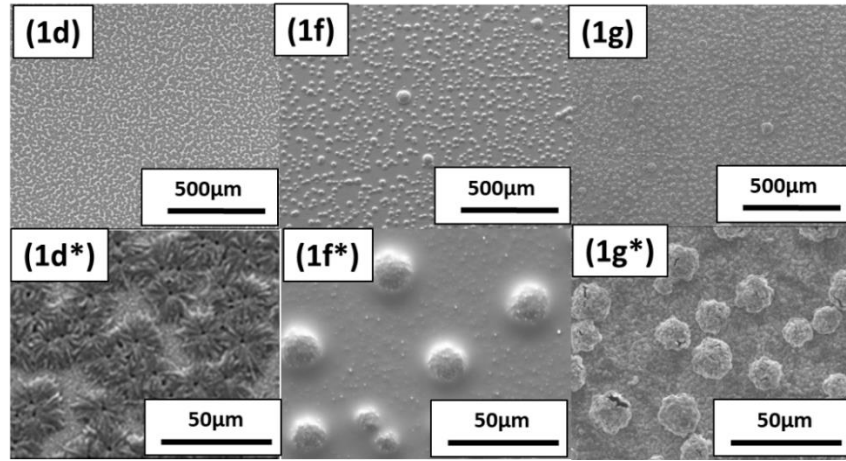


Figure 4-3. The plan-view SEM images of CZTSe ( $\text{Se} = 1.2\mu\text{m}$ ,  $\text{CZT} = 0.8\mu\text{m}$ ) after (1d, 1d\*)  $160^\circ\text{C}$ , (1f, 1f\*)  $160^\circ\text{C} - 300^\circ\text{C}$ , and (1g, 1g\*)  $160^\circ\text{C} - 550^\circ\text{C}$  are illustrated. The images are observed with two different magnifications of (1d to 1g) 100X, and (1d\* to 1g\*) 1000X.

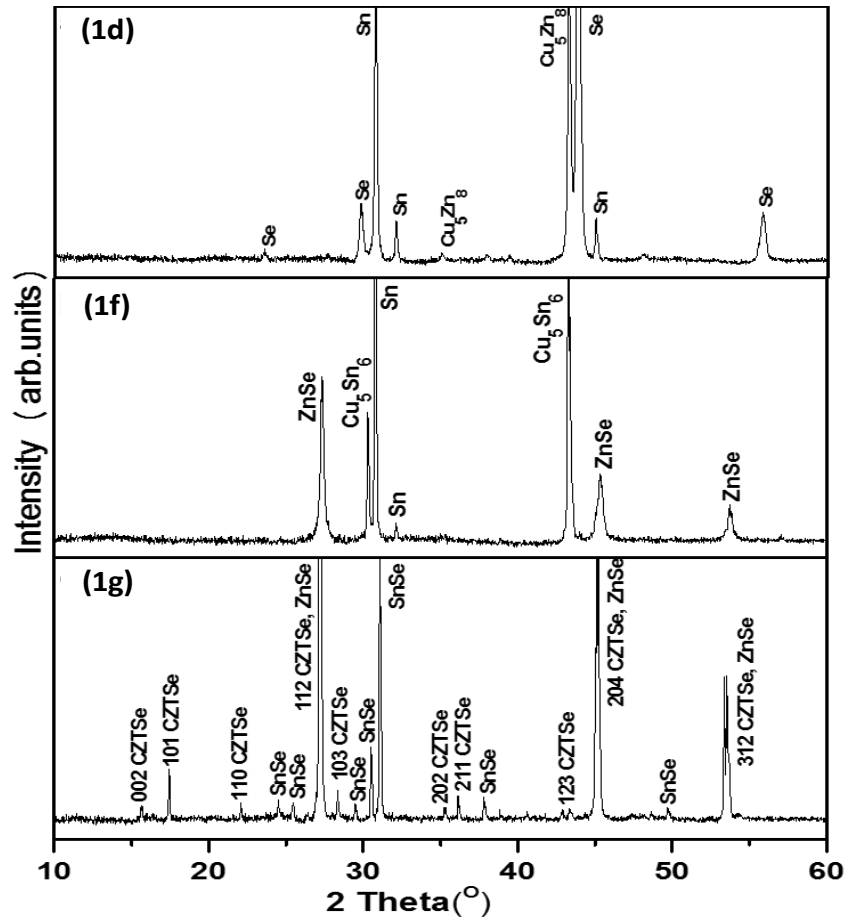


Figure 4-4. The XRD patterns of CZT samples selenised at temperature of (1d)  $160^\circ\text{C}$  (1f)  $300^\circ\text{C}$  (1g)  $550^\circ\text{C}$ .

In order to evaluate the influence of chalcogen supply on the morphology of the converted CZTSe thin films, an experiment has been carried out using Se pellets instead of Se-Cap layer. This experiment has been introduced as sample 1h in Table 4-1. The conversion condition used for sample 1h was selected as the optimum conversion condition achieved in the laboratory of Northumbria University and was re-examined during the work for this thesis (the details are presented in section 4.2.1). From the SEM images, the microstructure of absorber layer for the sample selenised using selenium pellets appears to exhibit greater uniformity (see Figure 4-5 (1h,1h\*)), compared to those synthesised using the Se-cap layer (see Figure 4-5 (1g,1g\*)). The area indicated by the red arrow in Figure 4-5 1g\*, shows the presence of binary compounds formed across the surface for the sample prepared using Se-cap layer. However, the macroscopic view of the sample with Se-cap layer appears to be more uniform than the one prepared with Se pellets (see Figure 4-7). The XRD patterns confirm the presence of Kesterite compounds for sample (1h) in which Se pellets was used as a source of chalcogen (see Figure 4-6). EDX measurements for samples (1d) to (1h) are presented in Table 4-2. The results show that sample (1g), which was converted using Se-cap layer at 550°C, has a very Zn-rich composition ( $\text{Cu}/(\text{Zn}+\text{Sn}) = 0.5$  and  $\text{Zn}/\text{Sn} = 2.6$ ). While, the composition ratio of sample (1h), in which Se pellets has been used, looks more promising compared to the other converted samples. Sample 1h shows the ratio of  $\text{Cu}/(\text{Zn}+\text{Sn}) = 0.8$  and  $\text{Zn}/\text{Sn} = 1.0$ , which is close to the stoichiometric ratio have been suggested as having the best performance for solar devices, as explained in Chapter 2.

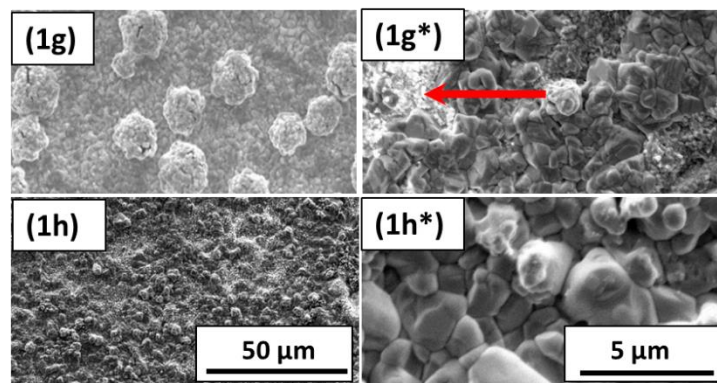


Figure 4-5. The plan-view SEM images of samples (1g, 1g\*) using Se-cap layer at 550°C, and samples (1h, 1h\*) using Se pellets at 500°C, with two magnifications of (1g, 1h) 1000X, and (1g\*, 1h\*) 10000X.

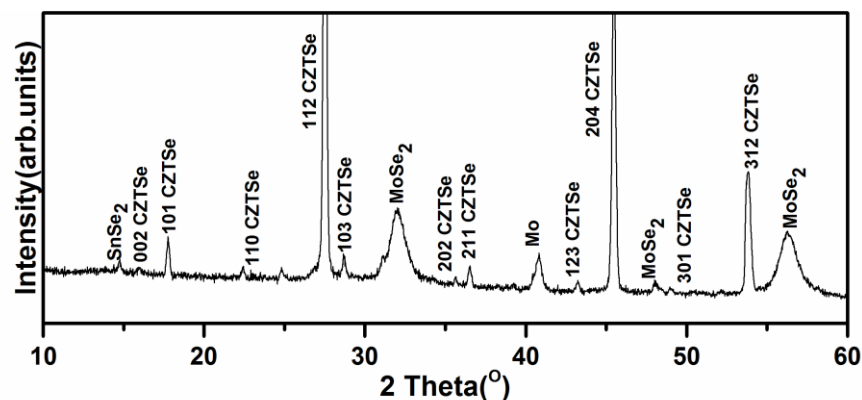


Figure 4-6. The XRD pattern of CZTSe thin film heated up to 500°C using Se pellets.

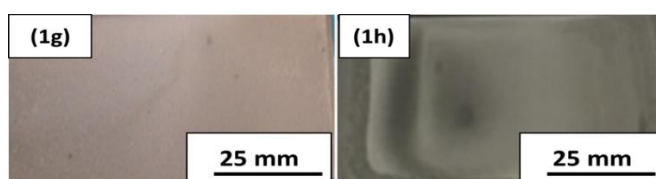


Figure 4-7. The macroscopic view of CZTSe sample synthesised using (1g) Se-cap layer and (1h) Se pellets.

Table 4-2. This table is showing the pre-treatment and conversion (selenisation) conditions for samples 1d to 1h. The table also presents the composition (at%) of the as-deposited and converted thin films of CZTSe, sample 1d to 1h.

Sample	Method of Supplying Selenium	Pre-treatment and Conversion status: Temp. (°C) / Dwell Time (hrs)	Cu (at%)	Zn (at%)	Sn (at%)	Se (at%)	$\frac{\text{Cu}}{\text{Zn} + \text{Sn}}$	$\frac{\text{Zn}}{\text{Sn}}$
	Cap layer	As-deposited precursor	33	38	29	0	0.5	1.3
1d		(160 ± 5 / 3) and no conversion	6	7.5	5.5	81	0.5	1.4
1e		(220 ± 5 / 0.5) and no conversion	7.5	8	6.5	79	0.5	1.2
1f		(160 ± 5 / 3) and 300 / 0.5	4	12	3	81	0.3	4.0
1g		(160 ± 5 / 3) and 550 / 0.5	16.5	26	10	47.5	0.5	2.6
1h	Pellets	no pre-treatment, 500 ± 5 / 0.25	21.5	13.5	13.5	51.5	0.8	1.0

For Se-cap layer, the ratio between the Se consumed during the evaporation to deposit the cap (Se placed in crucible) and the Se introduced into the graphite box is significantly high. However, supplying the Se pellets directly inside the graphite box reduces the amount of Se consumed and enables more efficient use of the chalcogen. Table 4-3 represents a comparison of the quantity of Se used in both processes and shows the significant advantage associated with the use of Se pellets for the synthesising process.

Table 4-3. The table shows the mass of selenium that was used together with the mass of consumed selenium during the pre-treatment and conversion (selenisation) processes of using Se pellets and cap layer as a source of the chalcogen.

Method of supplying Selenium	The mass of Selenium required (♠) to fabricate the cap-layer, and (†) to fabricate the CZTSe thin film based on its stoichiometric composition (mg)	The mass of Selenium required to introduce (♣) into the evaporator chamber, and (⌘) into graphite box during conversion (g)
Cap Layer	6♠	20 ♣
Cap layer	5†	
Pellets	5†	0.14 ⌘

Further optimisation of the quality of CZTSe absorber layers using selenium pellets (with the same conversion condition as sample 1h) is published by Dr. Jose Marquez Prieto from Northumbria University. This study includes the reduction of CZTSe based solar devices synthesised at a conversion temperature of 500°C using selenium pellets resulting in an efficiency of 8.1% [211].

#### 4.2.1 Pre-treatment by varying conversion pressure and temperature

This experiment has been done with the aim of evaluating the influence of preheating at different ambient pressure. To do so, the CZT thin films for this specific experiment were sputtered on molybdenum soda-lime glasses (Mo/SLG), as described in section 3.2.2.1. The thickness of sputtered CZT thin film was 0.78µm with a compositional ratio of Cu/(Zn+Sn) = 0.6 and Zn/Sn=1.1. Thereafter, the samples were selenised with different conversion conditions, as presented in Table 4-4. It should be noted that sample 2d has the same conversion condition as sample 1h, described in section 4.2. It should be also noted that argon was used as the ambient pressure for all the samples 2a to 2d.

Table 4-4. The table presnets the conversion conditions for selenisation of samples 2a to 2d by varying the preheating temperature and the ambient pressure.

Sample	Pre-treatment			Conversion		
	Temp. (°C)	Pressure (mbar)	Dwell time (min)	Temp. (°C)	Pressure (mbar)	Dwell time (min)
2a	250	1	20	500	300	15
2b	300	1	20	500	300	15
2c	350	1	20	500	300	15
2d	-	-	-	500	300	15

Analysing the XRD patterns of sample 2a to 2d have showed presence of Kesterite CZTSe together with SnSe<sub>2</sub> compounds at  $2\theta = 14.5^\circ$  and  $30.5^\circ$ , when the precursors are converted with pre-treatment step operating under a low pressure of argon ambient (see Figure 4-8). The SEM images from the morphology of samples (2a) to (2d) are shown in Figure 4-9. The ball like structures are seen when the sample is pre heated at temperatures above 300°C. However, performing a one-step conversion processing contributes to a reduction in the formation of ball like features (see Figure 4-9).

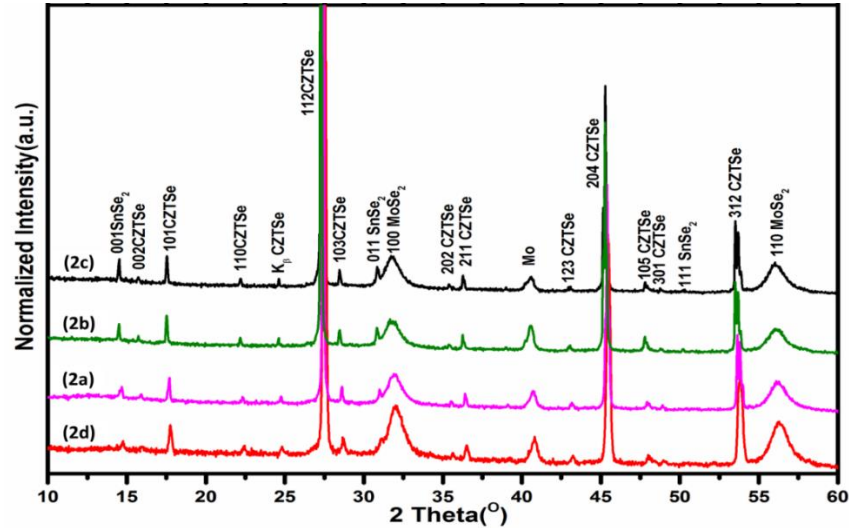


Figure 4-8. The XRD diffraction patterns of selenised samples converted at (2d) 500°C with a pressure of 300 mbar (2a) 250°C-500°C with a pressure of 1-300 mbar (2b) 300°C-500°C with a pressure of 1-300 mbar (2c) 350°C-500°C with a pressure of 1-300 mbar.



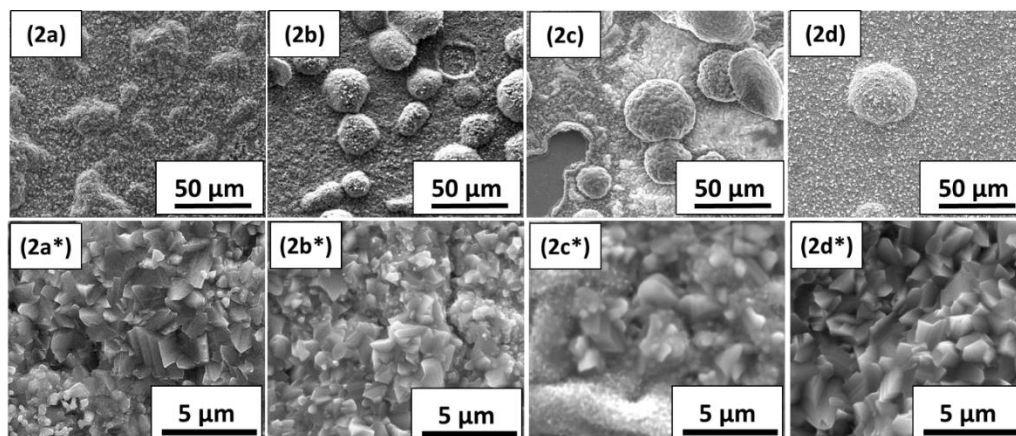


Figure 4-9. The plan-view SEM images of selenised samples with and without pre-treatment steps, converted at (2a, 2a\*) 250°C-500°C with a pressure of 1-300 mbar (2b, 2b\*) 300°C-500°C with a pressure of 1-300 mbar (2c, 2c\*) 350°C-500°C with a pressure of 1-300 mbar (2d, 2d\*) 500°C with a pressure of 300 mbar of argon. The images are observed with two different magnifications of (2a to 2d) 1000X, and (2a\* to 2d\*) 10000X.

Table 4-5. Displaying the composition ratio (at %) of the pre-treatment/converted thin films of CZTSe for samples of 2a to 2d.

Sample	Temp. (°C)	Time (min)	Pressure (mbar)	Cu/(Zn+Sn)	Zn/Sn	Se/(Cu+Zn+Sn)
2a	250/500	20/15	1/300	0.7	1.3	1.0
2b	300/500	20/15	1/300	0.6	1.1	1.1
2c	350/500	20/15	1/300	0.6	2.1	1.0
2d	500	15	300	0.8	1.0	1.1

#### 4.2.2 Summary of Results and Discussion

In case of using Se-cap layer, it is expected that during conversion, some regions of the precursor surface would be in intimate contact with liquid Se or Se/Sn droplets together with Se-vapour. Thus, it is highly likely that the difference in reactant states would contribute to a non-uniform reaction of the Cu-Zn-Sn precursors with the selenium. In such a condition, the kinetic of reactions could be very complex. Therefore, the synthesising process requires a very precise control over pressure and temperature. In this context, it is assumed that the segregation of selenium at specific points of the surface (the star-like positions) could be a proper nucleation point for the formation of selective binary compounds during the conversion at higher temperatures. However, in solid-

vapour equilibrium (in the case of using selenium pellets), the selenium does not start melting and segregating on the precursor surface. Ideally, the vapour pressure of the selenium could be partially controlled by adjusting the quantity of Se pellets in the graphite box. This might diminish the complexity of the kinetic of reactions; consequently, the formation of binary compounds will be restricted.

The results observed in this study are consistent with data reported by Yoo et al, as they indicated that at temperatures below 415°C, tin would be expected to alloy with copper or remain as an elemental metal rather than reacting with selenium [212]. However, at higher temperatures (~550°C), the SnSe was formed and the results have shown the formation of CZTSe Kesterite together with SnSe and ZnSe when the Se-cap layer was used as a source of chalcogen.

As explained in Chapter 2 (literature review), the formation of binary compounds together with CZTS(e) Kesterite across the absorber layer, can reduce the solar cell performance. The presence of secondary compounds can be detrimental to device performance by acting as centres for Shockley-Read-Hall recombination and reducing the open circuit voltage [213].

Considering the cation ratios for all synthesised samples during the current experiments, the EDX analyses illustrate the relatively good contribution of elements across the CZTSe thin films fabricated using the selenium pellets, with the composition of Cu-poor ( $\text{Cu}/(\text{Zn}+\text{Sn}) = 0.8$ ) and Zn-rich ( $\text{Zn}/\text{Sn} = 1.2$ ). This could lead to the highest efficiencies for solar devices as it is close to the stoichiometric composition of the so far highest efficiency solar devices [15, 58, 214]. However, the very Zn-rich composition ( $\text{Cu}/(\text{Zn}+\text{Sn}) = 0.5$ ) and Zn-rich ( $\text{Zn}/\text{Sn} = 2.6$ ) of sample with the Se-cap layer converted at 550°C, could result in the segregation of ZnSe which has a negative impact for the device performance as discussed earlier.

Moreover, the advantage of using selenium pellets is not only the formation of a relatively uniform microstructure, but also a more efficient material usage. Thermal evaporation of a cap layer requires the filling of the crucible with 20g of selenium. However, the majority of evaporated selenium is usually deposited on the walls of the evaporation chamber. Whereas, the mass introduced as Se pellets is significantly less when compared to the mass required in the stoichiometric composition of CZTSe thin films.

Both Se pellets and cap layer use significantly more Se than is needed for stoichiometry CZTSe compound. This is due to the fact that the selenium is a relatively unreactive

element. Thus, a sufficient partial pressure of chalcogen during the sulphurisation/selenisation process is necessary to (i) reduce the decomposition rate of CZTS(e) compound and (ii) to prevent the formation of  $V_{S(e)}$  in the crystal lattice of Kesterite structure. The Se pellets appears to be more than the cap layer (considering what is inside the graphite box only) but is significantly less wasteful, compared to the huge mass of selenium waste during thermal evaporation processing.

The study on the preheating at various pressure and temperature illustrated that the one-step process (without the pre-treatment stage) utilises the ambient gas pressure during conversion aids the process of CZTSe formation. During the experiment, it was observed that when the tube furnace is in vacuum, the pressure inside the tube is approximately  $3 \times 10^{-3}$  mbar. Since increasing the pressure at pre-treatment step to 1mbar is still very low, it is assumed that the situation at pre-treatment step is close to vacuum condition. As explained in Chapter 2, at low ambient pressures, the minimum temperature of 340°-350°C is required for the transformation of selenium from liquid to vapour state. Preheating the sample at around 300-350°C with low ambient pressure contributes to an increase in the probability of the presence of solid, vapour, and liquid states. This in turn could lead to the formation of selenium droplets on the surface together with the complexity of reaction on the precursors, and possibly the formation of selectively binary compounds with the components of precursors. However, when the preheating step at low ambient pressures was omitted, less ball like features were observed. This can be attributed to the instability of liquid states resulting in a higher probability of the presence of solid and vapour states, compared to that of the liquid state. This in turn can ensure a better uniformity with fewer formation of ball like features. Thus, a temperature higher than 350°C seems to be required to fill the graphite box with selenium vapour and avoid the creation of three complex reactions simultaneously in the system. Since, such a condition makes the reaction complex by the formation of selenium droplets on the precursor surface, the selectively binary compounds may create with the components of the precursor. It should be noted that the ball like features have also been observed when Se-cap layer had been used. Similarly, in that case, the formation of ball like features started to appear at temperatures higher than 300°C.

#### 4.3 The fabrication of precursor solution via ball milling, non-vacuum deposition technique

In non-vacuum deposition processing, the preparation of a precursor solution is one of the most important stages. In order to fabricate the precursor solution via ball milling process, several parameters were needed to be considered and these include the milling speed, ball-to-powder ratio, milling time, milling ball size, milling agent, and the use of an appropriate suspension solution. It is assumed that these factors could affect the quality of precursor solution and ultimately the quality of CZTS thin films. The milling speed and ball-to-powder ratio have been examined by Ming et al during an earlier study at Northumbria University. The investigation of the influence of other parameters was examined during the research reported in this thesis.

##### 4.3.1 Milling time

Cu<sub>2</sub>O compound was ground via ball milling apparatus with a range of milling times as follows: 4, 8, 12 and 24 hours with the zirconia balls of diameter, D = 2mm. The particle size of the powders were estimated using SEM. The results revealed that after 4 hours of grinding, the Cu<sub>2</sub>O particle size decreased from 3-10µm to < 600nm-1µm (see Figure 4-10). The SEM images illustrate that increasing the grinding time to more than 4 hours does not result in a further clear reduction in particle size. Therefore, the shorter process time was selected because it consumed less power and contributes to a higher throughput. The EDX mapping images of mixed ground powders (see Figure 4-11), clearly revealed that the Cu<sub>2</sub>O particles remained the largest particles when compared to those of ZnS and SnO, when all three compounds were milled for 4 hours. The identifications of samples is presented in Table 4-6.

Table 4-6. Sample identification and associated synthesising milling conditions

Sample	Milling time	Materials that are grounded
<b>3a</b>	No milling	Cu <sub>2</sub> O
<b>3a4</b>	4 hours	Cu <sub>2</sub> O
<b>3a8</b>	8 hours	Cu <sub>2</sub> O
<b>3a12</b>	12 hours	Cu <sub>2</sub> O
<b>3a24</b>	24 hours	Cu <sub>2</sub> O
<b>4b</b>	4 hours	Cu <sub>2</sub> O +SnO +ZnS

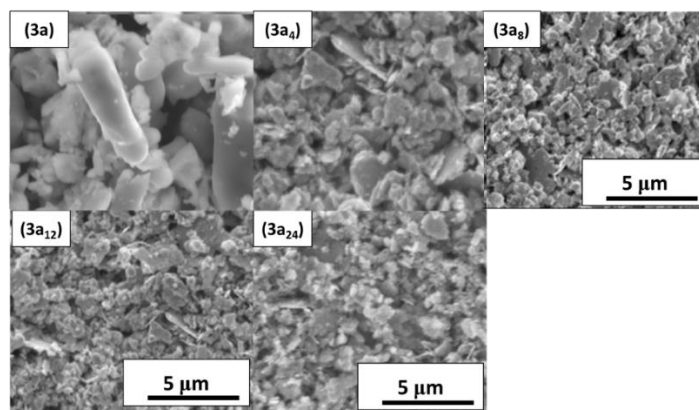


Figure 4-10. The variation in  $\text{Cu}_2\text{O}$  particle size after (3a) no milling (3a<sub>4</sub>) 4hrs (3a<sub>8</sub>) 8hrs (3a<sub>12</sub>) 12hrs and (3a<sub>24</sub>) 24hrs of milling.

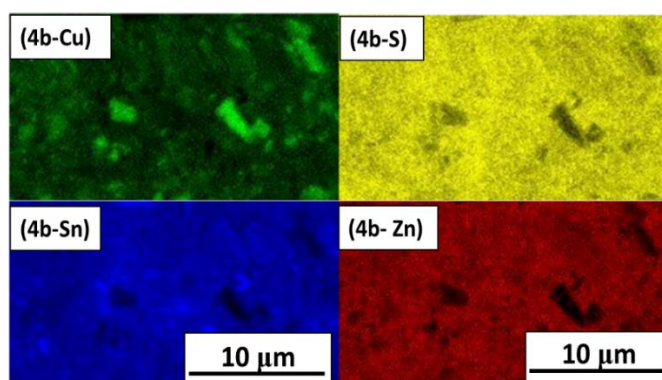


Figure 4-11. The EDX Mapping images are indicative of the elements in different colours of a mixture of  $\text{Cu}_2\text{O}$ ,  $\text{ZnS}$ , and  $\text{SnO}$  compounds milled and mixed for 4 hours (4b-Cu) Copper in green (4b-S) Sulphur in yellow (4b-Sn) Tin in blue (4b-Zn) Zinc in red.

### 4.3.2 Ball size

In order to assess the effect of using different ball sizes on the final particle size of milled compounds, the  $\text{Cu}_2\text{O}$  compound was grounded with different ball sizes as it was mentioned in section 3.3.2 (results summarised in Table 4-7, shown in (see Figure 4-12)). It can be concluded that the particle sizes of the milled  $\text{Cu}_2\text{O}$  compound are quite similar to the quantity which was advertised by the company (the Fritsch P6 Planetary). Nevertheless, the very slight inconsistency between the actual and the expected particle sizes might be resulted due to the agglomeration of particles or the poor dispersion of the compounds in the carrier solution. Moreover, the results have shown that the smaller

particle size of powders in precursor solutions could contribute to a better dispersion in the suspension solution.

Table 4-7. The table illustrates the results achieved using the Mastersizer for sample 5a to 5d, [d(0.5)] represents that the 50% of particles have the mean particle size of a given amount and [d(0.9)] represents that 90% of particles have the mean size of the given amount.

Sample	Ball Size (mm)	Expected Particle Size after milling based on the theory	Particle Size after milling [d(0.5)] (Measured by Mastersizer)	Particle Size after milling [d(0.9)] (Measured by Mastersizer)
5a	No milling	-	8 $\mu\text{m}$	50 $\mu\text{m}$
5b	5 mm	5 $\mu\text{m}$	4.5 $\mu\text{m}$	18 $\mu\text{m}$
5c	2 mm	2 $\mu\text{m}$	2.2 $\mu\text{m}$	4 $\mu\text{m}$
5d	0.5 mm	0.5 $\mu\text{m}$	1.2 $\mu\text{m}$	1.5 $\mu\text{m}$

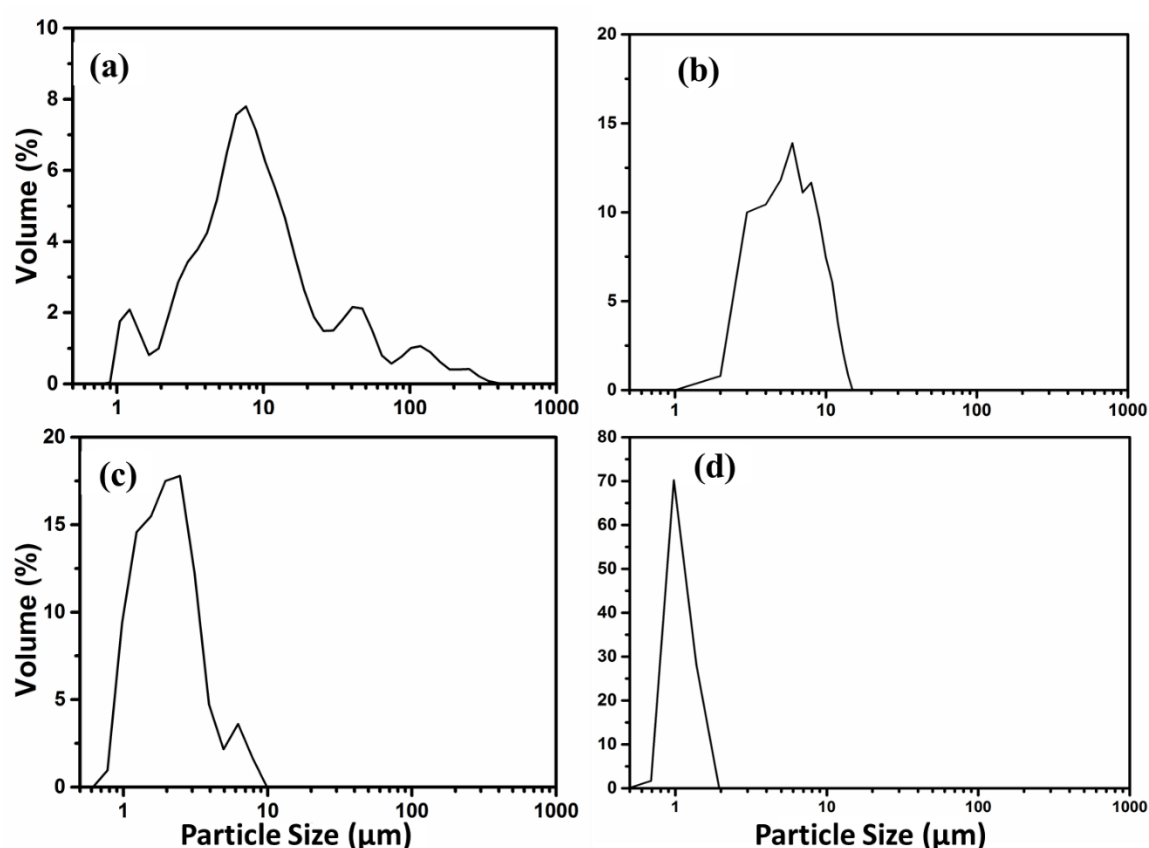


Figure 4-12. The graphs show the distribution of particle size (5a) un-milled Cu<sub>2</sub>O when they milled with the ball sizes of (5b) D = 5mm (5c) D = 2mm and (5d) D = 0.5 mm.

### 4.3.3 Suspension solution

As it was mentioned in section 2.2.7.2 , the choice of carrier solution is of great importance. To evaluate this factor, three different precursor solutions using Isopropyl Alcohol (IPA) and/or DI water were used as suspension solutions during the milling process with the weight ratio of liquid/powder = 3. The milling time was set at 4 hours with the ball size of  $D = 2\text{mm}$ . Figure 4-13 illustrates the more porous structure for the as-deposited and the converted precursor if the precursor solution contains the 90% water+10%IPA compared to the use of 100%IPA.

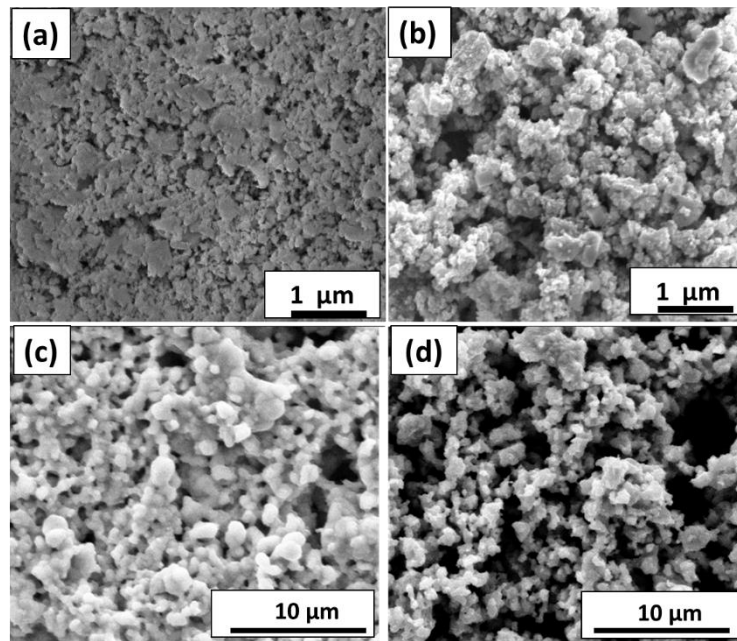


Figure 4-13. The plan-view SEM images of (a,b) as-deposited precursors and (c,d) the converted samples using a suspension solution of (a,c) 100% IPA (b,d) 90% deionized water + 10% IPA.

In order to assess the wetting of precursor solution on glass and molybdenum layer, the contact angle analysis has been performed at Swansea University by Dr. Greenwood. As shown in Table 4-8, changing the solvent from 90% water+10% IPA to 100% IPA, has shown a better wettability for the precursor solution. This in turn could contribute to a better uniformity of thin films on SLG/Mo. The results also indicate that the use of 90% water+10% IPA as a solvent has a better wettability if the substrate is only SLG. The experiments have been repeated three times for each sample. The average figures of contact angles are reported in Table 4-8.

Table 4-8. The table indicates the average figure of the contact angles analysed and reported by Dr. Peter Greenwood, Swansea University.

Substrate	Solvent	Contact Angle (°)
SLG	90% water +10% IPA	17.0
SLG	100% IPA	14.4
SLG/Mo	90% water +10% IPA	30.4
SLG/Mo	100% IPA	8.2

#### 4.3.4 Thin film fabrication via various non-vacuum deposition techniques

To provide a uniform and thin layer of coating on top of the substrates, several deposition techniques have been used. Initial trials have been carried out using the hand held rolling and doctor blade techniques. However, these methods were not that successful since the thickness of the coatings were relatively non-uniform and large (approximately 5-10  $\mu\text{m}$ ). Compared to rolling and doctor blade methods, the use of spraying technique with airbrush has shown the formation of thin and uniform coatings. This technique was the main and the only available technique for non-vacuum deposition processing at the laboratories in University of Northumbria.

To increase the reproducibility of the coated films, the nitrogen pressure was set at its maximum degree by pushing pack the button (number 3, see Figure 3-4) to its maximum degree. The distance and the solvent rate have been adjusted by the airbrush screws. According to the visual inspections, the uniform layer of sprayed films have been formed at the working distance of ~8-10 cm from the substrate surface.

#### 4.3.5 Results and Discussion

Preparing a uniform coating is a significant stage in solution processing. This requires a preparation of a homogenous precursor solution, the using of an appropriate carrier solution which aids materials to disperse uniformly, and eventually establishing a suitable method of deposition.

It is speculated that reducing the particle size of metal oxide is beneficial for the reduction process since sulphur tends to diffuse from the surface of particles. Thus, for large particles, the only surface or specific depth of the particles might be sulphurised. By increasing the milling time or by using the smaller ball size, the particle size can be reduced. Moreover, the target thin film thickness is 2-4  $\mu\text{m}$  therefore it is reasonable to produce particles that are smaller than this to enable a film with complete coverage. This



is also consistent with performing multiple coatings (spraying or printing) if needed. Furthermore, the results in the current study have shown a considerable difference in terms of the particle sizes of SnO, Cu<sub>2</sub>O, and ZnS compounds. Thus, it could be advantageous to reduce the particle size in order to provide a well-dispersed precursor solutions, as it is reported by Kim et al that the finely milled precursor particles promotes the CZTS crystallisation when the precursor is heated at high temperatures [127].

The study has shown that the use of IPA is an appropriate choice since it has a low boiling point and is a volatile organic compound. Therefore, it leaves the surface of coated samples during procedures of deposition and subsequent heat treatment. This is beneficial since as reported elsewhere [122], the presence of carbon in the absorber layer, which may exist due to the use of solvents with high boiling point, can reduce the grain growth and consequently the solar cell performance. In the current experiments, the deionised water has been also replaced instead of using IPA. However, the results have shown that, water remains on the surface for a longer time allowing the less wetting and adhesion of the particles. It is expected that this will lead to the agglomeration. Although the use of water as a carrier solution can be a safe and environmentally friendly alternative, the creation of agglomerated structure is assumed to cause difficulties in sulphurisation process with similar reason as the presence of large particle size of compounds. This is presumed to reduce the rate of reduction in further steps of processing.

Investigating the use of different deposition techniques resulted in the identification of a scalable and simple approach based on the use of an 'Airbrush'. The spraying technique has shown a relatively thin and uniform coating compared to the preliminary trials using doctor blade and rolling methods. However, the spraying technique which was used in this research was controlled manually. Practice was needed to enable the production of uniform coatings. It is speculated that if the spraying technique is executed automatically, the development and the degree of reproducibility could be enhanced.

#### 4.4 Summary

The use of Se pellets as a source of chalcogen was the starting point for further optimisation in order to develop CZTS absorber layers, considering the use of sulphur powders instead of sulphur cap layers. As the experiments have shown, the advantages of using an evaporated cap layer includes the macroscopically uniform surface of the film, allowing to control the amount of selenium in intimate contact with the precursor during

evaporation. However, this technique has demonstrated a microscopic non-uniformity with the formation of high degree of secondary compounds. By using Se pellets, although the macro-scale non-uniformity was significantly increased, the micro-uniformity and morphology improved. Moreover, the experiments have shown the more efficient material usage in case of using Se pellets. The investigation on varying various conversion conditions during heat treatment has shown the importance of pressure and temperature control on the formation of CZTSe absorber layer, which gives an understanding of the critical influence of ambient pressure and temperature on developing Kesterite structure. This in turn will be beneficial for the further study on the fabrication of CZTS Kesterite thin films which will be explained in next chapter.

In the second part of the preliminary experiments, the investigations contributed to establish an optimised condition of ball milling, using 4 hrs of milling with the  $D = 0.5\text{mm}$  zirconia balls, and the use of IPA as a suspension solution. The results have shown a better wettability of using pure IPA, compared to the use of a mixture of IPA and water on SLG/Mo substrate. Eventually, a scalable spraying technique using an airbrush has been established to prepare a uniform and thin layer of coating.

## **Chapter 5**

### **CZTS thin films' fabrication via non-vacuum deposition technique**

## **5 CZTS thin films' fabrication via non-vacuum deposition technique**

As was shown in Chapter 2 and shown in Chapter 4, one of the important issues in fabricating a good quality of absorber layer is to ensure an appropriate conversion/synthesising process. This chapter presents the fabrication of CZTS thin films via non-vacuum deposition technique based on the knowledge and optimised conditions achieved during the preliminary investigations. The main focus here is to study the influence of various conversion conditions on the quality of absorber layer. In addition, this study is followed by several follow-up trials aimed at improving the quality of absorber layer by investigating (i) the use of slot-die deposition technique and comparing it with the spraying method (ii) comparing the use of excess quantity of sulphur in both precursor solution and sulphurisation procedure, to use of sulphur only during the sulphurisation process and (iii) the fabrication of CZTSSe absorber layer by post selenisation of CZTS thin films.

### **5.1 The influence of conversion parameters on the formation of CZTS thin films**

The following subsections detail the investigation of different synthesising parameters that are assumed to be significant in the formation of CZTS absorber layers. These include the composition and the pressure of ambient gas used for the sulphurisation process, the precursor's composition, the dwell time and sulphurisation temperature, the heating profile, the quantity of sulphur, and post heat treatment procedure. It should be noted that adjusting an optimum condition is an iterative process and at times, it requires varying and re-examining the parameters to modify the conversion conditions.

#### **5.1.1 Ambient gas composition and total pressure**

As noted in Chapter 2 and 4, the ambient pressure during the synthesising of CZTS(e) thin films could have a critical impact on its final structure. Due to the importance of this having a key role during sulphurisation procedure on the quality of CZTSe Kesterite thin films, a study of optimising CZTS thin films was initiated that included the investigation of the influence of varying ambient gas composition and pressure. A combination of argon (Ar) and forming gas ( $H_2/N_2$ ) was used to assess the role of a reducing atmosphere. To do so, all the samples were sulphurised at 550°C for 4 hours using different ambient pressures, as detailed in Table 5-1. At this stage, the other parameters such as dwell time and sulphurisation temperature were chosen based on the study conducted by Ming et al at Northumbria University.

Table 5-1. Showing the ambient gas composition and pressure used for conversion samples 1a to 1d.

<b>Sample</b>	<b>Ambient pressure</b>
<b>1a</b>	500 mbar Ar
<b>1b</b>	500 mbar H <sub>2</sub> /N <sub>2</sub>
<b>1c</b>	100 mbar H <sub>2</sub> /N <sub>2</sub>
<b>1d</b>	100 mbar H <sub>2</sub> /N <sub>2</sub> + 400 mbar Ar

The results from XRD patterns, as shown in Figure 5-1, indicate that the 100mbar H<sub>2</sub>/N<sub>2</sub> is necessary to transform tin oxide, to tin and/or tin sulphide. However, increasing the pressure of forming gas to 500mbar may raise the degree of decomposition rate and will cause the loss of precursor from the surface and non-uniformity across the converted thin films (see Figure 5-2). Thus, it is important to provide a sufficient pressure of forming gas in order to reduce the oxide compounds completely, without the creation of non-uniformity across the thin films. The XRD patterns show that the use of argon as a background gas could be beneficial in providing well-crystallised Kesterite structure, compared to the use of only forming gas. The presence of unconverted SnO<sub>2</sub> was clearly present when only argon was used during the conversion. Therefore, at this stage, a combination of argon and forming gas could be the best option in order to achieve the advantages of both ambient gases. The XRD results illustrated that using 100mbar H<sub>2</sub>/N<sub>2</sub> and 400mbar Ar could be appropriate to form Kesterite structure, although SnS crystals are still present across the CZTS thin films. The 100 mbar H<sub>2</sub>/N<sub>2</sub> and 400 mbar Ar was selected as the optimum pressure and composition to prepare CZTS thin films during the subsequent study. This enabled the evaluation of other parameters to further improve the quality of absorber layers. The study on pressure was re-examined and this is presented later in this chapter, section 5.1.5 and 5.1.9.

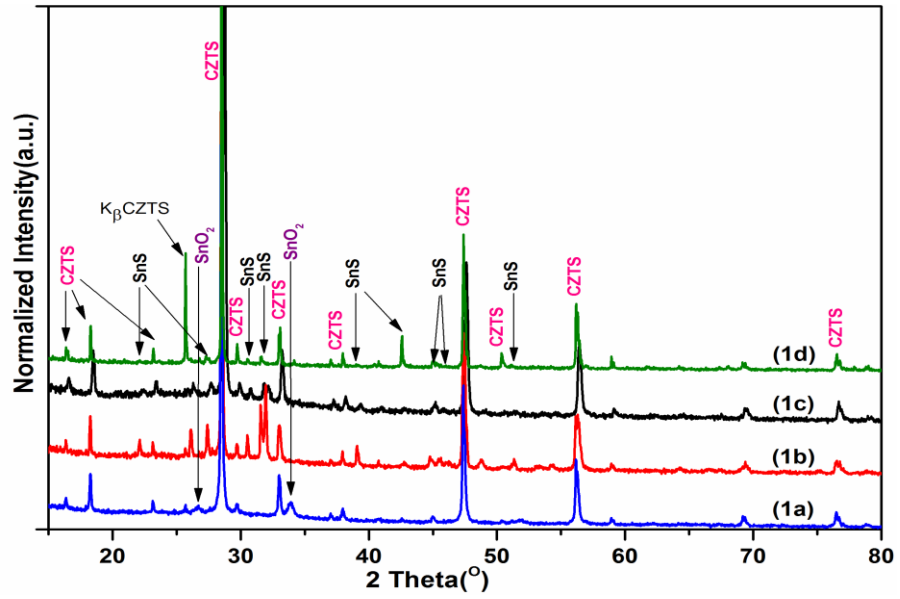


Figure 5-1. The XRD patterns of CZTS thin films converted under different background pressures of (1a) 500 mbar Ar (1b) 500 mbar H<sub>2</sub>/N<sub>2</sub> (1c) 100 mbar H<sub>2</sub>/N<sub>2</sub> (1d) 400 mbar Ar + 100 mbar H<sub>2</sub>/N<sub>2</sub>.

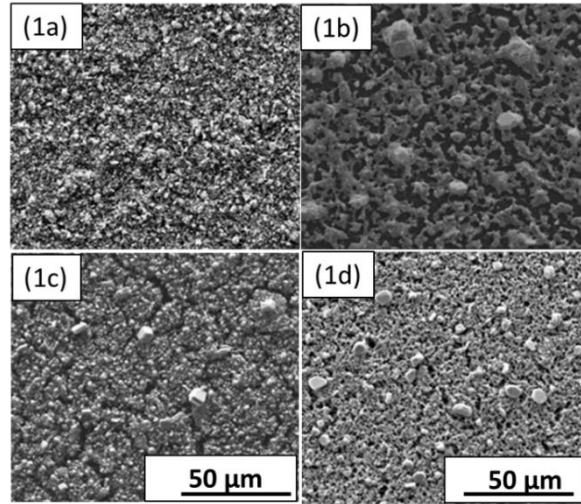


Figure 5-2. The plan-view SEM images shows the microstructure of CZTS thin films converted with the use of different background pressures of (1a) 100mbar H<sub>2</sub>/N<sub>2</sub> (1b) 500mbar H<sub>2</sub>/N<sub>2</sub> (1c) 500mbar Ar (1d) 400mbar Ar + 100mbar H<sub>2</sub>/N<sub>2</sub>.

### 5.1.2 Precursor's composition

As mentioned in chapter 2, one of the challenges in non-vacuum deposition techniques is the difficulty in controlling the chemical composition. Therefore, a specific experiment in this thesis was undertaken to evaluate the compositional changes of precursor solution and the converted thin films during the synthesising process. As a reference and in order

to compare the results with the data achieved earlier by Ming et al, the precursor solution was prepared with the ratio of  $\text{Cu}/(\text{Zn}+\text{Sn}) = 1$  and  $\text{Zn}/\text{Sn} = 1$ .

The results, as shown in Table 5-2, illustrated that the ratio of converted thin films was Cu-rich. This result, as mentioned earlier (in chapter 3) is not recommended for the Kesterite absorber layers. Thus, the theoretical atomic ratio has been changed to  $\text{Cu}/(\text{Zn}+\text{Sn}) = 0.7$  and  $\text{Zn}/\text{Sn} = 1.2$  (Cu-poor and Zn-rich). The latter atomic ratio for precursor solution was resulted in the fabrication of converted thin films with a very Zn-rich composition. Consequently, the precursor composition has been changed to  $\text{Cu}/(\text{Zn}+\text{Sn}) = 0.7$  and  $\text{Zn}/\text{Sn} = 1$ . The latest converted thin films was still obtained a very Zn-rich and Sn-poor composition ( $\text{Zn}/\text{Sn} \sim 1.7$ ), even though the sulphurisation time decreased from 4 hours to 1 hour. Nevertheless, the results of this converted sample (2d) have shown a better consequence compared to the previously examined experiments (2a, 2b, and 2c). Therefore, this initial ratio ( $\text{Cu}/(\text{Zn}+\text{Sn}) = 0.7$  and  $\text{Zn}/\text{Sn} = 1$ ) has been chosen for the following experiments in this thesis. In the rest of this chapter, the study is focused on varying the other conversion parameters in order to improve the quality of compositional ratio as well as the micro and crystal structure of converted thin films.

Table 5-2. The table shows the conversion time of samples 2a to 2d. It also presents the compositional changes (at %) of the thin films before and after conversion/sulphurisation.

Sample	Conversion time	Cu/(Zn+Sn) As-deposited	Zn/Sn As-deposited	Cu/(Zn+Sn) After conversion	Zn/Sn After conversion
2a	4 hours	1	1	~1.02	~ 1.1
2b	4 hours	0.7	1.2	~ 0.7	~ 2.0
2c	1 hour	0.7	1.2	~ 0.7	~ 1.8
2d	1 hour	0.7	1	~ 0.7	~ 1.7

### 5.1.3 Sulphurisation time (conversion time)

An experiment that used to evaluate the dwell time required for a complete reduction the oxide compounds and developing a compact structure with the correct composition is presented in this section. Whilst the conversion time may also influence the diffusion of elements and impurities from the substrates into the thin film (such as Sodium), this did not form part of the study reported here.

To evaluate the conversion time,  $\text{Cu}_2\text{O}$  and  $\text{SnO}$  were first heated separately in a tube furnace under a mixture of argon and forming gas (400 mbar Ar + 100 mbar  $\text{H}_2/\text{N}_2$ ) at a

temperature of 550°C as identified in section 5.1.1. The dwell time decreased from 4 hours to 1 hour, with no supply of sulphur in the graphite box. However, the tube furnace was previously used for the sulphurisation process and consequently, the atmosphere inside the tube furnace contained residual sulphur. As can be seen in XRD patterns (see Figure 5-3), the SnO requires at least 3 hours of heating at temperature of 550°C to be reduced completely within the sensitivity of the measurement, while Cu<sub>2</sub>O needs only 1 hour of heating with the same temperature to be reduced to Cu. Due to the presence of extra sulphur in the atmosphere of tube furnace, the XRD patterns indicate the presence of CuS, Cu<sub>2-x</sub>S, and SnS. A similar experiment has been carried out for the samples coated with the precursor solutions made of all three compounds of Cu<sub>2</sub>O, ZnS, and SnO. In this case, the excess quantity of sulphur has been used. The results indicate the formation of CZTS Kesterite structure even after 1 hour of conversion. In apparent contradiction to SnO needing at least 3 hours of heating to reduce to SnS or Sn. This might have been due to the small portion of SnO in precursor layer, compared to the only SnO coated samples, or the presence of excess quantity of sulphur in the tube furnace and graphite boxes or the presence of other compound in the precursor films. SEM images (see Figure 5-6) show a slight grain growth when the dwell time is increased, this difference does not clearly justify the additional energy consumed during 4 hours heat treatment. Accordingly, the study used a 1 hour dwell time for sulphurisation and to improve the quality of CZTS crystal structure the other conversion factors will be investigated in the following.

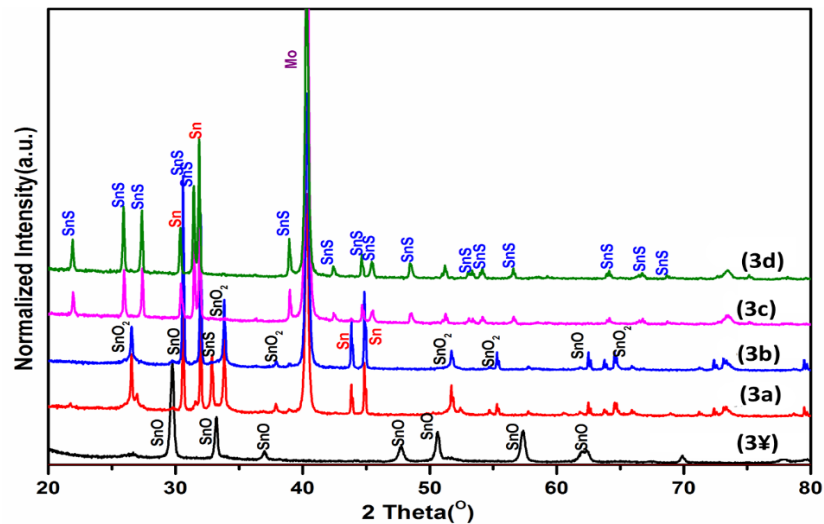


Figure 5-3. The XRD patterns of the (3a) SnO powders, and a thin film of SnO for (3a) 1 hour (3b) 2 hours (3c) 3 hours (3d) 4 hours of conversion at a temperature of 550°C.



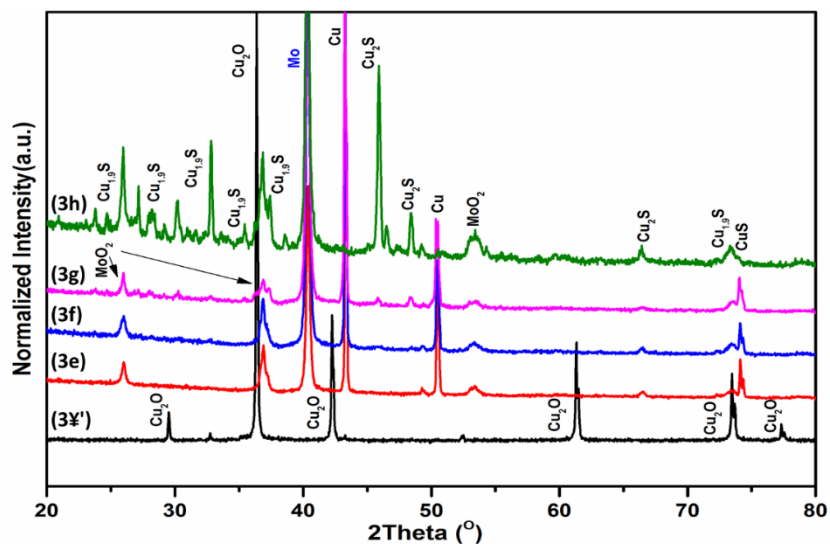


Figure 5-4. The XRD patterns of (3e) Cu<sub>2</sub>O powders, and a thin film of Cu<sub>2</sub>O for (3e) 1 hour (3f) 2 hours (3g) 3 hours (3h) 4 hours of conversion at a temperature of 550°C.

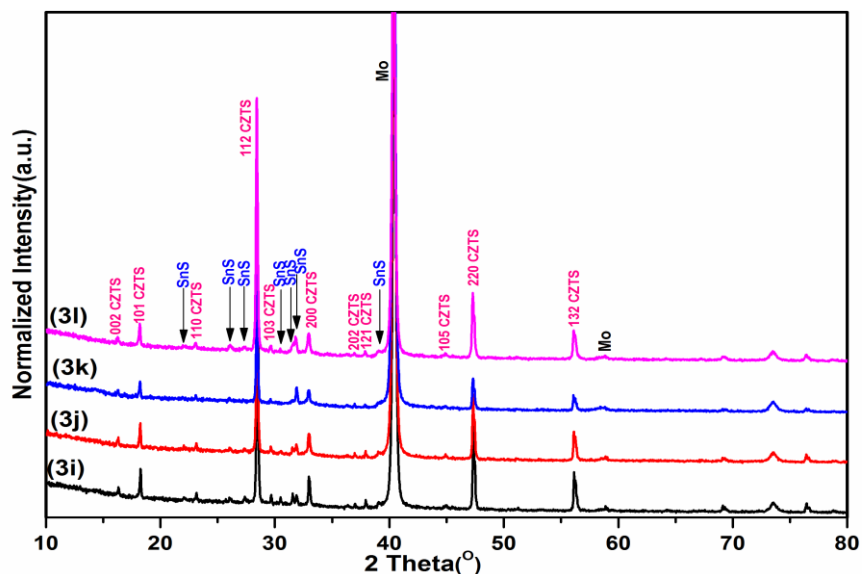


Figure 5-5. The XRD patterns of CZTS thin films after (3i) 1 hour (3j) 2 hours (3k) 3 hours and (3l) 4 hours of conversion.

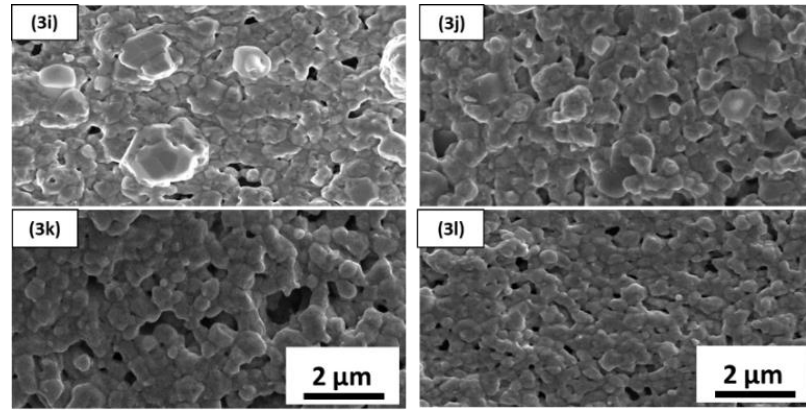


Figure 5-6. The plan-view SEM images of CZTS thin films after (3i) 1 hour (3j) 2 hours (3k) 3 hours and (3l) 4 hours of heat treatment.

#### 5.1.4 Heating profile during the sulphurisation process

To examine the influence of heating profile on the morphology and composition of CZTS thin films, three experiments have been defined, as described in Table 5-3. The schematic of sample 4a to 4c is presented in Figure 5-7. The tube furnace was filled with an ambient pressure of 400 mbar Ar + 100 mbar H<sub>2</sub>/N<sub>2</sub>, a conversion temperature of 550°C, and a dwell time of 1 hour.

Table 5-3. The table shows the compositional changes of elements on the converted samples sulphurised at 550°C for 1 hour at an ambient pressure of 400mbar Ar + 100mbar H<sub>2</sub>/N<sub>2</sub>. The measurement has been carried out with and without the considering of molybdenum.

Batch No.	Heating Profile	Mo	Cu	Zn	S
		(at %)	(Zn + Sn)	Sn	(Cu + Zn + Sn)
<b>4a</b>	Heating fast Cooling fast	37.5	0.9	2.5	0.8
		exclude	0.7	2.5	2.0
<b>4b</b>	Heating gradually Cooling naturally	21	0.8	1.8	1.0
		exclude	0.7	1.8	1.5
<b>4c</b>	Heating fast Cooling naturally	8.5	0.8	1.4	0.6
		exclude	0.9	1.4	1.0

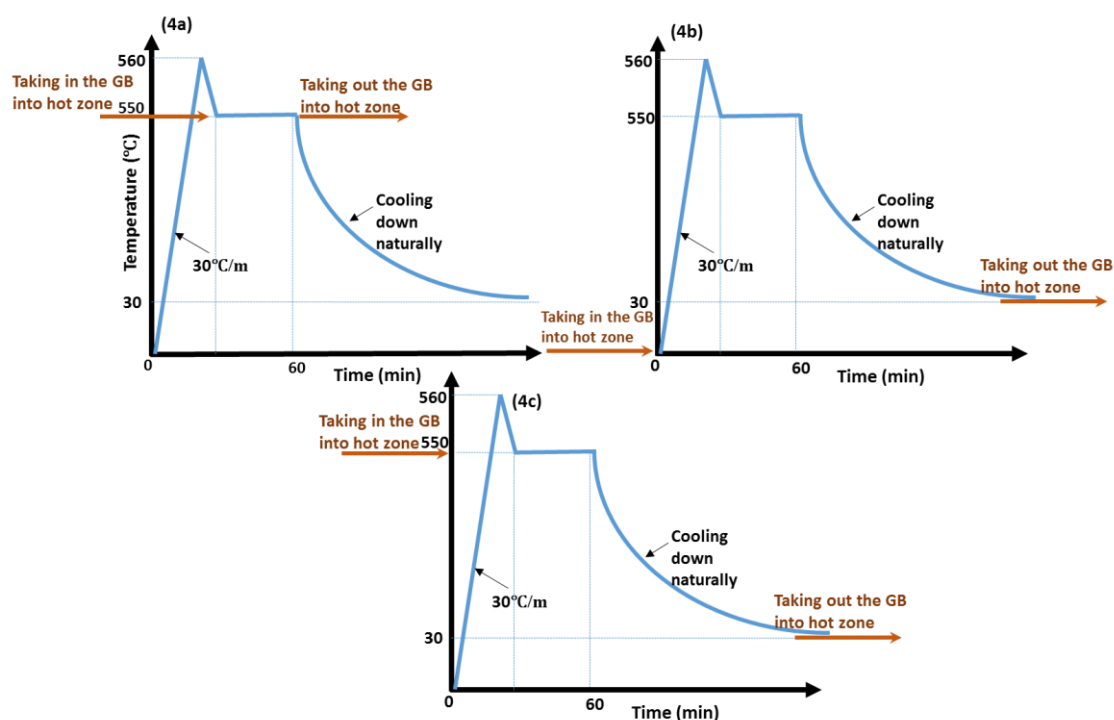


Figure 5-7. The figure shows the examples of heating profile for the sulphurisation process of samples (4a) heating fast and cooling fast (4b) heating gradually and cooling naturally (4c) heating fast and cooling naturally. The brown arrows display the positions at which the graphite box (GB) including the precursor was inserted into the hot zone and taken out from the hot zone of the tube furnace.

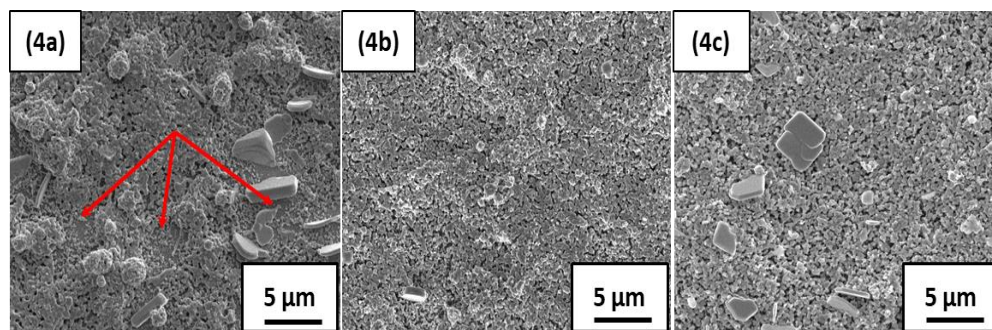


Figure 5-8. The plan-view SEM images of converted precursors with three different heating profiles of (4a) heating fast and cooling fast (4b) heating gradually and cooling naturally (4c) heating fast and cooling naturally. The red arrows exhibit the loss of precursor from the surface by showing the molybdenum substrate.

The results indicate that samples 4a and 4b are more vulnerable in terms of losing the precursor materials compared with sample 4c. This is shown by the detection of a high degree of molybdenum (the substrate) and a large quantity of pinholes on the surface of thin films, observed by SEM and EDX compositional analyses (see Figure 5-8 and Table

5-3). Although according to XRD patterns the SnS has been formed during the sulphurisation process of sample 4c, the final thin films include a better composition and microstructure compared to samples 4a and 4b. Therefore, the heating profile in which the sample is heated fast and cooled down naturally (sample 4c), appears to be an appropriate model to fabricate the CZTS thin films. However, its morphology and composition still needs to be modified. Another advantage of such a heating profile is the possibility of controlling the exact temperature of the conversion process. This is due to the fact that when the sample is inserted into the hot zone of the tube furnace at room temperature, it will undergo a gradual heating process. Thus, it is affected by the fluctuation of temperature from 550°C, which in turn contributes to an uncertainty of the exact processing temperature (The fluctuation of temperature using this particular system has shown a variation of  $\pm 10^\circ\text{C}$ ).

#### 5.1.5 Ambient gas composition and conversion/sulphurisation dwell time

This part of the study involves investigation of two parameters (i) the development of CZTS formation by decreasing the conversion time from 60 min to 15 min (ii) the effect of the total ambient gas pressure and composition during sulphurisation, as stated in Table 5-4.

Table 5-4 Sample identification and the associated synthesis conditions.

Sample	Pressure (mbar)	Time	Sample	Pressure (mbar)	Time
<b>5a.</b>	400Ar +100 H <sub>2</sub> /N <sub>2</sub>	60 min	<b>5f</b>	500 H <sub>2</sub> /N <sub>2</sub>	30 min
<b>5b</b>	250Ar + 250 H <sub>2</sub> /N <sub>2</sub>	60 min	<b>5g</b>	450Ar + 50 H <sub>2</sub> /N <sub>2</sub>	15 min
<b>5c</b>	450Ar + 50 H <sub>2</sub> /N <sub>2</sub>	30 min	<b>5h</b>	400Ar + 100 H <sub>2</sub> /N <sub>2</sub>	15 min
<b>5d</b>	400Ar + 100 H <sub>2</sub> /N <sub>2</sub>	30 min	<b>5i</b>	250Ar + 250 H <sub>2</sub> /N <sub>2</sub>	15 min
<b>5e</b>	250 Ar + 250 H <sub>2</sub> /N <sub>2</sub>	30 min	<b>5j</b>	500 H <sub>2</sub> /N <sub>2</sub>	15 min

XRD patterns (see Figure 5-5) illustrate the presence of CZTS compound for the thin films converted with 400mbar Ar +100mbar H<sub>2</sub>/N<sub>2</sub>, however, the XRD cannot make a clear distinction between the CZTS and other possible compounds such as Cu<sub>2</sub>SnS<sub>3</sub> and ZnS. To address this, Raman spectroscopy was carried out by partners to compliment the analysis and clearly identify the CZTS and other ternary or binary compounds. The Raman spectra (see Figure 5-9) indicate the formation of Kesterite compound even after 15min. SEM images, however, show that the sample sulphurised for 15min exhibited a slightly smaller grain size than those sulphurised for 30 min (see Figure 5-10). Raman

spectra have shown the formation of CZTS Kesterite with indicative peaks at the approximate values of  $98\text{ cm}^{-1}$ ,  $287\text{ cm}^{-1}$ ,  $340\text{ cm}^{-1}$ , and  $375\text{ cm}^{-1}$  together with  $\text{MoS}_2$  having an indicative peak of  $\sim 400\text{ cm}^{-1}$ . Peaks detected at the approximate values of  $218\text{ cm}^{-1}$  and  $310\text{ cm}^{-1}$  could be an indicator of  $\text{Cu}_2\text{O}$  compound. However, the peaks at about  $218\text{ cm}^{-1}$  can be also corresponded to  $\text{SnS}$  compound. There is no trace of this peak when the conversion time is increased from 15 min to 30 and 60 min. The  $\text{ZnS}$  compound, however, needs a wavelength excitation of  $325\text{ nm}$ , and could not be detected at  $\lambda = 532\text{ nm}$ . The Raman spectra shown in Figure 5-9 were measured at Swansea University by Dr. Wei Zhengfei.

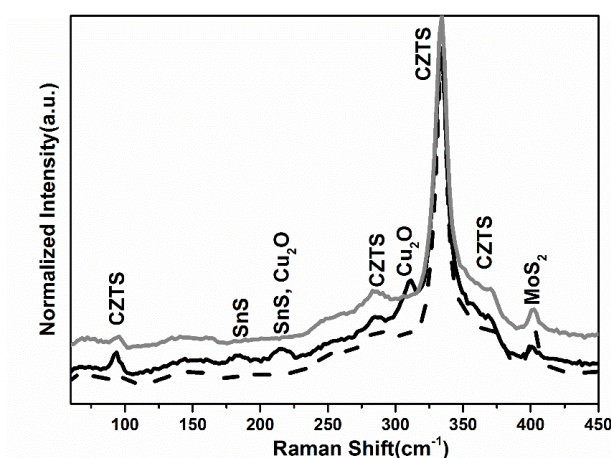


Figure 5-9. Raman spectra of the thin films converted at  $550^\circ\text{C}$  for (5b) 60min in grey line (5e) 30min in dashed line and (5i) 15min in black line ( The data have been taken at Swansea University by Dr.Wei Zhengfei )

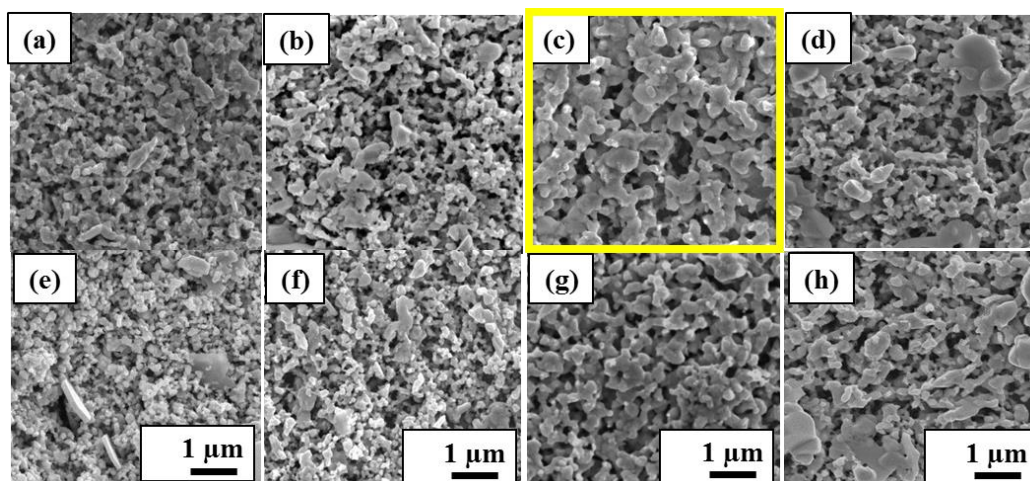


Figure 5-10. The plan-view of SEM images of (a, b, c, d) converted samples of 5c to 5f for 30min each, and (e,f,g,h) converted samples of 5g to 5j for 15min; The best morphology is highlighted in the yellow line.

Additional Raman spectra (Figure 5-12 and Figure 5-13) were measured at three different locations on the as-deposited and the converted sample that was sulphurised under the conditions as sample 5e. The measurements at three points were used in order to estimate the uniformity of samples. These analyses have been done by Dr. Sara Dale at University of Bath. The results indicate similar patterns for all three locations of 1, 2, and 3, (see Figure 5-11 ) representing the formation of uniform structures across the thin film. The Raman spectrometer has confirmed the formation of CZTS thin films together with SnS and ZnS binary compounds. While, there is no trace of oxide compounds through the structures of converted thin films (see Figure 5-12 and Figure 5-13). However, it should be noted that the use of two excitation wavelengths of 325nm and 532nm are not appropriate for the purpose of detecting the SnO characterisation peaks. This is due to the approximate overlap of  $\text{Cu}_2\text{O}$  and SnO peaks. Nevertheless, the ZnS and  $\text{Cu}_2\text{O}$  compounds can clearly be demonstrated through the Raman spectra. As reported in previous literature, the most appropriate Raman excitation wavelength to detect SnO compound is 632nm [199-203].

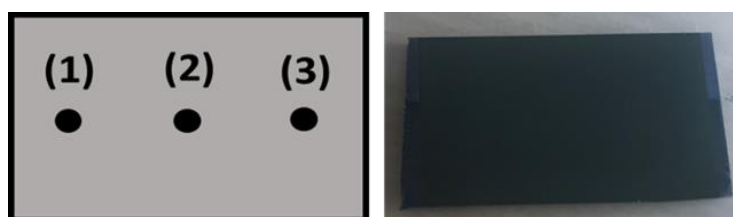


Figure 5-11. The schematic of a sample showing the approximate positions in which Raman analysis have been carried out (left picture), and converted sample (right picture).



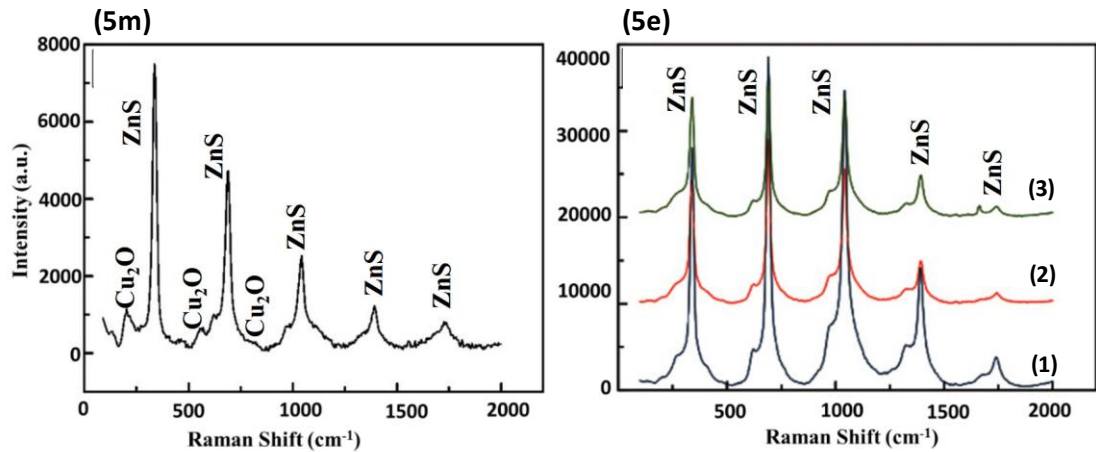


Figure 5-12. The Raman scattering with the excitation wavelength of 325nm shows the compounds formed on across the thin films for samples 5m (the as-deposited precursor) and 5e (the converted precursor). The positions of 1, 2, and 3 that the measurements have been carried out are displayed in the spectrum (The data have been taken by Dr. Sara Dale at Bath University).

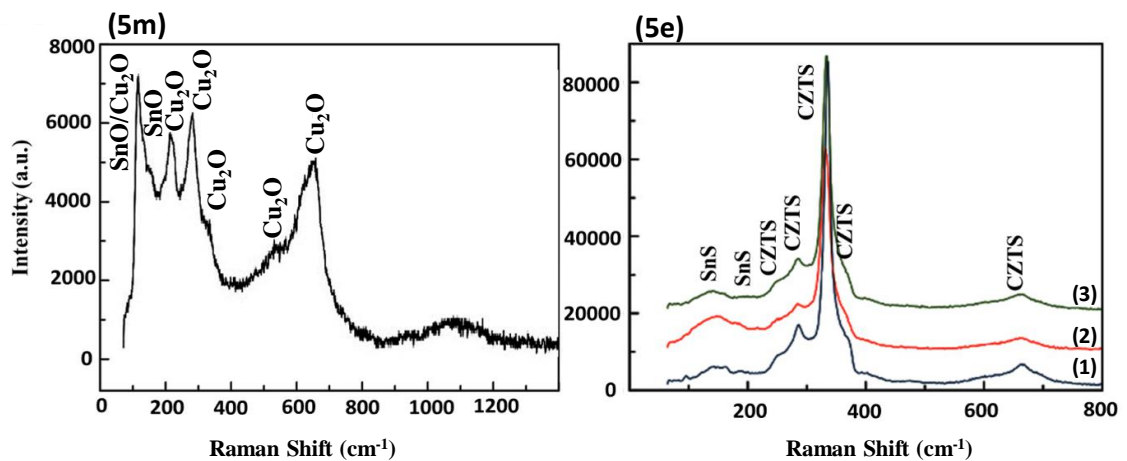


Figure 5-13. The Raman scattering with the excitation wavelength of 532nm shows the compounds formed on across the thin films for samples 5m (the as-deposited precursor) and 5e (the converted precursor) are shown. The positions of 1, 2, and 3 that the measurements have been carried out are displayed in the spectrum (The data have been taken by Dr. Sara Dale at Bath University).

#### 🌈 Optoelectronic characterisation

The optical properties of the samples have been examined via IMPS and EQE at Northumbria University and at Bath University, respectively.

The IMPS study was carried out by using three applied bias voltages of 0.35, 0.45, and 0.55V to the electrodes while the other parameters such as light flux and illumination area remained unchanged during the experiment.

As shown in Figure 5-14, the typical patterns achieved by CZTS thin films have shown a pattern corresponding to no recombination (similar to the configuration shown in Figure 3-21). The results show no sign of recombination of electrons and holes after 30 ms. When the light is switched off, the steady state moves to zero. The influence of using different wavelengths of incident light on the photocurrent response was also investigated. A photocurrent signal was not obtained when the wavelength of 450nm was applied. However, the signal started to appear at the wavelength of 565nm. When the wavelength increased to 940nm, similar patterns were obtained, but with considerably lower intensity than the one which emerged at the wavelength of 565nm. A typical configuration of photocurrent transient response versus time is presented in supplementary data (Appendix A). By varying the external applied voltage, a sharper initial response has been observed when the light cycle is at 0.35V, compared to the two applied voltages of 0.45V and 0.55V.

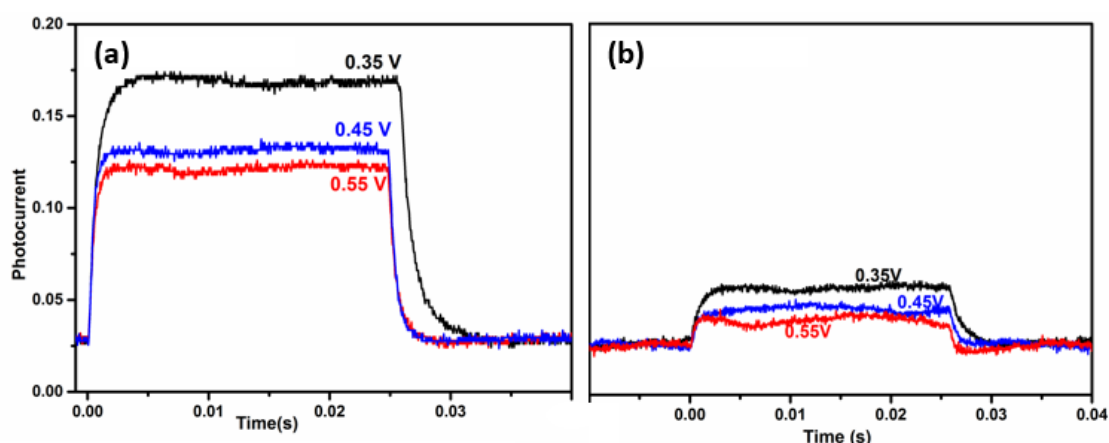


Figure 5-14. The figure shows the photocurrent transient responses of sample 5e with bias voltages varying from 0.35V to 0.55V at two different wavelengths of (a) 565 nm (b) 940 nm.

The EQE spectrum has obtained an approximate efficiency of 20% for the converted samples (see Figure 5-15a). Figure 5-15b shows the Tauc plot extrapolated from the EQE spectrum, as can be seen the band gap values is reported equal to 1.42 eV for the converted sample.



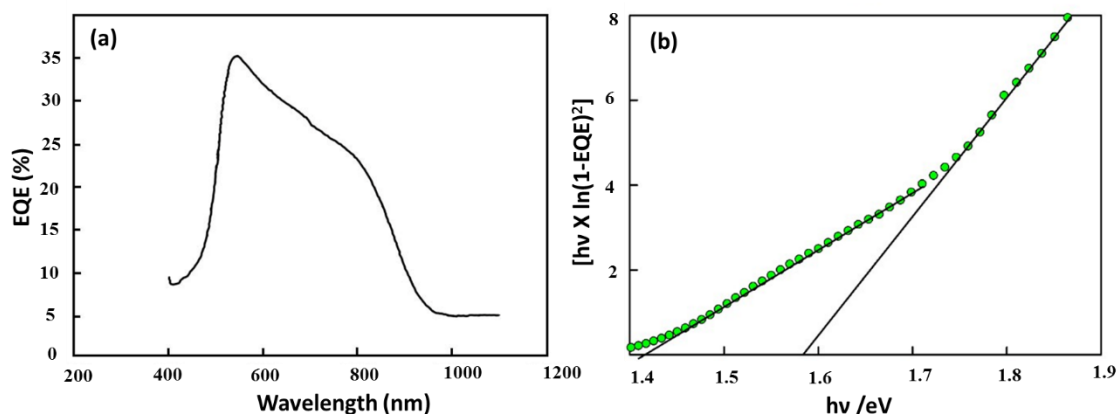


Figure 5-15. The figure shows (a) the EQE spectrum versus wavelength of sample 5e, (b) The Tauc plot showing the band gap and resulted by extrapolating the EQE spectrum (The Data have been taken by Dr. Sara Dale at Bath University).

### 5.1.6 Phase evolution by varying the conversion temperature

In order to analyse the phase evolution from oxide compounds to sulphide and CZTS Kesterite structure, several experiments were performed that heated the precursors at temperatures of 250°C, 350°C, 450°C, and 550°C for 1 hour. The XRD patterns illustrated in Figure 5-16 have revealed that at 250°C, a combination of oxide and sulphides of tin and copper is present across the thin film. While, the sample heated at 350°C, has shown the presence of SnO compounds, but not the copper oxides. Increasing the temperature to 450°C has shown no indicative peaks of oxide compounds. Nevertheless, the CZTS compounds are not well crystallised yet. When the temperature is increased to 550°C, the XRD shows the formation of CZTS together with the binary compound of SnS across the thin film. The CZTS Kesterite structure with tetragonal configuration is characterised with distinctive peaks at 2-theta values at diffraction plane (hkl) of 28.53° (112), 32.99° (200/004), 47.33° (220), and 56.18° (312). Figure 5-16 indicates the morphology of the precursors when the samples are heated at various temperatures.

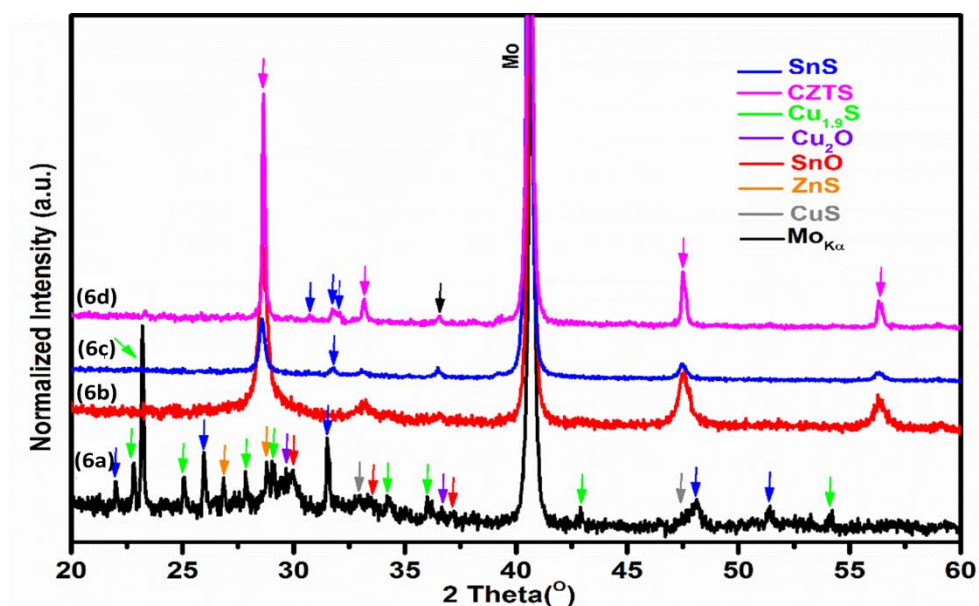


Figure 5-16. The X-ray patterns show the evolution of compounds of the thin films heated at different temperatures of (6a) 250°C (6b) 350°C (6c) 450°C (6d) 550°C.

### 5.1.7 Supplying the Sulphur during the conversion/sulphurisation

According to the data achieved in Chapter 4, with similar reasons as using Selenium as a chalcogen supply for the fabrication of CZTSe thin films, it was speculated that the use of sulphur powder could be more efficient than the use of sulphur as a cap layer. Thus, in order to fabricate the CZTS thin films in this thesis, the sulphur powders was used. Besides the method of supplying chalcogen, the mass of chalcogen should also be sufficient for the converted CZTS thin films. Thus, an experiment has been done with the aim of providing enough partial pressure of sulphur for the CZTS thin films, the graphite boxes were supplied with different amounts of sulphur from 0.05g to 2g. It should be noted that in order to measure the exact influence of sulphur on the quality of converted thin films by EDX compositional analysis, both Mo/SLG and SLG were used as a substrate. The reason being, the sulphur  $K_{\alpha}$  peak overlaps with Molybdenum  $L_{\alpha}$  Peak, as mentioned in section 3.3.4, and this leads to an inaccurate data of the thin film composition. From Table 5-5, it can be seen that increasing the mass of sulphur powder from 0.05g to 0.5g, showed a great difference in S/(Cu+Zn+Sn) ratio from 0.7 to 0.9, respectively. However, a further increase in the mass of sulphur from 0.5g to 2g does not result in a considerable improvement in the sulphur content of CZTS converted thin films.

Table 5-5. The table presents the experiments evaluating the influence of varying the mass of sulphur together with the information of the compositional changes of CZTS thin films, samples 7a to 7j. The samples 7a to 7f were fabricated on SLG as a substrate and samples 7g to 7j were prepared using molybdenum coated soda-lime glass (SLG/Mo).

Sample	Substrate	Mass of supplying sulphur (g)	$\frac{\text{Cu}}{(\text{Zn} + \text{Sn})}$	$\frac{\text{Zn}}{\text{Sn}}$	$\frac{\text{S}}{(\text{Cu} + \text{Zn} + \text{Sn})}$
7a	SLG	0.05	0.9	1.5	0.7
7b	SLG	0.1	0.7	1.2	0.8
7c	SLG	0.5	0.7	1.2	0.9
7d	SLG	0.7	0.7	1.2	0.9
7e	SLG	1	0.7	1.2	0.9
7f	SLG	2	0.7	1.3	0.9
7g	Mo/SLG	0.1	0.8	1.3	0.95
7h	Mo/SLG	0.5	0.9	1.2	0.95
7i	Mo/SLG	0.7	0.8	1.0	0.95
7j	Mo/SLG	1	0.9	1.1	0.95

### 5.1.8 Conversion/ Sulphurisation temperature

To evaluate the influence of conversion temperature on the quality of absorber layers, the precursors are placed in graphite boxes containing a large excess sulphur (1g). The precursors were converted with an ambient pressure of 250mbar Ar + 250mbar H<sub>2</sub>/N<sub>2</sub> with the dwell time of 30 min (based on the optimum conversion condition have been achieved to this point). The temperature, however, has been varied from 500°C to 570°C, as described in Table 5-6. The XRD, SEM, and EDX analyses of this study are reported below.

Table 5-6. Introducing the various sulphurisation/conversion temperatures used for the synthesising the CZTS thin films, samples 8a to 8g.

Sample	Conversion temperature (°C)
8a	500
8b	520
8c	540
8d	550
8e	560
8f	570
8g	580

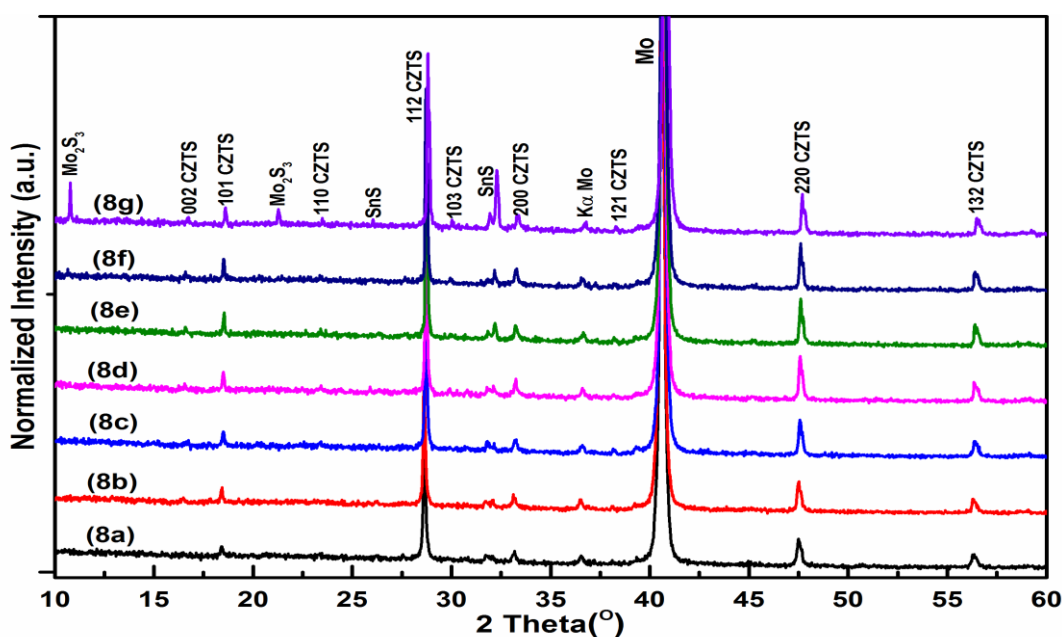


Figure 5-17 The figure shows the XRD patterns of sulphurised thin films at various temperatures of (8a) 500°C (8b) 520°C (8c) 540°C (8d) 550°C (8e) 560°C (8f) 570°C (8g) 580°C.

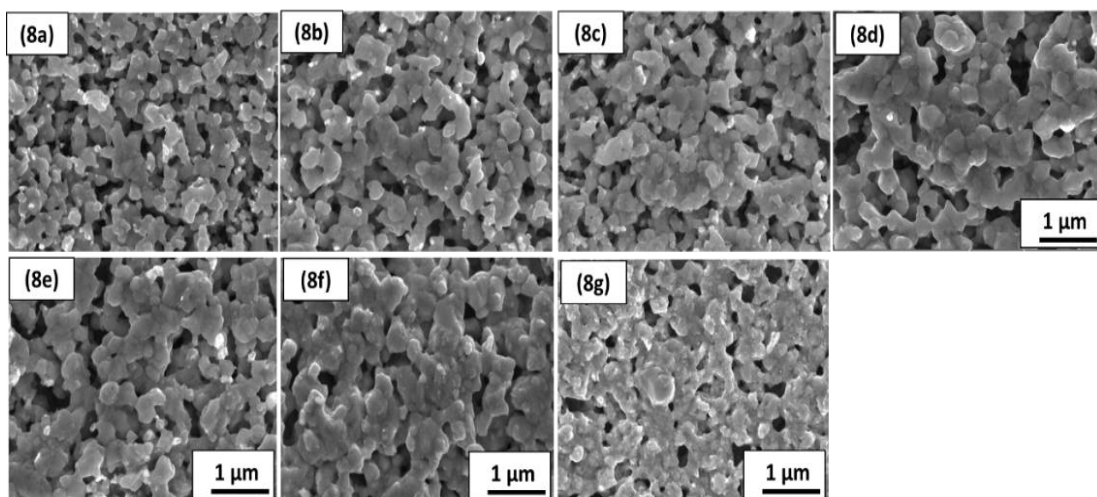


Figure 5-18. The plan-view SEM images of sulphurised thin film at the various temperatures of (8a) 500°C (8b) 520°C (8c) 540°C (8d) 550°C (8e) 560°C (8f) 570°C (8g) 580°C are displayed.

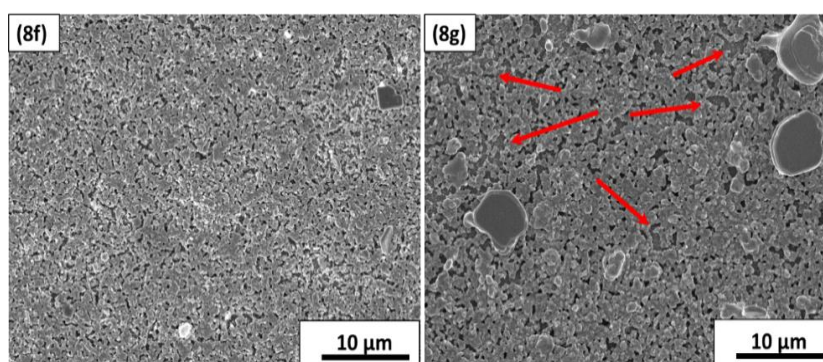


Figure 5-19. The plan-view SEM images of sulphurised samples at temperatures of (8f) 570°C and (8g) 580°C are displayed. The red highlighted arrows are pointed to the regions at which the loss of precursor has occurred.

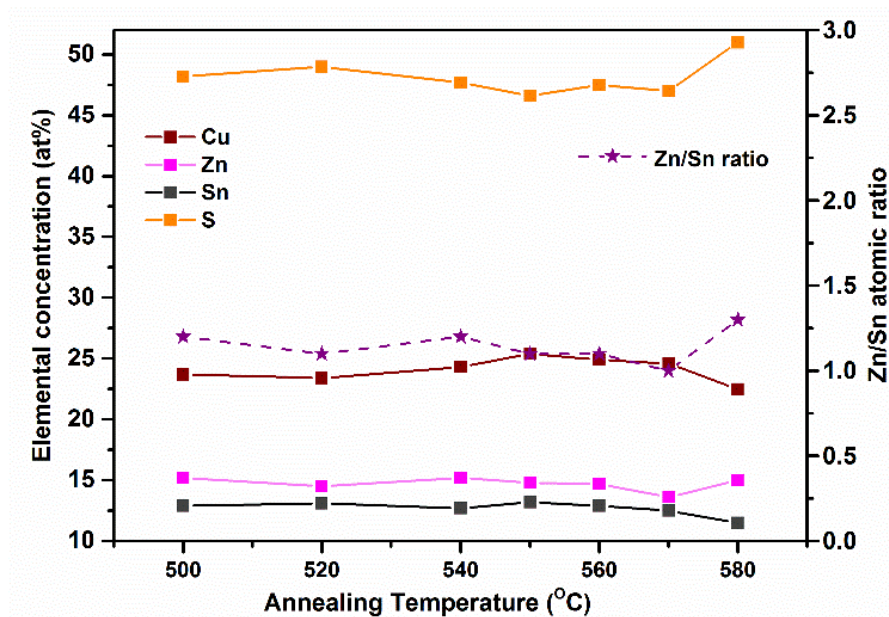


Figure 5-20. The graph shows the compositional changes (Zn/Sn ratio) of converted samples identified by the axes on the right and the elemental concentration in at% identified by the axes on the left. The data illustrate the EDX analyses of the converted samples sulphurised at different temperatures (samples 8a to 8g).

The XRD patterns illustrate a better crystallinity when the temperature is increased from 500°C to 570°C (see Figure 5-17). Furthermore, the XRD pattern of sample 8g reveals the formation of  $\text{Mo}_2\text{S}_3$  compound. The SEM images illustrate that increasing the temperature from 500°C to 570°C contributes to a grain growth of CZTS Kesterite structure (see Figure 5-18). However, a partial loss of precursor and the glass bending have been observed when the sample was converted at a temperature of 580°C (see Figure 5-19). The compositional changes of the converted samples are reported in Figure 5-20. According to the outcomes achieved through these experiments, the conversion temperature of 570°C (sample 8f) can be considered as a temperature in which a better degree of compactness and less formation of binary compounds have been noticed, compared to the other examined cases (samples 8a to 8e, and 8g).

### 5.1.9 Total ambient pressure and Temperatures

The key parameters including the pressure and composition of ambient gas, the conversion temperature and time, together with the quantity of sulphur powder have been investigated to improve the quality of the CZTS absorber layers. However, it was anticipated that this was an iterative process and therefore having achieved an optimum

set of each in a first iteration it was considered necessary to re-examine the certain parameters in order to further improve composition, crystal and micro structure of CZTS absorber layers. To do so, several experiments were undertaken that involved variation of the total ambient pressure, as detailed in Table 5-7, the table also presents the compositional changes of converted precursors. The results illustrate similar compositional changes for all examined samples (9a to 9f). The XRD, SEM, and EDX analyses are reported below.

Table 5-7. The table shows the variation of ambient pressures for examined samples of 9a to 9f, the compositional changes of sulphurised samples using EDX analysis have been also presented.

<b>Sample</b>	<b>Pressure (mbar)</b>	<b>Temp. (°C)</b>	<b><math>\frac{\text{Cu}}{(\text{Zn} + \text{Sn})}</math></b>	<b><math>\frac{\text{Zn}}{\text{Sn}}</math></b>	<b><math>\frac{\text{S}}{(\text{Cu} + \text{Zn} + \text{Sn})}</math></b>
<b>9a</b>	5 H <sub>2</sub> /N <sub>2</sub>	550	0.8	1.2	0.9
<b>9b</b>	250 H <sub>2</sub> /N <sub>2</sub>	550	0.9	1.1	0.9
<b>9c</b>	250H <sub>2</sub> /N <sub>2</sub> +250 Ar	550	0.8	1.0	0.9
<b>9d</b>	5 H <sub>2</sub> /N <sub>2</sub>	570	0.8	1.1	0.9
<b>9e</b>	250 H <sub>2</sub> /N <sub>2</sub>	570	0.9	1.2	0.9
<b>9f</b>	250H <sub>2</sub> /N <sub>2</sub> +250 Ar	570	0.9	1.3	0.8



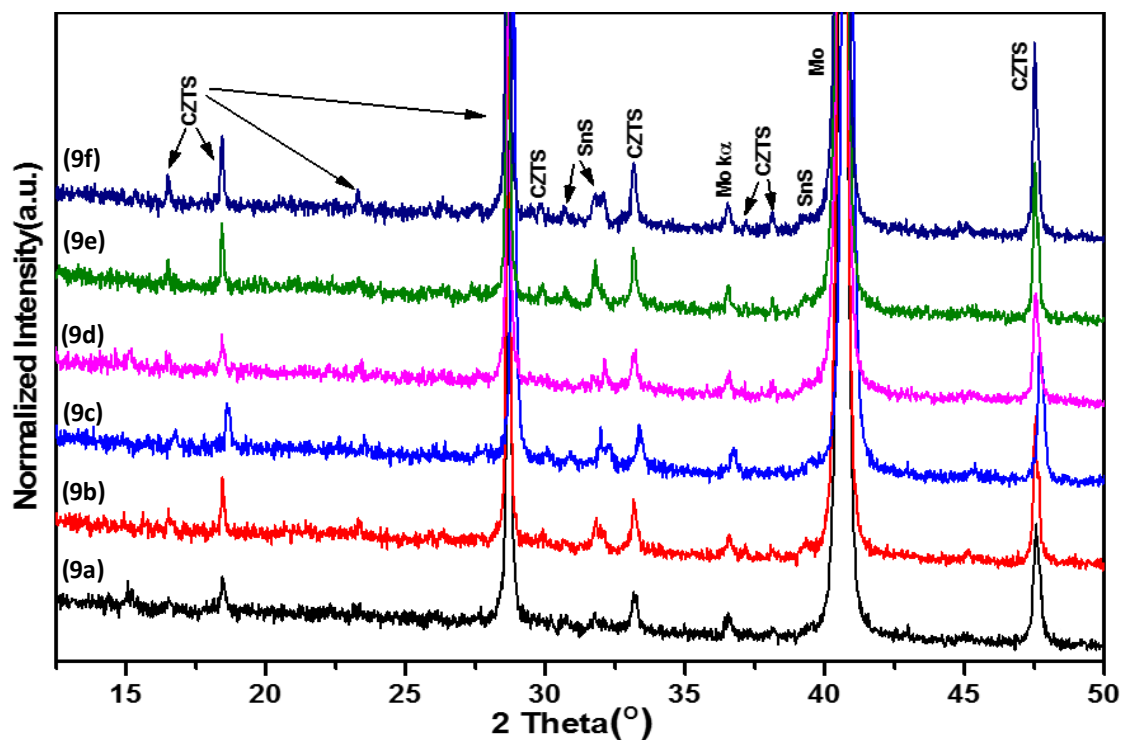


Figure 5-21. The XRD patterns of converted samples (9a to 9c) at temperature of 550°C and samples (9d to 9f) at temperature of 570°C are presented. The experiments have been done under various background pressures of (9a) and (9d) 5mbar  $H_2/N_2$ , (9b) and (9e) 250mbar  $H_2/N_2$ , (9c) and (9f) 250mbar  $H_2/N_2$  + 250mbar Ar.

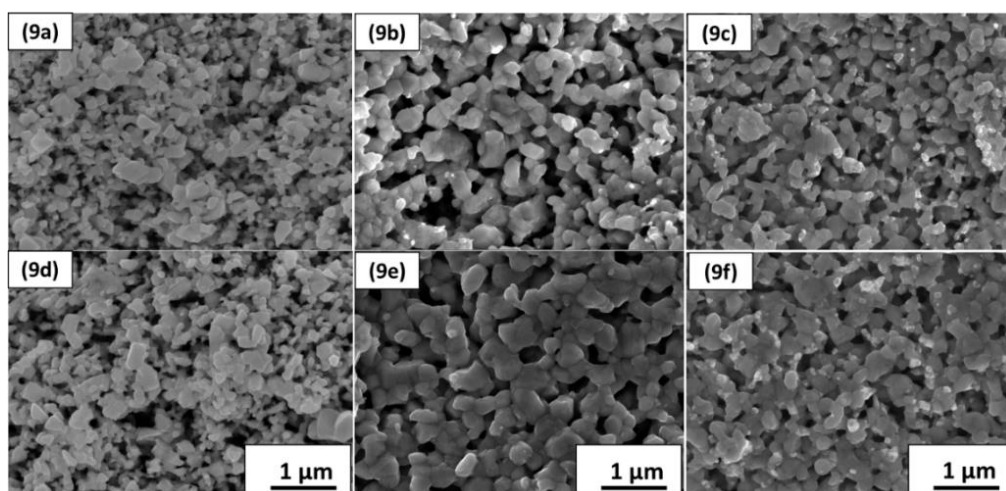


Figure 5-22. The plan-view SEM images of converted samples (9a to 9c) at temperature of 550°C and samples (9d to 9f) at temperature of 570°C are presented. The experiments have been done with various background pressure of (9a) and (9d) 5mbar  $H_2/N_2$ , (9b) and (9e) 250mbar  $H_2/N_2$ , (9c) and (9f) 250mbar  $H_2/N_2$  + 250mbar Ar.



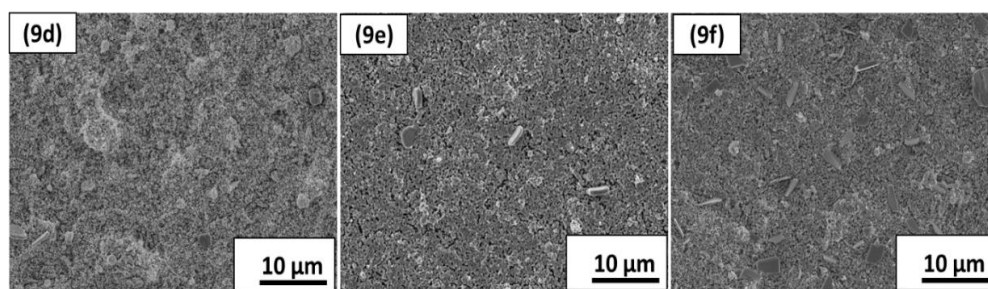


Figure 5-23. The plan-view SEM images of precursors converted at 570°C and with an ambient pressure of (9d) 5mbar H<sub>2</sub>/N<sub>2</sub>, (9e) 250mbar H<sub>2</sub>/N<sub>2</sub>, (9f) 250mbar Ar + 250mbar H<sub>2</sub>/N<sub>2</sub>.

The results illustrate that the peaks indicating SnS formation are less intense for the samples sulphurised at low ambient pressure of 5 mbar H<sub>2</sub>/N<sub>2</sub> compared to the other examined samples with higher total ambient pressures of 250 mbar and 500mbar. Although all XRD patterns show a similar trend (see Figure 5-21), the related peaks for CZTS crystal structures of samples (9e) and (9f) indicate a slightly better crystallinity when the temperature raises from 550°C to 570°C. The morphology of the sulphurised samples, however, indicate a significant difference when the total pressure is changed from 5mbar to 250 mbar of forming gas. The results revealed that the grain size formed slightly larger in case of using the 250mbar of H<sub>2</sub>/N<sub>2</sub> and a temperature of 570°C, compared to the other examined conditions (see Figure 5-22). Both XRD and SEM results indicate the presence of SnS compounds on the surface, when the total ambient pressure is increased to higher pressures (250 mbar or 500 mbar) (see Figure 5-23). However, the quantity of SnS compounds seems higher at the total ambient pressure of 500 mbar, compared to the use of 250 mbar.

#### 5.1.10 Conversion/Sulphurisation time with the new conversion conditions

To re-examine the influence of sulphurisation time on the quality of CZTS absorber layers with the new conversion conditions, four experiments have been defined, as described in Table 5-8. The XRD, SEM, and EDX analyses are reported below.

Table 5-8. Introducing the samples converted at various dwell time during conversion

Sample	Dwell time (min)
10a	30
10b	40
10c	50
10d	60

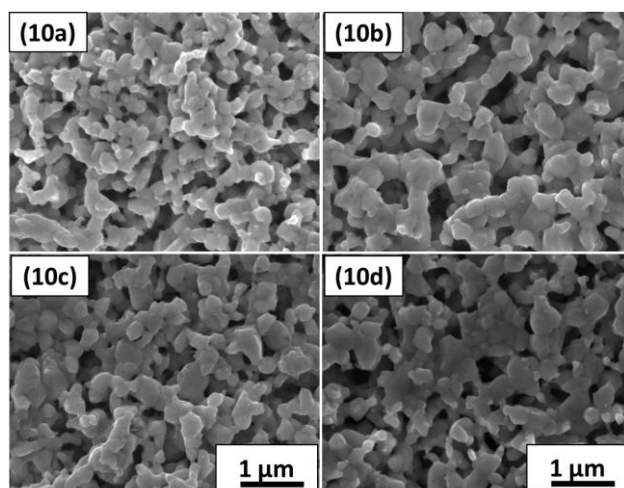


Figure 5-24. The plan-view SEM images of sulphurised samples with different dwell time of (10a) 30 min (10b) 40 min (10c) 50 min (10d) 60 min.

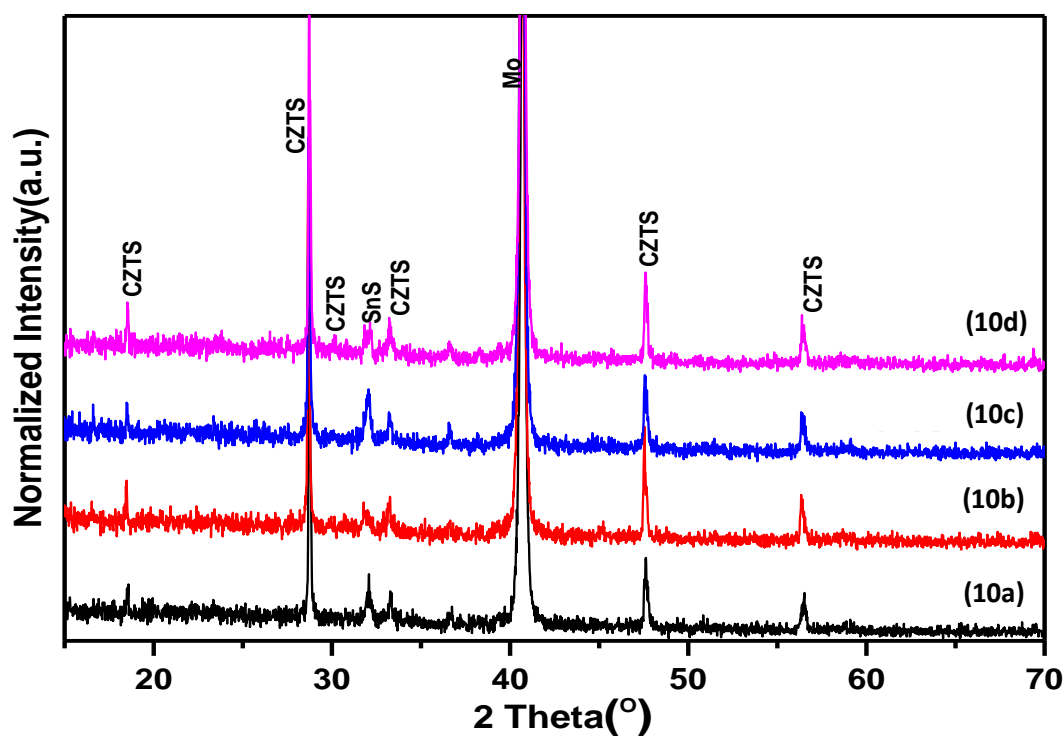


Figure 5-25. The XRD patterns of the sulphurised samples at 570°C with different dwell time of (10a) 30 min (10b) 40 min (10c) 50 min (10d) 60 min.

The XRD and SEM analyses indicate a slightly better crystalline structure and less secondary compounds, when the precursor was converted for 40 min, with the conversion temperature of 570°C, and an ambient pressure of 250 mbar of  $H_2/N_2$ . However, increasing the time to 60 min does not show a significant improvement in crystallinity

and grain growth (see Figure 5-24 and Figure 5-25). Thus, it is preferred to use the conversion time of 40 min considering the consumption of less energy for the processing of absorber layer. Figure 5-26 shows the cross section and plan-view SEM images of as-deposited and the sulphurised thin film of sample 10b which has shown the better morphology than the other examined samples to this point.

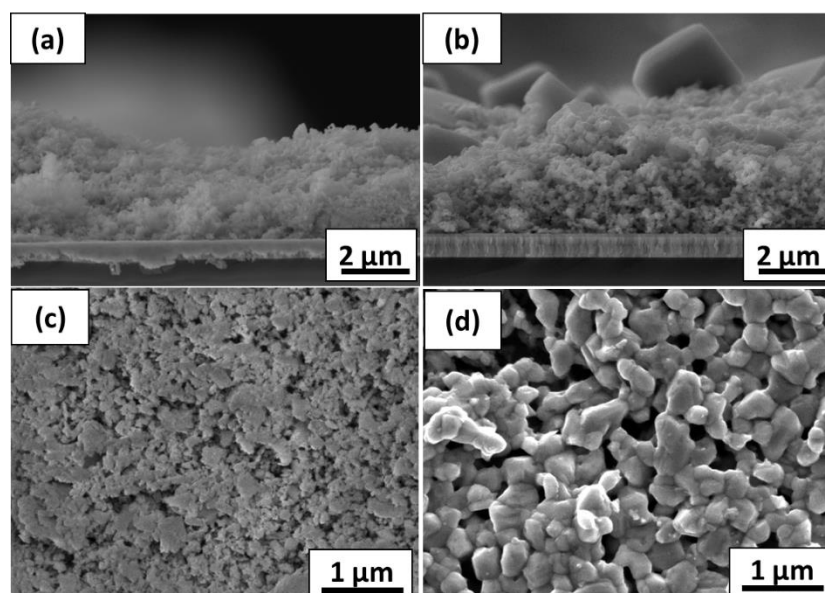


Figure 5-26. (a,b) The cross-section and (c,d) the plan-view SEM images of sample 10b which is described in Table 5-8, (a,c) as-deposited and (b,d) sulphurised thin films at 570°C with 250mbar  $H_2/N_2$  for 40min displayed above.

#### 5.1.11 Post-conversion heat treatment with excess mass of Chalcogen

In order to compensate for the sulphur deficiency of CZTS thin films, the sulphurised samples have undergone a post-conversion heat treatment procedure (post-sulphurisation) using two different ambient pressures of 5 and 500 mbar of argon. The details of the experiments are presented in Table 5-9. The SEM, XRD, and EDX analyses are presented below.

Table 5-9. The compositional ratio of CZTS samples after sulphurisation and post sulphurisation using two substrates of glass (SLG) and molybdenum coated glass (SLG/Mo) are listed. The highlighted parts in green are showing the experiments have been done on SLG substrates.

Sample	Substrates	Sulphurisation (S)/ Post Sulphurisation (PS)	Ambient Pressure (mbar)	$\frac{\text{Zn}}{\text{Sn}}$	$\frac{\text{Cu}}{(\text{Zn} + \text{Sn})}$	$\frac{\text{S}}{(\text{Cu} + \text{Zn} + \text{Sn})}$
<b>11a</b>	SLG	S	250 H <sub>2</sub> /N <sub>2</sub>	1.2	0.6	0.8
<b>11b</b>	SLG	PS	5 Ar	1.3	0.7	0.7
<b>11c</b>	SLG/Mo	S	250 H <sub>2</sub> /N <sub>2</sub>	1	0.6	0.8
<b>11d</b>	SLG/Mo	PS	5 Ar	1.1	1.1	0.8
<b>11e</b>	SLG	S	250 H <sub>2</sub> /N <sub>2</sub>	1.2	0.7	0.8
<b>11f</b>	SLG	PS	500 Ar	1.2	0.6	0.9
<b>11g</b>	SLG/Mo	S	250 H <sub>2</sub> /N <sub>2</sub>	1.1	0.8	0.9
<b>11h</b>	SLG/Mo	PS	500 Ar	1	0.8	0.9

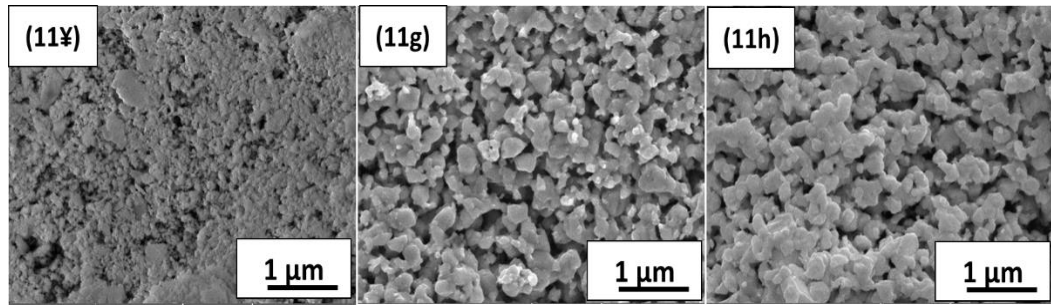


Figure 5-27. The SEM image of some of the samples described in Table 5-9, (11f) as-deposited (11g) sulphurised with 250mbar H<sub>2</sub>/N<sub>2</sub> of ambient pressure (11h) post sulphurised CZTS thin films with ambient pressure of 500mbar argon can be observed.

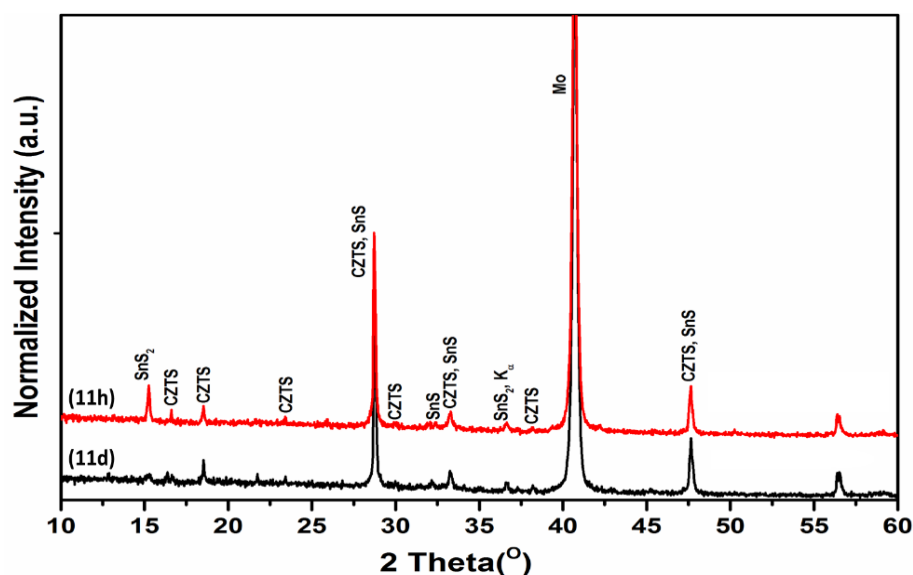


Figure 5-28. The XRD patterns of the post-sulphurised thin films at the ambient pressure of (11d) 5mbar Ar and (11h) 500mbar of Ar.

According to the results achieved and presented in Table 5-9, when the CZTS samples are post sulphurised under a low ambient pressure (5 mbar Ar), the sulphur deficiency is higher compared to the use of a high ambient pressure (500 mbar Ar). The XRD patterns illustrated that in case of using a high pressure of ambient gas (500 Ar), the SnS<sub>2</sub> is formed for the post sulphurised CZTS samples. However, this compound does not show a significant intensity when the sample was sulphurised at a low ambient pressure (5 mbar Ar). The formation of SnS<sub>2</sub> under high pressure of argon as an ambient gas, can be explained due to the higher concentration of sulphur vapour inside the graphite box.

#### 5.1.12 Surface etching

Contemplating the results achieved by EDX mapping, XRD, Raman scattering, cross section and plan-view SEM analyses, it is perceived that SnS secondary compounds are often formed together with the CZTS compound. The plan-view SEM images clearly show the presence of a high amount of SnS crystal structures on the surface, while the indicative peaks of SnS in XRD patterns have a very low intensity. Thus, it seems that this compound is mainly located at the interface of CZTS/CdS, rather than in the bulk or at the CZTS/Mo interface. Consequently, surface etching could be an appropriate strategy to remove the SnS compounds.

In this experiment, the etching process of CZTS thin films has been carried out with an etching duration of 1 min, 2 min, and 3 min. The experiments have been done at a room temperature of 22°C using the ammonium sulphide ((NH<sub>4</sub>)<sub>2</sub>S). The SEM and EDX



mapping have been recorded after each step of the etching procedure. The results indicate that at least 3min of etching is required to remove the SnS binary compounds from the surface of thin films (see Figure 5-29, Figure 5-30).

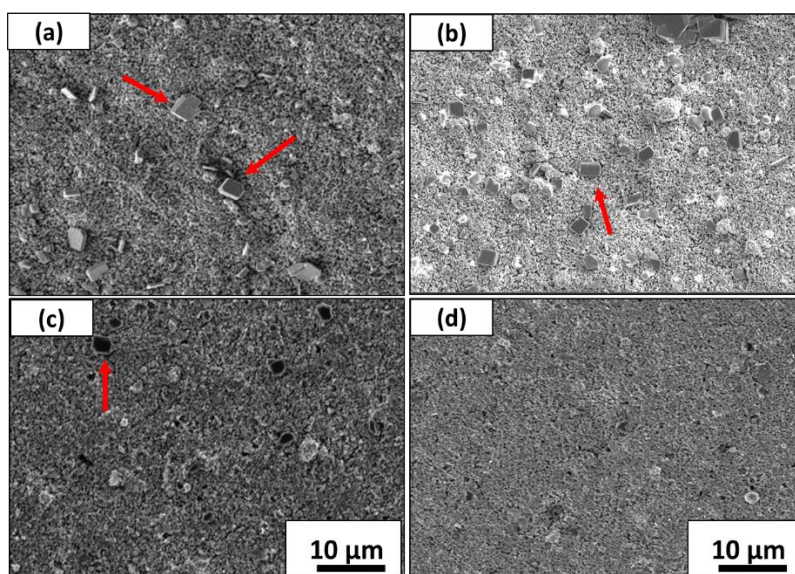


Figure 5-29. The SEM image of CZTS samples processed with (a) no etching (b) 1min of etching (c) 2 min of etching (d) 3 min of etching are illustrated. The red arrows in the images exhibit the presence of SnS crystal structures.

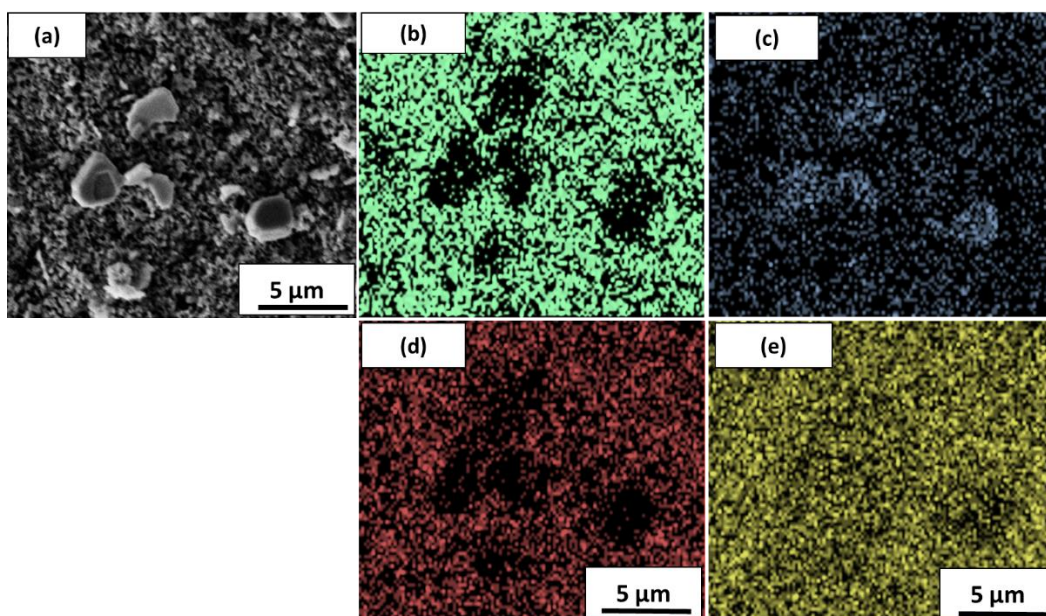


Figure 5-30. The EDX mapping of CZTS thin films before etching are indicative of the elements in different colours (a) SEM image (b) copper in green (c) tin in blue (d) zinc in red (e) sulphur in yellow.

### 5.1.13 Summary of Results and Discussion

The study on optimising the conversion conditions of CZTS thin films was initiated by a study on evaluating the influence of the composition and pressure of the ambient gases using forming gas and argon on the microstructure of thin films. The results have shown that although increasing the total ambient pressure would suppress the compounds in their vapour state to remain inside the graphite box, it is of great importance to optimise the pressure of applied ambient gas, especially when non-inert gases are used. In this experiment, due to the presence of SnO in the material precursor, the use of forming gas to reduce the oxide was required. As reported by Kim et al, and mentioned in section 2.2.6.2, SnO<sub>2</sub> can be reduced to tin in the atmospheres saturated by specific pressure of hydrogen and a temperature of 550°C. According to their study, increasing the pressure of forming gas would increase the rate of reduction. The results in the current study has confirmed the necessity of the presence of sufficient pressure of forming gas to reduce the SnO to SnS or Sn. However, the results achieved in this thesis also indicated that increasing the ambient pressure to 500 mbar, using the only forming gas, contributed to the loss of adhesion between the thin film and the Molybdenum back contact (non-uniformity of converted thin films). In fact, the morphology of converted thin films have shown that part of the thin film was removed and large area of molybdenum was appeared on the plan-view SEM images. Optimising the pressure of forming gas and dwell heating time has been examined in this thesis in order to remove oxygen from the initial compounds as well as preparing a uniform thin film with a right composition of CZTS Kesterite structure.

Varying the precursor composition ratio of Cu:Zn:Sn from 1:1:1 to 0.7:1:1.2, and finally 0.7:1:1, together with decreasing the conversion time from 4 hours to 40 min, have shown the formation of a better compositional ratio for the converted thin films (less Zn-rich and Sn-poor). Accordingly, a higher dwell time leads to a higher rate of SnS evaporation compounds contributing to a very Zn-rich and Sn-poor Kesterite structure across the absorber layer. This is in agreement with the previous literature [85], where it is said that decreasing the conversion time could limit the time available for the decomposition reactions and therefore reduce the tin loss. As Fella et al have reported when the composition of precursors prepared by non-vacuum processing are Zn-poor and Sn-rich (with a ratio of Zn/Sn<1), the converted thin film has the composition of Zn-rich and Sn-

poor (with a ratio of  $Zn/Sn > 1$ ). This is due to the Sn loss during crystallisation and a typical decomposition of CZTS compound. They have also reported that conversion in a sulphur saturated atmosphere could increase the rate of decomposition and the formation of SnS since the sulphur vapour bind the Sn excess. According to their study the initial precursor ratio of  $Zn/Sn < 1$  can significantly enhance the grain growth if the sulphurisation process take place in an inert atmosphere [100]. The study here confirms the aforementioned study in that the use of precursor ratio with the composition of  $Zn/Sn = 1$  was led to the formation of converted thin films with  $Zn/Sn > 1$ . However, in this thesis due to the presence of metal oxide compounds, the presence of forming gas and excess sulphur source during the conversion was necessary. Thus, decreasing the  $Zn/Sn$  ratio to less value than 1 could contribute to an increase in the rate of decomposition or forming CZTS crystal structure with considerable sulphur deficiency ( $V_s$ ).

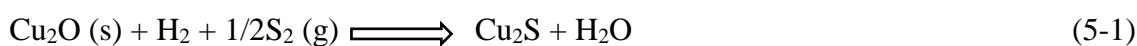
Investigating of the role of the heating profile on the morphology and composition of converted films, has showed that the tin lost is more critical in the case of fast heating and fast cooling procedure (ramp rate of  $\sim 1100^\circ\text{C}/\text{min}$ ). This could be due to the volatility of SnS and Sulphur in their vapour states at high temperatures during the sulphurisation. In fact, SnS(g) compound prefers to leave the system or even condense on the surface during cooling down, rather than contributing to the formation of CZTS. As a result, a very Sn-poor crystal structure of Kesterite CZTS has been formed. The SnS crystals have been observed on the surface of those samples heated fast and cooled down naturally. This demonstrates that SnS tends to condense on the surface at the cooling down procedure. In the case of heating gradually and cooling naturally, less SnS crystals were formed on the surface compared to the case of heating fast and cooling down naturally. This can be resulted from the reduction of SnS compounds during the heating procedure (at temperatures lower than  $550^\circ\text{C}$ ). Thus, the SnS in its vapour state have had sufficient time to leave the surface of the thin film. That is also consistent with the results achieved earlier which showed that SnS disappears by increasing the conversion dwell time. It should be noted that the use of SnO instead of SnS in this research was beneficial due to SnO being a stable compound. Hence, the formation of SnS in vapour state will occur with a delay. This could be advantageous to alleviate the rate of tin lost in case of using SnO instead of tin as an element. Furthermore, the  $\text{Cu}_2\text{SnS}_3$ (CTS) mainly appears from the combination

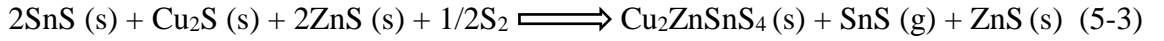
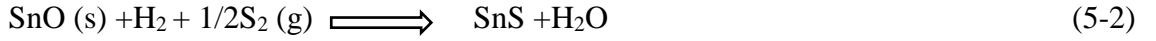


of SnS<sub>2</sub> and Cu<sub>2</sub>S at 300°C, as kim et al have reported [215]. Accordingly, the stability of SnO at high temperatures could be also beneficial in order to prevent the formation of CTS compounds at early stages of sulphurisation process.

Examining the influence of temperature and conversion time on the fabrication of CZTS thin films as it was expected has shown the considerable impact on the grain growth and the crystallinity. These parameters have been optimised in order to achieve the correct composition of converted thin films together with the formation of CZTS compound from metal oxide compounds. The results achieved in this thesis have shown that the quality of thin films was significantly improved by adjusting the conversion time and temperature to 40 min and 570°C, under the sufficient pressure of forming gas (250 mbar H<sub>2</sub>/N<sub>2</sub>). All the evidence from XRD, SEM, Raman, and also EDX mapping have shown the formation of SnS binary compounds, are mainly formed on the surface, together with CZTS Kesterite crystal structure. This illustrates that the atmosphere during the synthesising of CZTS is saturated with SnS(g). According to the experiments have been done to remove the SnS binary compounds from the surface by (NH<sub>4</sub>)<sub>2</sub>S, it was concluded that the surface etching of at least 3min at a temperature of 22°C (room temperature) is required to remove the SnS secondary compounds from the surface of converted thin films. Furthermore, the study on the post-conversion heat treatment of the converted samples has shown a slight compensation in the sulphur deficiency of converted thin films if the post-conversion heat treatment has been carried out under high ambient pressure with extra sulphur supply during the conversion.

Contemplating the results achieved through this research together with the literature review, which was explained in section 2.2.6.1, Reaction 5-1 to 5-5 are highly probable to occur in the specific study carried out through the current research. Thus, the metal oxides first react with sulphur (see reaction 5-1 and 5-2). Afterwards, the CZTS can be formed if the partial pressure of sulphur is sufficient (see reaction 5-3). At this stage of conversion, tin will partially be lost due to the volatility of SnS in vapour state. However, tin will be also condensed on the surface in the form of SnS(s). This process, as mentioned before, will occur during cooling step. This is due to the high partial pressure of sulphur during the conversion at high temperatures.





As for the optoelectronic analyses, the results achieved by IMPS technique have shown no signal (overshoot when the light is incident) at low wavelength of 430nm. In fact, at this wavelength the energy of photons are higher ( $E \sim 2.8\text{eV}$ ) than the band gap energy of CZTS compound ( $E_g \sim 1.5\text{eV}$ ). When the wavelength increases to 565nm, the signals appeared with a considerable overshoot effect at light on cycle. This indicates that at the incident of this wavelength ( $\lambda = 565\text{nm}$ ), the electrons are collected by  $\text{Eu}^{2+}$  (positively charged ions of the electrolyte). In comparison, increasing the wavelength to 940nm had shown signals but with less intensity. Considering the band gap energy of CZTS compound, it is expected that no signal appear by increasing the wavelength to 940nm. This can be attributed due to the use of non-monochromatic light source, as it is shown Appendix A.

At low voltage (reverse bias voltage), the generated electrons and holes can be separated. Accordingly, the electrons move towards the electrolyte side and they are attracted by the  $\text{Eu}^{2+}$  (positively charged ions of the electrolyte). In theory, when the external bias voltage increases, the electrons and holes will be separated with larger force contributing to signals with higher intensity. However, in the current experiment, increasing the bias leads to a decrease in the photocurrent response that can be attributed to the degradation of the  $\text{Eu}^{2+}$  ions in the electrolyte. Moreover, it is also assumed that the surface of films have been corroded and the results affected by the corroded compounds on the surface.

The EQE measurements had shown similar results in terms of the obtained spectrum not having a significant intensity at 430nm, while, the highest intensity has been observed at  $<600\text{nm}$ , with a lower intensity at higher wavelengths of  $\sim 940\text{nm}$ . According to the corresponding spectra in this particular experiment, the recombination losses in the bulk and/or probably low diffusion length are more dominant than surface recombination.

## 5.2 Follow-up trials

Although the conversion factors, especially the ambient pressure, time, and temperature indicate that there is a significant influence of these on the morphology and crystal structure of CZTS thin films, several issues were observed during the research. These

include (i) the formation of more porous structure across the converted CZTS thin films when they have been prepared via non-vacuum processing, compared to films fabricated via vacuum deposition techniques (ii) the sulphur deficiency of the examined experiments even with using large quantities of chalcogen during the conversion (iii) low degree of reproducibility of deposited thin films which occurs due to the deposition technique (hand held technique of spraying).

In order to address these issues, several follow-up studies have been carried out and will be presented in this section. However, more focus on these topics were beyond the scope of this PhD thesis and could be considered as future studies.

### **5.2.1 CZTS thin film fabrication using Slot-Die as a method of deposition**

In order to evaluate the influence of deposition technique on the uniformity of precursors and the fabricated CZTS thin films, an experiment has been done comparing the two techniques of slot-die and spraying. The spray deposition technique (with Airbrush at Northumbria University) was used to deposit sample 13b. The slot-die coating (with a Smart coater at Swansea University) was used to produce sample 13c. The precursor films were deposited on molybdenum coated soda-lime glass substrates. The sulphurisation was completed by heating the samples to 550°C for 30 min in an Ar : H<sub>2</sub>/N<sub>2</sub> ambient with the ratio of 4:1, and the total pressure of 500 mbar. It should be noted that the conversion condition used for the current experiment was based on the optimised conditions by the time this experiment has been carried out. As mentioned earlier the conversion conditions have been investigated and re-examined several times during the study.

The results reported by Swansea University indicated that in the process of deposition, the precursor solution has dried before it reaches the substrates. This is due to the very early evaporation of IPA. Figure 5-31 shows the dried precursors within the syringe. The delivery tube is used to conduct the precursor solution from the syringe to the slot-die head. However, the precursor solution could not be spread on the surface entirely, due to a blockage in the delivery tube (see Figure 5-31).

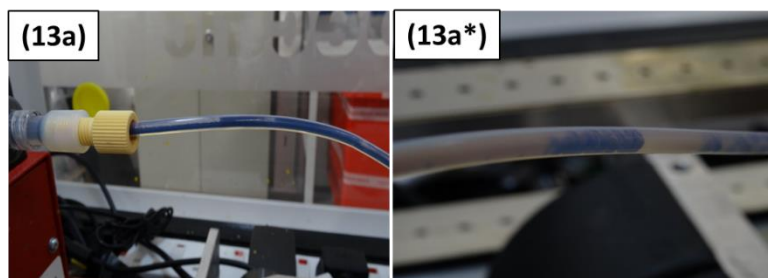


Figure 5-31. The two above pictures show part of the slot-die processing technique (13a) the syringe (13a\*) the tube which delivers the IPA from the syringe to the slot-die head.

The SEM images of as-deposited via slot-die and spraying technique are shown in Figure 5-33. The spray-coated samples exhibit localised agglomerated features in converted precursors that are not observed in slot-die coated films. This is attributed to the droplets of sprayed solution that may have settled on the surface of substrate during spraying. According to the visual inspections (see Figure 5-33); the as-deposited samples using slot-die coated technique were limited in number and have been damaged seriously which was possibly due to the packaging or posting. The XRD analyses have shown similar patterns for both slot-die and sprayed coated samples, illustrating the formation of CZTS Kesterite structure (see Figure 5-34). However, the Kesterites are not well-crystalised across the thin film. The presence of SnS crystals for all samples has been detected both with XRD and SEM analyses. The composition of converted thin films was characterised by EDX analysis. The results are detected in atomic percent and summarised in Table 5-10 which indicate a similar compositional changes for samples prepared via both slot-die and spraying method of deposition ( $\text{Cu}/(\text{Zn}+\text{Sn})=0.8$  and  $\text{Zn}/\text{Sn} = 1.1-1.2$ ).

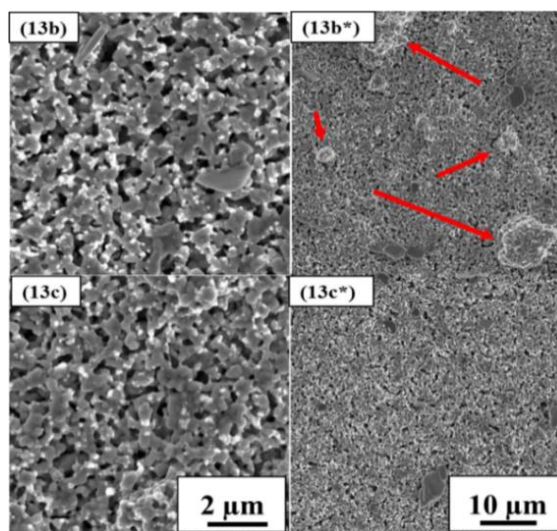


Figure 5-32. The SEM images show the morphology of (13b,13b\*) converted via spraying technique and (13c,13c\*) converted via slot-die technique are displayed. The images are observed with the magnification of (13b, 13c) ~20 kx and (13b\*, 13c\*) ~5 kx. The marked areas with red arrows show the agglomerated-like structures.

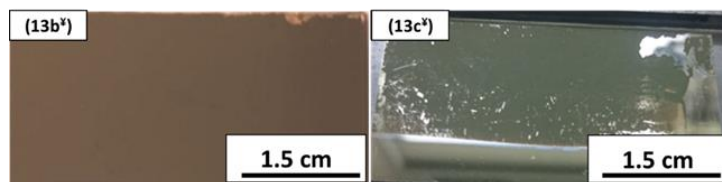


Figure 5-33. The images of visual inspection of (13b\*) as-deposited slot-die coated precursor and (13c\*) sprayed precursor.

Table 5-10. The EDX analyses of the samples prepared via two techniques of (13b) spraying and (13c) slot-die deposition technique.

Sample	Method of deposition	Cu (at%)	Zn (at%)	Sn (at%)	S (at%)	$\frac{\text{Cu}}{(\text{Zn} + \text{Sn})}$	$\frac{\text{Zn}}{\text{Sn}}$
13b	Spraying	22	14.5	12.5	46	0.8	1.1
13c	Slot-Die	24.3	16	13	46.5	0.8	1.2

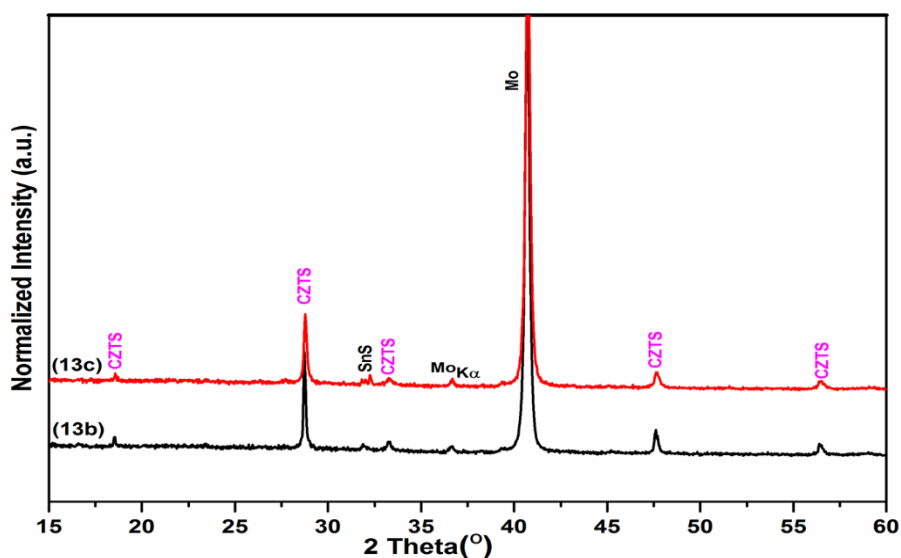


Figure 5-34. The XRD patterns of converted CZTS of (13b) spray coated sample and (13c) slot-die coated sample.

### 5.2.2 Supplying sulphur in precursor solution

In spite of a significant progress in improving the quality of CZTS thin films by adjusting the conversion parameters, it seems that there is still room to develop the CZTS thin films with a compact and dense structure with no sulphur deficiency. To do so, two precursor solutions have been prepared with (i)  $\text{Cu}_2\text{O} + \text{SnO} + \text{ZnS} + \text{IPA}$  with the atomic ratio of Cu:Zn:Sn:S equal to 0.7:1:1:0 (ii)  $\text{Cu}_2\text{O} + \text{SnO} + \text{ZnS} + \text{S} + \text{IPA}$  with the atomic ratio of Cu:Zn:Sn:S equal to 0.7:1:1:4. The as-deposited thin films were sulphurised at  $570^\circ\text{C}$  under the ambient pressure of 250 mbar  $\text{H}_2/\text{N}_2$  for 40 min with a given sulphur quantity as mentioned in Table 5-11.

Table 5-11. The table indicates the compositional variations of the sulphurised samples when a mass of sulphur is added to the precursor solution. The mass of sulphur is presented in the table refers to the excess amount added into the graphite box during the sulphurisation/conversion.

Sample	Substrate	Sulphur quantity (g)	$\frac{\text{Cu}}{(\text{Zn} + \text{Sn})}$	$\frac{\text{Zn}}{\text{Sn}}$	S (at%)	Mo (at%)
14 $\forall$	SLG	-	0.7	1.2	26 S 37.5 O	-
14a	SLG/Mo	0	1.0	0.5	33	17.5
14b	SLG/Mo	0.5	0.7	1.1	45	6
14c	SLG	0.5	0.7	1.5	43	-
14d	SLG	1	0.7	1.6	43	-
14e	SLG/Mo	1	0.7	1.3	44.5	7

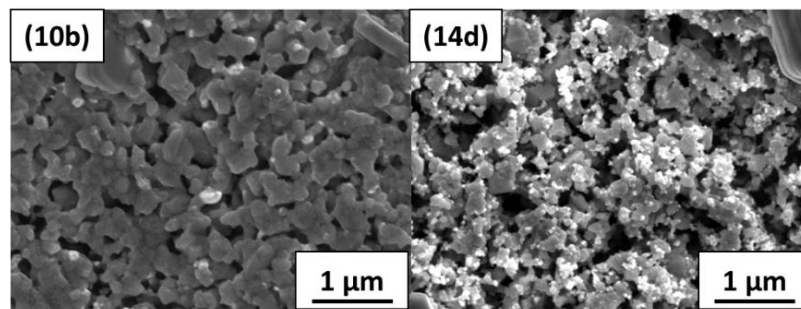


Figure 5-35. The plan-view SEM images shows the morphology of the samples sulphurised (10b) without sulphur in the precursor solution and (14d) with 1g sulphur added in the precursor solution.

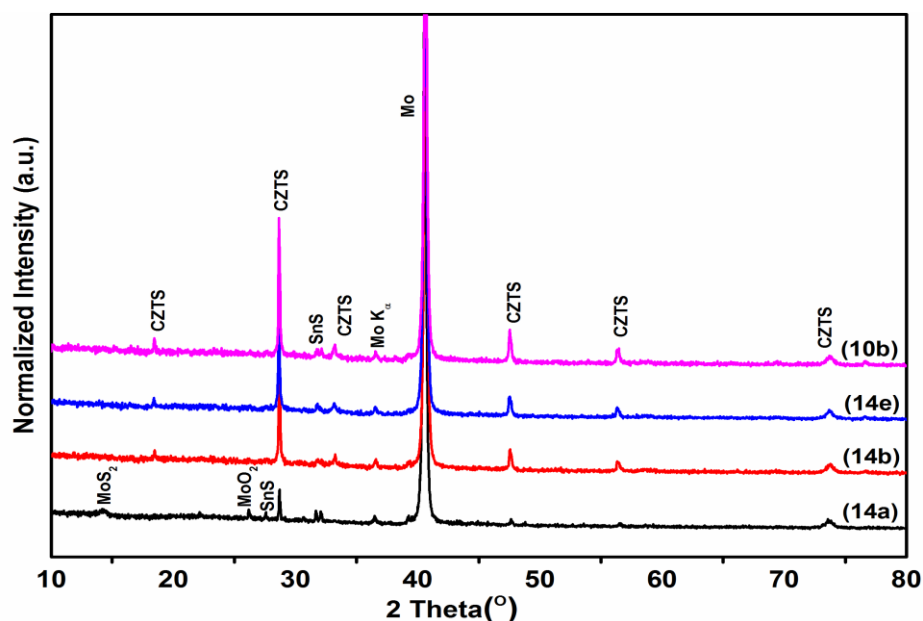


Figure 5-36. The XRD patterns of the sulphurised samples are shown with the precursors containing a mass of sulphur powder. (14a) (14b) (14e) patterns show the samples contained sulphur in precursor solutions and sulphurised with (14a) no excess sulphur during conversion, (14b) 0.5g excess sulphur during conversion, and (14e) 1g excess sulphur during conversion. The results have been compared with sample (10b) which was prepared without adding sulphur in the precursor solution but the use of 1g sulphur powders during the sulphurisation.

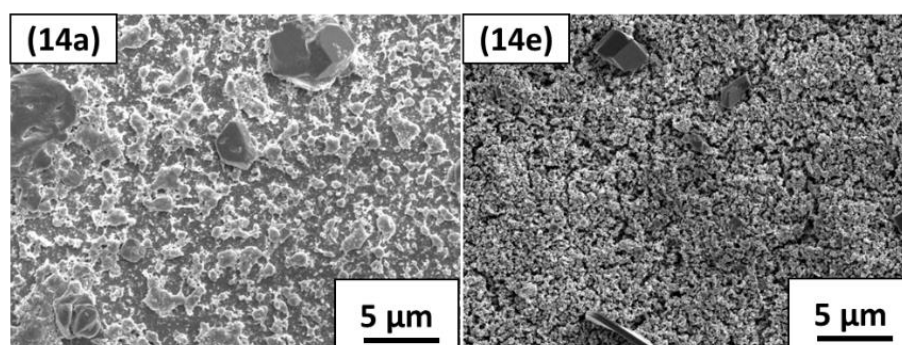


Figure 5-37. The plan-view SEM images of sulphurised sample with precursor including (14a) no sulphur (14e) 1 g sulphur during the conversion.

The results indicate the formation of very fine particle size of the CZTS crystals when the precursor solution contains elemental sulphur powder. This is clearly shown by SEM images (see Figure 5-35). The XRD patterns illustrate the very poor crystalline structure (see Figure 5-36). It is also perceived that if the sulphur only is provided via the precursor

solution and not during the conversion step, a considerable loss of material from the surface will occur (see Figure 5-37 ). This is due to the low partial pressure of sulphur during the conversion. The evaluation of compositional changes using EDX analysis, as shown in Table 5-11, indicates a very Zn-rich and Sn-poor structure for those samples prepared using the precursor solutions that contained of elemental sulphur.

### 5.2.3 CZTSSe thin film fabrication via non-vacuum deposition technique

The study on fabricating the CZTSSe thin films is divided into two sections including (i) pre and post selenisation of as-deposited samples using RTP technique, and (ii) post-selenisation of sulphurised thin films using the tube furnace.

#### Pre and Post selenisation with Rapid Thermal Processing (RTP)

The as-deposited precursors via non-vacuum deposition technique have been pre-selenised with different mass of selenium. The samples were heated at 550°C for 15 min in an atmospheric ambient pressure (ATM) with the ramp rate of 270°C/min for both heating and cooling procedure. The specification of the examined experiments are presented in Table 5-12. The table also illustrates the compositional changes of the converted thin films. The results from the EDX compositional analyses have shown that oxide compounds were reduced by 50% when samples were selenised for 15 min, as it presents in Table 5-12. However, increasing the further reduction of oxide compounds does not occur if the quantity of selenium is increased. Nevertheless, large grains of CZTSSe crystals have been formed and detected by SEM and EDX mapping analyses (see Figure 5-38 and Figure 5-39).

Table 5-12. The table summarises the experiments' specifications and the compositional changes. All selenisation processes mentioned here were performed in RTP system.

Sample	Sulphur and/or Selenisation time	Cu (Zn + Sn)	Zn Sn	S or S+Se (at%)	O (at%)
15a	after spraying and drying	0.7	1	6.37	~35
15b	60 min	0.7	1.3	34.56	~ 4
15c	15 min	0.8	1.3	47.61	~ 6
15d	15 min	0.7	1.3	42.44	~16
15e	15 min	0.7	1.2	45.23	~16
15f	15 min	0.68	1.2	40.31	~19

Sample 15a: The as-deposited precursor

Sample 15b: Sulphurised in tube furnace

Sample 15c: Post-selenisation of sample 15b using RTP technique



Sample 15d, 15e, and 15f: Pre-selenisation of the as-deposited precursors using RTP technique with 0.07g, 0.14g, and 0.28g of mass of selenium, respectively.

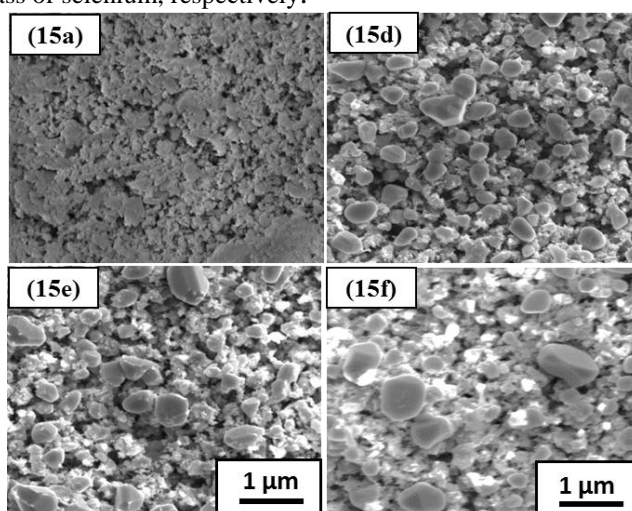


Figure 5-38. The plan-view SEM images shows the microstructure of (15a) as-deposited precursor (15d) selenisation with 0.07g mass of selenium (15e) selenisation with 0.14g mass of selenium (15f) selenisation with 0.28g mass of selenium.

The composition of two different structures that have been appeared through the SEM image of sample 15d have been characterised by EDX analysis with the mode of “Point and ID”. The results are shown in Figure 5-39 and Table 5-13.

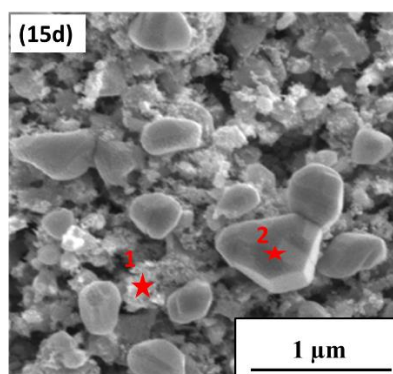


Figure 5-39. The plan-view of SEM image shows the microstructure of sample 15d. The points highlighted in red have been characterised by EDX analysis and the compositional changes of these points are presented in Table 5-13.

Table 5-13. The table indicates the atomic composition of highlighted points in Figure 5-39 using the Point and ID mode of EDX analysis.

Position	Cu (at %)	Zn(at %)	Sn(at %)	S (at %)	Se (at %)	O (at%)
1	10	10.5	15	1.0	39.5	24
2	26.5	12.5	14	0.3	44.2	2.5

## Post-selenisation with tube furnace

For this experiment, the process of conversion consists of three stages: sulphurisation, post sulphurisation, and selenisation with different mass of selenium. This is done with the purpose of providing enough mass of chalcogen to investigate the microstructure of the converted samples and to evaluate the influence of introducing selenium on the morphology and compactness of the final thin films. The details on the specification of the experiments are summarised in Table 5-14. This table also present the compositional changes of the converted thin films. It should be noted that the conversion condition for the post-selenisation (shown with ♣ in Table 5-14) is based on the optimum conditions have been achieved through preliminary study, Chapter 4.

Table 5-14. The compositional changes of sulphurised, post-sulphurised, post-selenised precursors are presented. The samples' specifications are displayed. (a, b, c refers to the samples sulphurised for 40min at a temperature of 570°C with an ambient pressure of 250 mbar H<sub>2</sub>/N<sub>2</sub>). (♠ symbol is used for those samples post-sulphurised for 10 min of heating at 550°C with an ambient pressure of 500 mbar Ar), (♣ symbol is used for those samples that post-sulphurised and then selenised for 15min of heating at a temperature of 500°C with an ambient pressure of 300 mbar Ar).

Sample	Mass of chalcogen	Ambient pressure (mbar)	S (at%)	Se (at%)	$\frac{\text{Zn}}{\text{Sn}}$	$\frac{\text{Cu}}{(\text{Zn} + \text{Sn})}$	$\frac{(\text{Se} + \text{S})}{(\text{Cu} + \text{Zn} + \text{Sn})}$
<b>16a</b>	1g of sulphur	250 H <sub>2</sub> /N <sub>2</sub>	47	0	1.3	0.9	0.9
<b>16a♠</b>	1g of sulphur	500 Ar	46.5	0	1.8	0.8	0.9
<b>16a♣</b>	0.07g of selenium	300 Ar	9.5	39	1.3	0.7	0.9
<b>16b</b>	1g of sulphur	250 H <sub>2</sub> /N <sub>2</sub>	47.5	0	1.2	0.8	0.9
<b>16b♠</b>	1g of sulphur	500 Ar	48.5	0	1.2	0.8	1
<b>16b♣</b>	0.14g of selenium	300 Ar	8	40.5	1.4	0.7	0.9
<b>16c</b>	1g of sulphur	250 H <sub>2</sub> /N <sub>2</sub>	48	0	1.3	0.8	0.9
<b>16c♠</b>	1g of sulphur	500 Ar	49	0	1.1	0.8	1
<b>16c♣</b>	0.28g of selenium	300 Ar	7.5	42	1.3	0.7	1

The results illustrate that increasing the selenium quantity for selenisation process will lead to a grain growth (see Figure 5-40).

The quantity of  $x$  in the  $\text{Cu}_2\text{ZnSn}(\text{S}_{1-x}\text{Se}_x)_4$  thin films can be controlled by varying the mass of selenium and sulphur used during the conversion procedure. When  $x$  changes linearly from 0 to 1, the diffraction angles ( $2\theta$ ) of the main peaks vary from  $27.07^\circ$  to  $28.42^\circ$ . The  $x$  quantity is 0.7, 0.65, and 0.6 for samples selenised with 0.07g, 0.14g, and 0.28g mass of selenium supply, respectively. Figure 5-41 and Figure 5-42 indicate the formation of well-crystallised Kesterite structure in case of post-sulphurisation and post-selenisation. The XRD and SEM analyses indicate the partial substitution of selenium instead of sulphur in SnS crystal structure. This is shown with the formation of  $\text{Sn}(\text{S},\text{Se})_2$  across the CZTSSe thin films (see Figure 5-42). The XRD patterns also exhibit a shift of diffraction angles of the indicative peaks of Kesterite structures towards lower values when large selenium atoms are replaced by smaller sulphur atoms in the crystal lattice structure.

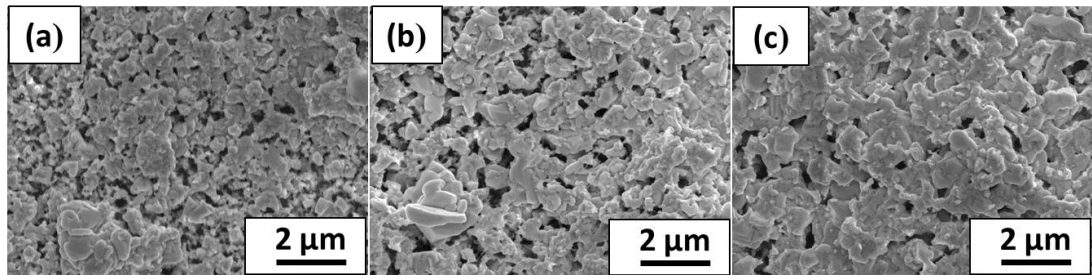


Figure 5-40. The plan-view SEM images shows the morphology of the post-selenised samples with (a) 0.07g mass of selenium, (b) 0.14g mass of selenium, and (c) 0.28g mass of selenium.

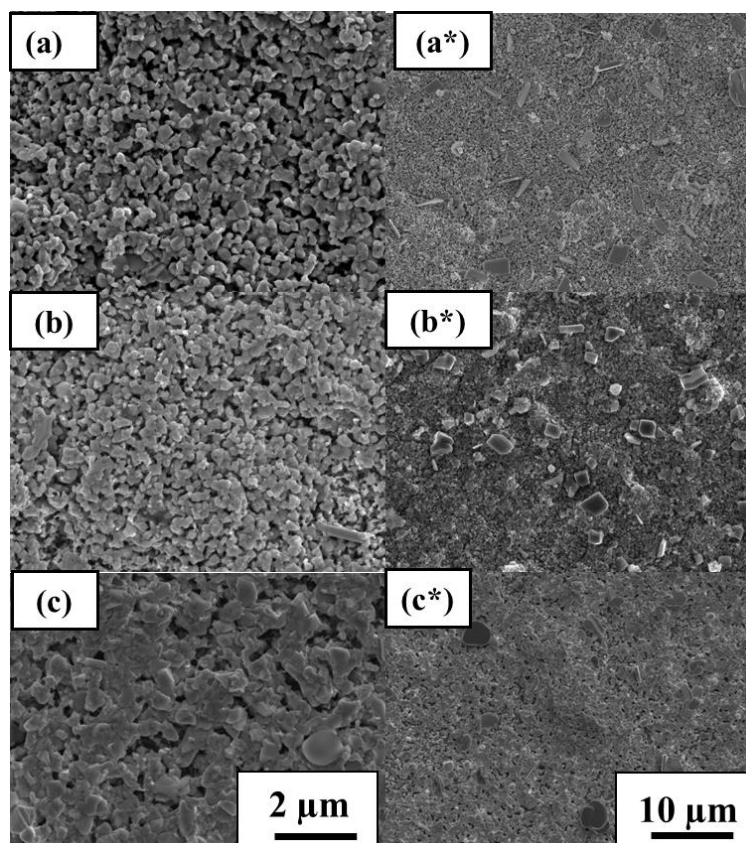


Figure 5-41. The plan-view SEM images shows the microstructure of the sample 16c which is described in Table 5-14, (a) sulphurised, (b) post-sulphurised, and (c) post-sulphur/selenised thin films. The SEM images are presented with two different magnifications of ~5kx and ~20kx presented with and without (\*), respectively.

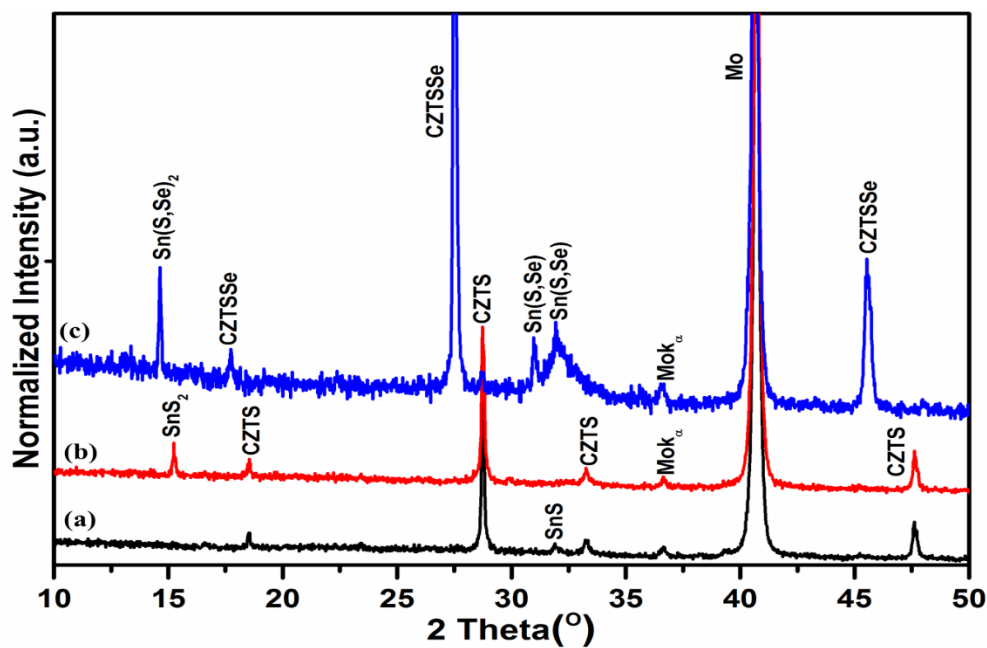


Figure 5-42. The XRD patterns of sample 16c which is described in Table 5-14, (a) sulphurised (b), post-sulphurised, and (c) post sulphur-selenised thin films.

#### 5.2.4 Summary of Results and Discussion

Although the slot-die coated samples were limited in number, the analyses based on the initial trials of these samples have shown promising results, since the samples were more uniform compared to the sprayed ones. Nevertheless, one of the challenges with the slot-die coating technique was the very early evaporation of IPA from precursor solutions. This caused a problem in the floating of precursor solution when it passes through the tube towards the substrates. In order to address this issue, one of the strategies could be the addition of surfactant to the precursor solution so that the precursor solution can be stable for longer time. This experiment has been carried out as a trial study by Dr. Peter Greenwood at University of Swansea and its outcome is presented in Appendix C. More collaboration on developing CZTS thin film with the slot-die technique and substituting it instead of the spraying technique is predicted to enhance the degree of reproducibility. However, this requires more time which was beyond the scope of this research.

As for the use of excess sulphur supply in the precursor solution, the results have shown a very different morphology of final thin films, compared to those samples synthesised with the typical precursor solutions (containing the only  $\text{Cu}_2\text{O}$ ,  $\text{ZnS}$ , and  $\text{SnO}$ ). In the case of using excess quantity of sulphur in precursor solution together with using the sulphur source during the conversion procedure, the SEM images have revealed the formation of very small grains. According to a study published by Bjorkman et al, the formation of small grains can be due to the large number of nuclei, which prevent the grain growth. However, it should be noted that their study was based on a comparison of precursors prepared via sputtering with and without elemental sulphur in the precursor [109]. The reason of such a different morphology might be also due to the complex reaction which may take place when the sulphur melts on the precursor surface having close contact with the precursor components, consequently similar to the use of Se-cap layer. However, the more investigation is required to make a clear verdict on this specific study. Since the precursor composition and processing has a great role in the final quality of converted thin films, this study could be improved by optimising the conversion condition for the particular experiment of using excess sulphur supply in precursor solution.

As it was mentioned before, one of the challenges in the fabrication of CZTS thin film by non-vacuum deposition technique was the formation of porous structures. The study has

shown that a better crystalline structure has been observed across the CZTSSe thin films, compared to the CZTS thin films. This is in agreement with the previous studies [112, 140], where it was explained that partial replacement of sulphur atoms with selenium could lead to the formation of larger crystals and eventually grain growth. The formation of Kesterite with large grain size and consequently less grain boundaries can affect the performance of solar device. This is due to the fact that grain boundaries can increase the rate of charge carrier recombination.

Thus, the selenisation (CZTSSe) shows a considerable grain growth contributing to a more compact structure. However, the use of toxic element of selenium instead of sulphur is a matter of concern when it comes to the consideration of developing the sustainable PV materials.

All the follow-up trials have been carried out in order to evaluate whether the three mentioned parameters can improve the quality of CZTS absorber layers. However, more focus on these investigations are required and that was beyond the time scale of this thesis. Nevertheless, the initial trials here could be a starting point for future investigations.

### **5.3 Conclusion**

The study in this chapter demonstrated the fabrication of CZTS thin film from metal/oxide/sulphide compounds by a low cost non-vacuum deposition technique. In the first part, the influence of different parameters including precursor composition, sulphurisation time, temperature and pressure, heating profile, chalcogen partial pressure, and post-conversion heat treatment have been investigated and presented. A model for the current particular experiment has been suggested based on the results achieved by the analyses and the previous literature.

The samples characterised by IMPS obtained a promising photocurrent response when the sample was exposed to an incident light with an specific wavelength. The EQE measurements also shown an approximate efficiency of 20% and a band gap energy of  $\sim 1.42$  eV by the advantage of Tauc plot. According to the follow-up trials, in spite of the promising results achieved by the use of spraying technique compared to doctor blade, the limited experiments using slot-die technique have resulted to the formation of uniform thin films superseding the spraying technique. In addition, the selenisation of CZTS thin films have shown a considerable grain growth contributing to a compact microstructure.

However, the study on the use of excess sulphur supply in precursor solution needs more investigation and modification of the conversion parameters.

Since the main aim of this study was to fabricate CZTS thin film via non-vacuum deposition technique, there was not enough time to optimise the fabrication of CZTS thin films via vacuum deposition technique and make a comparison between the optimised thin films fabricated by the two techniques. Although the previous literature showed that the precursor and the initial material processing has a great role in synthesising absorber layer, as a trial study, the sulphurisation of precursors processed by vacuum and non-vacuum deposition techniques have been examined and the results are presented in Appendix C.

## **Chapter 6**

# **Sustainability assessment of CZTS thin films as an absorber layer of PV solar device**



## **6 Sustainability assessment of CZTS thin films as an absorber layer of PV solar device**

So far, the focus of the research has been on the fabrication of a good quality CZTS absorber layer which can affect the performance of the PV device. Consequently, it is reasonable for it to be introduced to the PV market. The use of photovoltaic devices are inherently sustainable, unless they are too expensive and/or environmentally unsafe to produce. However, if the PV market would intend to promote a significant contribution to the global energy demand, issues of sustainability and cost will need to be addressed as well as the development of high performance solar devices.

To make an inline study with the experimental evaluations discussed in previous chapters, here in this Chapter, several aspects of environmental issues of PV thin films fabricated from  $\text{Cu}_2\text{ZnSnS}_4$  (CZTS) via vacuum and non-vacuum deposition techniques, will be presented and discussed. The main approach here is based on simulation by means of Life Cycle Assessment (LCA) and the IMPACT 2002+ is used as a framework with the advantage of the SimaPro software.

### **6.1 Introduction**

As mentioned in section 2.2.9, in order to evaluate the sustainability of a system, it is required to study at least three main measurable aspects of cost, resource availability, and environmental impacts. The study in this chapter involves the estimation of mainly environmental impacts. However, the resource availability is also evaluated since this factor is considered as a sub category in IMPACT 2002+ framework. The IMPACT 2002+ will be explained in section 6.2.3.

As mentioned earlier, the study here is conducted using the LCA as an approach to evaluate the environmental impacts of the PV thin films. To do so, the methodology used for the current study is based on the guidelines stated for this purpose (LCA study) in the relevant standards. According to ISO 14040 and ISO 14044, study on LCA can be broken down into four main phases, as mentioned below [163, 216].

- I. Goal and Scope Definition
- II. Life Cycle Inventory Analysis (LCI)
- III. Life Cycle Impact Assessment (LCIA)
- IV. Life Cycle Interpretation

It should be noted that since the LCA approach has been used for the current study, to make the study comprehensible, the structure of this chapter has been organised using the methodology suggested in ISO14040 (through the four phases introduced above).

## **6.2 Experimental design and System description**

The current research presents the definition of the four main phases of LCA, considering the particular study of CZTS thin films processed via vacuum and non-vacuum deposition techniques.

### **6.2.1 Goal and Scope of the study**

According to ISO 14040 (2006a), the goal of an LCA states the intended application and reasons for carrying out the study. The scope includes items such as an introduction of the functional unit of a product system, system boundary, data requirements, assumptions, and limitations. Introducing the functional unit is of great importance since it provides a reference to which the input and outputs are related [163].

In the current study, the goal is to evaluate the environmental impacts of the CZTS absorber layers that are currently being produced at laboratory scale, but may commercially be fabricated in scale-up production in the near future. The focus is to investigate several environmental impacts of using vacuum and non-vacuum deposition techniques to make the CZTS absorber layers. The study gives an overview on manufacturing the PV solar devices using different materials and processes in the future market.

#### **6.2.1.1 Functional Unit**

In PV LCA studies, the functional unit is expressed either in unit area of the solar module or the electricity generation capacity produced within one year. In this study, two functional units are defined including (i) the fabrication of 1m<sup>2</sup> of PV module, and (ii) 1GW electricity generation capacity manufactured per year.

Even though the specific fabrication of CZTS at commercial scale has not yet been realised, the study of LCA by considering 1GW electricity generation capacity per year, as a functional unit, is beneficial. This is because it could necessitate recognising the specifications that are needed to replicate the technology from lab-scale to manufacturing scale. Moreover, it could give an overview of the consequences and impacts of the solar cell fabrication prior to developing the technology in large-scale. The choice of electricity

generation capacity, as a functional unit, would require the consideration of conversion efficiency, as will be clarified in the next paragraph. However, since the databases are usually stated with regard to the production of  $1\text{m}^2$  as a functional unit, in order to compare the CZTS thin films with a reference, the functional unit of  $1\text{m}^2$  of PV module has also been considered. In the current study, CIGS thin film has been used as a reference. This is due to its similarity in the configuration and device structure with CZTS thin films. In the following, the other assumptions are stated.

A value of 15% efficiency was assumed for the fabricated CZTS thin films based on this being close and competitive to the commercialised CIGS PV modules [7]. The irradiation level is assumed to be  $\sim 1700 \text{ kWh/m}^2\cdot\text{year}$  with the performance ratio of 75%, the lifetime of 30 years, and 0.5% output degradation per year [217]. Clearly, the two parameters of life time and the degradation rate are not yet verified for CZTS PV modules, but these presumed values allow some comparison with studies reported from other materials. Moreover, it is important to note that the average European electricity mix (UCTE) was used for all modelling and calculations.

#### 6.2.1.2 System Boundary

The system boundary for this study is limited to only the fabrication process of absorber layer. The other steps in the module production processing are assumed to be equivalent to those for CIGS modules. Figure 6-1 shows the entire process of PV system manufacturing. It should be also noted that this study excludes manufacturing the other components of solar device including the buffer layer, anti-reflection coating, the back and front contact [197, 218, 219].

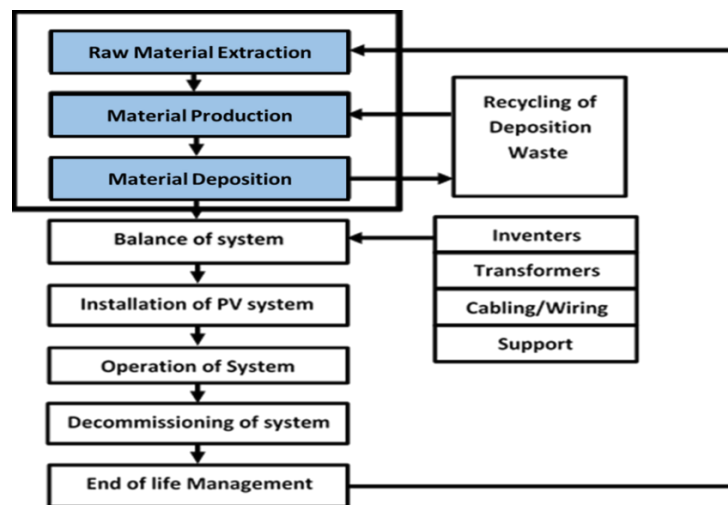


Figure 6-1. The highlighted blue boxes indicate the system boundary in this study.

### **6.2.1.3 Modelling of CZTS via vacuum and non-vacuum deposition technique**

CZTS thin films were fabricated via two main methods in the laboratory at University of Northumbria. The conventional structure of solar cells was shown in Figure 3-1b consisting of a substrate, a back contact, an absorber layer, a buffer layer, a transparent conductive oxide layer, and a front contact.

The first approach was the use of vacuum deposition technique. The details of the processing have been presented in section 3.2.2.1. The second approach was the use of non-vacuum deposition technique. The details of processing have been presented in section 3.2.2.2. It must be remembered that the Slot-Die coating technique has been assumed instead of spraying method. This was due to the availability of Slot-Die coating equipment as a scalable deposition technique.

The time and temperature of the heat treatment for the samples prepared via both vacuum and non-vacuum deposition techniques were estimated to be 30min and 550°C, respectively. The pressure and composition of ambient gas used for the above two processes were different. However, due to the very small contribution of argon and forming gas (ambient gas) that were used for both synthesising processes (compared to the mass of other materials), their effects on environmental impacts have been neglected in this study.

The vacuum co-evaporation deposition technique was considered for CIGS thin film production, which is regarded as a reference in the study. The Copper (Cu), Indium (In), Gallium (Ga), and Selenium (Se) are co-evaporated simultaneously from multiple sources in a single or sequential process. This is followed by the heat treatment at a temperature between 400-600°C. The inline process was designed with stationary sources and substrates moving past the targets (see Figure 6-2) [220]. The environmental impact of CIGS as a reference was modelled using SimaPro software, which will be described in section 6.2.4. The assumptions are provided by the Ecoinvent database according to the LCA study reported by Jungbluth et al 2012 [221].

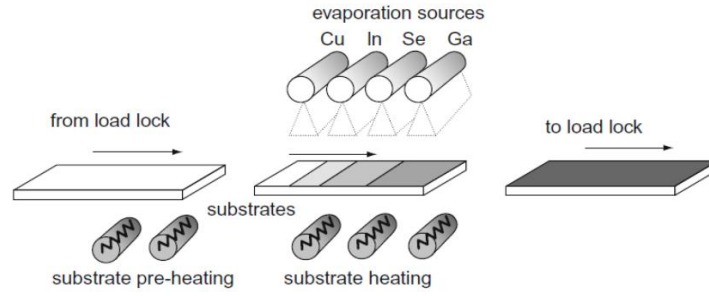


Figure 6-2. The schematic of an inline deposition system for co-evaporation of CIGS absorber layer [220]

Table 6-1. Introducing the fabrication processing of CZTS and CIGS absorber layers with the techniques assumed for the current study

Compound	Substrate	Back Contact	Absorber Layer Material (Process)	Buffer layer	Window layer	Front Contact
CIGS	Glass	Mo coated layer by Sputtering	(i) Copper, Indium, Gallium (ii) Co-evaporation (iii) Sulphurisation using tube furnace	CdS via CBD	Sputtering of ITO	Thermal evaporation of Al
CZTS	Glass	Mo coated layer by Sputtering	(i) Copper, Zinc, Tin (ii) Sputtering (vacuum deposition tech.) (iii) Sulphurisation using tube furnace	CdS via CBD	Sputtering of ITO	Thermal evaporation of Al
CZTS	Glass	Mo coated layer by Sputtering	(i) Cu <sub>2</sub> O, SnO, ZnS, IPA (ii) Mixing/Milling Cu-O, Sn-O, Zn-S using ball milling apparatus (iii) Slot-Die non-vacuum deposition tech.) (iii) Heating on hot plate (iv) Sulphurisation using tube furnace	CdS via CBD	Sputtering of ITO	Thermal evaporation of Al

#### 6.2.1.4 Limitations and assumptions for CZTS modelling

Since CZTS is regarded as a new PV compound, limited data is available relating to its commercial production and the study on this particular PV thin film technology is still restricted to laboratories. Thus, the assumptions presented in this study are mainly based on laboratory investigations, which were then used as a basis to allow simulation of an inline production process. The assumptions were also based on available equipment with the size and capacity that are currently applicable for similar manufacturing such as CIGS

PV cells or other similar devices. This has been estimated with regard to the specifications of the presumed equipment, as it is summarised in Table D1-D4 presented in Appendix D. Once the technology of CZTS PV devices is scaled up from lab to commercial scale, it is expected that equipment manufactured could be more appropriate and efficient in terms of material usage and energy consumption. This in turn can contribute to a reduction in adverse environmental impacts.

The thin films that were fabricated at the University of Northumbria at laboratory scale had an area of  $2.5 \times 5\text{cm}^2$ , for both mentioned techniques, with a thickness of 1 and  $3\mu\text{m}$  for CZTS thin films fabricated via vacuum and non-vacuum deposition techniques, respectively. The deposition efficiency of all used materials for each stage of the manufacturing process is provided in Table 6-2 and Table 6-3. It must be noted that the deposition efficiency is the ratio between the mass of material deposited on the substrates and the mass of material required to make the CZTS thin film [170].

### **6.2.2 Life Cycle Inventory analysis (LCI)**

In the Life Cycle Inventory (LCI) analysis, relevant data on inputs and outputs of a product system are required for conducting the LCA. Inventory analysis involves data collection and calculation procedures [220]. During the process, new data requirements, limitations, or other issues may be discovered to ensure that the goal of the LCA is still met [163]. Inventory analysis is regarded as a time consuming and demanding step of LCA because some data may be publicly available, and some often require to be collected for the particular case being studied. This can be done by contacting companies/industries involved in similar fabrication techniques. If achieving first hand data from industry is impossible, data from databases and previous literature could be used instead. However, the uncertainty in data might be relatively large.

The current study was carried out using the latest available version of the SimaPro software (version 8.2 [222]). The data used for the scale-up manufacturing was estimated based on the availability of equipment in industry, which is currently applicable for similar processes (see table D1 and D3 in Appendix D). To calculate the mass of material required for the fabrication of the absorber layer, the layer volume was measured considering the module area, thickness of absorber layer, density of material, and deposition efficiency. The input data required for each step, such as electricity usage, time consumption for each production step, material usage, and deposition efficiency, were

estimated based on laboratory scale and the specifications of the assumed manufacturing equipment. These data are summarised in Table 6-2 and Table 6-3. According to the specification of the equipment, the total energy consumption used to process the CZTS thin films, via vacuum and non-vacuum deposition techniques in large-scale production, is supposed to be approximately 5.02 E+7 kWh and 4.3 E+5 kWh, respectively. More details on the calculations of these figures and the specifications of the equipment are presented in Appendix D (Table D1-D4).

Table 6-2. The assumptions on material usage during the CZTS thin film processing using vacuum deposition technique are presented. Part A considers the material requirements for 1GW production per annum, whilst Part B provides the requirements for 1m<sup>2</sup> of absorber layer.

material usage	Part A. To produce 1GW electricity per year				Part B. To Produce 1 m <sup>2</sup> of PV panel			
	Considering a thickness of 1 μm							
	Require (ton)	Consume (ton)	Waste (ton)	Dep. efficiency (%)	Require (g)	Consume (g)	Waste (g)	Dep. efficiency (%)
	30.66 ton CZTS is required to produce the thin film				4.6 g CZTS is required to produce the thin film			
Copper target	7.3	9.2	1.9	80	1.1	1.38	0.28	80
Zinc target	5.8	7.25	1.45	80	0.87	1.09	0.22	80
Tin target	8.8	11.06	2.26	80	1.33	1.66	0.33	80
Sulphur	8.7	1733	1724	0.5	1.3	260	258.7	0.5
Water	0	4795	4795	0	0	720	720	0

Table 6-3. The assumptions on material usage during the CZTS thin film processing using non-vacuum deposition technique is shown. Part A considers the material requirements for 1GW production per annum, whilst Part B provides the requirements for 1m<sup>2</sup> of absorber layer.

Material usage	Part A. To produce 1GW electricity per year				Part B. To Produce 1 m <sup>2</sup> of PV panel			
	Considering a thickness of 3 μm							
	Require (ton)	Consume (ton)	Waste (ton)	Dep. efficiency (%)	Require (g)	Consume (g)	Waste (g)	Dep. efficiency (%)
	92 ton CZTS is required to produce the thin film				13.8 g CZTS is required to produce the thin film			
Cu <sub>2</sub> O	24.64	27.92	3.28	90	3.7	4.2	0.5	90
ZnS	26.64	29.97	3.33	90	4	4.5	0.5	90
SnO	29.97	37.3	7.33	90	4.5	5.6	1.1	90
S	26.64	5328	5301	0.5	4	800	796	0.5
IPA	0	303.3	303.3	0	0	45.3	45.3	0

As mentioned earlier, the database usually contains many products and processes, but not all that are required. In this study, all the data have been found from the database except the one for tin (II) oxide. Thus, due to the lack of data for this specific component, the LCI data of tin (II) oxide were simplified by using the category “chemical inorganic” as it was used elsewhere [223].

As for the waste created through the processing, the unused metals (targets) remaining after the use of vacuum deposition techniques are expected to be recycled and reused for further applications. However, emissions and waste streams associated with deposition were simulated as being released to different mediums during the production stages. The volatile organic compounds to be emitted into air and solid wastes from deposition are supposed to be emitted into ground. Solid wastes in the solution-based methods, which may form during the non-vacuum deposition processing, are assumed to be released in ground. These assumptions have been considered based on similar studies that were carried out by Collier et al [170]. It should be noted that at large-scale production, it might



be possible to recycle some of these wastes and prevent emissions with an economically feasible policy or approach, which would reduce the impacts below those calculated.

### 6.2.3 Life Cycle Impact Assessment (LCIA)

The LCIA provides information for the life cycle interpretation stage [163]. To do so, it is important to introduce the framework and the software that were used for the current study.

 The IMPACT 2002+

IMPACT 2002+ is an impact assessment framework, which is originally developed at the Swiss Federal Institute of Technology. According to this framework, the environmental impacts are divided into 14 midpoint categories (see Figure 6-3), which all link to four endpoint damage categories consisting of Human Health, Ecosystem Quality, Climate Change, and Resources. Figure 6-3 shows the overall scheme of the IMPACT 2002+ framework [224].

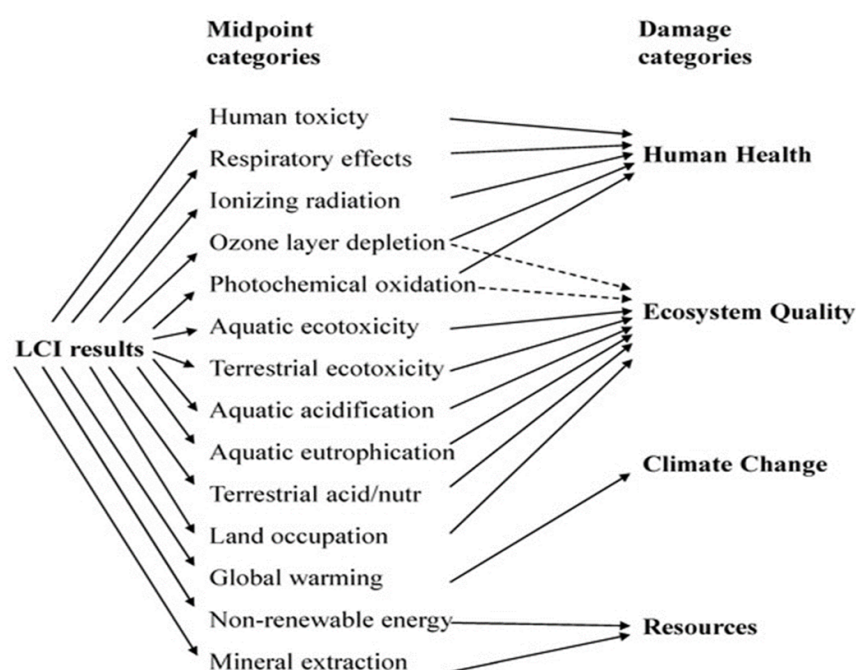


Figure 6-3. Overall scheme of the IMPACT 2002+ framework, linking the 14 midpoints of environmental impacts to the four main damage categories [224]

The definition of all 14 midpoints are summarised in the following, according to the User Guide published by ‘Swiss Federal Institute of Technology Lausanne’ on ‘IMPACT 2002+’ (see Table 7-4) [223-225].

- Human toxicity (carcinogenic and non-carcinogenic effects), respiratory effects (inorganic and organics), ionization radiation, and ozone layer depletion all contribute to “Human Health” damages. All above factors are expressed in “DALY/kg of emissions”. Human health impact is expressed in “DALYs” (Disability-Adjusted Life Years) which is sum of the years of life lost (YLL) and the years lost due to disability (YLD). Human toxicity is considered as two separate categories of carcinogenic and non-carcinogenic effects, which are related to the chemicals that may increase the risk of cancer and non-cancer diseases, respectively. The chronic toxicological effects on human health are expressed in “kg chloroethylene into air-eq”.
- The respiratory effect is expressed in “kg PM 2.5 into air-eq/kg”. Particle Matter (PM) 2.5 is defined as any particle smaller than 2.5  $\mu\text{m}$  in diameter, which is emitted from various sources into the air. This could be linked to serious health problems including heart, lung diseases, and premature deaths. It can also affect people from regions far from the source, since the particles can be transported in the air for long distances.
- Ionization radiation is expressed in “Bq Carbon-14 into air-eq”. The Becquerel (Bq) is a unit for the definition of the level of radioactivity. One Becquerel is defined as the quantity of decayed nuclei per second due to the radioactive material. The Bq is equivalent to  $\text{s}^{-1}$ .
- Ozone layer depletion is expressed in “CFC-11 into air-eq” (an organic compound that contains carbon, chlorine, and fluorine) emissions into air only, since it is assumed that these pollutants are barely emitted into soil or water.
- The photochemical oxidation refers to the formation of chemical compounds from certain air pollutants when they are exposed to sunlight. These pollutants can create breathing problems, eye irritation, and damage to crops as well as human health. Ozone ( $\text{O}_3$ ) is one of the examples of these compounds which is formed through the photochemical reactions. The Unit to evaluate the photochemical oxidation impact is considered as being approximately equivalent as “kg Ethylene into air-eq”.
- The “Ecosystem Quality” damage category is the sum of the midpoint categories including “Aquatic eco-toxicity”, “Terrestrial eco-toxicity”, “Aquatic acidification”, “Aquatic eutrophication”, and “Land occupation”. Ecosystem

quality impact is expressed in “PDF.m<sup>2</sup>.y”. This means the potentially disappeared fraction of species per 1m<sup>2</sup> of land within a year.

- The eco-toxicity refers to the impact of toxic substances emitted to terrestrial or aquatic ecosystems. The terrestrial ecosystems refer to the environments such as grasslands, forests, or deserts. The aquatic environment refers to freshwater, lakes, rivers, ocean, and sea.
- Acidification is mainly caused by the emission of sulphur dioxide (SO<sub>2</sub>) into the environment. The effect of acidification is expressed in “kg SO<sub>2</sub> into air-eq”.
- Eutrophication or excess nutrients (nitrification) in aquatic and terrestrial environment can be caused by an excess of nitrogen, phosphorus, and biodegradable organic matter. The aquatic ecosystems that are enriched with nutrients would induce the growth of plankton algae and higher aquatic plants that deteriorate water quality due to the depletion of oxygen. This in turn could contribute to the death of organisms living in water. The reference substance for the assessment of the eutrophication potential for each emission is expressed in “Kg (PO<sub>4</sub>)<sup>3-</sup> into water-eq” [224, 226].
- The land occupation refers to the use of land area for specific human-controlled purposes such as agriculture, forestry, or buildings. The land occupation is expressed in “m<sup>2</sup> organic arable land-eq.y”. It should be noted that the thin film solar panels can be installed and used on different areas such as rooftops, windows, buildings, desert lands, etc. Since in this particular thesis, the deployment phase is excluded, the impacts induced by land occupation are not regarded as a concern and are not included.
- Global Warming is linked to the environmental category of climate change. This is caused by greenhouse gas emissions, such as carbon dioxide and methane, which increases the heat radiation absorption of the atmosphere, contributing to the earth’s surface temperature rising. This factor is associated with only emissions into the air. The result of such a phenomenon might involve a change in climate pattern. The impact of an emitted gas is expressed in Global Warming Potential (GWP) in “kg CO<sub>2</sub> into air-eq”.

As for the units which are mentioned in Table 7-4, it should be noted that the kg equivalence of a reference substance indicates the amount of a reference material

that is equal to the impact of the considered pollutant (e.g. the GWP of fossil based methane is 27.75 times higher than CO<sub>2</sub>, thus its impact is defined as 27.75 kg CO<sub>2</sub>-eq).

- Non-renewable energy consumption refers to the total primary energy required for production, use, and disposal processes per kg unit of extracted or processed material. All energy resources that can be found in nature, such as coal, crude oil, and natural gas are called primary energy resources. This indicator could be an interesting parameter, especially for the current study. The reason being, it shows the quantity of non-renewable energy consumed for the processing of a solar device, which is supposed to reduce the dependency on non-renewable sources of energy to produce electricity!
- Mineral extraction is expressed as the energy needed in Mega Joule (MJ) per kg extracted of minerals and fossil fuels. This indicator refers to the resource availability for current and future generations, who may need to put greater investment and effort in extracting/mining the remaining resources.

Table 6-4. Characterisation factors, references substrates, and damage units according to IMPACT 2002+ framework [224]

Midpoint category	Midpoint reference Substrates	Damage category	Damage Unit
<b>Human toxicity (Carcinogens + non carcinogens)</b>	kg Chloroethylene into air-eq	Human Health	DALY
<b>Respiratory effects</b>	kg PM2.5 into air -eq	Human Health	DALY
<b>Ionization radiation</b>	Bq Carbon-14 into air-eq	Human Health	DALY
<b>Ozone Layer Depletion</b>	kg CFC-11 into air-eq	Human Health	DALY
<b>Photochemical oxidation (=Respiratory organic human health)</b>	kg Ethylene into air-eq	Human Health, Ecosystem Quality	DALY n/a
<b>Aquatic eco-toxicity</b>	kg Triethylene glycol into water -eq	Ecosystem Quality	PDF.m <sup>2</sup> .y
<b>Terrestrial eco-toxicity</b>	kg Triethylene glycol into soil-eq	Ecosystem Quality	PDF.m <sup>2</sup> .y
<b>Terrestrial acidification</b>	kg SO <sub>2</sub> into air-eq	Ecosystem Quality	PDF.m <sup>2</sup> .y
<b>Aquatic acidification</b>	kg SO <sub>2</sub> into water-eq	Ecosystem Quality	PDF.m <sup>2</sup> .y
<b>Aquatic eutrophication</b>	kg (PO <sub>4</sub> ) <sup>3-</sup> into water -eq	Ecosystem Quality	PDF.m <sup>2</sup> .y
<b>Land occupation</b>	m <sup>2</sup> Organic arable land.eq.y	Ecosystem Quality	PDF.m <sup>2</sup> .y
<b>Global warming</b>	kg CO <sub>2</sub> into air-eq	Climate change	Kg CO <sub>2</sub> into air-eq
<b>Non-renewable energy</b>	MJ or kg Crude oil-eq	Resources	Primary MJ
<b>Mineral extraction</b>	MJ or kg Iron-eq (in ore)	Resources	Surplus MJ

#### SimaPro Software/Databases

SimaPro is a tool which is often used for quantifying the environmental performance of products. This software is produced by the Dutch company Pré Consultants. SimaPro software has a 25-year reputation in industry and academia in more than 80 countries worldwide [222].

#### **6.2.4 Life Cycle Interpretation**

The interpretation phase is the last step of the LCA study and involves the iterative process of reviewing and revising the scope of LCA [163]. At this stage, the influence of using different processes and emissions should be investigated and discussed. Since this step has similar concepts to the results and discussion of the current chapter, the LCI will be explained in more detail in section 6.3.

### **6.3 Results and Discussion**

As discussed earlier, the study was divided into two sections. Part (i) will describe the environmental impacts considering only the material input, and Part (ii) will present the analysis extending to include the energy input to the processing.

#### **6.3.1 Part (i). The environmental impacts of fabricating CZTS thin films considering only material input**

In this section, a comparison of environmental impacts derived from CZTS thin films (prepared via vacuum and non-vacuum techniques) and CIGS absorber layers (as a reference) is presented, considering only the materials input to the layer. This analysis was carried out due to the fact that it demonstrates the generic potential of CZTS as a sustainable material, without the influence of the processing assumptions.

Figure 6-4 shows the comparative influences of CZTS fabrication via two approaches and the reference material of CIGS. The results indicate that the CIGS processing has a larger impact in almost all environmental aspects. However, in terms of the organic emissions and the energy requirement for mineral extraction, the risk is much higher in the cases of preparing CZTS thin films via the non-vacuum and vacuum deposition technique, respectively. The adverse effect of respiratory emissions (organic emissions) may result from the use of IPA during non-vacuum deposition technique. According to the safety data sheet of IPA, this product may cause transient irritation to the respiratory system. Moreover, inhalation of a high vapour concentration of IPA may cause central nervous

system depression [139]. Since IPA can produce carbon oxides when exposed to heat treatment, there is also an expectation that the use of IPA contributes to have an adverse effect on GWP (see Figure 6-6). The results observed showed that the vacuum processing of CZTS has a lower impact in almost all categories than the non-vacuum processing, except for the mineral extraction indicator. This happens when the study is only based on the material usage and the effect of energy consumption is excluded. The four endpoint environmental damages for the CZTS processed via vacuum and non-vacuum together with CIGS are presented in Table 6-5. The figures that highlighted in yellow in all tables presented in this chapter are indicating the item that has the higher adverse environmental impact in each category. Figure 6-5 to Figure 6-7 show the assessment of each material input individually for the fabrication of CZTS and CIGS absorber layer.

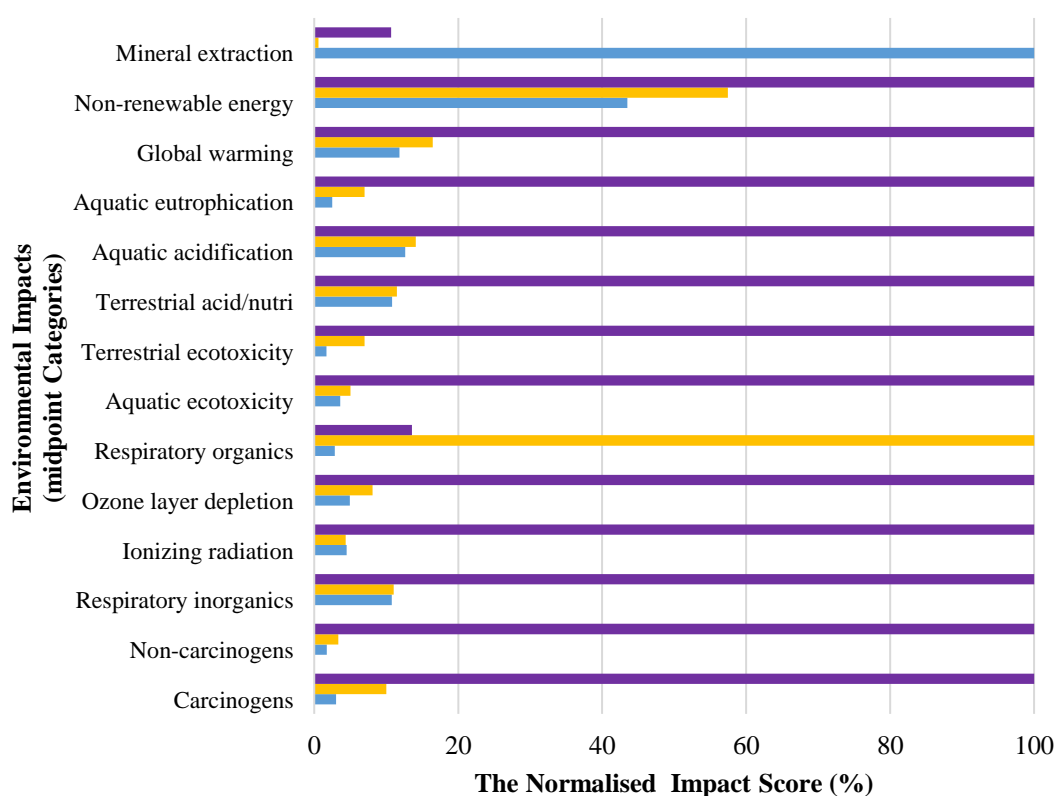


Figure 6-4. The environmental damages (the 14 midpoint categories) of the material usage of CZTS, via vacuum and non-vacuum deposition techniques, considering CIGS as a reference, with a functional unit of  $1\text{m}^2$  of absorber layer is shown. The bar charts for CZTS fabrication via vacuum has been displayed in blue, CZTS fabrication via non-vacuum is presented in orange, and CIGS fabrication via co-evaporation is illustrated in purple.

Table 6-5. The four endpoint environmental damages of material usage of the CZTS absorber layer prepared via vacuum and non-vacuum deposition techniques, considering CIGS as a reference and the assumption of 1m<sup>2</sup> production facility is presented.

Damage category (unit)	CZTS thin films fabricated via vacuum deposition processing	CZTS thin films fabricated via non- vacuum deposition processing	CIGS thin films fabricated via co- evaporation processing
Human health (DALY)	1.86 E-07	3.64 E-07	3.49 E-06
Ecosystem quality (PDF.m <sup>2</sup> .y)	1.07 E-01	4.33 E-01	6.17 E+00
Climate change (kg CO <sub>2</sub> eq)	1.66 E-01	5.19 E-01	3.04 E+00
Resources (MJ)	1.01 E+01	2.9 E+01	4.84 E+01

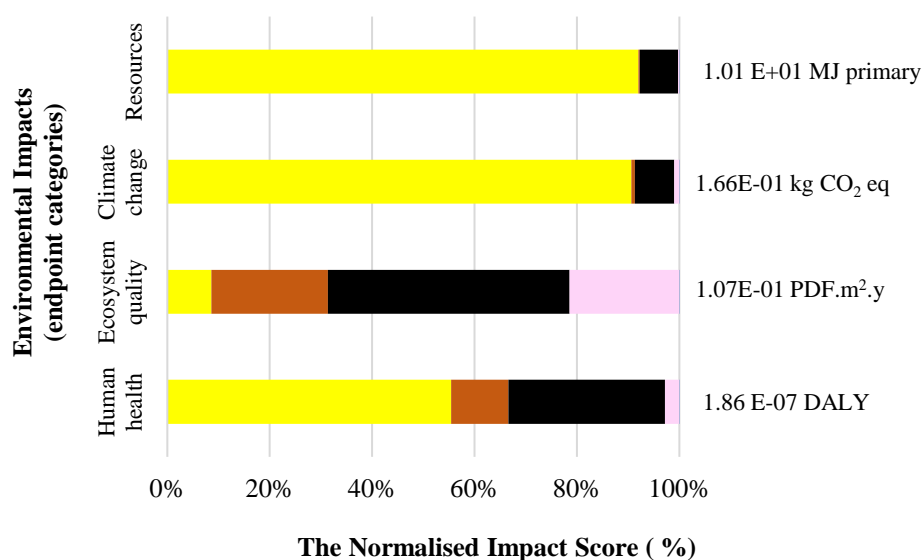


Figure 6-5. The environmental impacts of material usage for 1m<sup>2</sup> of CZTS fabrication via the vacuum deposition technique is displayed (copper in brown, zinc in pink, tin in black, and sulphur in yellow). There is also a small contribution from consumed water (required for cooling and processing), which is not large enough to be visible in the figure. The total quantity of each category is presented on the right hand side of the bar chart.



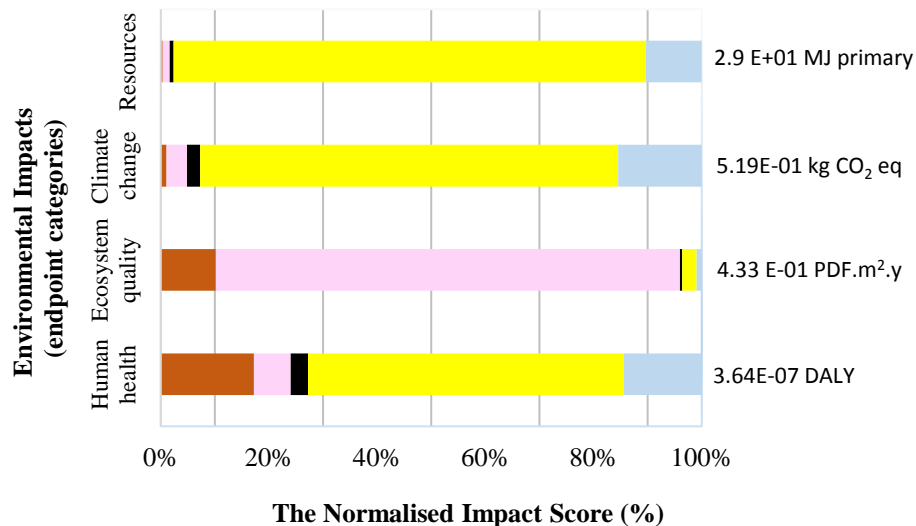


Figure 6-6. The environmental impacts of material usage that is used for 1m<sup>2</sup> of CZTS fabrication via non-vacuum deposition technique are demonstrated (copper oxide in brown, zinc sulphide in pink, tin oxide in black, sulphur in yellow, and IPA in light blue). The total quantity of each category is presented on the right hand side of the bar chart.

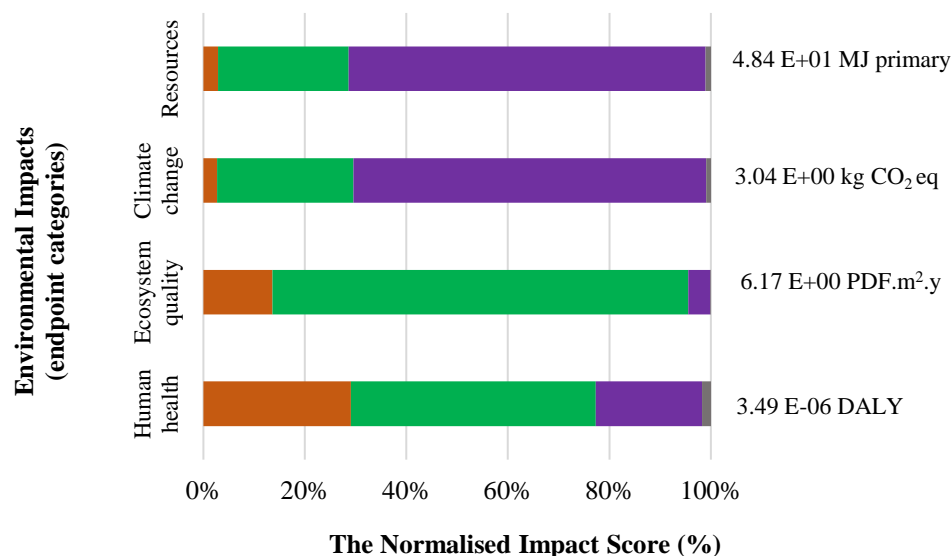


Figure 6-7. The environmental impacts of material usage for 1m<sup>2</sup> of CIGS fabrication (copper in brown, gallium in purple, indium in green, and selenium in grey) are illustrated. The total quantity of each category is presented on the right hand side of the bar chart.

The results show that in case of preparing CZTS via both vacuum and non-vacuum deposition technique, there is a large contribution from the use of sulphur, for all impacts except eco-system quality. These consequences can be resulted due to the assumption of a low sulphur deposition efficiency (approximately 0.5%), consequently the use of large quantity of sulphur for processing. It also can be resulted due to the lack of treatment of the waste sulphur. This deposition efficiency is assumed based on laboratory scale analysis (which was optimised in Chapter 5) and the calculations have been done based on the capacity of assumed equipment, as stated in Table 6-2 and 6-3, and Appendix D. It is expected that a suitable design for extraction and recycling process would reduce adverse environmental impacts. If the CZTS thin films are fabricated via non-vacuum processing, the disposal of zinc sulphide to the ground is a point deserving attention, since it significantly affects ecosystem quality (see Figure 6-6). The considerable adverse influence of copper and tin can be related to the mainly extraction and using procedures that contributes to a considerable environmental toxicity, as it is also reported in previous literature [169].

The results achieved by the analysis of CIGS absorber layer have illustrated that the use of gallium and indium has an adverse effect for all endpoint environmental damages (see Figure 6-7). The results achieved here are consistent with the data stated by Celik et al [169], as they also reported that the toxicity of gallium and indium is much higher than the toxicity of copper and tin. Although selenium is a toxic element, its effect on environmental damages seems to be less significant than that for gallium and indium. This is due to the less toxicity of selenium compared to gallium and indium during the extraction and using procedure, as it is mentioned in previous literature [169]. It also might be due to the use of selenium targets for the CIGS fabrication processing rather than the use of selenium powders or pellets (see Figure 6-7). In fact, the selenium target would be expected to produce less waste and the unused part of the target can be recycled. A comparison between the use of vacuum and non-vacuum techniques in the fabrication of CZTS thin film has been shown in Figure 6-8.

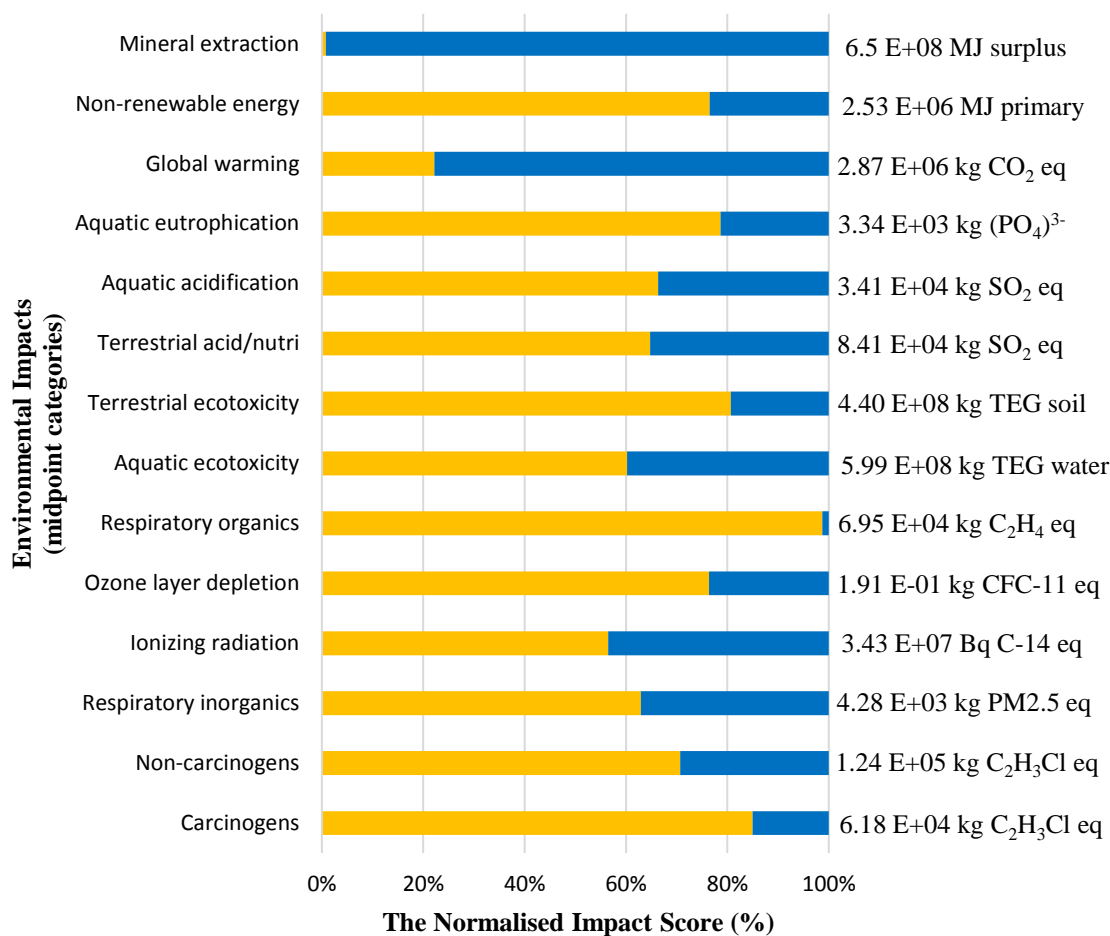


Figure 6-8. The environmental damages (the 14 midpoint categories) of material usage of CZTS thin film via vacuum (in blue) and non-vacuum deposition technique (in orange), with the functional unit of 1GW electricity generation per year is displayed. The total quantity of each category is presented on the right hand side of the bar chart.

When the quantity is increased from the production of small scale (1m<sup>2</sup> of PV modules) to large-scale (1GW electricity production per year), the endpoint environmental impacts of CZTS fabrication via non-vacuum processing are higher for all of the midpoint environmental categories with the exception of the mineral extraction and global warming indicators (see Figure 6-8). As can be seen in Figure 6-8, the adverse effect of using non-vacuum deposition technique on respiratory organics is still a matter of concern, as it was in the fabrication of small-scale production of CZTS thin films. Table 6-6 shows the influence of manufacturing CZTS thin films via vacuum and non-vacuum deposition technique on the four environmental impacts (endpoints) for large-scale production.

Table 6-6. The environmental damages (the endpoint categories) of material usage in the fabrication of CZTS thin film via vacuum and non-vacuum deposition techniques, with the functional unit of 1GW electricity generation per year is exhibited.

Damage Category (unit)	CZTS thin films fabricated via vacuum deposition technique	CZTS thin films fabricated via non- vacuum deposition technique
Human health (DALY)	1.2	2.4
Ecosystem quality (PDF.m <sup>2</sup> .y)	7.1 E+05	2.8 E+06
Climate change (kg CO <sub>2</sub> eq)	2.1 E+06	6.7 E+05
Resources (MJ)	6.3 E+08	1.5 E+07

The results of this section, as discussed earlier, show the importance of considering the use of material selection for non-vacuum deposition processing in order to reduce the environmental impacts, if this approach is going to substitute the expensive method of vacuum deposition technique. In the next section, the study is expanded to the consideration of both material and energy usage for the fabrication processing of the absorber layer.

### 6.3.2 Part (ii): The environmental impacts of fabricating CZTS thin films, considering material input and energy consumption

The comparison of the derived impacts of CZTS and CIGS processes for the fabrication of 1m<sup>2</sup> of absorber layer has been shown in Figure 6-9. The results indicate that the influence of the CIGS thin film fabrication on all environmental impacts (midpoint categories), for small-scale production (1m<sup>2</sup> of absorber layer), has higher quantities compared to the other two techniques, with the exception of respiratory organics indicator (see Figure 6-9).

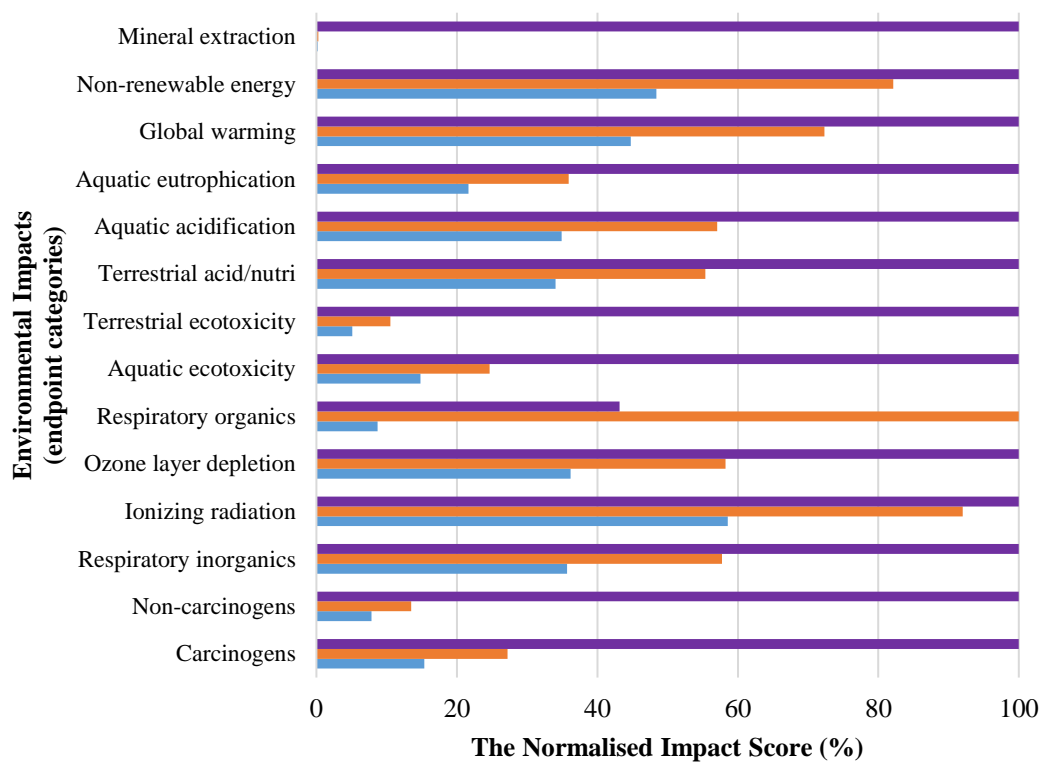


Figure 6-9. The environmental damages (the 14 midpoint categories) of material usage and energy consumption of CZTS thin films fabricated via vacuum (in blue), via non-vacuum deposition technique (in orange), considering CIGS as a reference (in purple) is displayed. The functional unit is  $1\text{m}^2$  of PV module.

Noting that the scale of the production assumed for CIGS in the Ecoinvent database is not clearly stated for large-scale production, here, the results are presented per kWh of output from the PV module (considering 75% performance ratio, 0.5% degradation per year, and lifetime equal to 30 years for the device (absorber layers)) (see Figure 6-10). Analyses have also been done, comparing only the vacuum and non-vacuum deposition techniques for the fabrication of CZTS thin film (see Figure 6-11).

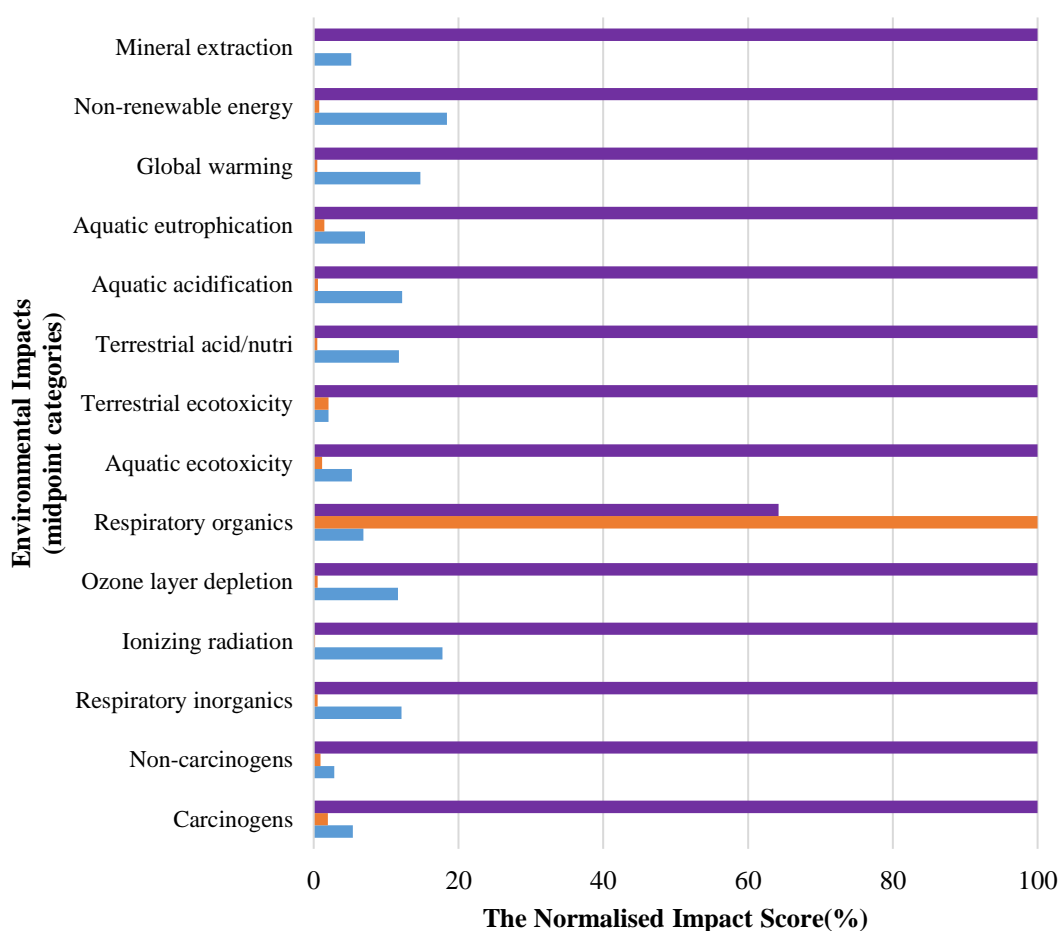


Figure 6-10. The environmental damages of material usage and energy consumption of the CZTS absorber layer via vacuum (in blue) and non-vacuum deposition techniques (in orange), considering CIGS thin film fabrication as a reference (in purple) is shown, with the functional unit of 1GW per annum production facility.

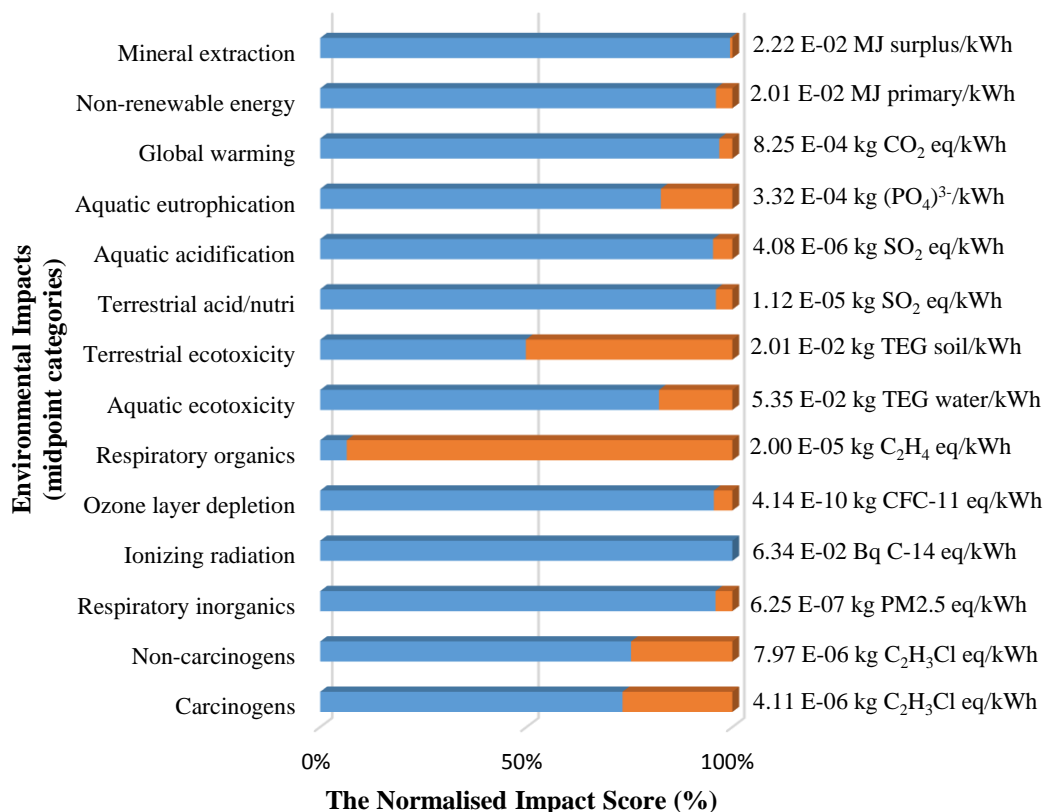


Figure 6-11. The environmental damages (the 14 midpoint categories) of material usage and energy consumption of CZTS via vacuum (in blue) and non-vacuum deposition techniques (in orange) is displayed. The fictional unit of 1GW electricity generation per year is considered. The total quantity of each category is presented on the right hand side of the bar chart.

As can be seen in Figure 6-9 and Figure 6-10 , the non-vacuum processing for small-scale production shows more adverse environmental impacts for almost all the indicators (midpoint categories), compared to the vacuum processing. However, when the production scale is increased to large-scale, except for the influence from the organic compounds creating respiratory problems, the rest of the impacts are considerably higher for the fabrication of CZTS thin films prepared via vacuum deposition technique compared to the non-vacuum deposition technique. The relatively high quantity of respiratory effect during the fabrication of CZTS thin films via the non-vacuum

deposition technique, results from the use of IPA during the process, as discussed before (see Figure 6-11).

Figure 6-12 and Figure 6-13 show the environmental impacts of each initial feedstock for the manufacturing process of CZTS thin films via vacuum and non-vacuum deposition techniques, respectively. The bar charts clearly indicate the considerable influence of high energy required for the vacuum processing technique on the environmental impacts. As for the influence of materials in the non-vacuum processing, the more critical ones for the environment could be the IPA for nearly all environmental issues, and the zinc sulphide for eco-toxicity, since zinc sulphide waste is supposed to be inserted into the ground. Furthermore, copper oxide seems to contribute human toxicity, as well. Moreover, Figure 6-12 shows the restriction of tin extraction for current and future generations. This might be due to limited number of mines and the difficulties in reduction of tin from its ores, which is mainly Cassiterite ( $\text{SnO}_2$ ). The other available ores are complex sulphides such as Stannite ( $\text{Cu}_2\text{FeSnS}_4$ ), Teallite ( $\text{PbSnS}_2$ ), Canfieldite ( $\text{Ag}_8\text{SnS}_6$ ), and Cylinderite ( $\text{PbSn}_4\text{FeSb}_2\text{S}_{14}$ ). The results here cause concern for the deficiency of tin resources and the high amount of energy required for mining tin when those resources become scarce. According to the tin recovery process, the reduction of  $\text{SnO}_2$  is performed using carbon and heat treatment in a furnace up to a temperature of  $\sim 1371^\circ\text{C}$  [227, 228]. Consequently, due to the above issues, a considerable quantity of the mineral extraction indicator is expected (see Figure 6-12).



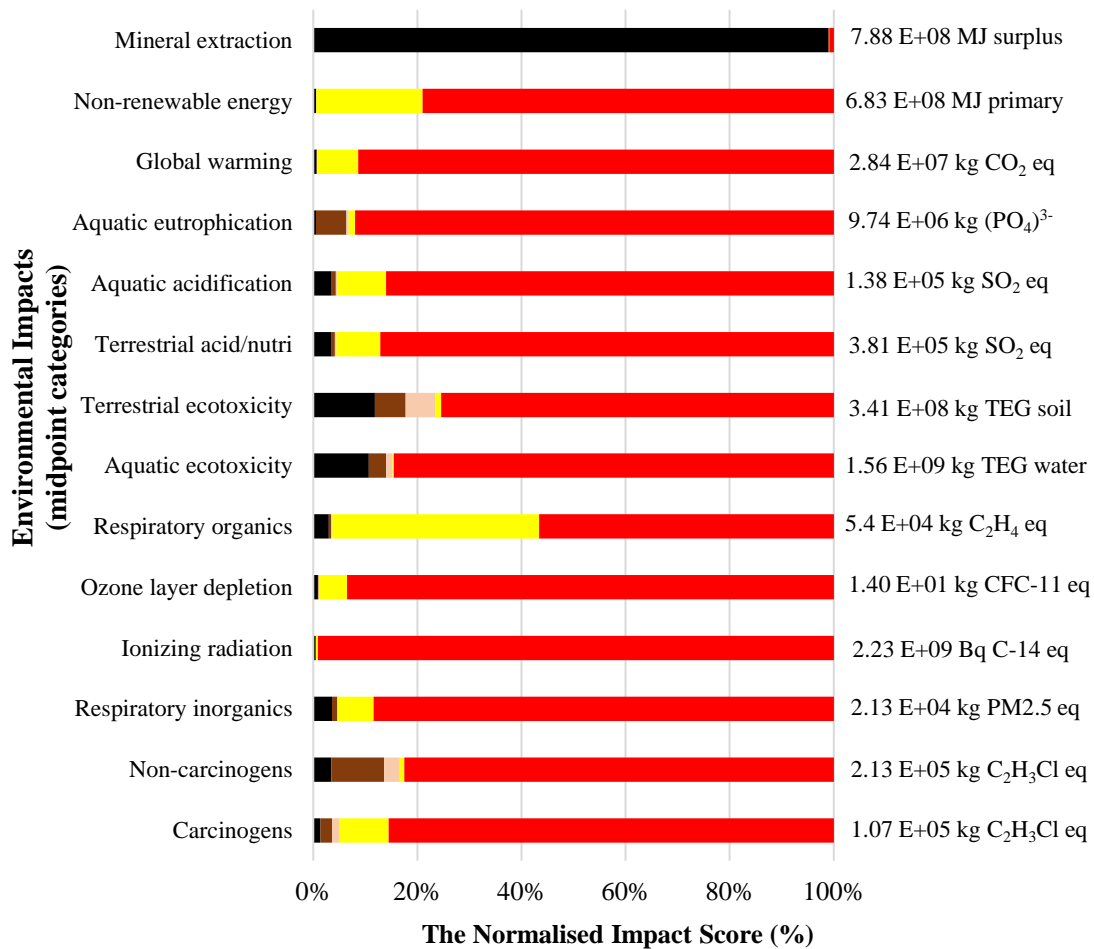


Figure 6-12. The environmental damages (the 14 midpoint categories) of material usage and energy consumption of CZTS thin films fabricated via vacuum deposition techniques, with the functional unit of 1GW electricity generation for one year is shown (copper in brown, tin in black, zinc in pink, sulphur in yellow, electricity consumption in red). The total quantity of each category is presented on the right hand side of the bar chart.

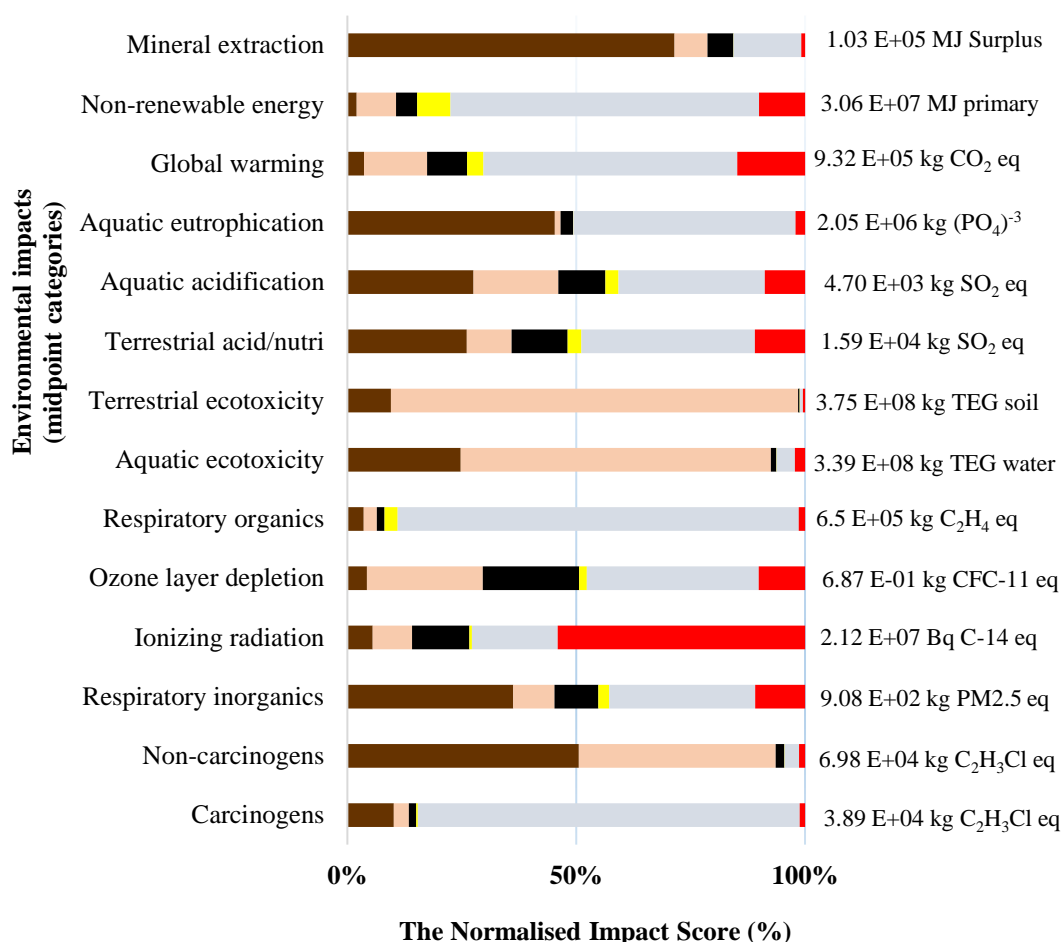


Figure 6-13. The environmental damages (the 14 midpoint categories) of material usage and energy consumption of CZTS thin films fabricated via non-vacuum deposition techniques, with the functional unit of 1GW electricity generation for one year is displayed. The different feedstocks are illustrated in different colours (copper oxide in brown, tin oxide in black, zinc sulphide in pink, sulphur in yellow, IPA in light blue, and electricity in red). The total quantity of each category is offered in the right hand side of the bar chart.

The results shown in Table 6-7 and Figure 6-14 illustrate that CZTS thin films exhibit a significant potential benefit over CIGS. This result shows that, although the material used for non-vacuum deposition technique could have adverse impacts on human health and ecosystem quality, the high quantity of energy consumed for vacuum processing seems to have a considerable adverse effect on the environment which needs to be taken into account.

Table 6-7. The environmental damages of energy and material usage of the CZTS absorber layer via vacuum and non-vacuum deposition techniques, considering CIGS as a reference, for an assumed 1GW per annum production facility

Impact category	CZTS thin films via vacuum deposition technique	CZTS thin film fabricated via non-vacuum deposition technique	CIGS thin film fabricated via co-evaporation technique
Human health (DALY/kWh)	4.57 E-10	3.05 E-11	3.91E-09
Ecosystem quality (PDF.m <sup>2</sup> .y/kWh)	9.42 E-05	8.07 E-05	3.71E-03
Climate change (kg CO <sub>2</sub> eq/kWh)	7.97 E-04	2.62 E-05	5.29E-03
Resources (MJ/kWh)	4.1 E-02	8.7 E-04	1.02E-01

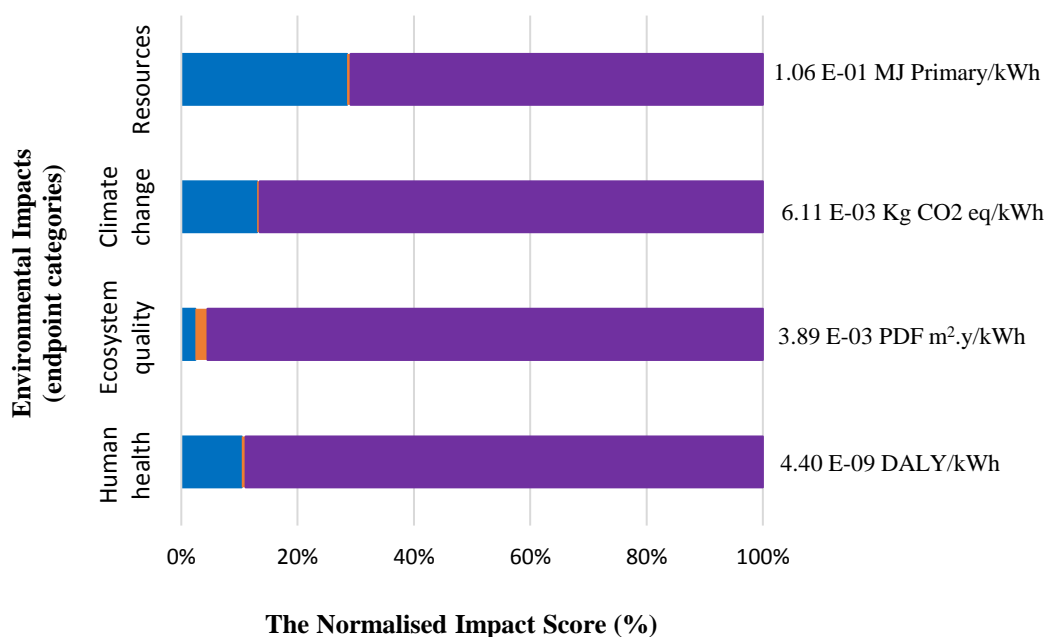


Figure 6-14. The environmental damages of energy and material usage of the CZTS absorber layer via vacuum (in blue) and non-vacuum (in orange) deposition techniques, considering CIGS as a reference (in purple) is displayed for an assumed 1GW per annum production facility. The total quantity of each category is given on the right hand side of the bar chart.

## 6.4 Conclusion

In the current study, the environmental impacts of CZTS absorber layers fabricated by two different techniques were investigated, considering the CIGS absorber layer as a

reference. The effects of material and energy consumption for each process were analysed by SimaPro software. The CZTS process is at the research and development stage and the material is not yet in commercial production. Therefore, the purpose of this analysis was to estimate (a) if the material itself is likely to yield environmental benefits over CIGS, (b) the effects of process assumptions on the environmental impacts, and (c) the important issues to address in the ongoing development from an environmental viewpoint. With regard to these, analysis of the input materials for the absorber layer shows that the CZTS films exhibit a significant potential benefit over CIGS, with the non-vacuum technique having a slight advantage over the vacuum deposition technique. This result does not mean that the vacuum deposition technique cannot have the potential to be produced at large-scale. In fact, this study would be beneficial for future research to take account of material selection and processing techniques as well as the effort to improve the performance of PV devices. A consequence that acquired from large-scale fabrication of absorber layers when only material usage have been considered was that the material used for non-vacuum processing could be harmful for the ecosystem and human health, while the climate change and resources are more affected by vacuum processing than non-vacuum technique. Extending the study onto estimating the environmental impacts, considering both material and energy consumption, the results indicated that the vacuum deposition technique could have more adverse influence on all the environmental indicators, compared to non-vacuum deposition technique. Moreover, the analysis showed that the use of sulphur, in terms of material usage and recycling of unused material, dominates for both vacuum and non-vacuum approaches. The disposal of zinc sulphide is also important for the non-vacuum processing. Since the assumptions of this study were held according to the projections of a large-scale production, it is clear that energy consumptions dominate the environmental impacts for the vacuum processing and so it is important to ensure that development of the process prioritises energy efficiency. Finally, it should be recognised that the analyses presented here are for a pre-commercial stage and should not be taken to represent the final values of the commercial processes. Rather than that, the analyses are useful to investigate the potential for sustainability and the fabrication aspects of interest. Moving forward, the impact of the rest of the module manufacturing process must also be considered, once the processes have been more fully defined.

## **Chapter 7**

### **Conclusion and outlook**

## **7 Conclusion and outlook**

This chapter presents a summary of the current research and the main outcomes achieved during this PhD thesis. It also offers several suggestions as recommendations for future studies.

### **7.1 Development in Kesterite absorber layer**

#### **7.1.1 CZTSe absorber layers through preliminary investigations**

- The study has shown that in case of using Se-cap layer, the CZTSe Kesterite crystal structure can be formed when the thickness of Se-cap layer is at least 1.5 times the thickness of CZT metallic precursors. This is when the conversion conditions to fabricate the CZTSe is adjusted at the preheating temperature of 160°C for 3 hour, the conversion time of 15 min at a temperature of 550°C, and 300 mbar ambient pressure of argon.
- The advantages of using an evaporated cap include the macroscopically uniform surface of the film and the possibility to control the amount of selenium in close contact with the precursor surface during the evaporation. However, this technique results in a microscopic non-uniformity by the formation of secondary compounds which can be attributed to the formation of star-like features at preheating temperatures (less than the melting point of selenium). The regions with the star-like features can be regarded as nucleation points and can be responsible for the selective creation of binary compounds. The formation of secondary compounds can be detrimental to the absorber layer quality by acting as centres of SRH recombination contributing to a reduction in open circuit voltage. By using selenium pellets, although the macro-scale non-uniformity is considerably increased, the micro-uniformity and morphology are significantly improved. This enabled the research group to achieve an 8.1% device efficiency.
- The advantage of using selenium pellets is not only the formation of a relatively uniform microstructure, but also a more efficient material usage. The study here has shown that in the case of using thermal evaporator to fabricate the Se-cap layer, the evaporation technique requires a quantity of selenium with a magnitude of ~140 times higher than that required for the case of using Se pellets in graphite box. This considerable mass of material usage and subsequently, the high quantity of material wastes together with the processing time and energy required for

thermal evaporator technique, makes this method less favourable than the use of Se pellets during the conversion processing.

- The study on the investigation of preheating steps at low ambient pressures has been compared to the one-step selenisation at high ambient pressure (without preheating). The results indicated the formation of micro non-uniformities across the surface of thin films for those samples preheated at low temperatures and low pressures. While the one-step selenisation at 500°C under the ambient pressure of 300 mbar of argon has shown a relatively uniform morphology with fewer formation of secondary compounds. This study offers the need for the use of a high ratio of ambient pressure during the conversion (selenisation) when the conversion temperature is higher than ~350°C. This is required to prevent the formation of liquid/vapour states of selenium and the subsequent complex reactions at lower temperatures, which are expected to increase the possibility of the formation of selective secondary compounds at early stages of conversion.

#### **7.1.2 Development of the precursor solution and deposition technique for the fabrication of CZTS thin films through preliminary investigations**

- The study in this thesis offers a low-cost and simple technique to fabricate a precursor solution. This has been done using a mechano-chemical approach. To do so, the metal oxide/sulphide powders including Cu<sub>2</sub>O, ZnS, and SnO have been mixed and milled in a ball milling apparatus. This process have been carried out with the advantage of using IPA as a suspension or carrier solution. In addition, the ZrO<sub>2</sub> balls were used as grinders for the process of milling. In order to prepare a homogenous precursor solution three parameters have been investigated. These include (i) the reduction of particle size of initial powders by increasing the milling time, (ii) the reduction of particle size of initial powders using ZrO<sub>2</sub> balls with three different diameters (D = 5, 2, 0.5 mm), and (iii) the choice of appropriate carrier solution.

The investigations on the effect of milling time have shown that in general, increasing the milling time causes a reduction in particle size of powders. However, milling the powders for 24 hours, compared to the milling for 4 hours has less contribution in providing fine particles. Thus, the choice of 24 hours of milling is less favourable. This is because of the importance of time and energy

consumption for the processing, especially when the technology is aimed to be used in a large-scale production. The study of using different ball sizes has shown that the reduction in particle size can be significantly achieved with reducing the ball size from 5 mm to 0.5 mm. The experiment has also shown a better homogeneity and distribution of particles across the solution when the smaller grinding balls were used ( $D = 0.5$  mm).

- In order to choose an appropriate carrier solution, the use of water and/or IPA has been used. Although water is less toxic and safer for environment than IPA, the study has shown a better disparity of powders in the case of using pure IPA. The study indicated that the formation of agglomerated features in the case of using 90% water + 10% IPA. Therefore, it is preferable to use pure IPA as a suspension solution as it is expected that the agglomerated structure of particles decreases the rate of reduction of oxide compounds in further steps of processing.
- Establishing a method of non-vacuum deposition technique has been achieved by offering a simple and scalable technique of spraying with an airbrush. The results have shown the formation of relatively uniform and thin layer of precursor on substrates. Moreover, a limited study on fabricating the precursor thin films via slot-die technique also indicated promising results, since the microstructure of fabricated thin films were even more uniform than those samples prepared by spraying method. Both techniques of spraying and slot-die have the advantage of using in large-scale production and less waste compared to the conventional method of spin coating deposition technique.
- Finally, the optimised conditions achieved in the current research were the fabrication of precursor solution by mixing and grinding metal compound powders ( $\text{Cu}_2\text{O}$ ,  $\text{ZnS}$ , and  $\text{SnO}$ ) with IPA as a carrier solution in a ball mill apparatus for 4 hrs with a speed of 500 rpm. Zirconia balls with the size  $D = 0.5$  mm have been used and the milling process has been done with 5 min and 7 min of grinding and pause time, respectively.

### **7.1.3 Development of the conversion conditions for the fabrication of CZTS thin films**

- The study in the current thesis indicates the importance of precursor composition, conversion time, temperature, and ambient pressure on the morphology and



crystal structure of the final CZTS thin films. The influence of all these parameters have been examined and presented in Chapter 5.

- The investigation on the composition of sulphurised absorber layers has been carried out and the optimum composition for this particular experiment is suggested to follow the atomic ratio of Cu:Zn:Sn equal to 0.7:1:1 for the precursor composition.
- The use of sufficient pressure of forming gas is necessary in order to convert the relatively stable SnO compound and remove the oxygen from the precursors. Besides, a control of the total ambient pressure has shown to be a critical parameter in the fabrication of uniform thin films, since the use of high rate of forming gas may lead to the loss of adhesion between the converted thin films and the back contact; consequently it causes the converted films to be separated from the substrates. A high total ambient pressure is important to prevent the tin loss. Thus, an optimisation of total ambient pressure was needed. The current study has suggested the use of 250 mbar  $H_2/N_2$  for the process of CZTS Kesterite thin films in this particular experiment.
- The influence of conversion time and temperature on the final quality of CZTS thin films have been investigated. The results have shown that the increase of both factors can affect the grain growth of CZTS Kesterite structures, subsequently creating a denser absorber layer. The study on the temperature profile has shown a better compositional result when the sample is heated fast and cooled down naturally. This could be due to the delay in the reduction of SnO in solid state to SnS in solid, and subsequently SnS in gas state. This will postpone the tin loss from the system. However, the results indicated that during the cooling step, the SnS can condense on the surface. Since the formation of SnS has been mainly observed on the surface of converted thin films, these compounds can be removed via surface etching.
- The experiment on surface etching has shown that SnS crystal structures can be completely removed from the surface when the sample is placed into the solution of 20 wt%  $(NH_4)_2S$  for at least 3 min at room temperature.
- The use of different supply of sulphur during the conversion have been investigated in order to provide adequate partial pressure of sulphur and prevent the deficiency of chalcogen quantity across the absorber layer. Moreover, the

post-conversion heat treatment under high ambient pressure of argon (500 mbar) with an excess sulphur supply (1g) has shown a slight decrease in sulphur deficiency of the converted thin films.

- The material characterisation and optoelectronic study on the fabricated CZTS thin films have revealed promising results showing approximately no surface recombination using IMPS technique. The XRD patterns and Raman spectra have shown the successful formation of CZTS Kesterite structure using the metal oxide/sulphide powders and the non-vacuum deposition technique. The EQE spectrum has illustrated a 20% efficiency.
- The follow-up studies on the selenisation of CZTS thin films have shown a considerable grain growth and a dense morphology of the CZTSSe thin films. However, the follow-up trial on investigating the use of extra elemental sulphur source in the precursor solution plus using sulphur powders during the conversion processing shows the formation of small grain of CZTS compounds with a more porous morphology of converted films compared to the use of extra elemental sulphur source only during the conversion procedure.

## **7.2 Environmental impacts of the fabrication of CZTS absorber layers via vacuum and non-vacuum processing techniques**

- In order to estimate the environmental impacts, the study was conducted using LCA approach with the use of IMPACT 2002+ as a framework and SimaPro as a software has been used. The system boundary defined for the current study only includes the fabrication of absorber layer. In this thesis, the fabrication of CZTS thin films prepared via vacuum and non-vacuum deposition technique have been considered. The CIGS absorber layer manufactured via co-evaporation technique has been used as a reference due to its similarity with CZTS in terms of device structure and configuration. Considering the assumption that the materials and processing techniques for fabricating a complete device are the same for the three examined absorber layers, the outcome of the study could be an indicator of the environmental impacts of the whole solar device. According to the study on LCA, the investigations have shown that regardless of the low efficiency of CZTS based solar cells, the use of this compound has a considerable advantage over the CIGS based solar cells. Comparing the two technique for fabrication of CZTS thin

films, the results have shown that in large scale production, the material used during non-vacuum processing are more harmful for the ecosystem and human health, but they have less adverse impacts on climate change and resources compared to the vacuum processing technique. However, considering the impacts of both material and the energy required for the processing, the vacuum technique seems to have more adverse influence on all environmental impacts than non-vacuum fabrication route.

- Regarding the results achieved by the study on LCA, if the non-vacuum deposition technique improves in terms of device performance, it could be a more environmentally friendly approach than the use of vacuum deposition route. Nevertheless, if the non-vacuum processing substitute instead of vacuum approach, it is required to address the issue of waste with an appropriate design for extraction, processing (considering the deposition efficiency), and recycling steps. That could be beneficial to reduce the environmental toxicity occurs during the processing and use.

### **7.3 Suggestions for future research**

- One of the challenges in the current study has been the low degree of reproducible results in case of using the handheld spraying technique. Thus, replacing this technique with slot-die method could provide a high degree of reproducibility with the formation of more uniform precursor layer. Optimising the precursor solution viscosity with an ideal binder to make the precursor solutions being stable for longer time could make a significant progress in the fabrication of a uniform absorber layer. Otherwise, the precursor solution will be dried while travelling through the delivery tube before it reaches the substrate. A trial study on this topic has been done by Dr. Greenwood at University of Swansea and the results are presented in Appendix B. This study could be an starting point for future investigations.
- It is expected that developing a strategy to provide a compact structure with less pinholes would be possible via the compressing of the precursor thin films using a table press that ensures an equal and even pressure across the surface. Chen et al have reported a promising results when they have used similar strategy for the fabrication of CIGS thin films [133]. It is assumed that similar approach could be beneficial to fabricate the CZTS thin films with a better degree of compactness.

- The study here have shown promising results on the fabrication of CZTS Kesterite structure using the metal oxides as initial materials. However, due to the necessity in optimising the precursor solution, deposition technique, and conversion conditions, less time has been devoted to the fabrication of a complete device. The limited manufactured devices have not been shown a considerable efficiency. Thus, future study can be devoted to the use of two mentioned suggestions, and subsequently the fabrication of a complete device.
- As the CZTS device develops, the LCA analyses can be revisited and, at that time, it may be reasonable to extend the study with considering the environmental impacts arises from the processing of the other components of solar device.

#### **7.4 Original Contribution**

This study has shown a successful synthesising of CZTS Kesterite structure from the metal oxide/sulphide compounds of  $\text{Cu}_2\text{O}$ ,  $\text{ZnS}$ , and  $\text{SnO}$ . To the best of our knowledge, this is the first time that the combination of these compounds have been used to prepare the CZTS absorber layer. This PhD thesis offers (i) the fabrication of a homogenous precursor solution via a mechano-chemical approach (ball milling), (ii) the establishment of a scalable and simple method of deposition to prepare a uniform and thin layer of precursor on substrate, (iii) the investigation of the conversion conditions on the morphology and crystal structure of CZTS thin films, and (iv) the study on the sustainability of the material usage and processing technique to fabricate the CZTS absorber layer. The morphology and the composition of CZTS thin films have been significantly improved by optimising the synthesising process and the conversion conditions. Investigating the micro and crystal structure together with the optoelectronic characteristic of fabricated CZTS thin films have revealed that the use of metal oxide/sulphide powders with a mechano-chemical technique could have the potential to be considered for PV technology. In order to evaluate whether the use of metal oxide/sulphide compounds and the non-vacuum processing is beneficial over the use of metal targets and the vacuum processing, the sustainability of these two techniques have been studied and compared via LCA approach. Such a study can provide an overview on the importance of the material selection and the processing used for the production of a solar device. Furthermore, it is expected that the use of solar device offers a cleaner and greener earth for current and future generation. Thus, the advantage of using solar energy

should not be sacrificed by the use of materials and processes which damage the human health, ecosystem quality, climate change, and resources.



## Appendices

### Appendix A: Liquid redox electrolyte and p-semiconductor junction

A Schottky junction can be formed when a p-semiconductor is immersed in a liquid redox electrolyte. The Figure A-1 shows the situation before and after the semiconductor and the electrolyte reach the thermodynamic equilibrium. As shown the Fermi level for the two sides have different values. Thus, an exchange of charges at electrolyte and the semiconductor is required to equalise the Fermi level. During the equilibrium condition, a depletion region is created into the semiconductor side of the interface together with a layer in the electrolyte side known as Helmholtz Layer in the electrolyte side. The band bending will occur as it forms an electrolyte-semiconductor junction.

The kinetics of electron-transfer processes can be measured by perturbing the potential and measuring the periodic current response via short light flashes [205]. Thus, the minority carriers (electrons) are generated by illumination and move towards the interface. They are then collected from the bulk of the semiconductor by the positive charge carrier in the electrolyte. With a choice of an electrolyte having the redox potential higher than the semiconductor Fermi level, the electrons can transfer through the electrolyte and reach the electrode (Counter Electrode). This produces a photocurrent in a short-circuited system and also it leads to the reduction of oxidised species in the electrolytic solution [229, 230]. A typical image of oscilloscope that have been observed during the experiments at University of Northumbria is presented in Figure A-2. The spectrum of the three collimated LEDs used for the experiments have been also shown in Figure A- 3.

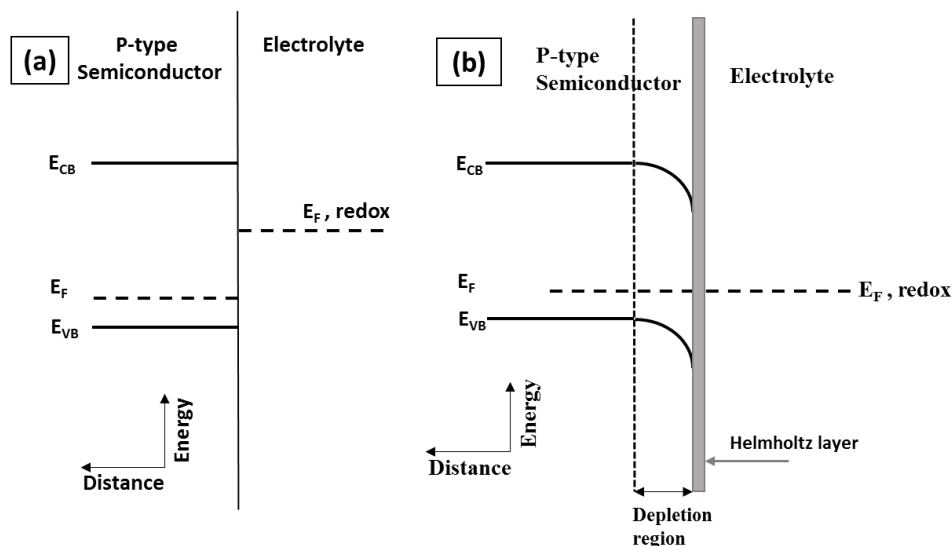


Figure A-1. The formation of a Schottky junction between a liquid redox electrolyte and a p-type semiconductor (a) before (b) after the thermodynamic equilibrium [2].

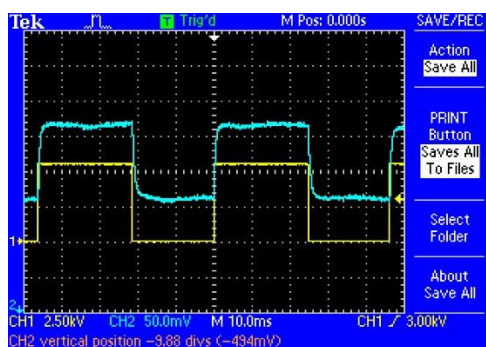


Figure A-2. A typical graph observed by oscilloscope using IMPS technique.

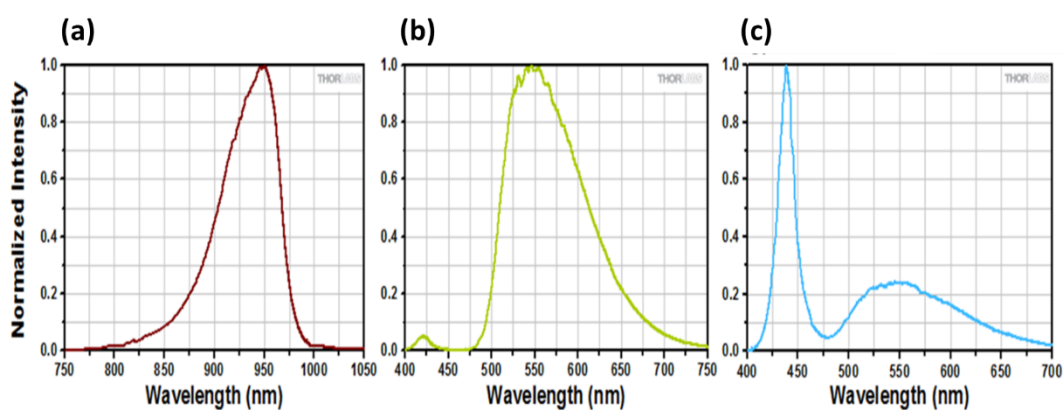


Figure A- 3.The spectrum of three collimated LEDs used for the experiments (a) 940nm (b) 565 nm (c) board white source [231].



## Appendix B: The use of surfactant in precursor solution preparation

Thermogravimetric analysis (TGA) is a method of characterising the mass loss of a material as a function of temperature or time. The analysis normally proceeds in a controlled atmosphere. This technique can be used to evaluate stability and lifetime of materials, the rate of decomposition, oxidation or dehydration of a product, and the degree of volatility over a range of temperature or a period of time.

In this study, an equipment with the identification of 'PerkinElmer STA6000' has been used to evaluate the weight lost. The experiments have carried out using nitrogen gas with a flow of 20 ml/min, temperature range of 30°C to 800°C, an isothermal hold for 1 minute, and a temperature scan of 10°C/min. The sample volume was prepared with the mixture of 30µL of precursor solution plus 10µL of surfactant. The non-ionic Alkanol 6112 (a combination of Polyethylene oxide monooctadecyl ether, Decon 1-ol, and water) with the boiling point of 100°C and the density of 0.91g/ml has been used as a surfactant. The solvent is relatively toxic and has a higher boiling point compared to IPA (~82.6°C). The four samples were prepared with the addition of 0%, 1%, 5% and 10% (by volume) to the initial precursor solution containing Cu<sub>2</sub>O, ZnS, SnO, and IPA. The four examined samples were stored on a rolling table for 48 hours, then the samples were removed and shaken vigorously. Afterwards, the samples were allowed to rest for 8 hours, the picture of the samples after this process as shown in Figure B-1, illustrates the difference in uniformity of the solutions.

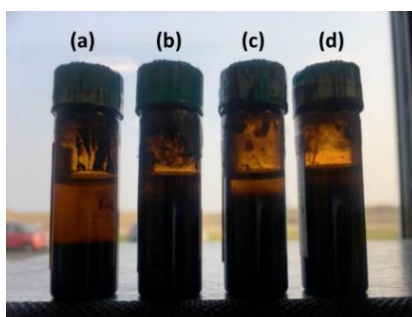


Figure B-1. The picture shows the precursor solutions after mixing with Alkanol 6112 as a surfactant with different values (by volume) of (a) 0% (b) 1% (c) 5% (d) 10%.

The results of a complete scan from 30°C to 800°C have shown that the initial mass-loss from dispersions of precursor solution prepared without surfactant occurred by approximately 100°C while with the use of surfactant in precursor solution, the mass loss plateau after 175°C, followed by a gradual decrease to 500°C (see Figure B-2). The results have shown that the dispersion mass-loss plateaus occurred at 10-12 wt% by 800°C, while

the surfactant mass-loss plateau at 0.5% by 560°C. No significant mass-loss has been observed from dispersion between 500°C and 560°C.

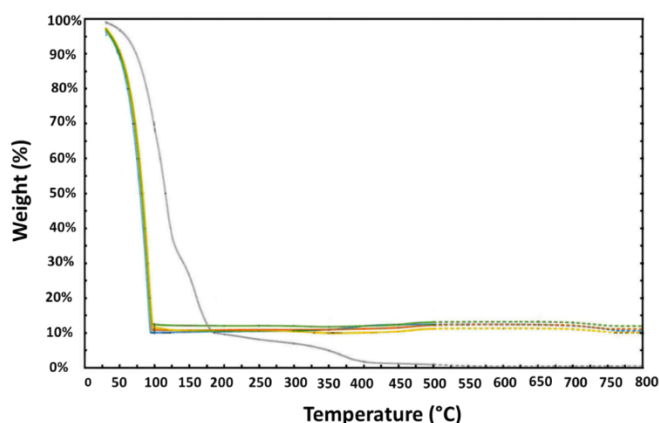


Figure B-2. The Thermo-gravimetric analysis of CZTS precursors

One of the major concerns of the use of surfactant was its influence on the micro and crystal structure of the converted thin films. Although due to the packaging and posting, the examined samples were not uniformly coated, the SEM/ XRD analyses of the samples coated with the solution formulated by surfactant did not show any new compounds. The examined samples have shown Kesterite crystal structure with partially binary compounds of SnS similar to the quality has been observed with the use of only IPA.

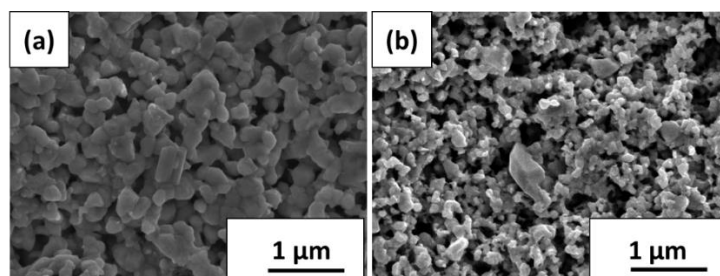


Figure B-3. The Plan-view SEM images of converted samples prepared using (a) precursor solutions without surfactant using spraying technique (b) precursor solution with surfactant using slot-die technique.

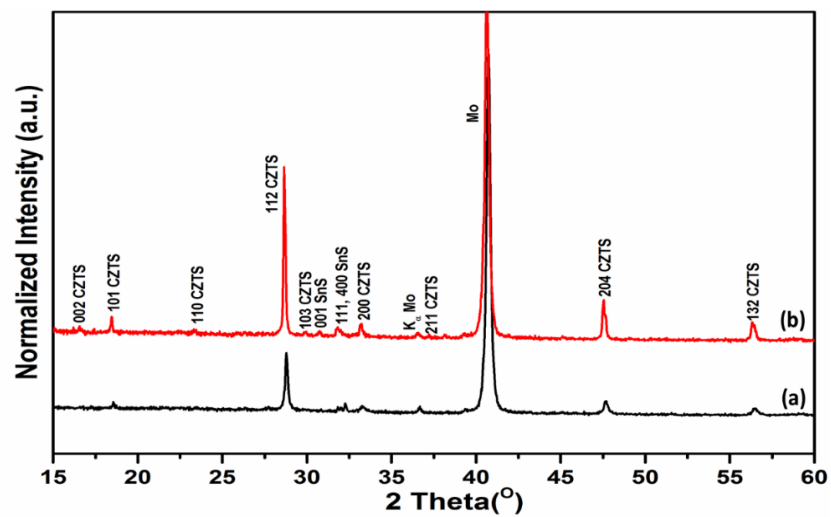


Figure B-4. The figure shows the XRD patterns of the converted samples prepared using (a) precursor prepared from the solution including the surfactant fabricated by slot-die technique (b) precursor prepared by the solution without surfactant fabricated by spraying technique

### Appendix C: Comparison of converted samples prepared via vacuum or non-vacuum deposition technique

The study here presents a trial of the conversion of the two precursors prepared via vacuum and non-vacuum deposition techniques. Of various processing methods for depositing the absorber layer, two methods were used (A) conversion of magnetron sputtered metal precursors (vacuum processing), and (B) reactive conversion of spray deposited films (non-vacuum processing).

The samples prepared via method (A) involved magnetron sputter deposition of Cu-Zn-Sn metal precursors on Mo/SLG substrates with composition of  $\text{Cu}/(\text{Zn}+\text{Sn}) = 0.7$  and  $\text{Zn}/\text{Sn} = 1$  and the thickness of  $0.5\ \mu\text{m}$ . The samples prepared via method (B) made with the same preparation and heat treatment procedure that was introduced as the optimum situation in chapter 6 (conversion time and temperature of 40 min and  $570^\circ\text{C}$ , respectively). However, the ambient pressure has been varied between two pressures of 5 and 250 mbar  $\text{H}_2/\text{N}_2$  for samples processed via both methods of A and B.

The plan-view and cross-section SEM images have shown the morphology of the converted samples (see Figure C-1 and Figure C-2). The X-ray diffraction of four experimental samples are shown in Figure C-3. The compositional changes are also presented in Table C-1.

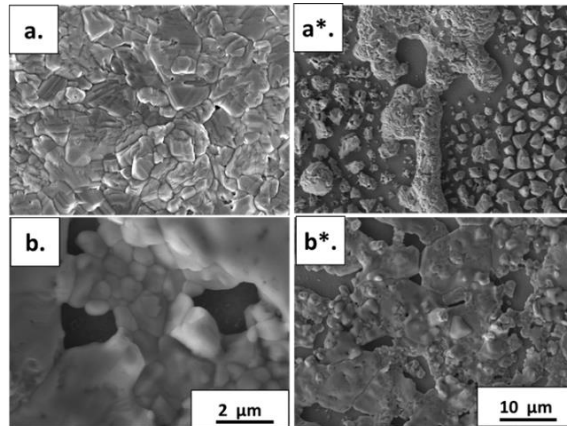


Figure C-1. The SEM images of samples processed via sputtering are displayed (a,a\*) 5 mbar Ar (b,b\*) 250 mbar  $\text{H}_2/\text{N}_2$ . The images are observed with two different magnifications of (a, b)  $\sim 24\text{kx}$ , and (a\*, b\*)  $\sim 5\text{kx}$ .

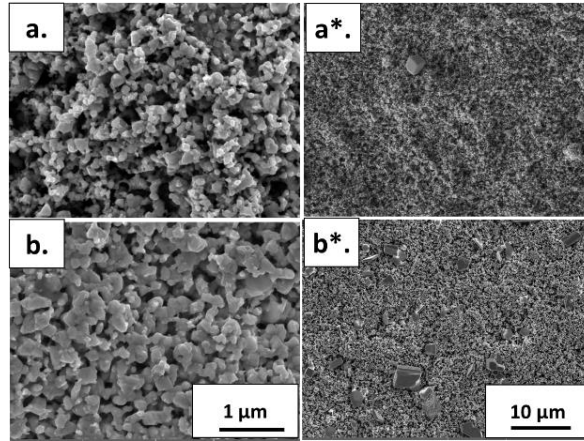


Figure C-2. The plan-view SEM images of non-vacuum deposited sample sulphurised under (a,a\*) 5 mbar Ar and (b,b\*) 250 mbar H<sub>2</sub>/N<sub>2</sub>. The SEM images have been observed with two different magnification of (a, b) ~48kx and (a\*, b\*) ~5kx.

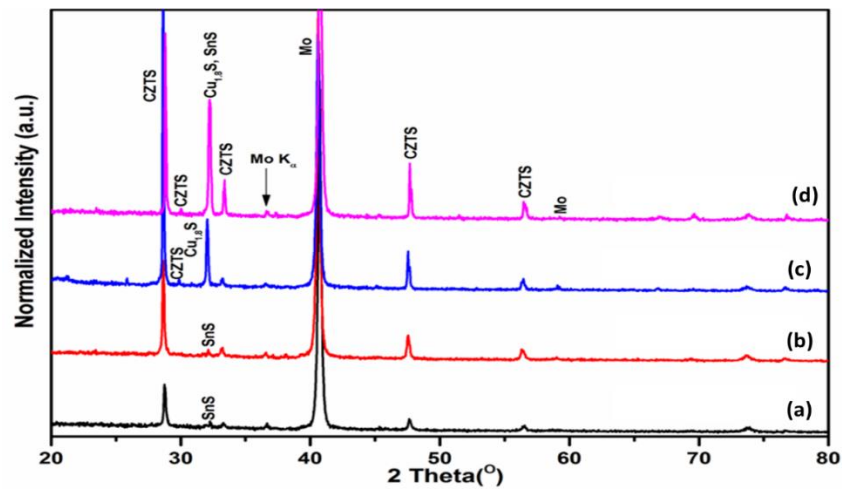


Figure C-3. The XRD patterns of (a, b) samples processed via non-vacuum deposition technique (NVD) (c, d) samples processed via vacuum deposition technique (VD) under (a, c) 5H<sub>2</sub>/N<sub>2</sub> and (b, d) 250 mbar H<sub>2</sub>/N<sub>2</sub>.

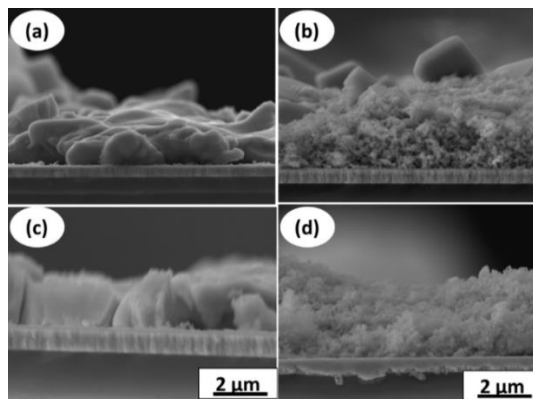


Figure C-4. The cross-section SEM images of (a, c) the sample prepared via sputtering (b, d) the samples prepared via spraying with the ambient pressure of (a, b) 250 mbar H<sub>2</sub>/N<sub>2</sub> (c, d) 5 mbar H<sub>2</sub>/N<sub>2</sub>

Table C-1. The table shows the compositional changes of the samples before and after sulphurisation, the first three samples named AN, BN, and CN indicate the samples prepared via non-vacuum deposition technique and those named AV, BV, and CV prepared via vacuum deposition technique.

Sample-Process of deposition	Ambient pressure (mbar)	Cu (at%)	Zn (at%)	Sn (at%)	S (at%)	$\frac{\text{Cu}}{(\text{Zn} + \text{Sn})}$	$\frac{\text{Zn}}{\text{Sn}}$
AN-(as-deposited)	-	15.5	12	11	13.5	0.7	1
BN	5 H <sub>2</sub> /N <sub>2</sub>	24	15	14	46	0.8	1.1
CN	250 H <sub>2</sub> /N <sub>2</sub>	25	15	13	47	0.9	1.1
AV-(as-deposited)	-	40	29	31	-	0.7	0.9
BV	250 H <sub>2</sub> /N <sub>2</sub>	18.5	28.5	8.5	44.5	0.7	1.6
CV	5 H <sub>2</sub> /N <sub>2</sub>	23	17	11	49	0.8	1.5

The results have shown that the samples prepared via non-vacuum deposition technique exhibited better uniformity in terms of composition while the microstructure of these samples indicates a high degree of porosity together with the formation of small grain of CZTS Kesterite. Samples prepared via vacuum deposition technique have shown a very zinc-rich composition of the converted samples, while the microstructure shows larger grains and well-crystallised Kesterite structure but lack of uniformity at some parts of the converted thin films. The results illustrated that at low ambient pressure, the more compact and well-crystallised CZTS structure has been created for the converted thin films prepared via sputtering deposition technique. However, using low ambient pressure for the precursors processed via non-vacuum deposition technique shows a poor quality of CZTS crystal structure (having small grains and poor crystallinity). Therefore, in the case of using forming gas as an ambient pressure, the higher pressure for the non-vacuum deposited precursors and lower pressure for vacuum deposited precursors yielded the better quality of CZTS thin films.

## Appendix D: Process Assumptions

Table D-1. Introducing the scalable equipment assumed for the fabrication of CZTS thin film using vacuum deposition technique, considering the established technology in large-scale.

Name of Apparatus	Identification of the system	Capacity (Dimension)	Roll-to-roll capability	Link to the website
<b>Sputtering Machine</b>	FHR Line 2500, with rotatable targets	width 0.5m	Yes	<a href="http://www.fhr.de/cms/en/91/FHRLine-product-series---for-glass-and-rigid-substrates">http://www.fhr.de/cms/en/91/FHRLine-product-series---for-glass-and-rigid-substrates</a>
<b>Furnace</b>	Belt Furnace HSH 2503-0310	width 0.5m	Yes	<a href="http://www.beltfurnaces.com/HSSolar.html">http://www.beltfurnaces.com/HSSolar.html</a>

Table D-2. The assumptions on energy consumption during the CZTS thin film processing using vacuum deposition technique for 1 m<sup>2</sup> of PV module and 1GW per year production facility.

Name of Apparatus	Assumed Speed	Assumed Power required per hour (kW)	Hours of Operation		Energy Consumption (kWh)	
Functional unit			1 m <sup>2</sup>	1GW per year	1 m <sup>2</sup>	1GW per year
<b>Sputtering machine</b>	82 m <sup>2</sup> /h	600	0.012	8.10 E+04	7.20 E+00	4.86 E+07
<b>Pumping for sputtering machine</b>	12 hours for pumping	250	12	5.76 E+03	3.00 E+03	1.44 E+06
<b>Furnace</b>	120 m <sup>2</sup> /h	2.07	0.008	5.56 E+04	1.66 E-02	1.15 E+05
<b>Total Energy Consumption (kWh)</b>					3.01 E+03	5.02 E+07

Table D-3. The introduction of the scalable equipment assumed for the fabrication of CZTS thin film using non-vacuum deposition technique, considering the existing technology in large-scale.

Name of Apparatus	Identification of the system	Capacity (Dimension)	Roll-to-roll capability	Link to the website
Ball Milling	EBF-7.5	100-500L	No	<a href="http://en.elemix.cn/productDetail/productId=34.html">http://en.elemix.cn/productDetail/productId=34.html</a>
Slot Die	RSC-300	Width 0.45 m	Yes	<a href="http://www.pems-korea.com/eng/030106">http://www.pems-korea.com/eng/030106</a>
Drying Process	RSC-300	Width 0.45 m	Yes	The slot die system is equipped with heating system.
Furnace	Belt Furnace HSH 2503-0310	4m × 0.5 m × 3 μm	Yes	<a href="http://www.beltfurnaces.com/HSHsolar.html">http://www.beltfurnaces.com/HSHsolar.html</a>

Table D-4. The assumptions on energy consumption during the CZTS thin film processing using non-vacuum deposition technique for 1GW per year production.

Name of apparatus	Assumed speed	Assumed power required per hour (kW)	Hours of operation		Energy Consumption (kWh)	
Functional unit			1 m <sup>2</sup>	1GW per year	1 m <sup>2</sup>	1GW per year
Ball Milling	500rpm	7.5	4	3.2 E+03	30	2.4 E+04
Slot-die	810 m <sup>2</sup> /h	2.2	1.2 E-03	8.2 E+03	2.7 E-03	1.8 E+04
Hot plate	810 m <sup>2</sup> /h	7.48	1.2 E-03	8.2 E+03	8.9 E-03	6.13 E+04
Furnace	120 m <sup>2</sup> /h	2.07	0.008	5.56 E+04	1.66 E-02	1.15 E+05
Total Energy Consumption (kwh)					3.00 E+01	4.3 E+05



## References

1. M. Dhankhar, O. Pal Singh and V. N. Singh, *Physical principles of losses in thin film solar cells and efficiency enhancement methods*. Renewable and Sustainable Energy Reviews, 2014. **40**: p. 214-223.
2. L. M. Peter, *Towards sustainable photovoltaics: the search for new materials*. Philosophical Transactions of the Royal Society a-Mathematical Physical and Engineering Sciences, 2011. **369**(1942): p. 1840-1856.
3. K. J. A. Smets, O. Iseaballa, R. Swaaij, M. Zeman, *Solar Energy: The Physics and Engineering of Photovoltaic Conversion, Technologies and Systems*. Published by UIT Cambridge Ltd, 2016.
4. S. M. N. Sze, Kwok K, *Physics of Semiconductor Devices (SzePhysics) Physics and Properties of Semiconductors-A Review*.
5. T. Kato, A. Handa, T. Yagioka, T. Matsuura, K. Yamamoto, S. Higashi, J.-L. Wu, K. F. Tai, H. Hiroi, T. Yoshiyama, T. Sakai and H. Sugimoto, *Enhanced Efficiency of Cd-Free Cu(In,Ga)(Se,S)<sub>2</sub> Minimodule Via (Zn,Mg)O Second Buffer Layer and Alkali Metal Post-Treatment*. IEEE Journal of Photovoltaics, 2017. **7**(6): p. 1773-1780.
6. M. A. Green, Y. Hishikawa, E. D. Dunlop, D. H. Levi, J. Hohl-Ebinger and A. W. Y. Ho-Baillie, *Solar cell efficiency tables (version 51)*. Progress in Photovoltaics: Research and Applications, 2018. **26**(1): p. 3-12.
7. K. Pickerel, *The advantages of flexible thin-film solar modules*. Report from MiaSolé, 2016.
8. *Fraunhofer Institute for Solar Energy Systems, ISE with support of PSE AG*. Photovoltaics-Report, 2017([www.ise.fraunhofer.de](http://www.ise.fraunhofer.de)): p. 1-44.
9. S. P. Johannes Mayer, Noha Saad, Hussein, Thomas Schlegel, Charlotte Senkpiel, *Current and Future Cost of PV*. Published by Fraunhofer ISE, 2015.
10. H. Katagiri and Ieee, *Survey of Development of CZTS-based Thin Film Solar Cells*. 3rd International Conference on Photonics 2012, 2012: p. 345-349.
11. X. Song, X. Ji, M. Li, W. Lin, X. Luo and H. Zhang, *A Review on Development Prospect of CZTS Based Thin Film Solar Cells*. International Journal of Photoenergy, 2014. **2014**: p. 1-11.
12. Q. Cai, X. Liang, W. Xiang, J. Zhong, M. Shao and X. Zhao, *The Development of Cu<sub>2</sub>ZnSnS<sub>4</sub> Thin Films*. Materials Review, 2012. **26**(2A): p. 138-143.
13. T. Kobayashi, K. Jimbo, K. Tsuchida, S. Shinoda, T. Oyanagi and H. Katagiri, *Investigation of Cu<sub>2</sub>ZnSnS<sub>4</sub>-based thin film solar cells using abundant materials*. Japanese Journal of Applied Physics Part 1-Regular Papers Brief Communications & Review Papers, 2005. **44**(1B): p. 783-787.
14. D. B. Mitzi, O. Gunawan, T. K. Todorov, K. Wang and S. Guha, *The path towards a high-performance solution-processed kesterite solar cell*. Solar Energy Materials and Solar Cells, 2011. **95**(6): p. 1421-1436.
15. J. Marquez, *Development of Cu<sub>2</sub>ZnSnS<sub>4</sub> Based Absorbers By PVD processes*. PhD Thesis at Northumbria University, 2016.
16. G. Zoppi, I. Forbes, R. W. Miles, P. J. Dale, J. J. Scragg and L. M. Peter, *Cu<sub>2</sub>ZnSnSe<sub>4</sub> in Film Solar Cells Produced by Selenisation of Magnetron Sputtered Precursors*. Progress in Photovoltaics, 2009. **17**(5): p. 315-319.
17. Y. S. Lee, T. Gershon, O. Gunawan, T. K. Todorov, T. Gokmen, Y. Virgus and S. Guha, *Cu<sub>2</sub>ZnSnSe<sub>4</sub> Thin-Film Solar Cells by Thermal Co-evaporation with 11.6% Efficiency and Improved Minority Carrier Diffusion Length*. Advanced Energy Materials, 2015. **5**(7): p. n/a-n/a.

18. J. J. Scragg, P. J. Dale, L. M. Peter, G. Zoppi and I. Forbes, *New routes to sustainable photovoltaics: evaluation of Cu<sub>2</sub>ZnSnS<sub>4</sub> as an alternative absorber material*. Physica Status Solidi B-Basic Solid State Physics, 2008. **245**(9): p. 1772-1778.
19. I. Forbes and L. M. Peter, *Materials for a sustainable future*. 2012: Royal Society of Chemistry, Cambridge, UK.
20. S. Siebentritt and S. Schorr, *Kesterites - a challenging material for solar cells*. Progress in Photovoltaics, 2012. **20**(5): p. 512-519.
21. S. Delbos, *K sterite thin films for photovoltaics : a review*. EPJ Photovoltaics, 2012. **3**: p. 35004.
22. Y. Tanaka and K. Matsuo, *Non-Thermal Effects of Near-Infrared Irradiation on Melanoma*, in *Breakthroughs in Melanoma Research*. 2011.
23. P. Wurfel, *Physics of Solar Cells : From Principles to New Concepts*. Published by WILEY-VCH Verlag GmbH & Co, 2005.
24. "Semiconductor diodes" available online at <http://www.physics-and-radio-electronics.com/electronic-devices-and-circuits/semiconductor-diodes/forwardbiasedpnjunctionsemiconductor-diode.html>.
25. P. Trehane, *Lecture on Junctions*, PVSAT conference 2014.
26. <https://www.gamry.com/application-notes/physechem/dssc-dye-sensitized-solar-cells/>.
27. S. Chen, A. Walsh, X.-G. Gong and S.-H. Wei, *Classification of Lattice Defects in the Kesterite Cu<sub>2</sub>ZnSnS<sub>4</sub> and Cu<sub>2</sub>ZnSnSe<sub>4</sub> Earth-Abundant Solar Cell Absorbers*. Advanced Materials, 2013. **25**(11): p. 1522-1539.
28. <https://www.pveducation.org/pvcdrom/solar-cell-operation/quantum-efficiency>.
29. R. B. Hall, R. W. Birkmire, J. E. Phillips and J. D. Meakin, *Thin-film polycrystalline Cu<sub>2</sub>S/Cd<sub>1-x</sub>Zn<sub>x</sub>S solar cells of 10% efficiency*. Applied Physics Letters, 1981. **38**(11): p. 925-926.
30. G. J. R. A. Ai-Dhafirit, And J Woods, *Degradation in CdS-Cu<sub>2</sub>S photovoltaic cells*. Semicond. Sci. Technol, 1992. **7**: p. 1052-1057.
31. L. L. Kazmerski, F. R. White and G. K. Morgan, *Thin-film CuInSe<sub>2</sub>/CdS heterojunction solar cells*. Applied Physics Letters, 1976. **29**(4): p. 268-270.
32. A. D. Sivagami, B. Sarma and A. Sarma, *Structural and optical analysis of single phase CuInS<sub>2</sub> nanocrystals for solar cell applications*. Japanese Journal of Applied Physics, 2016. **55**(1S).
33. S. Jung, S. Ahn, J. H. Yun, J. Gwak, D. Kim and K. Yoon, *Effects of Ga contents on properties of CIGS thin films and solar cells fabricated by co-evaporation technique*. Current Applied Physics, 2010. **10**(4): p. 990-996.
34. O. Lundberg, M. Edoff and L. Stolt, *The effect of Ga-grading in CIGS thin film solar cells*. Thin Solid Films, 2005. **480-481**: p. 520-525.
35. K. L. Chopra, P. D. Paulson and V. Dutta, *Thin-film solar cells: an overview*. Progress in Photovoltaics: Research and Applications, 2004. **12**(23): p. 69-92.
36. J. Ramanujam and U. P. Singh, *Copper indium gallium selenide based solar cells – a review*. Energy & Environmental Science, 2017. **10**(6): p. 1306-1319.
37. D. Colombara, F. Werner, T. Schwarz, I. Canero Infante, Y. Fleming, N. Valle, C. Spindler, E. Vacchieri, G. Rey, M. Guennou, M. Bouttemy, A. G. Manjon, I. Peral Alonso, M. Melchiorre, B. El Adib, B. Gault, D. Raabe, P. J. Dale and S. Siebentritt, *Sodium enhances indium-gallium interdiffusion in copper indium gallium diselenide photovoltaic absorbers*. Nat Commun, 2018. **9**(1): p. 826.
38. D. I. T. Nakada, H. Ohbo, A. Kunioka, *Effects of Sodium on Cu ( In , Ga ) Se 2-Based Thin Films and Solar Cells*. Jpn. J. Appl. Phys., 1997. **36**: p. 732-737.

39. H. O. Tokio Nakada, Masakazu Fukuda, Akio Kunioka, *Improved compositional flexibility of Cu(In,Ga)Se<sub>2</sub>-based thin film solar cells by sodium control technique* Solar Energy Materials and Solar Cells, 1997. **49**: p. 261-267.
40. U. P. Singh and S. P. Patra, *Progress in Polycrystalline Thin-Film Cu(In,Ga)Se<sub>2</sub>Solar Cells*. International Journal of Photoenergy, 2010. **2010**: p. 1-19.
41. X. Zhu, Z. Zhou, Y. Wang, L. Zhang, A. Li and F. Huang, *Determining factor of MoSe<sub>2</sub> formation in Cu(In,Ga)Se<sub>2</sub> solar Cells*. Solar Energy Materials and Solar Cells, 2012. **101**: p. 57-61.
42. S. Gao, Z. Jiang, L. Wu, J. Ao, Y. Zeng, Y. Sun and Y. Zhang, *Interfaces of high-efficiency kesterite Cu<sub>2</sub>ZnSnS(e)<sub>4</sub> thin film solar cells*. Chinese Physics B, 2018. **27**(1).
43. J. Bekaert, R. Saniz, B. Partoens and D. Lamoen, *Native point defects in CuIn(1-x)Ga(x)Se<sub>2</sub>: hybrid density functional calculations predict the origin of p- and n-type conductivity*. Phys Chem Chem Phys, 2014. **16**(40): p. 22299-308.
44. A. Polizzotti, I. L. Repins, R. Noufi, S.-H. Wei and D. B. Mitzi, *The state and future prospects of kesterite photovoltaics*. Energy & Environmental Science, 2013. **6**(11): p. 3171-3182.
45. Zsw, *ZSW Sets New World Record for Thin-film Solar Cells*. Press Release by Zentrum für Sonnenenergie- und Wasserstoff-Forschung Baden-Württemberg, 2016.
46. V. Petrova, *Hanergy Breaks Another Solar Efficiency World Record for CIGS Modules*. Hanergy Thin Film Power Group Ltd, 2018.
47. L. Gütay, D. Regesch, J. K. Larsen, Y. Aida, V. Depredurand and S. Siebentritt, *Influence of copper excess on the absorber quality of CuInSe<sub>2</sub>*. Applied Physics Letters, 2011. **99**(15).
48. D. Abou-Ras, G. Kostorz, A. Romeo, D. Rudmann and A. N. Tiwari, *Structural and chemical investigations of CBD- and PVD-CdS buffer layers and interfaces in Cu(In,Ga)Se<sub>2</sub>-based thin film solar cells*. Thin Solid Films, 2005. **480-481**: p. 118-123.
49. K. Ben Messaoud, M. Buffière, G. Brammertz, H. Elanzeery, S. Oueslati, J. Hamon, B. J. Kniknie, M. Meuris, M. Amlouk and J. Poortmans, *Impact of the Cd<sub>2</sub>+treatment on the electrical properties of Cu<sub>2</sub>ZnSnSe<sub>4</sub> and Cu(In,Ga)Se<sub>2</sub> solar cells*. Progress in Photovoltaics: Research and Applications, 2015. **23**(11): p. 1608-1620.
50. N. Naghavi, G. Renou, V. Bockelee, F. Donsanti, P. Genevee, M. Jubault, J. F. Guillemoles and D. Lincot, *Chemical deposition methods for Cd-free buffer layers in CIGS solar cells: Role of window layers*. Thin Solid Films, 2011. **519**(21): p. 7600-7605.
51. W. Witte, S. Spiering and D. Hariskos, *Substitution of the CdS buffer layer in CIGS thin-film solar cells*. Vakuum in Forschung und Praxis, 2014. **26**(1): p. 23-27.
52. O. Bierwagen, *Indium oxide—a transparent, wide-band gap semiconductor for (opto)electronic applications*. Semiconductor Science and Technology, 2015. **30**(2).
53. H. Han, J. W. Mayer and T. L. Alford, *Band gap shift in the indium-tin-oxide films on polyethylene naphthalate after thermal annealing in air*. Journal of Applied Physics, 2006. **100**(8).
54. D. G. A. Chirila, D. Brémaud, S. Buecheler, R. Verma, S. Seyrling, S. Nishiwaki, S. Haenni, G. Bilger, and A. N. Tiwari *CIGS Solar cells grown by a three stage process with different evaporation rates*. IEEE, 2009. **978**: p. 812-816.
55. V. Fthenakis, W. Wang and H. C. Kim, *Life cycle inventory analysis of the production of metals used in photovoltaics*. Renewable and Sustainable Energy Reviews, 2009. **13**(3): p. 493-517.
56. A. O. A. <http://Periodictable.Com/Elements/050/Data.Html>.
57. N. V. Ingrid Repins, Carolyn Beall, Su-Huai Wei, Yanfa Yan, Manuel Romero, Glenn Teeter, Hui Du, Bobby to, Matt Young, and Rommel Noufi *NREL, Kesterites and Chalcopyrites: A Comparison of Close Cousins*. Materials Research Society Spring Meeting, 2011.

58. W. Wang, M. T. Winkler, O. Gunawan, T. Gokmen, T. K. Todorov, Y. Zhu and D. B. Mitzi, *Device Characteristics of CZTSSe Thin-Film Solar Cells with 12.6% Efficiency*. Advanced Energy Materials, 2013: p. n/a-n/a.
59. S. Schorr, *The crystal structure of kesterite type compounds: A neutron and X-ray diffraction study*. Solar Energy Materials and Solar Cells, 2011. **95**(6): p. 1482-1488.
60. S. Chen, X. G. Gong, A. Walsh and S.-H. Wei, *Crystal and electronic band structure of  $\text{Cu}_2\text{ZnSnX}_4$  ( $X=\text{S}$  and  $\text{Se}$ ) photovoltaic absorbers: First-principles insights*. Applied Physics Letters, 2009. **94**(4): p. 041903-041903.
61. T. Shibuya, Y. Goto, Y. Kamihara, M. Matoba, K. Yasuoka, L. A. Burton and A. Walsh, *From kesterite to stannite photovoltaics: Stability and band gaps of the  $\text{Cu}_2(\text{Zn,Fe})\text{SnS}_4$  alloy*. Applied Physics Letters, 2014. **104**(2): p. -.
62. S. W. Shin, I. Y. Kim, K. V. Gurav, C. H. Jeong, J. H. Yun, P. S. Patil, J. Y. Lee and J. H. Kim, *Band gap tunable and improved microstructure characteristics of  $\text{Cu}_2\text{ZnSn}(\text{S}_{1-x}\text{Se}_x)_4$  thin films by annealing under atmosphere containing S and Se*. Current Applied Physics, 2013. **13**(8): p. 1837-1843.
63. A. Lafond, L. Choubrac, C. Guillot-Deudon, P. Deniard and S. Jobic, *Crystal Structures of Photovoltaic Chalcogenides, an Intricate Puzzle to Solve: the Cases of CIGSe and CZTS Materials*. Zeitschrift Fur Anorganische Und Allgemeine Chemie, 2012. **638**(15): p. 2571-2577.
64. J. Márquez-Prieto, Ren, Y., Miles, R. W., Pearsall, N., Forbes, I., *The influence of precursor Cu content and two-stage processing conditions on the microstructure of  $\text{Cu}_2\text{ZnSnSe}_4$* . Thin Solid Films, 2015. **582**: p. 220-223.
65. J. Timo Wätjen, J. Engman, M. Edoff and C. Platzer-Björkman, *Direct evidence of current blocking by ZnSe in  $\text{Cu}_2\text{ZnSnSe}_4$  solar cells*. Applied Physics Letters, 2012. **100**(17): p. -.
66. S. López-Marino, Y. Sánchez, M. Placidi, A. Fairbrother, M. Espindola-Rodríguez, X. Fontané, V. Izquierdo-Roca, J. López-García, L. Calvo-Barrio, A. Pérez-Rodríguez and E. Saucedo, *ZnSe Etching of Zn-Rich  $\text{Cu}_2\text{ZnSnSe}_4$ : An Oxidation Route for Improved Solar-Cell Efficiency*. Chemistry – A European Journal, 2013. **19**(44): p. 14814-14822.
67. M. Kumar, A. Dubey, N. Adhikari, S. Venkatesan and Q. Qiao, *Strategic review of secondary phases, defects and defect-complexes in kesterite CZTS–Se solar cells*. Energy Environ. Sci., 2015.
68. H. Xie, M. Dimitrievska, X. Fontané, Y. Sánchez, S. López-Marino, V. Izquierdo-Roca, V. Bermúdez, A. Pérez-Rodríguez and E. Saucedo, *Formation and impact of secondary phases in Cu-poor Zn-rich  $\text{Cu}_2\text{ZnSn}(\text{S}_{1-y}\text{Se}_y)_4$  ( $0 \leq y \leq 1$ ) based solar cells*. Solar Energy Materials and Solar Cells, 2015. **140**: p. 289-298.
69. T. Schwarz, O. Cojocar-Miredin, P. Choi, M. Mousel, A. Redinger, S. Siebentritt and D. Raabe, *Atom probe study of  $\text{Cu}_2\text{ZnSnSe}_4$  thin-films prepared by co-evaporation and post-deposition annealing*. Applied Physics Letters, 2013. **102**(4): p. 042101.
70. S. Gao, Z. Jiang, L. Wu, J. Ao, Y. Zeng, Y. Sun and Y. Zhang, *Interfaces of high-efficiency kesterite  $\text{Cu}_2\text{ZnSnS(e)}_4$  thin film solar cells*. Chinese Physics B, 2018. **27**(1): p. 018803.
71. S. Temgoua, R. Bodeux, N. Naghavi and S. Delbos, *Effects of  $\text{SnSe}_2$  secondary phases on the efficiency of  $\text{Cu}_2\text{ZnSn}(\text{S}_x\text{Se}_{1-x})_4$  based solar cells*. Thin Solid Films, 2015. **582**: p. 215-219.
72. H. Xie, Sanchez, Y., S. Lopez-Marino, M. Espindola-Rodriguez, M. Neuschitzer, D. Sylla, A. Fairbrother, V. Izquierdo-Roca, A. Perez-Rodriguez and E. Saucedo, *Impact of  $\text{Sn}(\text{S,Se})$  secondary phases in  $\text{Cu}_2\text{ZnSn}(\text{S,Se})_4$  solar cells: a chemical route for their selective removal and absorber surface passivation*. ACS Appl Mater Interfaces, 2014. **6**(15): p. 12744-51.

73. J. Koike, K. Chino, N. Aihara, H. Araki, R. Nakamura, K. Jimbo and H. Katagiri, *Cu<sub>2</sub>SnS<sub>3</sub> Thin-Film Solar Cells from Electroplated Precursors*. Japanese Journal of Applied Physics, 2012. **51**(10).
74. T. Nomura, T. Maeda, K. Takei, M. Morihama and T. Wada, *Crystal structures and band-gap energies of Cu<sub>2</sub>Sn(S,Se)<sub>3</sub> (0 ≤ x ≤ 1.0) solid solution*. physica status solidi (c), 2013. **10**(7-8): p. 1093-1097.
75. A. Crossay, *Electrodeposition and selenization of mettalic thin films for Kesterite solar cells application*. PhD thesis, 2016.
76. H. Du, F. Yan, M. Young, B. To, C.-S. Jiang, P. Dippo, D. Kuciauskas, Z. Chi, E. A. Lund, C. Hancock, W. M. Hlaing Oo, M. A. Scarpulla and G. Teeter, *Investigation of combinatorial coevaporated thin film Cu<sub>2</sub>ZnSnS<sub>4</sub>. I. Temperature effect, crystalline phases, morphology, and photoluminescence*. Journal of Applied Physics, 2014. **115**(17).
77. A. Walsh, S. Chen, X. G. Gong and S.-H. Wei, *Crystal structure and defect reactions in the kesterite solar cell absorber Cu<sub>2</sub>ZnSnS<sub>4</sub> (CZTS): Theoretical insights*, in *Physics of Semiconductors: 30th International Conference on the Physics of Semiconductors*, J. Ihm and H. Cheong, Editors. 2011.
78. A. Walsh, S. Chen, S.-H. Wei and X.-G. Gong, *Kesterite Thin-Film Solar Cells: Advances in Materials Modelling of Cu<sub>2</sub>ZnSnS<sub>4</sub>*. Advanced Energy Materials, 2012. **2**(4): p. 400-409.
79. C. J. Bosson, Birch, Max T., Halliday, Douglas P., Tang, Chiu C., Kleppe, Annette K., Hatton, Peter D., *Polymorphism in Cu<sub>2</sub>ZnSnS<sub>4</sub> and New Off-Stoichiometric Crystal Structure Types*. Chemistry of Materials, 2017. **29**(22): p. 9829-9839.
80. L. Risch, L. Vauche, A. Redinger, M. Dimitrievska, Y. Sánchez, E. Saucedo, T. Unold, T. Goislard, C.M. Ruiz, L. Escoubas and J. J. Simon, *Overcoming the Voc limitation of CZTSe solar cells*. IEEE, 2016: p. 0188-0192.
81. M. Courel, F. A. Pulgarín-Agudelo, J. A. Andrade-Arvizu and O. Vigil-Galán, *Open-circuit voltage enhancement in CdS/Cu<sub>2</sub>ZnSnSe<sub>4</sub>-based thin film solar cells: A metal–insulator–semiconductor (MIS) performance*. Solar Energy Materials and Solar Cells, 2016. **149**: p. 204-212.
82. M. Neuschitzer, K. Lienau, M. Guc, L. C. Barrio, S. Haass, J. M. Prieto, Y. Sanchez, M. Espindola-Rodriguez, Y. Romanyuk, A. Perez-Rodriguez, V. Izquierdo-Roca and E. Saucedo, *Towards high performance Cd-free CZTSe solar cells with a ZnS(O,OH) buffer layer: the influence of thiourea concentration on chemical bath deposition*. Journal of Physics D: Applied Physics, 2016. **49**(12): p. 125602.
83. S. Schorr, A. Weber, V. Honkimäki and H.-W. Schock, *In-situ investigation of the kesterite formation from binary and ternary sulphides*. Thin Solid Films, 2009. **517**(7): p. 2461-2464.
84. J. J. Scragg, P. J. Dale, D. Colombara and L. M. Peter, *Thermodynamic Aspects of the Synthesis of Thin-Film Materials for Solar Cells*. ChemPhysChem, 2012. **13**(12): p. 3035-3046.
85. A. Redinger, D. M. Berg, P. J. Dale and S. Siebentritt, *The Consequences of Kesterite Equilibria for Efficient Solar Cells*. Journal of the American Chemical Society, 2011. **133**(10): p. 3320-3323.
86. J. J. Scragg, T. Ericson, T. Kubart, M. Edoff and C. Platzer-Björkman, *Chemical Insights into the Instability of Cu<sub>2</sub>ZnSnS<sub>4</sub> Films during Annealing*. Chemistry of Materials, 2011. **23**(20): p. 4625-4633.
87. J. Zhong, Z. Xia, M. Luo, J. Zhao, J. Chen, L. Wang, X. Liu, D.-J. Xue, Y.-B. Cheng, H. Song and J. Tang, *Sulfurization induced surface constitution and its correlation to the performance of solution-processed Cu<sub>2</sub>ZnSn(S,Se)<sub>4</sub> solar cells*. Scientific Reports, 2014. **4**.

88. J. He, L. Sun, Y. Chen, J. Jiang, P. Yang and J. Chu, *Influence of sulfurization pressure on Cu<sub>2</sub>ZnSnS<sub>4</sub> thin films and solar cells prepared by sulfurization of metallic precursors*. Journal of Power Sources, 2015. **273**(0): p. 600-607.
89. H. Katagiri, K. Jimbo, S. Yamada, T. Kamimura, W. S. Maw, T. Fukano, T. Ito and T. Motohiro, *Enhanced conversion efficiencies of Cu<sub>2</sub>ZnSnS<sub>4</sub>-based thin film solar cells by using preferential etching technique*. Applied Physics Express, 2008. **1**(4).
90. B.-S. Kim, J.-C. Lee, H.-S. Yoon and S.-K. Kim, *Reduction of SnO<sub>2</sub> with Hydrogen*. Materials Transactions, 2011. **52**(9): p. 1814-1817.
91. X. Zhang and M. Kobayashi, *Study of the Growth Mechanism of Cu<sub>2</sub>ZnSnS<sub>4</sub> Films Fabricated by Nanoparticle during the Annealing Process*. Progress In Electromagnetic Research Symposium (PIERS), 2016.
92. M. Raghuwanshi, *Influence of Grain Boundary Chemistry on the properties of CIGS photovoltaic cells*. PhD thesis, 2016.
93. Z. R. Bouchama Idris, Djessas Kamal, Boulouf Abdessalam and Ghribi Faouzi, *Size and Grain-Boundary Effects on the Performance of Polycrystalline CIGS-Based Solar Cells*. 6th International Renewable Energy Congress (IREC), 2015.
94. Y.-R. Lin, T.-C. Chou, L.-K. Liu, L.-C. Chen and K.-H. Chen, *A facile and green synthesis of copper zinc tin sulfide materials for thin film photovoltaics*. Thin Solid Films, 2016. **618**: p. 124-129.
95. K. Maeda, K. Tanaka, Y. Nakano and H. Uchiki, *Annealing Temperature Dependence of Properties of Cu<sub>2</sub>ZnSnS<sub>4</sub> Thin Films Prepared by Sol–Gel Sulfurization Method*. Japanese Journal of Applied Physics, 2011. **50**(5).
96. A. Emrani, P. Vasekar and C. R. Westgate, *Effects of sulfurization temperature on CZTS thin film solar cell performances*. Solar Energy, 2013. **98**, Part C(0): p. 335-340.
97. T. K. Todorov, J. Tang, S. Bag, O. Gunawan, T. Gokmen, Y. Zhu and D. B. Mitzi, *Beyond 11% Efficiency: Characteristics of State-of-the-Art Cu<sub>2</sub>ZnSn(S,Se)<sub>4</sub> Solar Cells*. Advanced Energy Materials, 2013. **3**(1): p. 34-38.
98. A. Emrani, P. Vasekar and C. R. Westgate, *Effects of sulfurization temperature on CZTS thin film solar cell performances*. Solar Energy, 2013. **98**: p. 335-340.
99. G. Chen, W. Liu, G. Jiang, B. Pan and C. Zhu, *Effect of compact structure on the phase transition in the oxides derived Cu<sub>2</sub>ZnSnSe<sub>4</sub> thin films*. Solar Energy, 2013. **92**: p. 172-175.
100. C. M. Sutter-Fella, A. R. Uhl, Y. E. Romanyuk and A. N. Tiwari, *Large-grained Cu<sub>2</sub>ZnSnS<sub>4</sub> layers sintered from Sn-rich solution-deposited precursors*. physica status solidi (a), 2014: p. n/a-n/a.
101. S. M. Pawar, A. I. Inamdar, K. V. Gurav, S. W. Shin, Y. Jo, J. Kim, H. Im and J. H. Kim, *Growth of void free Cu<sub>2</sub>ZnSnS<sub>4</sub> (CZTS) thin films by sulfurization of stacked metallic precursor films*. Vacuum, 2014. **104**(0): p. 57-60.
102. K. Timmo, M. Kauk-Kuusik, M. Pilvet, T. Raadik, M. Altosaar, M. Danilson, M. Grossberg, J. Raudoja and K. Ernits, *Influence of order-disorder in Cu<sub>2</sub>ZnSnS<sub>4</sub> powders on the performance of monograin layer solar cells*. Thin Solid Films, 2017. **633**: p. 122-126.
103. J. J. S. Scragg, L. Choubrac, A. Lafond, T. Ericson and C. Platzer-Björkman, *A low-temperature order-disorder transition in Cu<sub>2</sub>ZnSnS<sub>4</sub> thin films*. Applied Physics Letters, 2014. **104**(4).
104. G. E. Norman, Saitov, I. M., *Fluid–fluid–solid triple point on melting curves at high temperatures*. Journal of Physics: Conference Series, 2016. **774**.
105. L. Son, G. Rusakov and N. Katkov, *Pressure–temperature phase diagrams of selenium and sulfur in terms of Patashinski model*. Physica A: Statistical Mechanics and its Applications, 2003. **324**(3-4): p. 634-644.



106. I. Martinez, *Basic and applied thermodynamics, Chapter 6: Thermodynamics of phase change*. Available online at <http://webserver.dmt.upm.es/~isidoro/bk3/c06/Phase%20change.pdf>.
107. G. Brammertz, Y. Ren, M. Buffière, S. Mertens, J. Hendrickx, H. Marko, A. E. Zaghi, N. Lenaers, C. Köble, J. Vleugels, M. Meuris and J. Poortmans, *Electrical characterization of Cu<sub>2</sub>ZnSnSe<sub>4</sub> solar cells from selenization of sputtered metal layers*. Thin Solid Films, 2013. **535**: p. 348-352.
108. J. Zhong, Z. Xia, M. Luo, J. Zhao, J. Chen, L. Wang, X. Liu, D. J. Xue, Y. B. Cheng, H. Song and J. Tang, *Sulfurization induced surface constitution and its correlation to the performance of solution-processed Cu<sub>2</sub>ZnSn(S,Se)<sub>4</sub> solar cells*. Sci Rep, 2014. **4**: p. 6288.
109. C. Platzer-Bjorkman, J. Scragg, H. Flammersberger, T. Kubart and M. Edoff, *Influence of precursor sulfur content on film formation and compositional changes in Cu<sub>2</sub>ZnSnS<sub>4</sub> films and solar cells*. Solar Energy Materials and Solar Cells, 2012. **98**: p. 110-117.
110. Y. Ren, M. Richter, J. Keller, A. Redinger, T. Unold, O. Donzel-Gargand, J. J. S. Scragg and C. Platzer Björkman, *Investigation of the SnS/Cu<sub>2</sub>ZnSnS<sub>4</sub> Interfaces in Kesterite Thin-Film Solar Cells*. ACS Energy Letters, 2017. **2**(5): p. 976-981.
111. U. Ghorpade, M. Suryawanshi, S. W. Shin, K. Gurav, P. Patil, S. Pawar, C. W. Hong, J. H. Kim and S. Kolekar, *Towards environmentally benign approaches for the synthesis of CZTSSe nanocrystals by a hot injection method: a status review*. Chemical Communications, 2014. **50**(77): p. 11258-11273.
112. X. G. Weiwei Sun, Lohnathan. Armstrong , Lingbiao Cui, and Tar-Pin Chen, *Experimental and Theoretical Study on Band Gap Tuning of Cu<sub>2</sub>ZnSn(Si<sub>x</sub>Se<sub>1-x</sub>)<sub>4</sub> Absorbers for Thin-Film Solar Cells*. IEEE, 2014: p. 421-424.
113. M. P. Suryawanshi, G. L. Agawane, S. M. Bhosale, S. W. Shin, P. S. Patil, J. H. Kim and A. V. Moholkar, *CZTS based thin film solar cells: a status review*. Materials Technology, 2013. **28**(1-2): p. 98-109.
114. H. Katagiri, K. Saitoh, T. Washio, H. Shinohara, T. Kurumadani and S. Miyajima, *Development of thin film solar cell based on Cu<sub>2</sub>ZnSnS<sub>4</sub> thin films*. Solar Energy Materials and Solar Cells, 2001. **65**(1-4): p. 141-148.
115. I. Repins, C. Beall, N. Vora, C. Dehart, D. Kuciauskas, P. Dippo, B. To, J. Mann, W. C. Hsu, A. Goodrich and R. Noufi, *Co-evaporated Cu<sub>2</sub>ZnSnSe<sub>4</sub> films and devices*. Solar Energy Materials and Solar Cells, 2012. **101**: p. 154-159.
116. K. I. a. T. Nakazawa, *Electrical and Optical Properties of Stannite-Type Quaternary Semiconductor Thin Films*. Japanese Journal of Applied Physics Letters A, 1988. **27**: p. 2094-2097.
117. N. Momose, M. T. Htay, T. Yudasaka, S. Igarashi, T. Seki, S. Iwano, Y. Hashimoto and K. Ito, *Cu<sub>2</sub>ZnSnS<sub>4</sub> Thin Film Solar Cells Utilizing Sulfurization of Metallic Precursor Prepared by Simultaneous Sputtering of Metal Targets*. Japanese Journal of Applied Physics, 2011. **50**.
118. S. Tajima, M. Umehara, M. Hasegawa, T. Mise and T. Itoh, *Cu<sub>2</sub>ZnSnS<sub>4</sub> photovoltaic cell with improved efficiency fabricated by high-temperature annealing after CdS buffer-layer deposition*. Progress in Photovoltaics: Research and Applications, 2017. **25**(1): p. 14-22.
119. L. D. R. D. P. W. Siripala, K.T.L. De Silva, J.K.D.S. Jayanetti, I.M. Dharmadasa, *Study of annealing effects of cuprous oxide grown by electrodeposition technique*. Solar Energy Materials and Solar Cells, 1996. **44**: p. 251-260.
120. L. Vauche, L. Risch, Y. Sánchez, M. Dimitrievska, M. Pasquinelli, T. Goislar De Monsabert, P.-P. Grand, S. Jaime-Ferrer and E. Saucedo, *8.2% pure selenide kesterite thin-film solar cells from large-area electrodeposited precursors*. Progress in Photovoltaics: Research and Applications, 2016. **24**(1): p. 38-51.

121. F. J. S. I. T. H. M. Matsumura, *Pure Sulfide Cu<sub>2</sub>ZnSnS<sub>4</sub> Thin Film Solar Cells Fabricated by Preheating an Electrodeposited Metallic Stack* Advanced Energy Materials, 2014. **4**(7).
122. Y. Cai, J. C. Ho, S. K. Batabyal, W. Liu, Y. Sun, S. G. Mhaisalkar and L. H. Wong, *Nanoparticle-induced grain growth of carbon-free solution-processed CuIn(S,Se)<sub>2</sub> solar cell with 6% efficiency*. ACS Appl Mater Interfaces, 2013. **5**(5): p. 1533-7.
123. W. Li, J. M. R. Tan, S. W. Leow, S. Lie, S. Magdassi and L. H. Wong, *Recent Progress in Solution-Processed Copper-Chalcogenide Thin-Film Solar Cells*. Energy Technology, 2018. **6**(1): p. 46-59.
124. T. Todorov and D. B. Mitzi, *Direct Liquid Coating of Chalcopyrite Light-Absorbing Layers for Photovoltaic Devices*. European Journal of Inorganic Chemistry, 2010(1): p. 17-28.
125. K. Tanaka, M. Oonuki, N. Moritake and H. Uchiki, *Cu<sub>2</sub>ZnSnS<sub>4</sub> thin film solar cells prepared by non-vacuum processing*. Solar Energy Materials and Solar Cells, 2009. **93**(5): p. 583-587.
126. T. K. Todorov, K. B. Reuter and D. B. Mitzi, *High-Efficiency Solar Cell with Earth-Abundant Liquid-Processed Absorber*. Advanced Materials, 2010. **22**(20): p. E156-E159.
127. K. Woo, Y. Kim and J. Moon, *A non-toxic, solution-processed, earth abundant absorbing layer for thin-film solar cells*. Energy & Environmental Science, 2012. **5**(1): p. 5340-5345.
128. C. K. Miskin, W.-C. Yang, C. J. Hages, N. J. Carter, C. S. Joglekar, E. A. Stach and R. Agrawal, *9.0% efficient Cu<sub>2</sub>ZnSn(S,Se)<sub>4</sub> solar cells from selenized nanoparticle inks*. Progress in Photovoltaics: Research and Applications, 2014: p. n/a-n/a.
129. W. Wang, M. T. Winkler, O. Gunawan, T. Gokmen, T. K. Todorov, Y. Zhu and D. B. Mitzi, *Device Characteristics of CZTSSe Thin-Film Solar Cells with 12.6% Efficiency*. Advanced Energy Materials, 2014. **4**(7): p. n/a-n/a.
130. G. Chen, C. Yuan, J. Liu, Z. Huang, S. Chen, W. Liu, G. Jiang and C. Zhu, *Fabrication of Cu<sub>2</sub>ZnSnS<sub>4</sub> thin films using oxides nanoparticles ink for solar cell*. Journal of Power Sources, 2015. **276**: p. 145-152.
131. V. K. Kapur, A. Bansal, P. Le and O. I. Asensio, *Non-vacuum processing of CuIn<sub>1-x</sub>GaxSe<sub>2</sub> solar cells on rigid and flexible substrates using nanoparticle precursor inks*. Thin Solid Films, 2003. **431-432**: p. 53-57.
132. M. Wu, G. Chen, X. Wu, J. Zhao, L. Lin, J. Liu, W. Wang and F. Lai, *Sulfurization and post-selenization of oxides precursors for high quality CuIn(S, Se)<sub>2</sub> thin films*. Materials Science in Semiconductor Processing, 2016. **48**: p. 33-38.
133. G. Chen, B. Pan, L. Jin, G. Jiang, W. Liu and C. Zhu, *Compression for smoothing and densifying CuInSe<sub>2</sub> and Cu<sub>2</sub>ZnSnSe<sub>4</sub> thin films coating from oxides nanoparticles precursor*. Journal of Alloys and Compounds, 2014. **610**: p. 20-26.
134. Y. Wang and H. Gong, *Cu<sub>2</sub>ZnSnS<sub>4</sub> synthesized through a green and economic process*. Journal of Alloys and Compounds, 2011. **509**(40): p. 9627-9630.
135. W. Yao, Y. Wang, L. Wang, X. Wang and Z. Zhang, *Characterization and preparation of Cu<sub>2</sub>ZnSnS<sub>4</sub> thin films by ball-milling, coating and sintering*. Materials Letters, 2014. **134**(0): p. 168-171.
136. C. L. A. Ricardo, M. S. Su'ait, M. Mueller and P. Scardi, *Production of Cu-2(Zn,Fe)SnS<sub>4</sub> powders for thin film solar cell by high energy ball milling*. Journal of Power Sources, 2013. **230**: p. 70-75.
137. C. Suryanarayana, *Mechanical alloying and milling*. Progress in Materials Science, 2001. **46**(1-2): p. 1-184.
138. N. Kotake, M. Kuboki, S. Kiya and Y. Kanda, *Influence of dry and wet grinding conditions on fineness and shape of particle size distribution of product in a ball mill*. Advanced Powder Technology, 2011. **22**(1): p. 86-92.



139. *Material Safety Data Sheet, Isopropyl Alcohol*. Online Available at [http://www.tsi.com/uploadedFiles/Site\\_Root/Products/Literature/MSDS/1080546-MSDS-Isopropyl-Alcohol-TSI.pdf](http://www.tsi.com/uploadedFiles/Site_Root/Products/Literature/MSDS/1080546-MSDS-Isopropyl-Alcohol-TSI.pdf), 2015.
140. B. Ananthoju, J. Mohapatra, M. K. Jangid, D. Bahadur, N. V. Medhekar and M. Aslam, *Cation/Anion Substitution in Cu<sub>2</sub>ZnSnS<sub>4</sub> for Improved Photovoltaic Performance*. Sci Rep, 2016. **6**: p. 35369.
141. P. Mao, Q. Zhou, Z. Jin, H. Li and J. Wang, *Efficiency-Enhanced Planar Perovskite Solar Cells via an Isopropanol/Ethanol Mixed Solvent Process*. ACS Appl Mater Interfaces, 2016. **8**(36): p. 23837-43.
142. B. M. Basol, *Low cost techniques for the preparation of Cu(In,Ga)(Se,S)<sub>2</sub> absorber layers*. Thin Solid Films, 2000. **361**: p. 514-519.
143. Y. M. J. Kubo, T. Wada, A. Yamada, and M. Konagai *Fabrication of Cu(In,Ga)Se<sub>2</sub> films by a combination of mechanochemical synthesis, wet bead milling, and screen-printing/sintering process*. Material Research Society, 2009: p. 13-19.
144. M. Kaelin, D. Rudmann and A. N. Tiwari, *Low cost processing of CIGS thin film solar cells*. Solar Energy, 2004. **77**(6): p. 749-756.
145. B. Vidhya, S. Velumani, J. A. Arenas-Alatorre, A. Morales-Acevedo, R. Asomoza and J. A. Chavez-Carvayar, *Structural studies of mechano-chemically synthesized CuIn<sub>1-x</sub>Ga<sub>x</sub>Se<sub>2</sub> nanoparticles*. Materials Science and Engineering: B, 2010. **174**(1-3): p. 216-221.
146. A. E. Zaghi, M. Buffière, J. Koo, G. Brammertz, M. Batuk, C. Verbist, J. Hadermann, W. K. Kim, M. Meuris, J. Poortmans and J. Vleugels, *Effect of selenium content of CuInSe<sub>x</sub> alloy nanopowder precursors on recrystallization of printed CuInSe<sub>2</sub> absorber layers during selenization heat treatment*. Thin Solid Films, 2015. **582**: p. 11-17.
147. Z. Zhou, Y. Wang, D. Xu and Y. Zhang, *Fabrication of Cu<sub>2</sub>ZnSnS<sub>4</sub> screen printed layers for solar cells*. Solar Energy Materials and Solar Cells, 2010. **94**(12): p. 2042-2045.
148. C. Li, B. Yao, Y. Li, Z. Xiao, Z. Ding, H. Zhao, L. Zhang and Z. Zhang, *Fabrication, characterization and application of Cu<sub>2</sub>ZnSn(S,Se)<sub>4</sub> absorber layer via a hybrid ink containing ball milled powders*. Journal of Alloys and Compounds, 2015. **643**: p. 152-158.
149. D. Pareek, K. R. Balasubramaniam and P. Sharma, *Synthesis and characterization of bulk Cu<sub>2</sub>ZnSnX<sub>4</sub> (X: S, Se) via thermodynamically supported mechano-chemical process*. Materials Characterization, 2015. **103**: p. 42-49.
150. D. Pareek, K. R. Balasubramaniam and P. Sharma, *Reaction pathway for synthesis of Cu<sub>2</sub>ZnSn(S/Se)<sub>4</sub> via mechano-chemical route and annealing studies*. Journal of Materials Science: Materials in Electronics, 2016. **28**(2): p. 1199-1210.
151. S. Zhuk, A. Kushwaha, T. K. S. Wong, S. Masudy-Panah, A. Smirnov and G. K. Dalapati, *Critical review on sputter-deposited Cu<sub>2</sub>ZnSnS<sub>4</sub> (CZTS) based thin film photovoltaic technology focusing on device architecture and absorber quality on the solar cells performance*. Solar Energy Materials and Solar Cells, 2017. **171**: p. 239-252.
152. C. Y. Kaiwen Sun, Fangyang Liu, Jialiang Huang, Fangzhou Zhou, John A. Stride, Martin Green, Xiaojing Hao, *Over 9% Efficient Kesterite Cu<sub>2</sub>ZnSnS<sub>4</sub> Solar Cell Fabricated by Using Zn<sub>1-x</sub>Cd<sub>x</sub>S Buffer Layer*. Advanced energy Material, 2016. **6**(12).
153. S. K. Jianjun Li, Dahyun Nam, Xiaoru Liu, Junho Kim, Hyeonsik Cheong, Wei Liu, Hui Li, Yun Sun, Yi Zhang, *Tailoring the defects and carrier density for beyond 10% efficient CZTSe thin film solar cells*. Solar Energy Materials and Solar Cells, 2017. **159**: p. 447-455.
154. R. A. Wibowo, H. Yoo, A. Hoelzing, R. Lechner, S. Jost, J. Palm, M. Gowtham, B. Louis and R. Hock, *A study of kesterite Cu<sub>2</sub>ZnSn(Se,S)<sub>4</sub> formation from sputtered Cu-Zn-Sn metal precursors by rapid thermal processing sulfo-selenization of the metal thin films*. Thin Solid Films, 2013. **535**: p. 57-61.

155. N. S. Homare Hiroi, Takuya Kato, and Hiroki Sugimoto, *High Voltage Cu<sub>2</sub>ZnSnS<sub>4</sub> Submodules by Hybrid Buffer Layer*. IEEE 2013(39): p. 0863-0866.
156. K. W. Byungha Shin, Oki Gunawan, Kathleen B. Reuter, S. Jay Chey, Nestor A. Bojarczuk, Teodor Todorov, David B. Mitzi, and Supratik Guha, *High efficiency Cu<sub>2</sub>ZnSn(S<sub>x</sub>Se<sub>1-x</sub>)<sub>4</sub> thin film solar cells by thermal coevaporation*. J. Watson Research Center, 2011. **978**(1): p. 2510-2514.
157. J. M. R. T. Z. Su , X. Li , X. Zeng , S. K. Batabyal , L. H. Wong, *Cation Substitution of Solution-Processed Cu<sub>2</sub>ZnSnS<sub>4</sub> Thin Film Solar Cell with over 9% Efficiency*. Advanced energy Material, 2015. **5**(19): p. 1500682.
158. M. D. S. G. Haass, M. Werner, B. Bissig, Y. E. Romanyuk, A. N. Tiwari, *11.2% Efficient Solution Processed Kesterite Solar Cell with a Low Voltage Deficit*. Advanced Energy Material, 2015. **5**(18): p. 1500712.
159. R. H. E. R. Don, *The structure of CuInSe<sub>2</sub> films formed by co-evaporation of the elements* Solar Cells, 1986. **16**: p. 131-142.
160. V. Fthenakis, *Sustainability metrics for extending thin-film photovoltaics to terawatt levels*. MRS Bulletin, 2012. **37**(04): p. 425-430.
161. R. Ayres, *Life cycle analysis: A critique Resources, Conservation and Recycling and recycling*. Resources, Conservation and Recycling and recycling, 1995. **14**(3-4): p. 199-223.
162. V. M. Fthenakis and H. C. Kim, *Photovoltaics: Life-cycle analyses*. Solar Energy, 2011. **85**(8): p. 1609-1628.
163. I. 14040, *Environmental management — Life cycle assessment — Principles and framework*. 2006.
164. M. J. D. W.-S. E.A. Alsema, *Environmental life cycle assessment of Advanced silicon solar cell technologies*. Conference paper, 2004. **19th European Photovoltaic Solar Energy Conference**.
165. C. E. L. Latunussa, F. Ardente, G. A. Blengini and L. Mancini, *Life Cycle Assessment of an innovative recycling process for crystalline silicon photovoltaic panels*. Solar Energy Materials and Solar Cells, 2016. **156**: p. 101-111.
166. B. P. K. Collins, A. Anctil, *Life cycle assessment of Silicon Solar Panels manufacturing in the United states*. IEEE, 2005.
167. V. Fthenakis, *Sustainability of photovoltaics: The case for thin-film solar cells*. Renewable and Sustainable Energy Reviews, 2009. **13**(9): p. 2746-2750.
168. V. Fthenakis, J. E. Mason and K. Zweibel, *The technical, geographical, and economic feasibility for solar energy to supply the energy needs of the US*. Energy Policy, 2009. **37**(2): p. 387-399.
169. Z. S. Ilke Celik , Michael J. Heben, Yanfa Yan and Defne S. Apul, *Life Cycle toxicity analysis of emerging PV cells*. IEEE, 2016.
170. J. Collier, S. Wu and D. Apul, *Life cycle environmental impacts from CZTS (copper zinc tin sulfide) and Zn<sub>3</sub>P<sub>2</sub> (zinc phosphide) thin film PV (photovoltaic) cells*. Energy, 2014. **74**(0): p. 314-321.
171. <https://www.powersystemsdesign.com/articles/lbm-solar-frontier-tok-and-delsolar-partner-to-develop-low-cost-czts-pv-cells/10/5550>.
172. S. Swann, *Magnetron Sputtering*. Phys Techno1, 1988
173. <http://www.semicore.com/news/71-thin-film-deposition-thermal-evaporation>.
174. O. a. A. <https://opsdiagnostics.com/notes/ranpri/mediatypes.htm>.
175. M. M. A. Berni, H. Schmidt, *Chapter 10 Sol-Gel Technologies for Glass Producers and Users Doctor Blade*. 2004: p. 89-92

176. Q.-M. Chen, Z.-Q. Li, Y. Ni, S.-Y. Cheng and X.-M. Dou, *Doctor-bladed Cu<sub>2</sub>ZnSnS<sub>4</sub> light absorption layer for low-cost solar cell application*. Chinese Physics B, 2012. **21**(3): p. 038401.
177. F. C. Krebs, *Fabrication and processing of polymer solar cells: A review of printing and coating techniques*. Solar Energy Materials and Solar Cells, 2009. **93**(4): p. 394-412.
178. R. R. Søndergaard, M. Hösel and F. C. Krebs, *Roll-to-Roll fabrication of large area functional organic materials*. Journal of Polymer Science Part B: Polymer Physics, 2013. **51**(1): p. 16-34.
179. O. a. A. <https://sites.google.com/site/donsairbrushtips/badger-sotar>.
180. X. Ding, J. Liu and T. a. L. Harris, *A review of the operating limits in slot die coating processes*. AIChE Journal, 2016. **62**(7): p. 2508-2524.
181. Z. W. S. Mazzamuto, G. Kissling, T.M. Watson, L.M. Peter, N.M. Pearsall, I. Forbes, *Two-Stage Synthesis of CZTS thin Films and the Influence of Geometry and Sulphur and Tin Sulphide Supply* PVSAT-12 Conference, 2015.
182. J. B. Chaudhari, *Growth and study of optical and electrical properties of chemically deposited CdS<sub>1-x</sub>Sex:Ag nanocomposite thin films for sensor application*. PhD thesis, Chapter 4 2014.
183. B. N. S. Business, *DektakXT Stylus Profilometer User Manual*. 2011.
184. M. I. Ltd., *Mastersizer-2000-manual guide*. 2007(1).
185. M. I. Ltd, *Wet or liquid dispersion method development for laser diffraction particle size measurements*. 2013.
186. L. Grahame, *Scanning electron microscopy and x-ray microanalysis*. 1987.
187. C. S. a. W. D. Kaplan, *Introduction to Scanning Electron Microscopy* 2012.
188. M. N. Daniel Abou-Ras, Manuel J. Romero, and Sebastian S. Schmidt, *Advanced Characterization Techniques for Thin Film Solar Cells* Chapter 12, Electron Microscopy on Thin Films for Solar Cells, 2011.
189. F. Y. Zhu, Q. Q. Wang, X. S. Zhang, W. Hu, X. Zhao and H. X. Zhang, *3D nanostructure reconstruction based on the SEM imaging principle, and applications*. Nanotechnology, 2014. **25**(18): p. 185705.
190. "Signals in Scanning Electron Microscopy" online available at [http://www.microscopy.ethz.ch/sem\\_detectors.htm](http://www.microscopy.ethz.ch/sem_detectors.htm).
191. "The energy table for EDX analysis" available online at <https://www.unamur.be/services/microscopie/sme-documents/Energy-20table-20for-20EDS-20analysis-1.pdf>.
192. M. N. Daniel Abou-Ras, Manuel J. Romero, and Sebastian S. Schmidt, *Advanced Characterization Techniques for Thin Film Solar Cells* Daniel Chapter 12, Electron Microscopy on Thin Films for Solar Cells, 2016.
193. J. J. Friel, *X-Ray and image analysis in electron microscopy*. 2003.
194. C. S. Susan Schorr, Tobias Torndahl, and Roland Mainz, *Advanced Characterization Techniques for Thin Film Solar Cells*. Chapter 13, X-Ray and Neutron Diffraction on Materials for Thin-Film Solar Cells, 2011.
195. A. W. H. Zhou Jian, *The Physical Meanings of 5 Basic Parameters for an X-Ray Diffraction Peak and Their Application*. Chinese Journal of Geochemistry 2003. **22**(1): p. 38-44.
196. V. I.-R. Jacobo Alvarez-García, And Alejandro Perez-Rodríguez, *Advanced Characterization Techniques for Thin Film Solar Cells*. Chapter 14, Raman Spectroscopy on Thin Films for Solar Cells, 2016.
197. B. Pani, R. K. Singh and U. P. Singh, *Impact of pre-annealing temperature on the formation of Cu<sub>2</sub>ZnSnS<sub>4</sub> absorber layer*. Journal of Alloys and Compounds, 2015. **648**: p. 332-337.

198. S. Y. a. O. Akkus, *Fluorescence Background Problem in Raman Spectroscopy: Is 1064 nm Excitation an Improvement of 785 nm?* 2013.
199. G. J.-D. H. Solache-Carranco, M. Galván-Arellano, J. Martínez-Juárez, G. Romero-Paredes R, and R. Peña-Sierra, *Raman Scattering and Photoluminescence Studies on Cu<sub>2</sub>O* IEEE, 2008: p. 421-424.
200. X. W. Guo, X. P. Fang, Y. Sun, L. Y. Shen, Z. X. Wang and L. Q. Chen, *Lithium storage in carbon-coated SnO<sub>2</sub> by conversion reaction*. Journal of Power Sources, 2013. **226**: p. 75-81.
201. M. Abdelfatah, J. Ledig, A. El-Shaer, A. Wagner, A. Sharafeev, P. Lemmens, M. M. Mosaad, A. Waag and A. Bakin, *Fabrication and characterization of flexible solar cell from electrodeposited Cu<sub>2</sub>O thin film on plastic substrate*. Solar Energy, 2015. **122**: p. 1193-1198.
202. L. Sangaletti, L. E. Depero, B. Allieri, F. Pioselli, E. Comini, G. Sberveglieri and M. Zocchi, *Oxidation of Sn Thin Films to SnO<sub>2</sub>. Micro-Raman Mapping and X-ray Diffraction Studies*. Journal of Materials Research, 2011. **13**(09): p. 2457-2460.
203. M. Dimitrievska, A. Fairbrother, X. Fontané, T. Jawhari, V. Izquierdo-Roca, E. Saucedo and A. Pérez-Rodríguez, *Multiwavelength excitation Raman scattering study of polycrystalline kesterite Cu<sub>2</sub>ZnSnS<sub>4</sub> thin films*. Applied Physics Letters, 2014. **104**(2): p. -.
204. D. Colombara, P. J. Dale, G. P. Kissling, L. M. Peter and S. Tombolato, *Photoelectrochemical Screening of Solar Cell Absorber Layers: Electron Transfer Kinetics and Surface Stabilization*. The Journal of Physical Chemistry C, 2016. **120**(29): p. 15956-15965.
205. L. M. Peter, *Dynamic Aspects of semiconductor photo electrochemistry* Chem. Rev., 1990. **90**: p. 753-769.
206. S. Khoshmashrab, M. J. Turnbull, D. Vaccarello, Y. Nie, S. Martin, D. A. Love, P. K. Lau, X. Sun and Z. Ding, *Effects of Cu content on the photoelectrochemistry of Cu<sub>2</sub>ZnSnS<sub>4</sub> nanocrystal thin films*. Electrochimica Acta, 2015. **162**: p. 176-184.
207. S. S. Hegedus and W. N. Shafarman, *Thin-film solar cells: device measurements and analysis*. Progress in Photovoltaics: Research and Applications, 2004. **12**(23): p. 155-176.
208. D. Colombara, E. V. C. Robert, A. Crossay, A. Taylor, M. Guennou, M. Arasimowicz, J. C. B. Malaquias, R. Djemour and P. J. Dale, *Quantification of surface ZnSe in Cu<sub>2</sub>ZnSnSe<sub>4</sub>-based solar cells by analysis of the spectral response*. Solar Energy Materials and Solar Cells, 2014. **123**(0): p. 220-227.
209. N. Vora, J. Blackburn, I. Repins, C. Beall, B. To, J. Pankow, G. Teeter, M. Young and R. Noufi, *Phase identification and control of thin films deposited by co-evaporation of elemental Cu, Zn, Sn, and Se*. Journal of Vacuum Science & Technology A, 2012. **30**(5).
210. J. J. Scragg, T. Kubart, J. T. Wätjen, T. Ericson, M. K. Linnarsson and C. Platzer-Björkman, *Effects of back contact instability on Cu<sub>2</sub>ZnSnS<sub>4</sub> devices and processes*. Chemistry of Materials, 2013. **25**(15): p. 3162-3171.
211. J. Márquez-Prieto, M. V. Yakushev, I. Forbes, J. Krustok, P. R. Edwards, V. D. Zhivulko, O. M. Borodavchenko, A. V. Mudryi, M. Dimitrievska, V. Izquierdo-Roca, N. M. Pearsall and R. W. Martin, *Impact of the selenisation temperature on the structural and optical properties of CZTSe absorbers*. Solar Energy Materials and Solar Cells, 2016. **152**: p. 42-50.
212. H. Yoo, R. A. Wibowo, A. Hoelzing, R. Lechner, J. Palm, S. Jost, M. Gowtham, F. Sorin, B. Louis and R. Hock, *Investigation of the solid state reactions by time-resolved X-ray diffraction while crystallizing kesterite Cu<sub>2</sub>ZnSnSe<sub>4</sub> thin films*. Thin Solid Films, 2013. **535**: p. 73-77.

213. H. X. A. D. Collord, And H. W. Hillhouse, *Combinatorial Exploration of the Effects of Intrinsic and Extrinsic Defects in Cu<sub>2</sub>ZnSn(S,Se)<sub>4</sub>*. IEEE Journal of Photovoltaics, 2015. **5**(1): p. 288-298.
214. J. Márquez, M. Neuschitzer, M. Dimitrievska, R. Gunder, S. Haass, M. Werner, Y. E. Romanyuk, S. Schorr, N. M. Pearsall and I. Forbes, *Systematic compositional changes and their influence on lattice and optoelectronic properties of Cu<sub>2</sub>ZnSnSe<sub>4</sub> kesterite solar cells*. Solar Energy Materials and Solar Cells, 2016. **144**: p. 579-585.
215. H. R. Jung, S. W. Shin, K. V. Gurav, M. P. Suryawanshi, C. W. Hong, H. S. Yang, J. Y. Lee, J. H. Moon and J. H. Kim, *Phase evolution of Cu<sub>2</sub>ZnSnS<sub>4</sub> (CZTS) kesterite thin films during the sulfurization process*. Ceramics International, 2015.
216. S. B. S. Gerbinet , A. Léonard, *Life Cycle Analysis (LCA) of photovoltaic panels: A review*. Renewable and Sustainable Energy Reviews, 2014. **38**: p. 747-753.
217. K. P. Bhandari, J. M. Collier, R. J. Ellingson and D. S. Apul, *Energy payback time (EPBT) and energy return on energy invested (EROI) of solar photovoltaic systems: A systematic review and meta-analysis*. Renewable and Sustainable Energy Reviews, 2015. **47**: p. 133-141.
218. S. Tajima, T. Fukano and H. Katagiri, *Chemical bath deposition (CBD) solution for buffer layers of photoelectric elements e.g. copper-zinc-tin sulfide type semiconductors, comprises aqueous solution containing sulfide synthetic adjuvant, cadmium acetate, and sulfur source*. Toyota Chuo Kenkyusho Kk; Dokuritsu Gyosei Hojin Kokuritsu Kenko.
219. J. Rousset, E. Saucedo, K. Herz and D. Lincot, *High efficiency CIGS-based solar cells with electrodeposited ZnO:Cl as transparent conducting oxide front contact*. Progress in Photovoltaics, 2011. **19**(5): p. 537-546.
220. K. Bekkelund, *Thesis: A Comparative Life Cycle Assessment of PV Solar Systems*. Norwegian University of Science and Technology, 2013.
221. M. S. Niels Jungbluth, Karin Flury, Rolf Frischknecht, Sybille Büsser, *Life Cycle Inventories of Photovoltaics*. 2012.
222. M. O. Pré Consultants, Ruba Dolfing, *Update Instructions Sima Pro 8.2 to Sima Pro 8.3*. 2016.
223. C. S. D. Kralisch, D. Ott, S. Bensaid, G. Saracco, P. Bellantonio, and P. Loebd, *Process design accompanying life cycle management and risk analysis as a decision support tool for sustainable biodiesel production*. Green Chem., 2013. **15**(2): p. 463-477.
224. A. D. S. S. Humbert, M. Margni, O. Jolliet, *IMPACT 2002+: A new life cycle impact assessment methodology*. The International Journal of Life Cycle Assessment, 2003. **8**(6): p. 324-330.
225. Z. S. I. Celik, A. J. Cimaroli, Y. Yan, M. J. Heben, D. Apul, *Life Cycle Assessment (LCA) of perovskite PV cells projected from lab to fab*. Solar Energy Materials and Solar Cells, 2016. **156**(0): p. 157-169.
226. Bruno Peuportier, Sabina Scarpellini, Mauritz Glaumann, Tove Malmqvist, Guri Krigsvol, Christian Wetzels, Heimo Staller, Zsuzsa Szalay, Valeria Degiovanni and Evelina Stoykova, *Energy Saving through Promotion of Life Cycle Assessment in Buildings*.
227. N. Y. William H. Osborn, N. Y., *Tin Recovery Process*. 1942. **United States Patent Office**.
228. W. H. O. I. Geneva, *Tin and inorganic tin compounds*. Concise International Chemical Assessment Document 65 2005.
229. A. W. G. Marco De Paoli, *Electrochemistry, Polymers and Opto-Electronic Devices: A Combination with a Future*. J. Braz. Chem. Soc, 2002. **13**(4): p. 410-424.
230. P. Dias, T. Lopes, L. Andrade and A. Mendes, *Temperature effect on water splitting using a Si-doped hematite photoanode*. Journal of Power Sources, 2014. **272**: p. 567-580.
231. A. O. A. [https://www.thorlabs.com/Newgrouppage9.cfm?Objectgroup\\_Id=2615](https://www.thorlabs.com/Newgrouppage9.cfm?Objectgroup_Id=2615).

## List of Publications

### Journal Paper

- Mehrnoush Mokhtarimehr, Ian Forbes, Nicola Pearsall, “LCA study of the fabrication of  $\text{Cu}_2\text{ZnSnS}_4$  (CZTS) thin film photovoltaic cells”, Japanese Journal of applied Physics, 57, 2018

### Conference Papers

- Mehrnoush Mokhtarimehr, Ian Forbes, Nicola Pearsall, “Deposition by Vacuum or Non-Vacuum?  $\text{Cu}_2\text{ZnSnS}_4$  (CZTS) precursors and their conversion”, PVSAT-14, London, UK (April 2018)
- Mehrnoush Mokhtarimehr, Ian Forbes, Nicola Pearsall, “Environmental assessment of vacuum and non-vacuum techniques for the fabrication of  $\text{Cu}_2\text{ZnSnS}_4$  thin film photovoltaic cells”, PVSEC-27, Otsu, Japan. (November 2017)
- Mehrnoush Mokhtarimehr, Zhengfei Wei, Trystan Watson, I. Forbes, N. Pearsall, “The effect of annealing time and ambient pressure on the formation of  $\text{Cu}_2\text{ZnSnS}_4$  (CZTS) thin films based on mixed powder precursors”, PVSAT-13, Bangor, UK. (April 2017)
- Mehrnoush Mokhtarimehr, Jose Marquez Prieto, Ian Forbes, Nicola Pearsall, “Macroscopic versus microscopic uniformity in  $\text{Cu}_2\text{ZnSnSe}_4$  absorber layers: the role of temperature and selenium supply”, PVSAT-12, Liverpool, UK. (April 2016)